Ab Initio and TDDFT Investigations of the Electronic Spectra of $[MoOCl_4]^-$ and of Mixed-Valency in Polyferrocenyl Pyrroles

A THESIS SUBMITTED TO THE GRADUATE SCHOOL OF

THE UNIVERSITY OF MINNESOTA BY

Casey Michael Van Stappen

IN PARTIAL FULFILLMENT OF THE REQUIREMENTS FOR THE

DEGREE OF MASTER OF SCIENCE

Advised by Dr. Victor Nemykin

September 2013

Acknowledgements

I would like to specially extend my gratitude and thanks to Dr. Victor Nemykin for his resourcefulness, insight, and guidance throughout my research both as an undergraduate and graduate student. I would also like to especially extend my deep gratitude to Dr. Paul Siders, whom has been an incredible support and aide throughout my research career. I would also to extend my appreciation to Dr. Pavlo Solntsev for his aide and contributions to dealing technical difficulties which plague computational work. I would also like to thank Wil Goestch and Jared Sabin for their parallel work in synthesis and spectroscopy. Of course, I must give thanks to my loving family, Julie and Jessica Van Stappen, and John Olson for their support throughout my life and graduate career.

This research would not have been possible without the opportunity from the University of Minnesota Duluth Department of Chemistry and Biochemistry, funding from the National Science Foundation (Grant CHE-1110455), NSF MRI (Grant CHE-0922366), support from the Minnesota Super Computing Institute, and University of Minnesota Grant-in-Aid.

"*We are made of star stuff. We are a way for the cosmos to know itself.*"

-Carl Sagan

In Loving Memory of Michael Francis Van Stappen

Abstract

The UV-Vis and magnetic circular dichroism (MCD) spectra of the d^1 oxomolybdenum tetrachloride ($[MoOCl_4]^-$) anion in C_{4v} symmetry have been calculated using the *ab initio* complete-active-space self-consistent-field (CASSCF)/multi-reference configurational interaction (MRCI) theory. The influence of active space used in these calculations was investigated, and the use of a differential treatment of charge-transfer and ligand-field type transitions through partitioning of active space was found to be effective. Additionally, the influence of Hartree-Fock exchange on the vertical excitation energies of $[MoOCl_4]^-$ has been investigated through DFT/TDDFT methods. The combined results provide a promising direction for the prediction of MCD spectroscopy in oxomolybenal complexes.

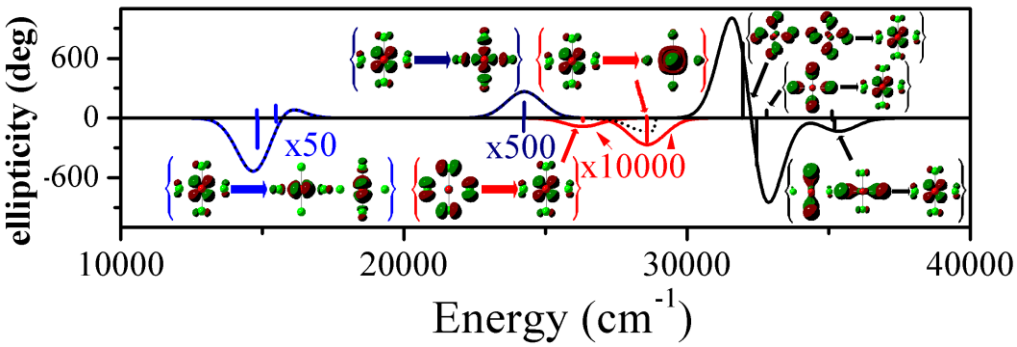

The mixed-valence properties of aromatic polyferrocenyl heterocycles have received considerable attention in recent years due to their model properties for electronic intercommunication. While α, β, and α-β saturated ferrocenyl pyrroles have been synthesized and characterized, current studies of these complexes have lacked a theoretical investigation of their electronic properties. In this study, these complexes are characterized using TDDFT methods, and their mixed-valence states explored in order to provide insight to the first oxidation process of 2,3,4,5-tetraferrocenyl-pyrrole.

Table of Contents

List of Tables

List of Figures

Chapter One: Ab Initio and TDDFT Calculation of the Electronic Spectra of $[MoOCl_4]^-$

Introduction

Molybdenum acts as the catalytic site for a variety of enzymes including oxotransferases and oxidases, which play a key role in the global cycling of arsenic, sulfur, and nitrogen.[1,2,3,4] The molybdenum-containing cofactor of these enzymes cycles through the +4, +5, and +6 oxidation states during catalytic transformation of substrate. Crystal structures of these enzymes in the +4 and +6 oxidation states have been characterized through crystallography[3,4,5]; investigating the rapid +5 oxidation state, however, relies upon spectroscopic techniques such as EPR, UV-vis spectroscopy, EXAFS/XAS, and magnetic circular dichroism (MCD).[6] Discrete inorganic analogs of the active sites of these oxomolybdenyl enzymes including several penta- and hexacoordinated Mo^V-complexes have played a key role in the understanding of native protein function.[7] The spectroscopic investigation of model compounds and characterization of their electronic structure continues to provide valuable insight into molybdopterin enzyme active centers and their functions. Generally, the results of these investigations may be interpreted using ligand-field theory and ground-state electronic structure calculations. While excited state electronic calculations have not yet been applied to the biomimetic molybdenum systems due to their large computational cost, such calculations have been applied to a variety of inorganic molybdenum compounds which mimic these systems.[8,9,10] In particular, a large body of experimental and

theoretical work has been accumulated for the relatively simple inorganic Mo(V) complex $[MoOCl_4]^-$.[8,9,11,12,13] Despite extensive investigation of this C_{4v} penta-coordinated compound, debate over the assignment of vertical electronic excitations still remains regarding the presence of the symmetry forbidden and higher energy transitions, as well as their relative energies and intensities.[8,9,11]

Magnetic Circular Dichroism (MCD) spectroscopy provides a valuable complement to absorption spectroscopy, aiding in the characterization of electronic structure and assignment of corresponding excited states. In particular, low-temperature MCD spectra of Mo(V) d^1 systems are dominated by *C*-terms.[14] *C*-terms are particularly useful in the investigation of paramagnetic systems due to their temperature dependence, making low-temperature MCD a prime tool for the investigation of $[MoOCl_4]^-$ Recently, it has become possible to calculate MCD *A*-, *B*-, and *C*-terms in inorganic compounds using time-dependent density functional theory (TDDFT)[15] and through the use of multi-reference type methods such as multi-reference configuration-interaction (MRCI) coupled with complete active space self-consistent-field (CASSCF).[16,17] The TDDFT-calculated MCD spectrum of $[MoOCl_4]^-$ has been published in an elegant work by Ziegler and co-workers.[9] These calculations, however, have raised questions regarding band assignments in the UV-Vis spectrum of $[MoOCl_4]^-$ provided earlier by several independent groups.[8,11,12] In particular, energies and intensities of the first charge-transfer (CT) transition as well as second d-d transition ($d_{xy} \rightarrow d_{x2-y2}$) were questioned on the basis of TDDFT calculations. In this paper, we will discuss energies and intensities of the MCD bands in the $[MoOCl_4]^-$ complex using the sophisticated CASSCF/MRCI approach, as well as explore the possibility of treating these kinds of systems from a

partitioned active space approach. These results will be complemented with TDDFT calculations using several exchange-correlation functionals with differing amounts of Hartree-Fock exchange. The presented results provide a better understanding of the electronic structure and spectroscopy of Mo(V) systems and present a potential approach for the treatment of larger Mo(V) molybdoenzyme analogues, making a useful step forward for understanding molybdopterin enzyme reactivity.

Computational Details

The initial geometry of $[MoOCl_4]^-$ was restricted to the C_{4v} point group and optimized at the DFT level using the following exchange-correlation functionals: Becke's three-parameter hybrid exchange functional[18] and the gradient corrections provided by Perdew, along with his 1981 non-local correlation functional[19] (B3P86) as well as the Lee-Yang-Parr non-local correlation functional[20] (B3LYP); Becke's 1988 exchange functional[21] and the gradient corrections of Perdew, along with his 1981 local correlation functional P86[19] (BP86); The 1996 pure functional of Perdew, Burke, and Ernzerhof combined with the gradient-corrected correlation functional of Perdew, Burke and Ernzerhof[22,23] (PBE1PBE); the half-and-half functional BHandH, composed of a 50/50 contribution of Hartree-Fock and LSDA (local spin density approximation) contribution to the exchange, utilizing the non-local Lee-Yang-Parr (LYP) correlation correction[20,24,25]; the half-and-half functional BHandHLYP, composed of 50/50/50 contributions from Hartree-Fock, LSDA (local spin density approximation), and Becke's 1988 exchange functional[21] to the exchange component, and utilizes the non-local Lee-Yang-Parr (LYP) correlation.[20,24,25] Additionally, the Möller-Plesset second order perturbation theory was used for pure HF optimization and electronic structure

calculations[26,27,28,29], while the CIS[30] (single-excitation configuration interaction) method was utilized for corresponding excited state calculations. The influence of basis set on the optimized geometry of $[MoOCl_4]^-$ has been well explored previously[8]; based upon this work, a DGauss full electron double-ζ basis set (DZVP) with polarization and a (18s, 12p, 9d) →(6s, 5p, 3d) contraction scheme[31] was used for molybdenum while a 6-311G(d) basis set[23] was used for remaining atoms in both DFT and TDDFT calculations. The higher quality Gaussian new triple-ζ basis set with two sets of polarization functions[32] along with the zeroth-order relativistic approximation[33] (def2-TZVPP-ZORA) was used for all atoms in both CASSCF and MRCI calculations. All CASSCF and MRCI calculations utilized the restricted-open Hartree-Fock type wavefunctions. Unrestricted Hartree-Fock type wavefunctions were calculated via DFT for initial guesses in the DFT-CASSCF-MRCI method utilizing partitioned (1,5) and (13,7) active spaces; a set of diffuse functions from the Dunning aug-cc-pVTZ basis[34] were added to the def2-TZVPP-ZORA basis (def2-aug-TZVPP-ZORA) in these calculations. Geometry optimization, frequencies, single point energy, and TDDFT calculations were carried out on the Linux version of the Gaussian09 program.[35] All CASSCF and MRCI calculations were performed using the Linux version of ORCA 2.9.0.[36] which utilizes the libint2 library for two electron integral calculations.[37] The first 25 vertical excitation energies were calculated for $[MoOCl_4]^-$ in the case of TDDFT.

The active spaces of the CASSCF and MRCI calculations were chosen based upon work performed by Carducci, Brown, Solomon, and Enemark[11] and from guidelines presented by Veryazov and Roos[38] in order to accurately compare and assess the electronic band assignments of experimental low temperature $[MoOCl_4]^-$ MCD spectrum.

The lowest 24 vertical excitation energies were considered in the (9,9) MRCI calculations of the uB3LYP, and uB3P86 optimized geometries. Additionally, a higher unoccupied orbital was found to be necessary in the uBP86 geometry, where the active space was expanded to (9,10), for which the first 16 states were calculated. A (9,9) active space was used for the uPBE1PBE optimized geometry, and the first 16 excited states calculated. In order to fully model the transitions previously assigned by Solomon and co-workers[11], a larger (13,11) active space was also utilized; however, due to the computational cost of calculations involving large active spaces, this expanded model was limited to the uPBE1PBE optimized geometry. In studying the influence of active space on the vertical electronic excitation energies, the CASSCF wavefunctions generated for each of the active spaces described above were utilized, and orbitals were rotated in or out from the active to the internal or external space as necessary. The DFT-CASSCF-MRCI study partitioned the desired (13,11) active space into (13,7) and (1,5) active spaces in the CASSCF and MRCI portions of the calculation. All electronic states necessary to include the single electron vertical excitations were used in each; the first 7 electronic states were considered for the (13,7) active space, and the first 5 for the (1,5) active space.

Results and Discussion

Comparison of X-Ray and DFT predicted geometries

The X-ray crystallographically[39] determined and DFT predicted bond distances and angles for $[MoOCl_4]^-$ are provided in table 1.

Table 1. Geometries of X-ray and DFT optimized $[MoOCl_4]^-$ structure.

CSD code/method	M=O Å	Mo-Cl Å	O-Mo-Cl deg
TIXLIV[d]	1.589	2.328	104.84
PASCMO[a]	1.609	2.333	105.26
JAJRIV[e]	1.640	2.355	100.94
LIMRUV[f]	1.646	2.342	105.24
NABQIQ[b]	1.668	2.354	101.53
PASCMO1[c]	1.717	2.337	104.52
average	1.645	2.342	103.72
uBP86 (0%)	1.716	2.392	105.28
uB3LYP (20%)	1.698	2.400	105.28
uB3P86 (20%)	1.690	2.375	105.30
uPBE1PBE (25%)	1.685	2.373	105.21
uBHandHLYP (50%)	1.669	2.381	105.21
uBHandH (50%)	1.658	2.344	105.33
uMP2 (100%)	1.638	2.377	106.63

Percentages in parentheses refer to percent Hartree-Fock exchange contribution to the exchange-correlation functional. X-ray structure superscripts refer to corresponding publications, provided in Reference 34. Significant differences are seen between the experimentally determined geometries of $[MoOCl_4]^-$, with ranges of 0.128 Å and 4.314º in the Mo=O bond lengths and O-Mo-Cl bond angles, respectively. Deviations in the Mo-Cl bond distances are much smaller, at most 0.027 Å. Because of the ranges of experimental Mo=O bond distances and O=Mo-Cl angles, their comparison to DFT-

predicted geometries is rather arbitrary. The influence of basis set on geometry optimization at the DFT level has been well explored previously[9] and was not explored further in this study. It may be inferred from table 1 that as the Hartree-Fock exchange contribution to the exchange-correlation functional increases, there is a general decrease in both Mo-Cl and Mo=O bond lengths. This trend is consistent and linear for the Mo=O bond length, as illustrated in figure 1.

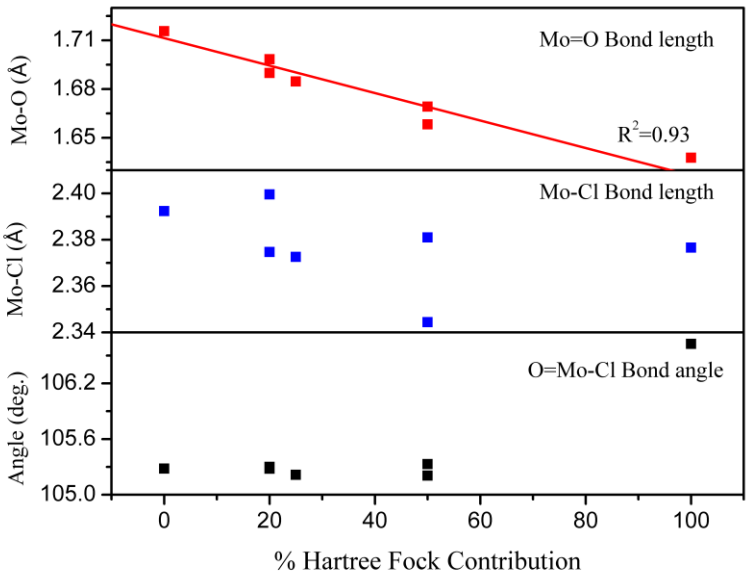

Figure 1. Dependence of the optimized bond distances and angles on the percent Hartree-Fock exchange contribution to the exchange-correlation functional.

The Mo-Cl bond length and O-Mo-Cl angle both decrease with increasing Hartree-Fock contribution to the exchange-correlation functional; however, these geometric factors appear to be more sensitive to the exchange-correlation functional employed than to the Mo=O bond length, generating a more complex trend. For *ab initio*

and DFT methods, typical criteria of ±0.03 Å for bond lengths and ±1° or less for angles are used to evaluate the goodness of fit.[40] Using these criteria, all methods provide reasonable estimates of the Mo=O and Mo-Cl bond lengths. The O=Mo-Cl angle is overestimated in all cases, though this is most pronounced in the MP2 optimized geometry.

CASSCF predicted electronic structure of $[MoOCl_4]^-$ complex

Orbital energies, compositions, and surfaces were calculated using CASSCF for the uBP86, uB3LYP, uB3P86, and uPBE1PBE DFT optimized geometries. Since the goal of these CASSCF calculations was to provide an accurate initial wavefunction for MRCI calculations and MCD generation, active spaces were selected based upon previous experimental band assignments.[11,12] Thus, calculations using a (9,9) active space were performed for the uB3LYP, uB3P86, and uPBE1PBE geometries; due to the presence of a near degenerate virtual orbital in the case of the uBP86 geometry, the active space for this geometry was expanded to (9,10) to allow for better convergence. To fully model all experimentally assigned transitions, the active space of the uPBE1PBE geometry was expanded to (13,11).

Geometric Dependence

Previous computational studies[8] have investigated the sensitivity of the molecular orbital energies on the O-Mo-Cl bond angle and the Mo=O and Mo-Cl bond lengths. It has been shown that variation in the Mo=O bond length has the greatest effect on the energy of the out-of-plane molybdenum-centered d_{z2}, d_{xz}, and d_{yz} orbitals with a much smaller effect on the energies of the in-plane d_{x2-y2} and d_{xy} orbitals. Meanwhile, the O-Mo-Cl bond angle is believed to have a greater effect on energies of the in-plane orbitals.

An increase in Mo-Cl bond length is expected to result in a lowering of energies for both molybdenum and chlorine in-plane orbitals. Increasing the O-Mo-Cl bond angle is expected to decrease the energy of in-plane molybdenum and chlorine orbitals, while raising the energy of out-of-plane Cl^- centered orbitals due to an increase in anti-bonding character. A comparison of the CASSCF calculated orbital energies is provided in figure 2.

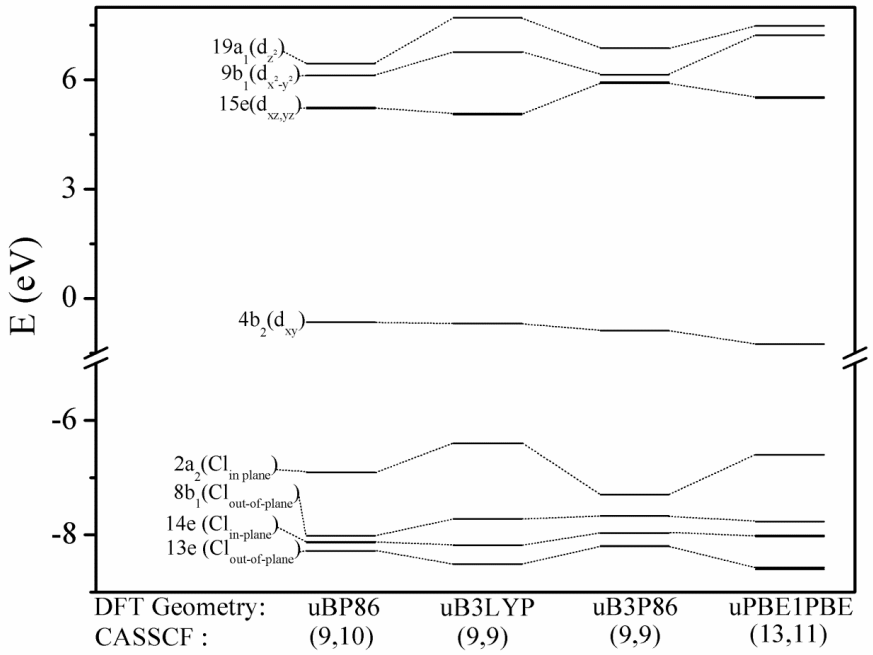

Figure 2. Molecular orbital energies for each respective geometry and active space generated using the CASSCF method.

Correlation diagrams of the energetic trends for each orbital as a function of the terminal oxomolybdenyl bond-length are provided in S1-S2. It can be seen that as the Mo=O bond length decreases the out-of-plane d_{xz}, d_{yz}, and d_{z2} orbital energies increase,

while the in-plane d_{xy} orbital energies decrease slightly. The energy of the in-plane unoccupied d_{x2-y2} orbital is seen to increase with decreasing Mo=O bond length as well; however, there is not a clear trend in the energetic gap between in-plane and out-of-plane d-orbitals due to the complex dependence of the in-plane orbitals on Mo-Cl bond length and O-Mo-Cl bond angle.

Orbital Ordering/Characteristics

The molecular orbital composition diagrams predicted for the (9,10), (9,9), and (13,11) CASSCF calculations can be found in S3 –S7, along with molecular orbital surfaces of interest in S8 Molybdenum centered d-orbitals are found in the order of $d_{xy} < d_{xz,yz} < d_{x2-y2} < d_{z2} < 5s$, with the singly occupied HOMO orbital being composed primarily of the d_{xy} orbital with small contributions from the chlorine p_y orbitals. This agrees with the ordering predicted by ligand field theory[41] (LFT), experimental EPR, UV-Vis, and MCD spectral data,[11,12,42] as well as previous theoretical studies.[8,9,13]

The HOMO-1 to HOMO-6 molecular orbitals are found to be predominantly chlorine centered, with the greatest contributions of ~13% Mo and ~3% O being observed (in this case, for the B3LYP- and PBE1PBE-optimized geometries, respectively). The occupied, ligand-centered orbitals generally follow the $13e < 14e \approx 8b_2 < 2a_2$ ordering where the $8b_2$ and 14e sets are near degenerate in energy. It can be noted that the in-plane chlorine-centered 14e orbitals are higher in energy than the out-of-plane 13e orbitals, and the in-plane $2a_2$ orbital has higher energy than the out-of-plane $8b_2$, as predicted by Xα calculations.[13,43]

CASSCF-MRCI Vertical Excitation Energies and MCD

To calculate the vertical excitation energies of the $MoOCl_4^-$ complex and investigate the influence of geometry on said excitation energies, the CASSCF generated wavefunctions for the uBP86, uB3LYP, uB3P86, and uPBE1PBE DFT optimized geometries were used as initial guesses for their respective MRCI calculations. A (9,9) active space was utilized for the uB3LYP, uB3P86, and uPBE1PBE geometries, while a (9,10) active space was used for the uBP86 geometry due to the close energies of the Mo d_{z2} and 5s orbitals for this model. Additionally, the active space was expanded to (13,11) to include a lower set of degenerate ligand-centered orbitals for the uPBE1PBE optimized geometry.

The MRCI-predicted vertical excitation energies, as well as experimental spectra adopted from the literature are labeled according to the band assignments proposed by Solomon and co-workers[11] in order to provide a clear comparison of MRCI calculations with the experimental UV-Vis and MCD spectra. Experimental band assignments were made based upon a ligand-field basis along with DVXα calculations performed by Deeth[13], where $[MoOCl_4]^-$ was treated with a C_{4v}-symmetric molecular orbital scheme. Higher-energy excitations found in simulated spectra that are beyond those assigned previously[11,12] are labeled in order of their occurrence.

Calculation of MCD using MRCI with (9,9) and (9,10)active spaces

Energies of the respective UV-vis and MCD bands are provided in table 2 for the (9,9) and (9,10) CASSCF calculations, and corresponding oscillator strengths in S9. Additionally, ΔE has been provided for the ^2E states.

Table 2. Summary of CASSCF-MRCI vertical excitation energies for $[MoOCl_4]^-$ (cm^{-1}).

		Geometry:	uBP86		uB3LYP		uB3P86		uPBE1PBE			
	Electronic	CASSCF:	9,10		9,9		9,9		9,9		13,11	
Band	Transition	experimental[a]		Δ		Δ		Δ		Δ		Δ
1	$d_{xy} \rightarrow d_{xz,yz}$	15,100	14,933	670	15,508	629	16,535	671	16,051	797	16,293	670
			15,603		16,137		17,206		16,848		16,933	
2	$d_{xy} \rightarrow d_{x2-y2}$	23,800	22,673		23,026		23,796		23,905		24,259	
3	$2a_2 \rightarrow d_{xy}$	24,200[b]	33,910		32,402		34,437		34,238		33,506	
4	$8b_1 \rightarrow d_{xy}$	26,900	40,751		38,950		41,205		40,990		39,313	
5	$14e \rightarrow d_{xy}$	28,000	38,747	302	37,894	656	39,567	688	39,033	601	38,405	565
			39,049		38,550		40,255		39,634		38,970	
6	$13e \rightarrow d_{xy}$	30,000	N.A.[c]		N.A.[c]		N.A.[c]		N.A.[c]		41,072	179
											41,251	
7	$d_{xy} \rightarrow d_z^2$	N.A.[d]	25,637		27,796		27,856		28,385		28,843	
8	$2a_2 \rightarrow d_{xz,yz}$	N.A.[d]	47,035	531	44,330	489	46,301	478	47,730	1,031	45,973	535
			47,566		44,819		46,779		48,761		46,508	
9	$8b_1 \rightarrow d_{xz,yz}$	N.A.[d]	40,891	432	38,498	421	42,984	411	41,655	934	40,917	434
			41,323		38,919		43,409		42,589		41,351	

[a]Reference 7. [b]Clearly observed only in the $[MoOCl_4(H_2O)]^-$ complex. [c]Not calculated due to limited active space considerations. [d]Unassigned in the experimental spectrum.

It can be seen from table 4 that the energies of the calculated d-d transitions correspond well with their experimentally proposed assignments. However, the energies of all LMCT type transitions are significantly overestimated. UV-vis and MCD spectra calculated using a CASSCF-MRCI (9,9 or 9,10 active space) approach for four DFT-based geometries (uBP86, uB3LYP, uB3P86, and uPBE1PBE) are shown in figures 3 and 4 in order of increasing HF-contribution to the initial geometry optimization.

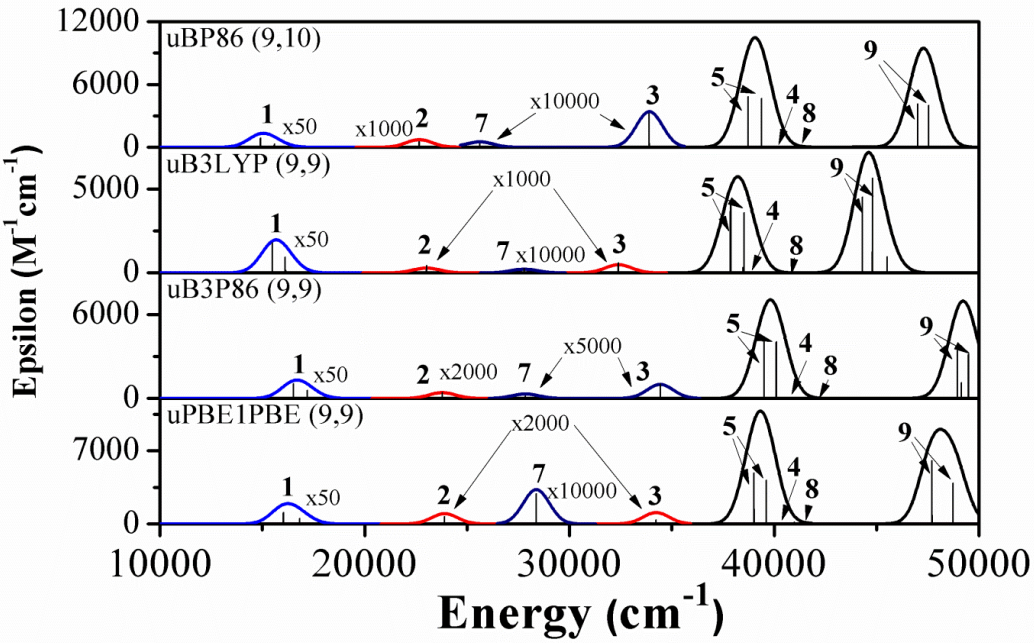

Figure 3. Comparison of UV-Vis spectra of $[MoOCl_4]^-$ calculated using the CASSCF-MRCI method for the four respective DFT-optimized geometries under consideration.

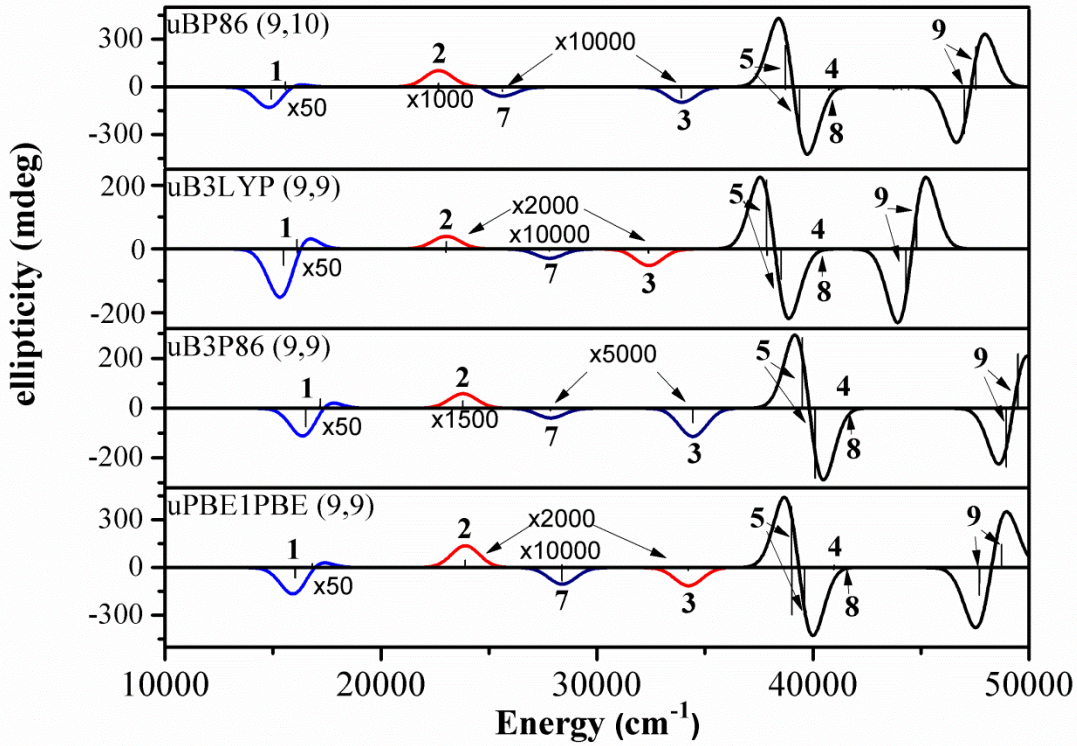

Figure 4. Comparison of MCD spectra of $[MoOCl_4]^-$ calculated using the CASSCF-MRCI with method with a (9,9) active space (9,10 for BP86) for the four respective DFT-optimized geometries under consideration.

Correlation diagrams of the transition energies as a function of Mo=O bond length are provided in figures 5 and 6. Because the theoretical method (CASSCF-MRCI) is consistent across the (9,9) active space calculations (and close for the uBP86 (9,10)), shifts in energies of the calculated transitions can be attributed primarily to geometric factors in $[MoOCl_4]^-$ as predicted by the varying unrestricted DFT methods.

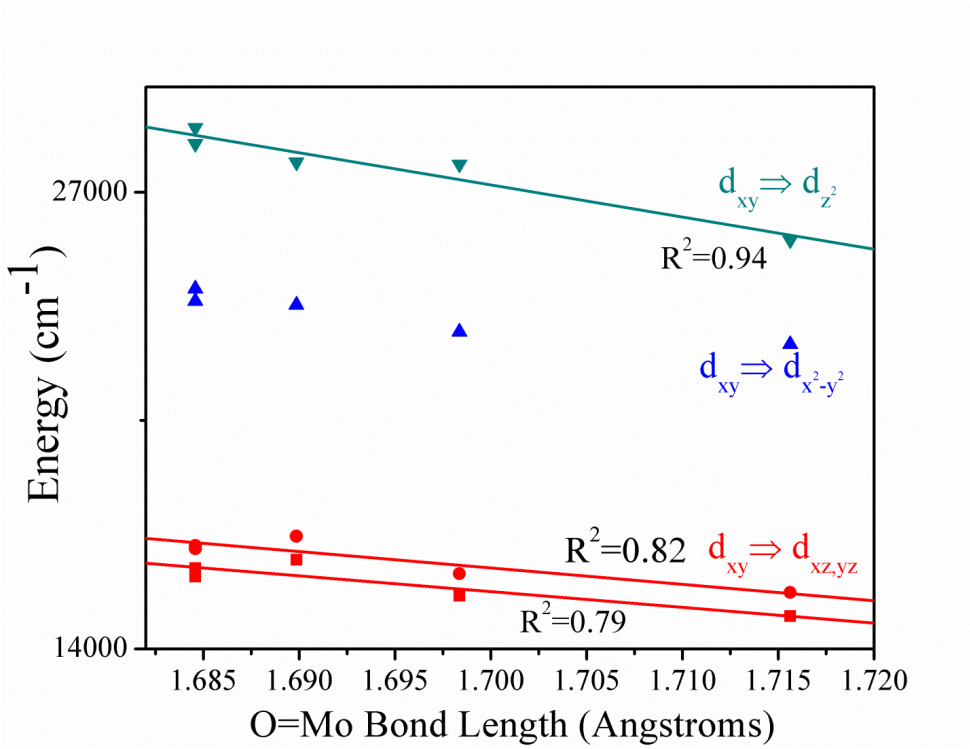

Figure 5. Dependence of MRCI-CASSCF calculated d-d transitions on Mo=O bond length

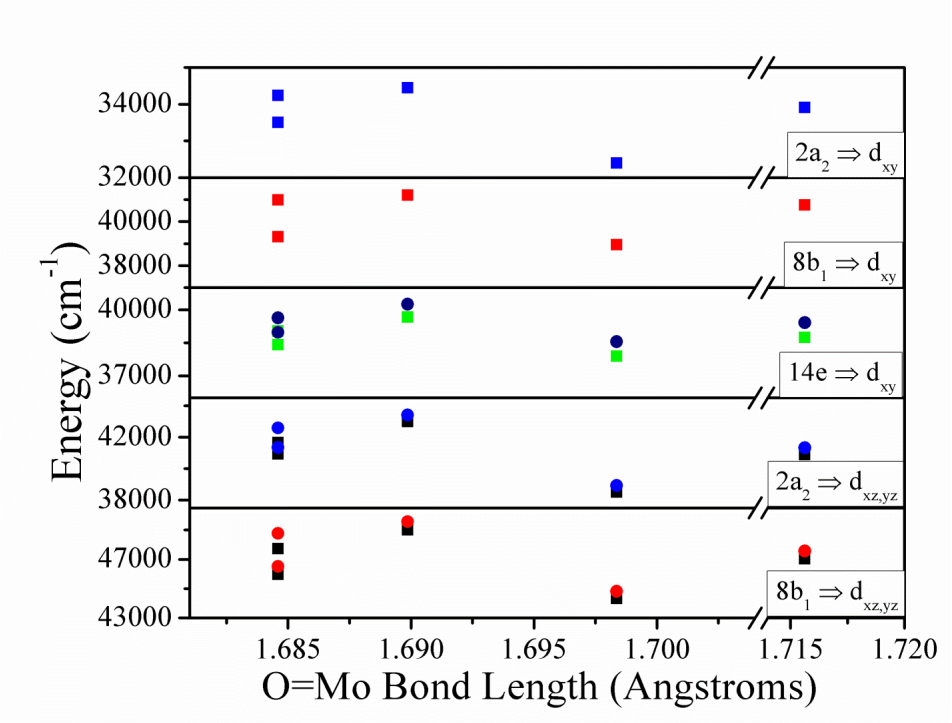

Figure 6. Dependence of CASSCF-MRCI calculated ligand-to-metal charge transfer transitions on Mo=O bond length

The spin-orbit coupling and magnetic-field splitting analyses of the observed transitions for the $[MoOCl_4]^-$ d^1 system have been discussed previously from a group-theoretical approach[11], and are expanded here. Inclusion of spin-orbit coupling results in a ground state of Γ_7 symmetry for $[MoOCl_4]^-$ in C_{4v}', as shown in figure 7. Degenerate ^2E states are split into Γ_6 and Γ_7 spinor functions. Due to the opposite signs of the Mo^{+5} and Cl^- spin-orbit coupling constants (900 and -587 cm^{-1}, respectively[41,44]), the Γ_6 function lies lower in energy for molybdenum centered transitions, while Γ_7 is lower for chlorine centered transitions. Spin-orbit selection rules allow $\Gamma_7 \leftarrow \Gamma_7$ transitions with x, y, and z polarization; $\Gamma_6 \leftarrow \Gamma_7$ with x and y polarization.

The presence of an external magnetic field along the z axis lowers the molecular symmetry to C_4'. The Zeeman perturbation further splits states of C_{4v}' Γ_6 symmetry into C_4' Γ_5, Γ_6 Kramer's doublets; C_{4v}' Γ_7 into C_4' Γ_7, Γ_8 doublets. From the C_{4v}' ground state, the external magnetic-field perturbation generates the Γ_7 and Γ_8 Kramer's doublet, with Γ_7 as the lower energy component. At conditions of 4.2 K and 5 T the population ratio of Γ_7:Γ_8 is about 5:1, making transitions that arise from Γ_7 more intense than those from Γ_8. In C_4', states arising from $\Gamma_5 \leftarrow \Gamma_7$ transitions are RCP allowed, resulting in a negative signal, while $\Gamma_7 \leftarrow \Gamma_7$ transitions are LCP allowed, resulting in a positive signal according to MCD selections rules. Weaker signals from the less-populated Γ_8 state ($\Gamma_6 \leftarrow \Gamma_8$ RCP, $\Gamma_8 \leftarrow \Gamma_8$ LCP) are not considered further in this discussion, although they contribute to the CASSCF-MRCI predicted band-shapes.

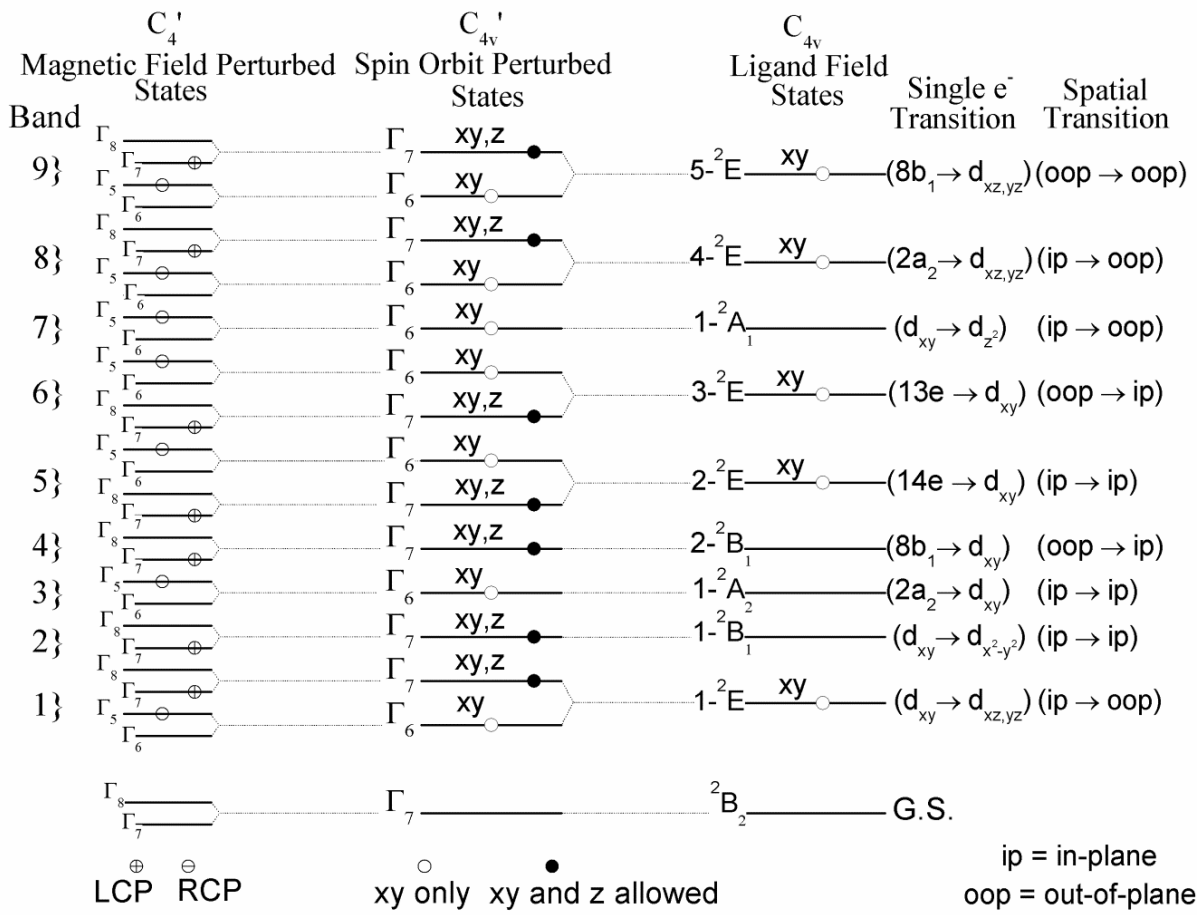

Figure 7. State diagram for the predicted transitions of the $[MoOCl_4]^-$ in C_{4v} symmetry with the inclusion of spin-orbit and magnetic-field splitting effects. LCP and RCP indicate transitions which are allowed from the Γ_7 ground state, for left and right circularly polarized light.

Band 1, which has been assigned through both experiment and theory[8,9,11,12,13] is composed primarily of the $d_{xy} \rightarrow d_{xz,yz}$ transition contributions, giving rise to the 1-^2E first excited state. This state is observed to undergo splitting into the Γ_6 and Γ_7 spinor functions with the inclusion of spin-orbit coupling. According to MCD selection rules, the resulting $\Gamma_5 \leftarrow \Gamma_7$ RCP allowed and $\Gamma_7 \leftarrow \Gamma_7$ LCP allowed transitions give rise to a temperature-dependent Faraday *C*-term. These terms would have equal intensities if only in-state SOC were to be considered; including out-of-state SOC, in particular coupling with bands 2 and 4, accounts for the relative weakness of the positive peak. This mechanism was demonstrated by Gerstman and Brill for cupric compounds previously.[45] The MRCI-module properly takes these effects into consideration as demonstrated in figure 4. Experimentally, the spin-orbit splitting of band 1 was determined to be 810 cm^{-1}, slightly less than the spin-orbit coupling constant for the free Mo^{+5} ion.[41] The MRCI-calculated spin-orbit splitting of band 1 is underestimated for each geometry, being closest estimated in the (9,9) active space calculation for the uPBE1PBE optimized geometry as shown in table 2. The MCD intensities for these transitions are well approximated by the MRCI calculations. The experimental/calculated intensity ratios for the observed $\Gamma_5 \leftarrow \Gamma_7$ transition were found to be ~1:1 with the single-crystal MCD (at 4.2 K, 5.0 T) and 2:1 with the mull MCD (at 4.2 K, 5.0 T). Predicted energies for the SOC split $\Gamma_7 \leftarrow \Gamma_7$ and $\Gamma_5 \leftarrow \Gamma_7$ transitions also increase linearly with increasing Mo=O bond length, as shown in figure 5.

Band 2, assigned to the $d_{xy} \rightarrow d_{x2-y2}$ excitation, is LCP allowed from the $\Gamma_7 \leftarrow \Gamma_7$ transition. As mentioned before, this band appears as a weak, symmetry forbidden state which gains intensity through vibronic coupling and SOC with excited states. An

experimental/calculated intensity ratio of 4:1 was observed for the 4.2 K single crystal MCD at 5 T. Additional intensity can be gained through an E vibrational mode, allowing the 1-$^2B_1 \leftarrow {}^2B_2$ transition vibrationally in *xy*-polarization, which was not included in calculations. As the Mo=O bond length increases, the energy of the transition appears to decrease as illustrated in figure 5. However, due to the limited number of geometries studied, a linear assumption cannot be made for the CASSCF-MRCI predicted energies.

Band 3 has been assigned as the first LMCT from $2a_2 \rightarrow d_{xy}$, which corresponds to the RCP allowed $\Gamma_5 \leftarrow \Gamma_7$ transition. This transition is symmetry forbidden with a predicted intensity equal to one tenth that of band 2. This transition is not observed experimentally in $[MoOCl_4]^-$, likely due to the combination of its weak intensity and the "sloping background" of the spectrum. However, it is observed in the closely related $[MoOCl_4(H_2O)]^-$ complex,[11] whose electronic spectra corresponds reasonably well with that of $[MoOCl_4]^-$. Therefore, for our purposes, comparisons involving the calculated energies of band 3 to experimental will be made based upon the assignment of band 3 in the $[MoOCl_4(H_2O)]^-$ MCD and UV-Vis spectra, as proposed by Solomon, et. al.[11] Due to the dependence of the ligand and in-plane Mo 4d orbitals on O-Mo-Cl bond angle and Mo-Cl bond length, there is no clear correlation of band 3 energy with Mo=O bond length (figure 6).

Band 4 has been assigned to the symmetry forbidden 2-$^2B_1 \leftarrow {}^2B_2$ ($8b_1 \rightarrow d_{xy}$) transition, which may gain intensity through SOC in both xy and z polarization as a $\Gamma_7 \leftarrow \Gamma_7$ LMCT. While found as the first LMCT of $[MoOCl_4]^-$, the MRCI-calculated energies place this transition as the third LMCT, slightly higher than the large negative pseudo-*A* term arising from the $14e \rightarrow d_{xy}$ transition. Due to the lesser overlap of the

out-of-plane chlorine orbitals with the in-plane molybdenum d_{xy} orbital, the intensity of band 4 is anticipated to be weaker than that of band 3, which originates from an in-plane to in-plane transition.[46]

Band 5, as mentioned above, forms a large, Faraday *C*-term which arises from the symmetry allowed 2-$^2E \leftarrow {}^2B_2$ (14e $\rightarrow$ d_{xy}) LMCT transition. It can be seen in both figures 9 and 10 that this band forms the most prominent feature of the calculated $[MoOCl_4]^-$ UV-Vis and MCD spectra. The large Faraday *C*-term of the experimental MCD spectrum, centered at ~30,000 cm^{-1}, has been partially attributed to this band. Interestingly, this transition was considered the weaker component arising from the charge transfer from the out-of-plane chloride p-π orbitals to d_{xy}. In this study, it has been found as a charge-transfer from the in-plane chloride p-π orbitals, resulting in a greater intensity.

Band 6 corresponds to the third experimentally assigned LMCT transition, arising from the 3-$^2E \leftarrow {}^2B_2$ (13e $\rightarrow$ d_{xy}) which is symmetry allowed in x,y polarization. This band has been assigned experimentally[2] as the primary contributor to the large Faraday *C*-term around 30,000 cm^{-1}. This transition does not appear in the spectra presented in figures 9 or 10 because the lower energy degenerate 13e orbitals are not included in the (9,9) or (9,10) active spaces.

Band 7 arises from symmetry forbidden 1-$^2A_1 \leftarrow {}^2B_2$ ($d_{xy} \rightarrow d_{z2}$) transition, the highest energy of the possible d-d excitations. This transition becomes allowed in xy-polarization with the inclusion of SOC, leading to a $\Gamma_5 \leftarrow \Gamma_7$ transition under MCD selection rules. While not assigned definitively, this transition has been suggested to appear at 34,400 cm^{-1}.[12] It can be seen that the energies predicted by CASSCF-MRCI

range from ~25,600 to ~28,800 cm^{-1}, depending upon geometry, which would place this transition in the low, sloping background of the experimental spectra. Based upon the quantitative results for the d-d transitions which compose bands 1 and 2, along with the very weak predicted intensity of band 7, the presence of the $d_{xy} \rightarrow d_{z2}$ transition in the MRCI calculated range is possible, but may be obscured by the intense bands 4 and 5. As expected from the dependence of the out-of-plane Mo-d orbitals on the terminal Mo=O bond, a linear correlation of the transition energy with Mo=O bond length is seen, as shown in figure 5. This follows the same pattern observed for the $d_{xy} \rightarrow d_{xz,yz}$ transition.

Bands 8 and 9, both previously unassigned likely due to their high energies and possible convolution with bands 5 and 6, arise from the $4\text{-}^2E \leftarrow {}^2B_2$ and $5\text{-}^2E \leftarrow {}^2B_2$ ($2a_2 \rightarrow d_{xz,yz}$ and $8b_2 \rightarrow d_{xz,yz}$, respectively) transitions, producing Faraday *C*-terms. A relatively weak intensity for band 8 is observed due to the poor overlap of the in-plane chlorine ligand p_y orbitals with the out-of-plane molybdenum $d_{xz,yz}$ degenerate set.[41,46] Conversely, a higher energy Faraday *C*-term is observed for band 9 from the excitation of the out-of-plane chlorine p-orbitals to the out-of-plane molybdenum $d_{xz,yz}$ orbitals. Experimentally, the large Faraday *C*-term centered around 30,000 cm^{-1} was assigned to the overlapping $14e \rightarrow d_{xy}$ and $13e \rightarrow d_{xy}$ transitions, both of which are symmetry allowed. To model the $13e \rightarrow d_{xy}$ transition and investigate this assignment, the active space for the uPBE1PBE geometry was expanded to (13,11) to include the lower degenerate ligand 13e orbitals. The resulting calculated UV-Vis and MCD spectra, along with the corresponding experimentally observed spectra as adopted from Reference 11, are shown in figures 8 and 9.

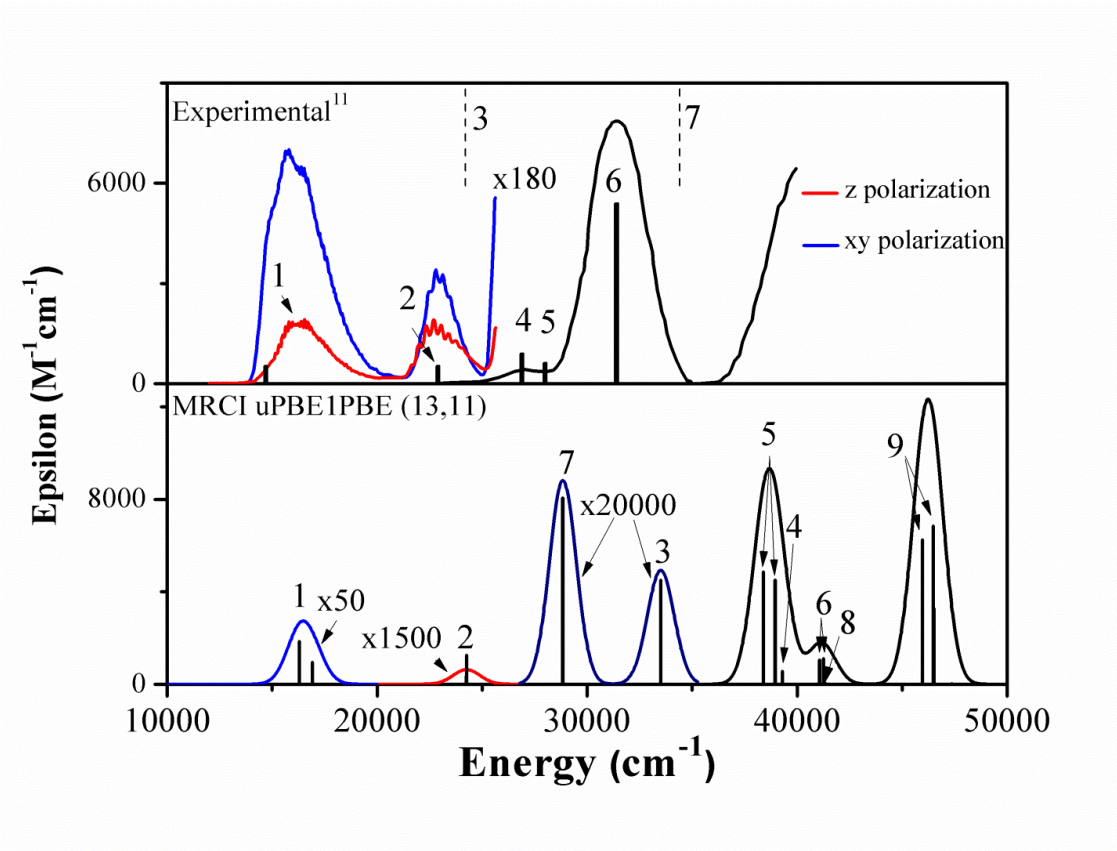

Figure 8. Comparison of the room temperature experimental UV-Vis spectrum, as adopted from Reference 11, with the (13,11) CASSCF-MRCI calculated spectrum for the uPBE1PBE DFT-optimized geometry.

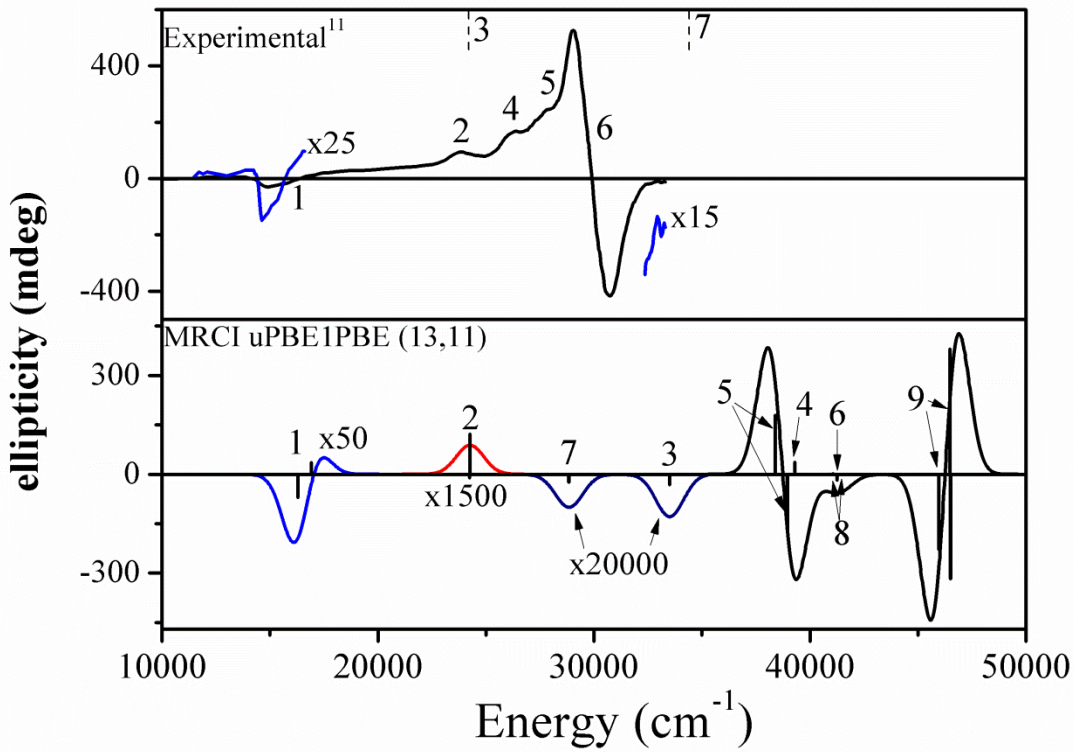

Figure 9. Comparison of the 5K, 5T experimental MCD spectrum of $[MoOCl_4]^-$, as adopted from Reference 11, and the (13,11) CASSCF-MRCI calculated spectrum for the uPBE1PBE DFT-optimized geometry.

These spectra include band 6 which appears as a Faraday *C*-term shifted approximately 3000 cm^{-1} higher in energy than band 5; the positive sign of this transition is offset by the negative portion of band 5. This transition has a relatively low intensity due to the poor overlap of the out-of-plane chlorine p orbitals with the in-plane d_{xy} orbital.[46] A small gaussian band can be seen in the experimental spectrum which appears to be shifted similarly, potentially corresponding to band 6. This band appears in a region where proposals for the presence of possible $d_{xy} \rightarrow d_{z2}$ (band 7), $8b_2 \rightarrow d_{xy}$ (band 4), and $14e \rightarrow d_{xz,yz}$ (band 5) transitions have been made.[12]

The CASSCF-MRCI method accounted for all expected d-d transitions with only small energetic errors. The general increase in energy for d-d transitions with decreasing O=Mo bond length was observed. The two lowest energy d-d transitions have been well established in experiment and previous computational studies,[8,11,12,13] and are again confirmed here with good energetic agreement. The $d_{xy} \rightarrow d_{z2}$ transition was tentatively proposed to occur at ~34,400 cm^{-1} by Sabel and Gewirth[12]; however, due to factors including the consistency of the energies of the lower calculated d-d transitions, the extremely weak intensity of the $d_{xy} \rightarrow d_{z2}$ transition, and the appearance of bands 6 and 8 in the same energetic region relative to the large and intense Faraday *C*-term, it is proposed that this excitation occurs at a somewhat lower energy. While there are no clear linear energetic trends observed for the LMCT transitions as a function of terminal oxomolybdenum bond length, the calculated energies of these bands consistently overestimate those observed experimentally[2] by ~9,000-14,000 cm^{-1}, as demonstrated in S11. The relative shifts of the LMCT's are consistent between geometries for bands 3-5 as well as 8 and 9, as shown in figure 4.

Exploration and Partitioning of the (13,11) Active Space

The CASSCF-MRCI (13,11) predicted MCD spectrum is able to account for all experimentally assigned transitions with proper sign, as well as predict the presence of unassigned transitions in the experimental spectrum giving rise to bands 3, 7, 8, and 9. These results are useful in better understanding of the electronic spectra of $[MoOCl_4]^-$; however, the large overestimation of all LMCT vertical excitation energies shows the limited ability of this particular approach, as applied by the current study, in predicting spectra containing charge-transfer transitions. While the CASSCF method is well known

to overestimate dynamic correlation, deviations (up to ~2 eV for band 4) of the LMCT's are still unexpectedly large for a charge-transfer type transition.[47] This raises question of why such a drastic shift is observed for the LMCT transitions in this particular system, and how to better estimate the energies these particular vertical excitations.

The initial impetus in calculating these electronic excitations, naturally, is to include all orbitals necessary to describe the desired spectrum in the active-space of both the CASSCF and MRCI calculations. However, this "one-shot" kind of approach provided no detail about the configurational interactions between excited states. To investigate the influence of electronic states involving the virtual d-orbitals on the LMCT states, and conversely the influence of the LMCT electronic states on calculated d-d transitions, the active spaces used in the MRCI-MCD calculation were varied for each of the geometries previously considered. The same CASSCF wavefunctions, solved for the complete active spaces discussed above, were used as initial guesses.

First, the energetic influence of electronic states involving the unoccupied d-orbitals on the LMCT vertical electronic excitations was investigated. In the first of these calculations the higher d_{x2-y2} and d_{z2} orbitals were moved from the active space to the external space in the MRCI calculation; second, all unoccupied virtual orbital were moved from the active space to the external space. The resulting energetic trend for the calculated LMCT's (as well as possible d-d transitions) is illustrated in figure 10 for the DFT-optimized uPBE1PBE geometry; energies for the LMCT's which compose bands 3, 4, 5, and 6 for each geometry are provided in table 3. Trends for the uBP86, uB3LYP, and uB3P86 geometries are provided in S12 through S14; energies for each active space and geometry in which $d_{xz,yz}$ are the only virtual orbitals considered are provided in S15.

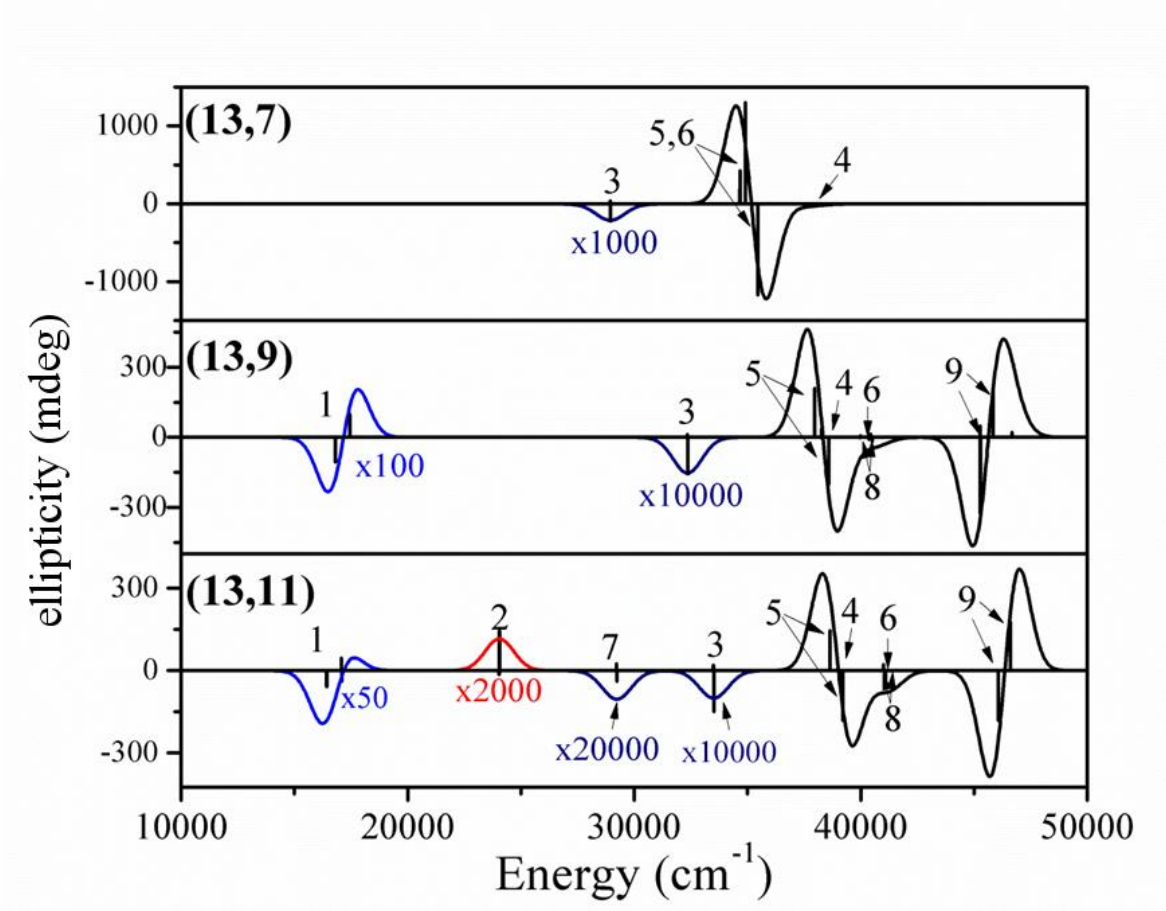

Figure 10. Comparison of MRCI-calculated MCD spectra for the (13,7), (13,9), and (13,11) active spaces, using the uPBE1PBE DFT-optimized geometry.

Table 3. Compilation of LMCT energies for the varying active spaces of each geometry.

		DFT-optimized Geometry											
	Active	uBP86			uB3LYP			uB3P86			uPBE1PBE		
Band	Space:	(9,10)	(9,7)	(9,5)	(9,9)	(9,7)	(9,5)	(9,9)	(9,7)	(9,5)	(13,11)	(13,9)	(13,7)
3		33,910	31,694	26,591	32,402	31,354	28,184	34,437	32,656	28,530	33,506	32,352	28,947
4		40,751	38,728	33,601	38,950	37,950	34,683	41,205	39,537	35,231	39,514	38,271	34,675
5		38,747	36,908	32,531	37,894	36,934	33,995	39,567	38,127	34,571	38,657	37,973	34,915
		39,049	37,636	33,265	38,550	37,591	34,608	40,255	38,771	35,189	39,215	38,596	35,461
6		---	---	---	---	---	---	---	---	---	41,020	40,375	37,570
		----	---	---	---	---	---	---	---	---	41,091	40,517	37,630

It can be clearly seen that as unoccupied orbitals (and in turn electronic states involving them) are moved from the active space to the external space, the LMCT vertical excitations decrease in energy. While moving the d_{z2} and d_{x2-y2} orbitals from the active space into the external space does affect these energies, the removal of the $d_{xz,yz}$ orbitals has the most dramatic effect on the LMCT energies. Interestingly, the vertical excitation comprising band 6 shifts significantly higher in energy with the inclusion of electronic states involving the $d_{xz,yz}$ orbitals. This makes it difficult to formulate an argument as to whether or not this band is convoluted with band 5 in the large Faraday *C*-term, which appears as the distinguishing feature of the $[MoOCl_4]^-$ MCD spectrum; it would appear this shift is dependent on the degree of interaction of the 3-^2E with the 1-$^2E_2$, 4-$^2E_2$, and 5-$^2E_2$ electronic states.

In addition to examining the influence of electronic states involving the virtual d-orbitals on the relative energies of the LMCT vertical electronic excitations, the effects of the LMCT electronic states on one another as well as on the d-d transition states were investigated. The influence of the LMCT electronic states on one another was explored by considering only the fully occupied orbitals and the SOMO-d_{xy}; beginning with a (3,2) active space, ligand orbitals were added and/or rotated into the active space from the internal space until all ligand-centered orbitals which had been previously considered were included ((9,5) for the BP86, uB3LYP and uB3P86 geometries, and (13,7) for the uPBE1PBE geometry). A representative illustration of these results for the uPBE1PBE geometry, focusing on the 14e$\rightarrow d_{xy}$ transition, is provided in figure 11. Vertical excitation energies and for bands 3, 4, 5, and in the uPBE1PBE-geometry, 6, for each

active space and geometry considered are provided in S16; additionally, representative illustrations comparing LMCT energies for the uBP86, uB3P86, and uB3LYP geometries are provided in S17 through S19.

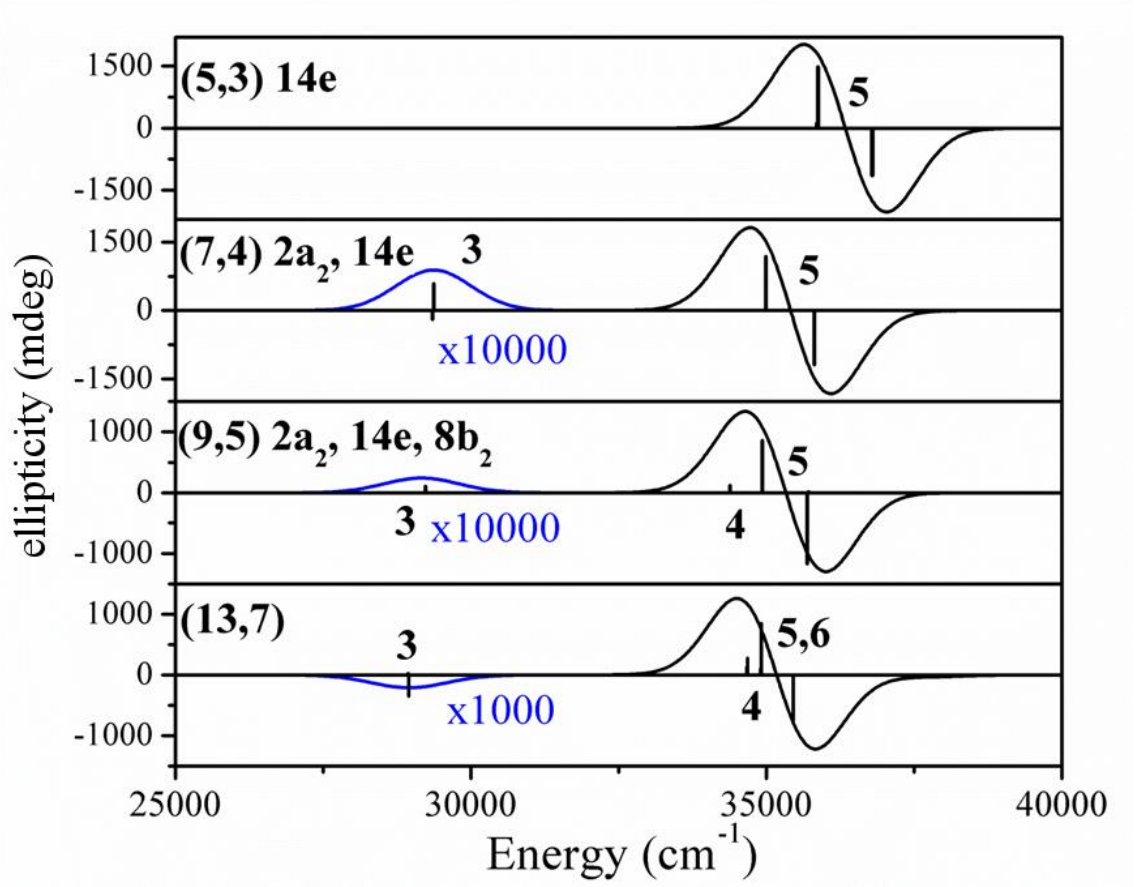

Figure 11. Comparison of MRCI-calculated MCD spectra for the (5,3), (7,4), (9,5), and (13,7) active spaces, with focus on band 5, using the uPBE1PBE DFT-optimized geometry.

The energies of all LMCT vertical electronic excitations shift down in energy with increasing active space, as may be expected with a better estimation of the electronic correlation energy in the ligand-centered orbitals due to a more complete CI estimation. While the energetic trend with the inclusion of lower ligand orbitals is not surprising, figure 11 subtly shows there are no apparent advantages in individual calculation of the

LMCT electronic states; rather better estimates in terms of energy, sign, and intensity are found with the inclusion of all ligand-centered orbitals necessary to describe the LMCT electronic states. Interestingly the sign and intensity of band 3 appears dependent on active space, decreasing in intensity between the (7,4) and (9,5) active spaces, and changing sign with a greatly increased relative intensity once expanding to the (13,7) active space. This suggests the out-of-state spin-orbit coupling with the 3-^{2}E state plays a significant role in predicting the proper sign of band 3.

To study the influence of the LMCT electronic states on the d-d transition energies, a similar approach was taken. The active spaces were expanded from including only the SOMO-d_{xy} and unoccupied d-orbitals to the full active spaces considered previously; thus, trends begin with a (1,5) active space and are expanded to (9,9) for the uBP86, uB3LYP, and uB3P86 geometries, and (13,11) for the uPBE1PBE. A representative example for the uPBE1PBE-geometry is provided in figure 12. Examples for the uBP86, uB3LYP, and uB3P86 geometries are provided in S20 through S22, with energies for each active space and geometry considered available in S23.

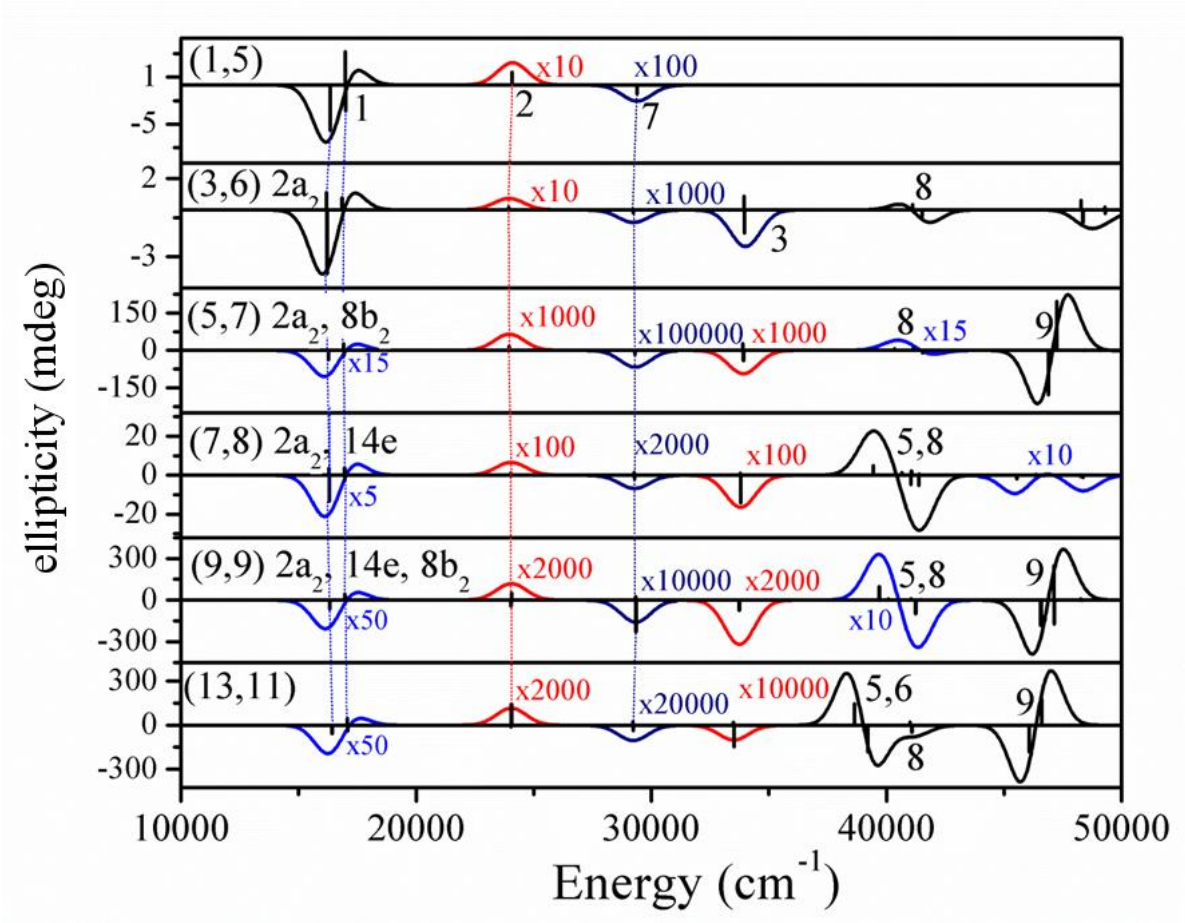

Figure 12. Comparison of MRCI-calculated MCD spectra for the (1,5), (3,6), (5,7), (7,8), (9,9), and (13,11) active spaces, with focus on the d-d transitions, using the uPBE1PBE DFT-optimized geometry.

While a reasonable decrease is observed for the LMCT's, the changes in both intensity and energy for the vertical electronic excitations confined to the 4*d* shell are insignificant. This is not surprising since there is little dynamic correlation to account for in the Mo-d^1 system; it has been shown previously that the radial correlation effects within the 4*d* shell are small, leading to relatively little effect on the corresponding d-d transitions.[47] This leads directly to the point that the d-d vertical electronic excitations of

$[MoOCl_4]^-$ are well modeled with the modest (1,5) active space, without further consideration of the occupied ligand orbitals.

These results show that calculation of the vertical excitation energies of $[MoOCl_4]^-$ and in turn the corresponding MCD spectrum more closely relate to those found experimentally when the active-space is partitioned to separately treat charge transfer and d-d type electronic transitions. To ensure that these results were not an artifact of using a complete active-space wavefunction as an initial guess in the MRCI calculation, CASSCF wavefunctions for the (1,5) and (13,7) active-spaces were generated for each geometry under consideration, using the corresponding DFT-calculated natural orbitals as an initial model. MRCI was then used to generate the MCD spectra for each active-space and geometry. The resulting vertical excitation energies are compared with the experimentally assigned band energies in figure 13. Energies for each calculated band and geometry are provided in S24.

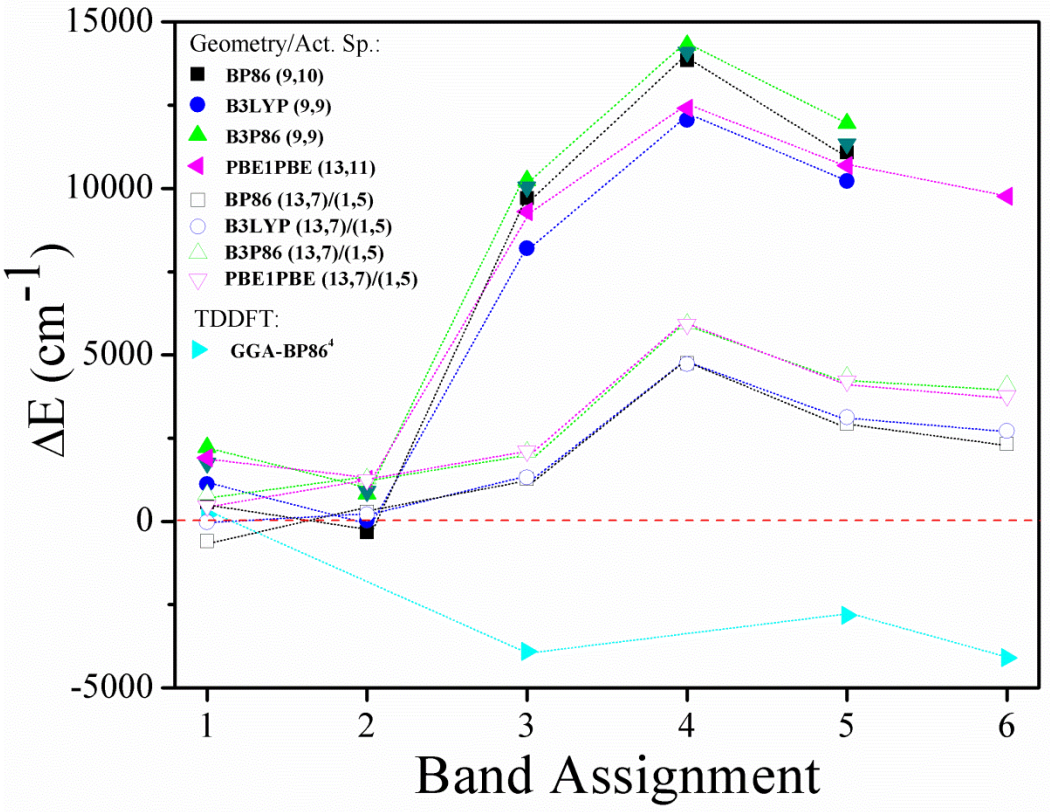

Figure 13. Energetic deviation of calculated vertical excitations from their respective experimental assignments.

It can be seen that the changes in the energies of the d-d electronic vertical excitations are negligible when comparing the active spaces including only the d-centered orbitals, aka (1,5), versus those including ligand orbitals, such as (9,9) or (13,11). Meanwhile, elimination of the unoccupied d-orbitals from the active space results in a drastic shift of the LMCTs energies, which are all lowered by 6000-9100 cm^{-1}, bringing them into significantly better agreement with experiment.

Besides providing a better estimation of the experimentally assigned LMCT vertical excitation energies, this partitioned active-space approach provides a relatively

inexpensive method of modeling all predicted transitions when compared to a full active space approach. Consider that the CASSCF method requires the generation of $(2x)!/(y!(2x-y)!)$ configuration state functions, where x is the number of orbitals and y is the number of electrons in the active space. The (13,11) active space required to model the experimentally assigned spectrum of $[MoOCl_4]^-$ demands the calculation of 7,726,160 configuration state functions, compared to a mere 24 total for both the (1,5) and (13,7) spaces. Similar approaches made through partitioning of the active space in CAS and RAS based *ab initio* calculations which reduce computational cost and better model charge-transfer states have been taken previously,[47,48,49,50] and are indeed not uncommon.

Comparison of DFT-CASSCF-MRCI and TDDFT approaches

Through partitioning the active space and use of the DFT-CASSCF-MRCI approach, it has been shown that a reasonable quantitative agreement with experiment is attainable for the LMCT vertical excitation energies. In addition to MRCI based calculations, methods utilizing density-functional theory have been developed for the prediction of Faraday *A*-, *B*-, and *C*-terms. Currently, these DFT methods are limited to the use of pure generalized gradient approximation (GGA) exchange-correlation functionals, such as GGA-BP86.[51,52] Thus, it was interesting to draw comparisons between data resulting from CASSCF-MRCI calculations with those obtained from the TDDFT GGA-BP86 method.

Figure 14 provides a comparison of the experimentally observed MCD spectrum at 5K, 5T , as adopted from Reference 11, against those calculated via GGA-BP86[9] and DFT-CASSCF-MRCI, respectively. The GGA-BP86 spectrum, as adopted from Reference 9, consists of an overlay of the predicted electronic spectra for a) the C_{4v}

structure (illustrated with a solid line) with b) the distorted crystal structure (illustrated with a dashed line). The provided DFT-CASSCF-MRCI consists of an overlay of spectra calculated for the (13,7) and (1,5) active spaces for the uPBE1PBE geometry.

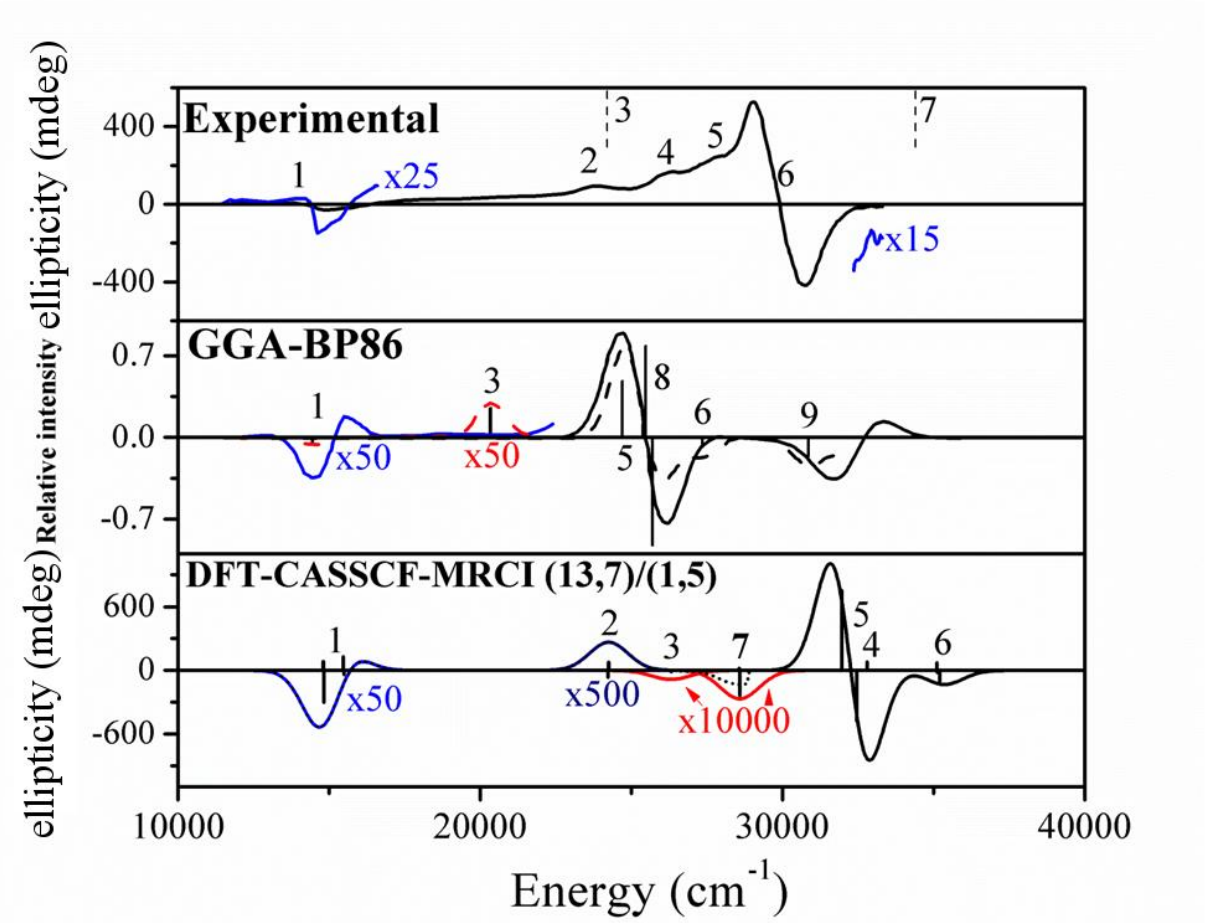

Figure 14. Comparison of GGA-BP86[9] and DFT-CASSCF-MRCI calculated MCD spectra against experimental[11] at 5K, 5T for $[MoOCl_4]^-$. The experimental spectrum is adopted from Reference 11. The GGA-BP86 MCD spectrum is adopted from Reference 9. The dotted line seen in the DFT-CASSCF-MRCI calculated spectrum represents a summation of bands, due to overlapping in bands 2, 3, and 7.

Both the GGA-BP86 and DFT-CASSCF-MRCI predicted spectra appear in good qualitative and reasonable quantitative agreement with the experimentally observed MCD spectrum. The GGA-BP86 method predicts the allowed d-d and LMCT transitions which

give rise to bands 1, 5, 6, 8, and 9 with proper sign, though underestimating the energies of 5 and 6 by ~3000 cm^{-1}, as shown in figure 13. Similar to the DFT-CASSCF-MRCI calculations, the GGA-BP86 results show the large Faraday *C*-term as being primarily constituted by band 5 rather than a convolution of bands 5 and 6 as was predicted experimentally. Band 6 appears shifted ~2000 cm^{-1} higher in energy relative to band 5 in both of the calculated spectra. The forbidden transition assigned in this study as band 3 also appears, contrary to ligand-field theory based MCD selection rules, as a positive intensity in the GGA-BP86 predicted spectrum for the crystal structure due to distortion and loss of symmetry. However, none of the other symmetry forbidden transitions are predicted by this method.

In comparing the GGA-BP86 predicted spectrum and those calculated by CASSCF-MRCI, it can be noticed that the pure GGA functional tends to underestimate transition energies while CASSCF-MRCI, which is based on pure HF-exchange approach, overestimates said energies as can be clearly seen in figure 13. This raises the question of how Hartree-Fock exchange contribution to the exchange correlation functional influences the geometry, molecular orbital energies, and TDDFT predicted electronic transitions in $[MoOCl_4]^-$. To investigate this effect, a range of exchange-correlation functionals utilizing between zero and fifty percent Hartree-Fock exchange, as well as a pure-HF method, were used to calculate single point and vertical excitation energies.[35]

DFT predicted electronic structure of the $[MoOCl_4]^-$ complex

Orbital energies, compositions, and surfaces for $[MoOCl_4]^-$ were calculated for all DFT or MP2 optimized geometries using DFT, or *ab initio* post-Hartree-Fock methods.

Just as predicted by CASSCF, the molybdenum centered d-orbitals are found above all occupied ligand orbitals in the order of $d_{xy} < d_{xz,yz} < d_{x2-y2} < d_{z2} < 5s$ for all DFT methods. The MP2 method, however, predicts $d_{xy} < 2a_2 < d_{xz,yz} < d_{x2-y2} < d_{z2} < 5s$ ordering where $2a_2$ is the singly-occupied ligand-orbital. The HOMO-1 to HOMO-5 orbitals are predominantly chlorine centered, with small contributions from oxygen and molybdenum to the 14e and 13e orbitals. Similar to CASSCF, the energies of the $8b_1$ and 14e orbitals are predicted to be near degenerate in unrestricted DFT methods. Alternation in ordering of these orbitals occurs depending on spin-polarization effects. The orbital compositions for α and β unrestricted Hartree Fock (UHF) orbitals are provided in S25-S38. The effect of Hartree-Fock exchange contribution on spin-polarization is most pronounced for the splitting of the singly occupied d_{xy} orbital, as shown in figure 15.

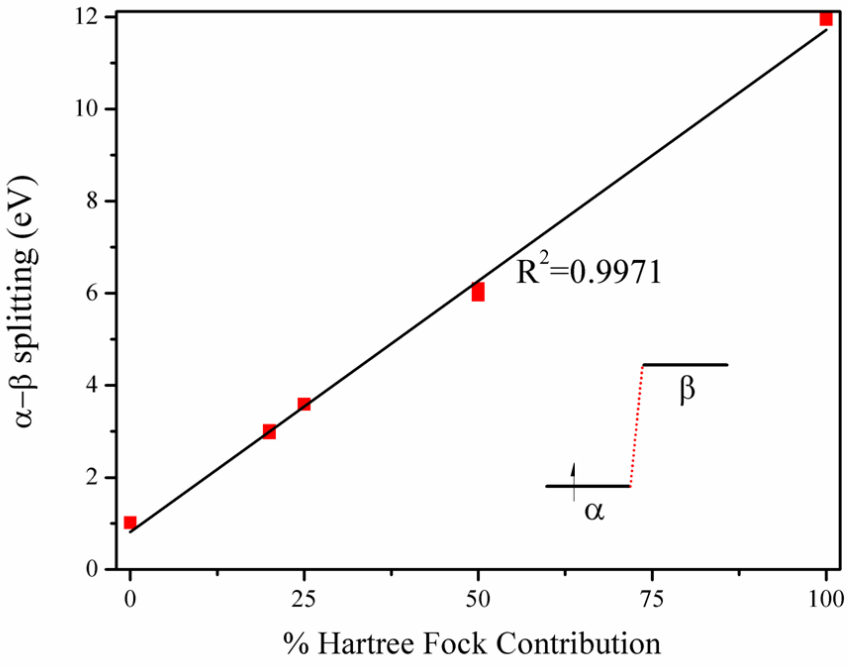

Figure 15. Dependence of the α-β spin polarization of the molybdenum d_{xy} orbital on the percent Hartree-Fock contribution to the exchange functional.

For the MP2 optimized geometry, this effect generates a large enough splitting such that the α-d_{xy} orbital appears as the α-HOMO-1 (below the energy of the α-$2a_2$ orbital), while the β-d_{xy} orbital remains as the β-LUMO. The effects of Hartree-Fock exchange on spin-polarization for the remaining d-orbitals are shown in S39. Since the CASSCF orbitals were generated from an ROHF wavefunction, spin could not be investigated at the CASSCF level. The energies for the α and β-spin unrestricted DFT orbitals are shown in figures 16 and 17.

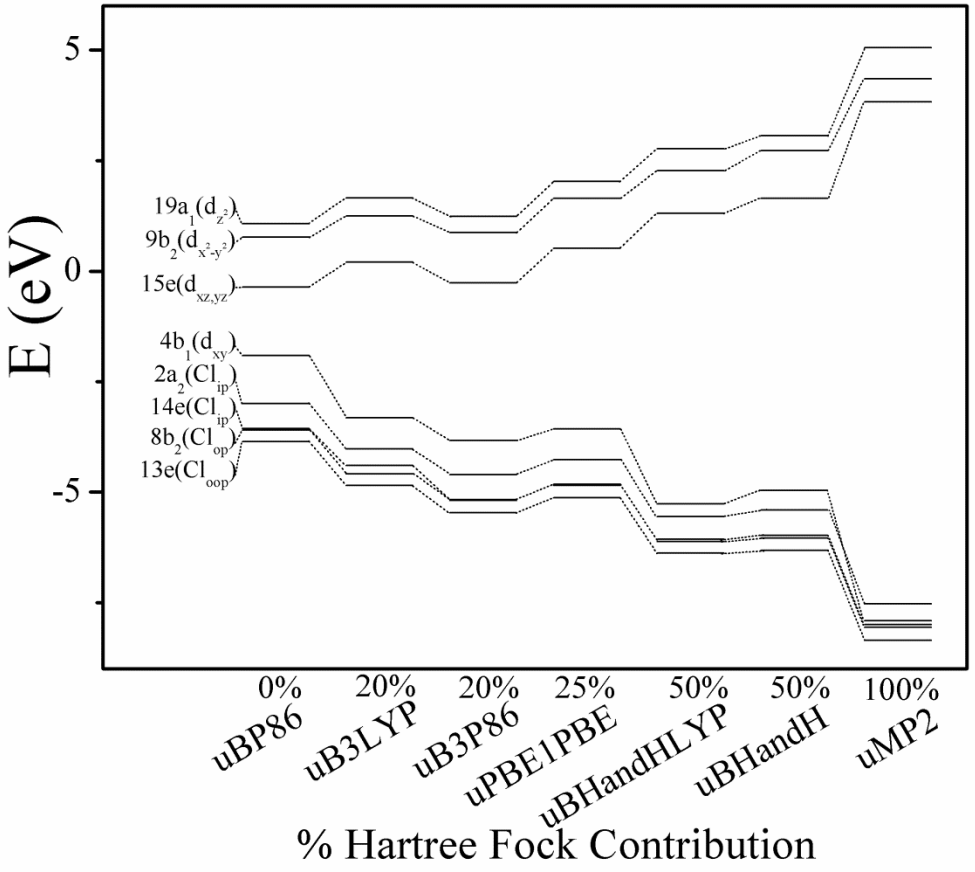

Figure 16. DFT and MP2 calculated α-molecular orbital energies for each method with the respective percent Hartree-Fock contribution to the exchange.

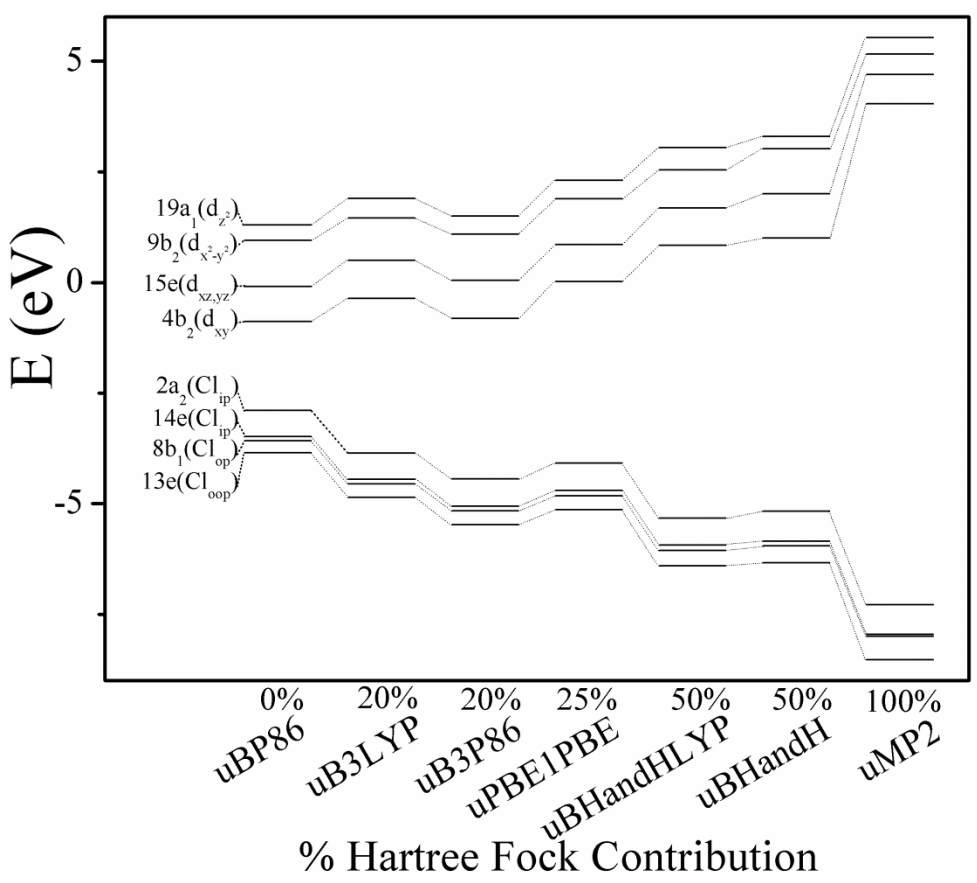

Figure 17. DFT and MP2 calculated β-molecular orbital energies for each method with the respective percent Hartree-Fock contribution to the exchange

It can be seen that as the Hartree-Fock exchange contribution to the exchange-correlation functional increases, all virtual orbitals increase in energy fairly uniformly, and all occupied orbitals decrease uniformly; an interesting exception to this is seen for uMP2, in which the ordering of the occupied orbitals shifts such that the α-$2a_2$ orbital becomes the SOMO. While the DFT-uB3P86 case appears to be an exception to these trends, a lowering of energies for all orbitals under consideration is observed, and is likely due to the consideration of correlation effects. For the DFT-calculated orbitals, the in-plane unoccupied α,β-d_{x2-y2} and β-d_{xy} orbitals are seen to increase with increasing

Hartree-Fock contribution as well. However, there is not a clear trend in the energy gap between in- and out-of-plane d-orbitals due to the complex dependence of the in-plane orbitals on the Mo-Cl bond length and O-Mo-Cl bond angle. Correlation diagrams for the DFT calculated d-orbital energies are provided in S40 through S43.

The HOMO-1 to HOMO-6 are almost purely chlorine-centered, with at most ~5% Mo and ~8% O contribution to the total orbital composition in any case for the unrestricted DFT calculations. The fully-occupied ligand orbitals follow the 13e < 14e ≈ $8b_1$< $2a_2$ ordering where the $8b_1$ and 14e sets are nearly degenerate. Additionally, the in-plane chlorine-centered 14e orbitals are seen to be higher in energy than the out-of-plane 13e orbitals, as predicted by Xα calculations.[13,43] A representative sample of Mulliken molecular-orbital compositions is provided in table 4.

Table 4. Calculated Molecular Orbital Energies and Compositions of $[MoOCl_4]^-$ for PBE1PBE method

		α set composition %				β set composition %		
Orbital	E, eV	Mo	O	Cl	E, eV	Mo	O	Cl
13e (oop)	-5.124	0.83	6.65	92.52	-5.137	0.68	7.05	92.27
14e (ip)	-4.849	1.99	3.14	94.87	-4.818	0.15	0	99.85
$8b_2$ (oop)	-4.826	0.17	0	99.82	-4.705	1.64	1.58	96.78
$2a_2$ (ip)	-4.264	0	0	100	-4.085	0	0	100
$4b_1$ (d_{xy})	-3.568	71.72	0	28.28	0.025	86.08	0	13.92
15e ($d_{xz,yz}$)	0.516	73.34	14.85	11.81	0.857	75.87	12.96	11.17
$9b_2$ (d_{x2-y2})	1.647	60.68	0	39.32	1.888	61.88	0	38.12
$19a_1$ (d_{z2})	2.033	73.89	13.67	12.44	2.312	75.55	12.72	11.72

TDDFT predicted Vertical Excitation Energies and HF Dependence

In order to explore the influence of Hartree-Fock exchange contribution to the exchange-correlation functional on the vertical excitation energies and corresponding UV-Vis spectra of $[MoOCl_4]^-$, TDDFT calculations were performed using the uBP86, uB3LYP, uB3P86, uPBE1PBE, uBHandHLYP, and uBHandH exchange-correlation

functionals. In addition, CIS calculations were performed for the uMP2 optimized structure of $[MoOCl_4]^-$. Vertical excitations calculated via TDDFT were assigned to their appropriate bands using the same labeling scheme as the CASSCF-MRCI study. Since neither vibronic nor spin-orbit coupling were taken into consideration in these calculations, transitions which are considered to be symmetry forbidden had oscillator strengths equal to zero. The TDDFT and CIS predicted vertical excitation energies are listed in table 5, and the corresponding spectra are provided in figure 13. Oscillator strengths are provided in S44.

Table 5. Vertical excitation energies of both experimentally[11,12] determined and DFT-calculated bands.

	experimental		Method						
Band	C.B.S.E.[a]	S&G[b]	BP86	B3LYP	B3P86	PBE1PBE	BHandH	BHandHLYP	CIS
1	15,100	16,000	12315	13774	14133	14643	16523	16354	23593
2	23,800	23,900	20510	21175	22309	22783	26925	26948	25416
3	24,200[c]	N.A.	17259	19909	20819	22328	24354	23127	44709
4	26,900	26,200	21693	24510	25659	27289	32343	32005	49073
5	28,000	28,200	21883	24300	25387	26839	31504	30998	47081
6	30,000	30500	23916	26803	28011	29638	34966	34378	53160
7	N.A.[d]	34400	24143	26604	27337	28286	31098	30875	38223
8	N.A.	N.A.	21142	25416	26281	27638	34588	33228	49603
	N.A.	N.A.	22600	26511	27472	28934	35613	34378	50756
9	N.A.	N.A.	26191	29744	30280	32037	38580	36668	48207
	N.A.	N.A.	28718	32542	33766	35218	41906	40174	---

[a]Reference 11. [b]Reference 12. [c]Observed only in the $[MoOCl_4(H_2O)]^-$ complex. [d]Unassigned in the experimental spectrum.

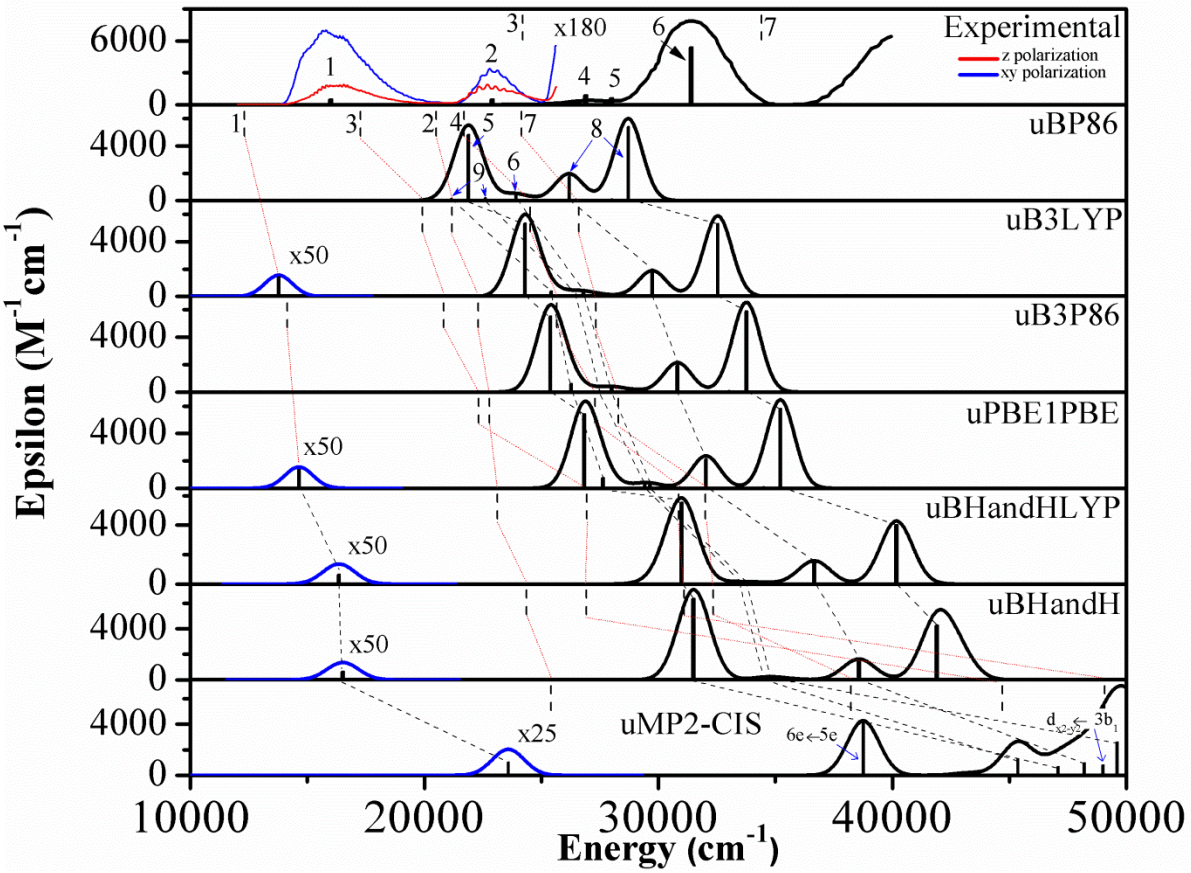

Figure 18. Comparison of the TDDFT/CIS calculated with experimental (adopted from Reference 11) UV-Vis spectra of $[MoOCl_4]^-$. The single-crystal experimental spectrum illustrating the vibronic progressions of the first two d-d transitions is provided in combination with the room-temperature absorption spectrum.

In general, the TDDFT-predicted vertical excitation energies depend strongly on the amount of Hartree-Fock exchange present in the exchange-correlation functional. Such dependence has already been clearly established for π–π* transitions in aromatic macrocycles.[53] As Hartree-Fock exchange contribution to the exchange-correlation functional increases, the vertical excitation energies of both d-d and LMCT type transitions shift to higher energies. The uMP2-CIS vertical excitation energies are still

greater. Moreover, the TDDFT and CIS predicted energies for the d-d transitions correlate linearly with the amount of Hartree-Fock exchange utilized; this trend is less obvious for CT transitions. These trends are discussed for each band, below.

Band 1 This band has been observed experimentally (as a well defined vibronic progression in single-crystal polarized spectroscopy at 5K)[2] at ~15,100 cm^{-1} and is assigned to the symmetry allowed $^2E_2 \leftarrow {}^2B_2$ ($d_{xy} \rightarrow d_{xz,yz}$) ligand field transition, which is in agreement with all previous band assignments.[8,11,12,42,54,55] The energy of this transition, provided in table 5, increases linearly with increasing Hartree-Fock contribution, with the pure GGA BP86 functional (0% HF contribution) predicting the lowest energy and CIS (100% HF contribution) the highest.

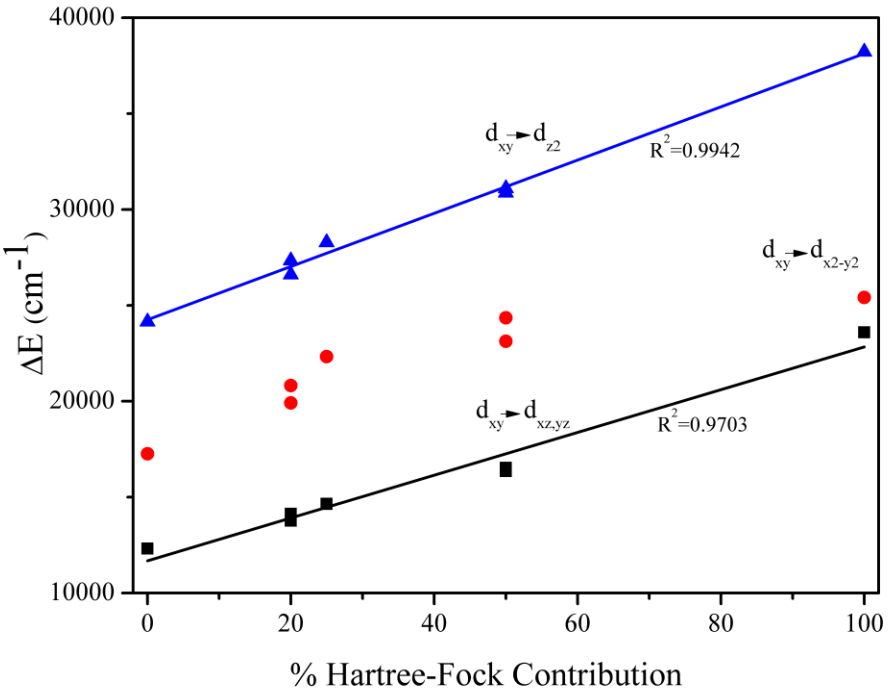

Figure 19. Correlation of the TDDFT or CIS predicted d-d transition energies as a function Hartree-Fock contribution to the exchange part of the exchange-correlation functional. For CIS, identity of the SOMO switches from d_{xy} to $2a_2$ due to spin-polarization effects.

Figure 19 illustrates the dependence of transition energy on HF exchange contribution, which also linearly correlates with the length of the Mo=O bond. Because the transition occurs between the equatorial d_{xy} and axial $d_{xz,yz}$ orbitals, the terminal Mo=O bond length influences the relative energies of the out-of-plane d-orbitals, resulting in a linear correlation. Band 1 is missing for the uBP86 and uB3P86 functionals in figure 18 due to an oscillator strength threshold of 0.0001; it can be noted that the oscillator strengths for this transition with uB3LYP and uPBE1PBE are at the minimum of this threshold.

Band 2 This band was observed experimentally (as a well-defined vibronic progression in single-crystal polarized spectroscopy at 5K)[11] at ~23,800 cm^{-1} and was assigned to the symmetry-forbidden $^2B_1 \leftarrow {}^2B_2$ ($d_{xy} \rightarrow d_{x2-y2}$) d-d transition. The influence of the exchange-correlation functional on the energy of this transition follows the expected trend, with the energy of the d-d transition increasing with increasing Hartree-Fock contribution to the exchange functional. There is no linear correlation of excitation energy with Hartree-Fock exchange observed for this transition, as demonstrated in figure 19.

Band 3 This band was assigned to the $^2A_2 \leftarrow {}^2B_2$ ($2a_2 \rightarrow d_{xy}$) first ligand to metal charge transfer transition, arising from the chlorine 3p in-plane orbital to molybdenum d_{xy} orbital excitation. This transition is symmetry forbidden, and thus has zero oscillator strength predicted by TDDFT and CIS approaches. While not observed in the experimental spectrum of $[MoOCl_4]^-$ due to a very weak intensity, it has been observed in the case of the lower symmetry $[MoOCl_4(H_2O)]^-$ complex in *xy*-polarization at ~24,200 cm^{-1} as previously discussed.[11] Because the relative energies of in-plane chlorine and

molybdenum centered d_{xy} orbitals depend primarily on the Mo-Cl bond length and O-Mo-Cl bond angle, this transition does not linearly correlate with the amount of Hartree-Fock contribution, as shown in figure 20.

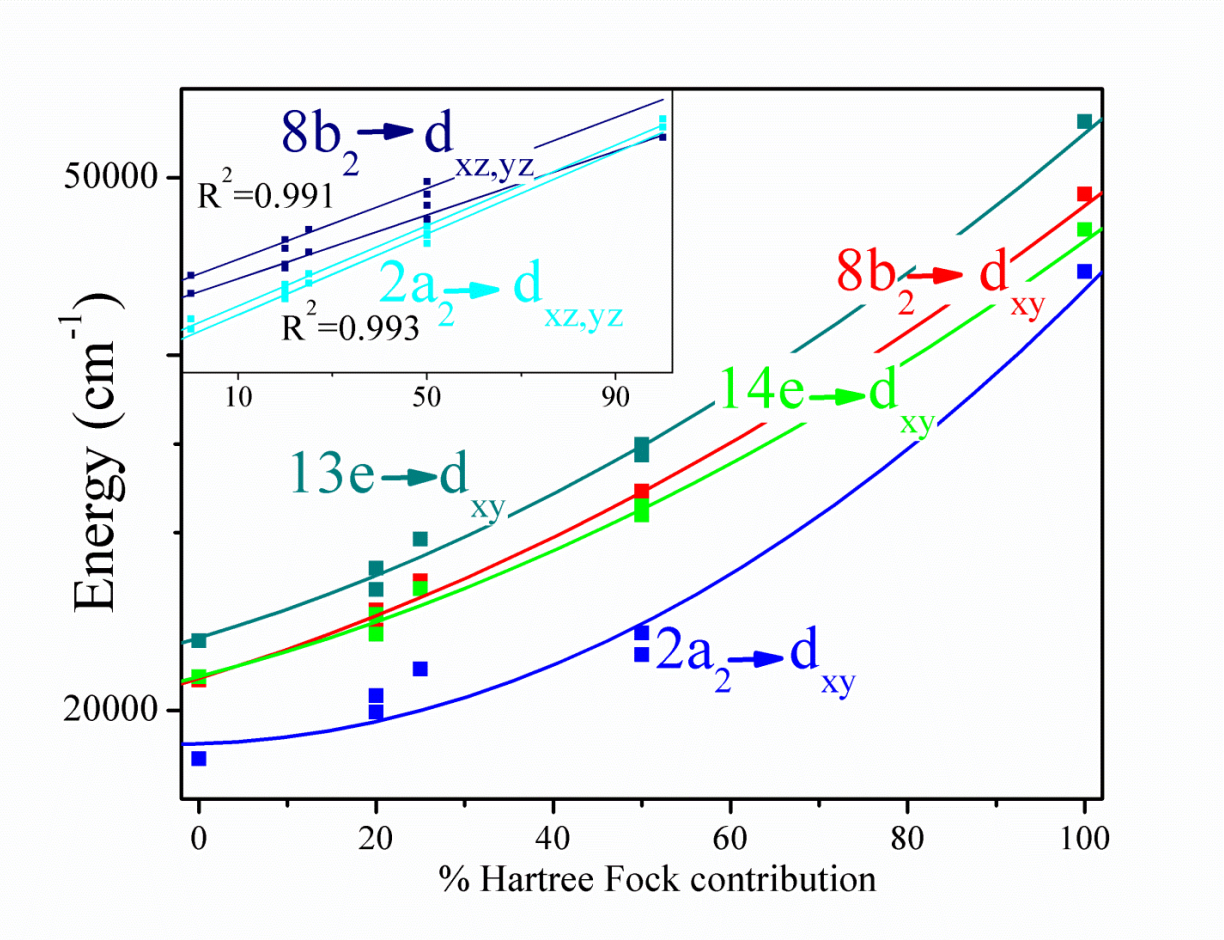

Figure 20. Correlation of the TDDFT or CIS predicted LMCT transition energies as a function Hartree-Fock contribution to the exchange portion of the exchange-correlation functional. For CIS, identity of the SOMO switches from d_{xy} to $2a_2$ due to spin-polarization effects.

Band 4 This band was assigned to the symmetry forbidden $^2B_1 \leftarrow {}^2B_2$ ($8b_2 \rightarrow d_{xy}$) ligand-to- metal charge transfer process, which has been experimentally observed at ~26,300 cm^{-1}. This transition predominantly arises from the out-of-plane chlorine 3p to molybdenum d_{xy} orbital excitation. The energy of this transition follows the expected

dependence on Hartree-Fock exchange contribution. Interestingly, the TDDFT predicted energy of this band was higher than the energy of the third ligand-to-metal 14e → d_{xy} transition when a pure GGA BP86 functional was used, while exchange-correlation functionals with non-zero Hartree-Fock exchange move it to lower energy.

Band 5 The most prominent feature of the TDDFT or CIS predicted spectrum of $[MoOCl_4]^-$ is associated with the symmetry allowed $^2E_2 \leftarrow {}^2B_2$ (14e → d_{xy}) transition, corresponding to the ligand-to-metal charge transfer from the 5e MO set composed primarily of the in-plane chlorine 3p orbitals to the metal centered d_{xy} orbital. As mentioned previously, this band has been assigned as one of two transitions which compose the characteristic absorption centered at 30,000 cm^{-1} experimentally.[11] According to all TDDFT and CASSCF calculated electronic transitions, this broad feature is composed almost entirely of the $^2E_2 \leftarrow {}^2B_2$ (14e → d_{xy}) which has a large oscillator strength. Small contributions from the $2a_2$ → $d_{xz,yz}$ transition (band 8) to this broad feature appeared when the GGA-BP86 functional was used; however, this transition shifts up in energy quickly with increasing of HF-exchange.

Band 6 This band corresponds to the $^2E_2 \leftarrow {}^2B_2$ (13e → d_{xy}) ligand-to-metal charge transfer transition which is symmetry allowed in x,y polarization. This band has been assigned as the primary contributor to the large characteristic absorption mentioned above. It can be seen in figure 18 and table 5 that the energy of this transition is shifted significantly higher than the 14e → d_{xy} transition for all TDDFT and CIS calculations. Additionally, the oscillator strengths of this transition have been calculated to be at most ~10% of those for band 5. Interestingly, this band appears in a region where the presence

of possible $d_{xy} \rightarrow d_{z2}$ (band 7), $8b_2 \rightarrow d_{xy}$ (band 4), and $14e \rightarrow d_{xz,yz}$ (band 5) transitions have been proposed[12], as mentioned previously.

Band 7 This band is assigned to the symmetry forbidden $^2A_1 \leftarrow {}^2B_2$ ($d_{xy} \rightarrow d_{z2}$) ligand field transition. While not assigned experimentally, this transition was calculated by Deeth[13] to be higher-energy than band 6, and was tentatively assigned at ~34,500 cm^{-1} by Sabel and Gewirth, as mentioned previously.[12] Similarly to band 1, this transition shows a linear dependence on the Hartree-Fock exchange contribution as seen in figure 19. Assignment of this band has raised some debate as to its possible experimental observation.[8,9] While it is symmetry forbidden, this transition may still gain intensity through a vibronic mechanism or spin-orbit coupling.

Band 8 This band is assigned to the weak symmetry allowed $^2E_2 \leftarrow {}^2B_2$ ($2a_2 \rightarrow d_{xz,yz}$) ligand-to-metal charge transfer transition which predominantly arises from in-plane chlorine 3p orbitals to the degenerate out-of-plane molybdenum $d_{xz,yz}$ orbitals. It can be seen in figure 20 that the energy of this transition linearly increases with increasing HF contribution due to the dominant effect of the Mo=O bond length on the out-of-plane d-orbitals. This transition has not been recognized experimentally, likely due to its relatively low intensity due to poor orbital overlap, and due to convolution with the intense LMCT which composes band 5. Assignments for this transition have appeared in several previous theoretical TDDFT investigations with the $\alpha\text{-}2a_2 \rightarrow d_{xz,yz}$ transition appearing at 25,520 cm^{-1} (uBP86 exchange-correlation functional)[9], and the $\alpha\text{-}1a_2$, $\beta\text{-}2a_2 \rightarrow d_{xz,yz}$ transitions appearing at 26,697 and 27826 cm^{-1}, respectively (B3P86 exchange-correlation functional).[8]

Band 9 This band is assigned to the symmetry allowed $^2E_2 \leftarrow {}^2B_2$ ($13e \rightarrow d_{xz,yz}$) ligand-to-metal charge transfer transition which predominantly arises from the $8b_1$ ligand orbital, composed of the out-of-plane chlorine 3p orbitals, to the degenerate out-of-plane molybdenum $d_{xz,yz}$ orbitals excitations. A strong intensity is observed due to the significant overlap of the out-of-plane chlorine and out-of-plane $d_{xz,yz}$ orbitals.[46] Similar to band 8, there is a linear correlation of transition energy with increasing HF contribution, as shown in figure 15. This band has not been observed or assigned experimentally since it would appear to occur beyond the experimental UV-vis cutoff. A theoretical assignment for this transition was previously made at 30,850 cm^{-1} for the uBP86 optimized geometry utilizing a TZVP basis for all atoms.[9] In the current study, the α-$3b_1$, β-$3b_1 \rightarrow d_{xz,yz}$ transitions for the uBP86 exchange-correlation functional were calculated at 26,191 and 28,718 cm^{-1} respectively.

Summary and Comparison of TDDFT studies

As shown in figures 18-20, all transitions are seen to increase in energy as a function of increasing Hartree-Fock exchange contribution to the exchange-correlation functional. This trend is linear when involving excitations to the out-of-plane LUMO, LUMO+1, and LUMO+3 orbitals (bands 1, 7-9), while displaying a more complex dependence for excitations to the in-plane SOMO and LUMO+2 orbitals (bands 2-6). The uMP2/CIS calculated excitations have a large degree of deviation from the experimental spectrum as well as from the TDDFT calculated vertical electronic excitations. This is in part due to a large spin-polarization causing a change in the identity of the SOMO orbital. The agreement of each method with the experimentally assigned transition energies is shown in figure 21.

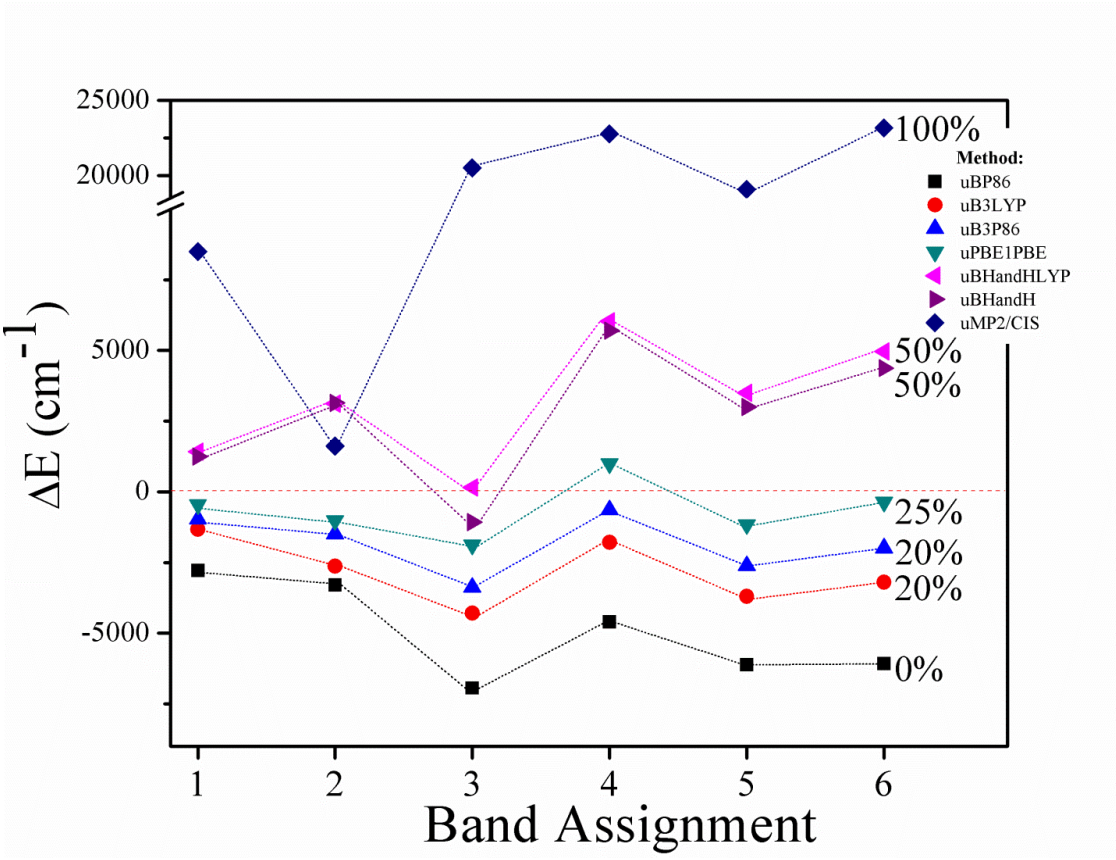

Figure 21. Energy deviations (ΔE) of TDDFT and CIS predicted vertical excitation energies from the corresponding experimental[11] assignments.

A high degree of consistency is seen across all TDDFT methods, clearly underlining the importance of exchange considerations in this system. Hybrid TDDFT, utilizing between 25-50% Hartree-Fock exchange, appears to best quantitatively predict the experimental vertical excitation energies. While relativistic mechanisms such as ZORA have been well implemented for ground state DFT and closed-shell TDDFT applications,[56,57]calculation of spin-orbit coupled excitation energies for open-shell systems by TDDFT are currently restricted to a single-determinant description of the ground state and single-electron excitations.[58] MRCI-CASSCF, on the other hand, has been shown here to not only predict the presence of the symmetry forbidden transitions,

but provide good agreement between theory and experiment in terms of both intensity and energy of the vertical electronic excitations. Additionally, partitioning of the active space provides an improvement in the quantitative agreement of the LMCT vertical electronic excitations with experiment which is comparable if not superior to TDDFT based methods.

The CASSCF-MRCI method has provided excellent qualitative agreement in this study and can accurately account for the spin-orbit coupling mechanism. However, these calculations become exceedingly expensive as both active space and molecular size increase. Therefore such calculations are currently limited to small systems when the spectra of interest require numerous occupied and unoccupied orbitals. Calculation of the vertical electronic excitations and corresponding MCD spectra through partitioning of the active space provides a cheap alternative to these expensive calculations; however, a detailed knowledge of the system at hand is required. Methods such as DFT-CASSCF-MRCI may be capable of dealing with larger systems if handled cautiously. Because TDDFT handles large molecules with reasonable efficiency[55], TDDFT is a promising method for predicting MCD in larger molecules. However, there is yet no readily available implementation to properly account for intensities due to symmetry forbidden transitions; while said transitions appear very weak in systems of greater ionic character, such as $[MoOCl_4]^-$, they may contribute more to the spectra of systems with greater metal-ligand covalency. Additionally, the ability to use hybrid exchange-correlation functionals in the calculation of MCD terms is necessary in order to accomplish an accurate fit to experimental data, advancing the application of TDDFT in modeling of MCD spectra.[59]

Conclusion

The electronic structure and vertical excitation energies of $[MoOCl_4]^-$ have been determined using multiple levels of theory and for a variety of geometries. Both CASSCF and DFT based calculations confirm previous studies on this complex and illuminate the dependence of the geometry, electronic structure, and vertical transitions on the amount of Hartree-Fock exchange present in the exchange-correlation functional. Of the TDDFT-methods, the electronic transitions calculated using the uPBE1PBE exchange-correlation functional were found to best correlate with the experimental spectrum energetically. The electronic transitions calculated using the CASSCF-MRCI approach are in good agreement with both experimental assignments and ligand-field theory predictions in terms of sign, intensity, and relative position for all bands, as well as quantitatively for the energy of the d-d transitions. The energies of the LMCT transfer transitions are consistently overestimated, though significantly improved through the use of a partitioned active space. The intensities for the symmetry forbidden transitions were slightly lower than those observed experimentally, in part because this study did not account for intensity gained through vibronic coupling. Despite both of these drawbacks, this method was still able to account for all experimental transitions including several higher-energy transitions as well as all three possible d-d transitions, something that TDDFT does not currently provide. While pure CASSCF-MRCI is computationally expensive, the use of partitioned active spaces in DFT-CASSCF-MRCI provides a potent method for the quick and accurate prediction of MCD spectra for open-shell, second row transition metals.

Chapter 2: Mixed-Valency of Polyferrocenyl Pyrroles

Introduction

Aromatic polyferrocenyl heterocyclic complexes have received growing attention[60,61,62,63] in recent years due to their mixed-valence properties which make this class of organometallic compounds ideal models for the study of electron transfer through π-conjugated systems and design of novel electro-active materials.[64] The term "mixed-valence", as defined by Creutz,[65] refers to materials which contain an element or elements in more than one oxidation state, for example an M and M^+. Such compounds are characterized by their ability to undergo electron transfer between donor and acceptor ion sites through absorption of a photon of appropriate energy giving rise to the mixed-valence state and in turn the presence of an inter-valence charge transfer in their absorption spectra.[65,66,67,68,69] Light absorption causing an electron transfer between two of the same elements is referred to as a *homonuclear inter-valence charge-transfer*, while absorption

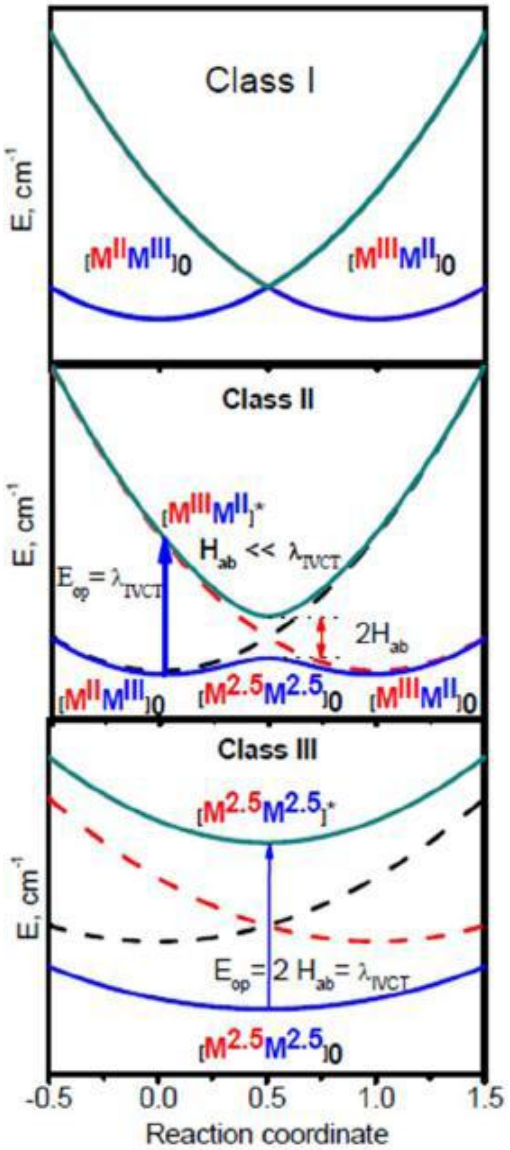

Figure 22. Illustration[70] of the Robin-Day classification[67] for mixed-valence state compounds.

resulting from transfer between two different elements is referred to as a *heteronuclear intervalence charge-transfer*.[66]

Robin and Day have proposed a three-fold classification scheme for compounds falling under the definition of mixed-valence which is based primarily upon ligand field strength and symmetry.[67] A diagram describing these three classes is provided in figure 22.[70] Compounds which contain M and M^+ but exhibit only the properties of the individual M and M^+ ions are considered to be Class I systems. In Class I type systems, there is no or very little interaction between M and M^+ due either to differing symmetry and field strength around the ion sites or a significant separation of M-M^+, making inter-valence electron transfer impossible.[65] Class III systems present the opposite extreme, in which the symmetry and ligand field around M and M^+ are equivalent, making the sites impossible to differentiate.[67] In these systems, the interaction between M and M^+ is so large that only the properties of the $(M\text{-}M)^+$ complex are observed rather than the individual properties of M and M^+.[65] Finally, Class II systems present an intermediate in which an inter-valence charge-transfer occurs, while the M and M^+ sites remain distinguishable and exhibit some perturbed characteristics of the individual M and M^+ ions.[65,66] In such compounds, electron transfer may occur either electronically by absorption of λ_{IVCT} or through thermal activation.[65,67,69] Since electron transfer occurs relatively slowly in such systems, it is possible to characterize the separate redox processes for each metal center. For example, in the case of dinuclear iron complexes, Fe(II) and Fe(III) centers exhibit different spectroscopic signatures in the UV-Vis-NIR region; therefore, electronic spectra of such complexes contain not only a solvent

independent inter-valence charge-transfer band, but bands corresponding to the individual Fe(II and Fe(III) centers.[8]

Recently, the Class II mixed-valence state behaviors of 2,3,4,5-tetraferrocenyl-1-phenyl-pyrrole (1) and 2,5-diferrocenyl-1-phenyl-pyrrole (2) were reported by Lang and co-workers.[60] An electrochemical analysis of (1) resulted in four diffusion controlled ferrocenyl-related reversible redox events which were contrasted to results obtained for (2); however without a beta-disubstituted(ferrocenyl)pyrrole for comparison, oxidation waves were difficult to assign. The synthesis and electrochemical study of 3,4-diferrocenyl-1-(triisopropylsilyl)pyrrole (3) was undertaken by Nemykin and coworkers in an attempt to clarify the assignment of each oxidation wave in (1) as no experimental results had been reported prior for β-substituted(ferrocenyl)pyrroles.[70] The resulting electrochemical analysis of (3) resulted in little clarification due to the close similarity of redox properties observed for (2) and (3).

Thus far, assumptions regarding the oxidation waves and electronic properties associated with compounds (1), (2), and (3) have been assigned unaided by computational methods, and the electronic structures of these molecules remain uninvestigated from a theoretical perspective. This chapter reports the electronic characterization of (3) as well as the model 3,4-diferrocenyl-1-H-pyrrole (4), 2,5-diferrocenyl-1-H-pyrrole (5) and 2,3,4,5-tetraferrocenyl-1-H-pyrrole (6) complexes using DFT/TDDFT methods. In addition, the mixed-valence states of (1^+), (4^+), (5^+), and (6^+), are investigated in order to gain a greater understanding of the metal-metal coupling processes in (1) and (6), and to provide clarification to the oxidation analysis of (1). The structures of compounds (1) through (6) are depicted in figure 23.

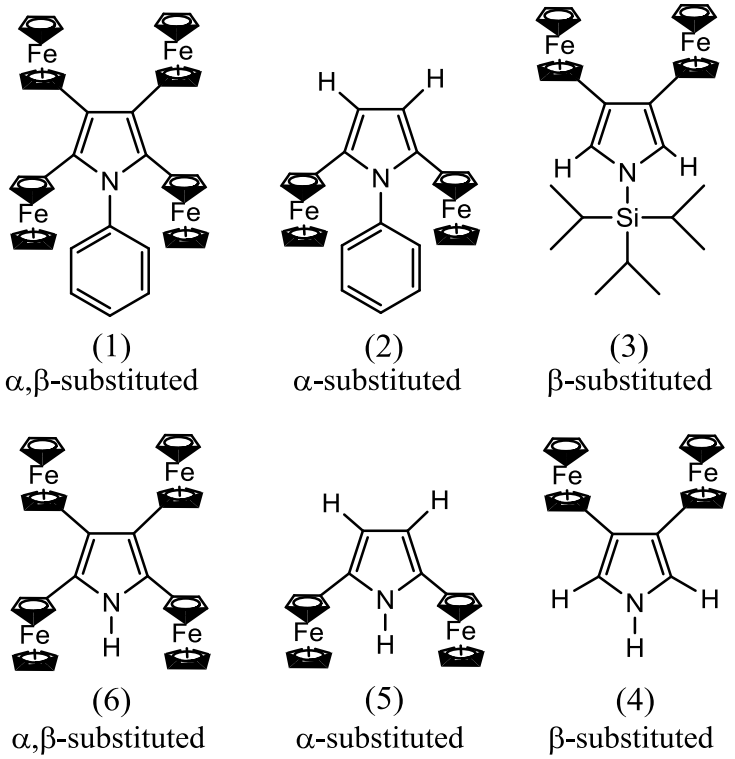

Figure 23. Structures of polyferrocenyl complexes under investigation. Superscripts indicate references for the previously synthesized compounds.[60,70]

Computational Details and Methods

Various DFT calculations were performed for compounds (1), (3), (4), (5), and (6). TDDFT calculations were limited to (3) and (4) for purposes of comparison with the experimental electronic spectrum. The initial geometry of (6) was obtained from the X-ray crystal structure data of (1) previously determined by Hildebrandt, Schaarschmidt, and Lang[60] by replacement of the benzene ring with a hydrogen. The torsion angles between the ferrocenyl substituents and the central pyrrole ring were then set to zero such that the cyclopentadienyl rings of each ferrocene were planar with central pyrrole ring, giving the compound C_2 symmetry. To generate (5), ferrocenes in the β-positions were

removed, while those in the α-positions were removed to create (4). All three molecules were then restricted to the C_2 point group and optimized using the following methods: Becke's three-parameter hybrid exchange functional[18] (1988) with the Lee-Yang-Parr non-local correlation functional[20] (B3LYP); Becke's 1988 exchange functional[21] and the gradient corrections of Perdew, along with his 1981 local correlation functional P86[19] (BP86); The 1996 pure functional of Perdew, Burke, and Ernzerhof combined with the gradient-corrected correlation functional of Perdew, Burke and Ernzerhof[22] (PBE1PBE). Additionally, (4^+), (5^+), and (6^+) were optimized in the same manner using the corresponding unrestricted exchange-correlation functionals. Further calculations involving the C_1 symmetric (6^+) and (1^+) were performed using the uB3LYP exchange-correlation functional. All geometry optimization and single point calculations were performed using a 6-311+G basis set for iron where a set of diffuse functions are necessary to account for the double d-shell effect[47], a 6-311G(d) basis for all carbon and nitrogen atoms, and the contracted 6-31G basis for hydrogen atoms.[31] Optimization, frequency, single point energy, and TDDFT calculations were carried out on the Linux version of the Gaussian09 program.[35] Molecular orbital energy and composition analysis were performed using the open source software QMforge.[71] Frequency calculations were performed for all (4), (5) and (6) optimized structures in order to confirm local energy minima.

Results and Discussion

Electronic Characterization and UV-Vis of (3) and (4)

The first goal of this study was to characterize compound (3) and prove that compound (4) provides a suitable model; advantages of using (4) from a computational

perspective include the use of C_2 symmetry in calculation of molecular properties, as well as reduced size. For simplicity, ferrocene will be referred to as "Fc"; when accompanied by a number, it will refer to the ferrocene at a given position on the central pyrrole ring where the *N*-position is considered as 1 ex. "Fc-2" refers to the ferrocene substituted at the second position of pyrrole.

The molecular orbital composition and comparative energy diagrams of the neutral C_2 symmetry optimized (3) and (4) are provided in S46 through S51 for each of the three exchange correlation functionals under consideration; for compound (3), only the B3LYP functional is utilized. The HOMO and HOMO-1 of (4) are Fc-centered, with contributions from the pyrrole-π orbital increasing with increasing Hartree-Fock exchange contribution to the exchange-correlation functional. The LUMO and LUMO+1 of (4) are predominantly Fc-centered, with an increasing contribution from iron with increasing Hartree-Fock exchange. A similar orbital ordering for the frontier orbitals of (3) were found in both crystal and optimized structures, with only minor contributions from the tris(isopropyl)silyl group. The relative energies of these orbitals are comparable to those calculated for (4) as well, as shown in figure 24.

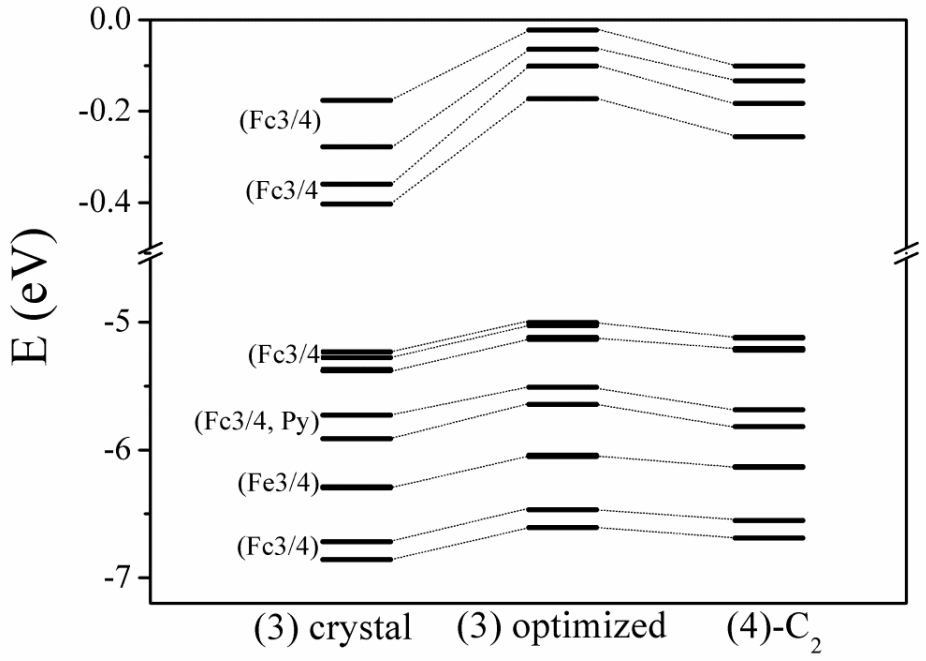

Figure 24. Energetic comparison of the B3LYP calculated molecular orbitals for both C_1 crystal and optimized (3) with those of the C_2 optimized structure of (4).

From figure 24, we see that compounds (3) and (4) share the very similar frontier orbitals, with only minor changes in their relative energies. This demonstrates how (4) serves as a reasonable model to use for further study of compound (3). To further confirm this, as well as assign the electronic spectrum of (3), TDDFT calculations were performed for (3) and (4) using the B3LYP exchange-correlation functional. The experimental UV-Visible spectrum of (3) is provided in figure 25 along with the B3LYP-calculated UV-Visible spectrum and corresponding vertical excitations for compound (4). Vertical excitation energies and transition assignments are provided in table 6. The TDDFT calculated vertical electronic excitations for B3LYP-(3) as well as BP86 and PBE1PBE-(4) are provided in S53 through S55.

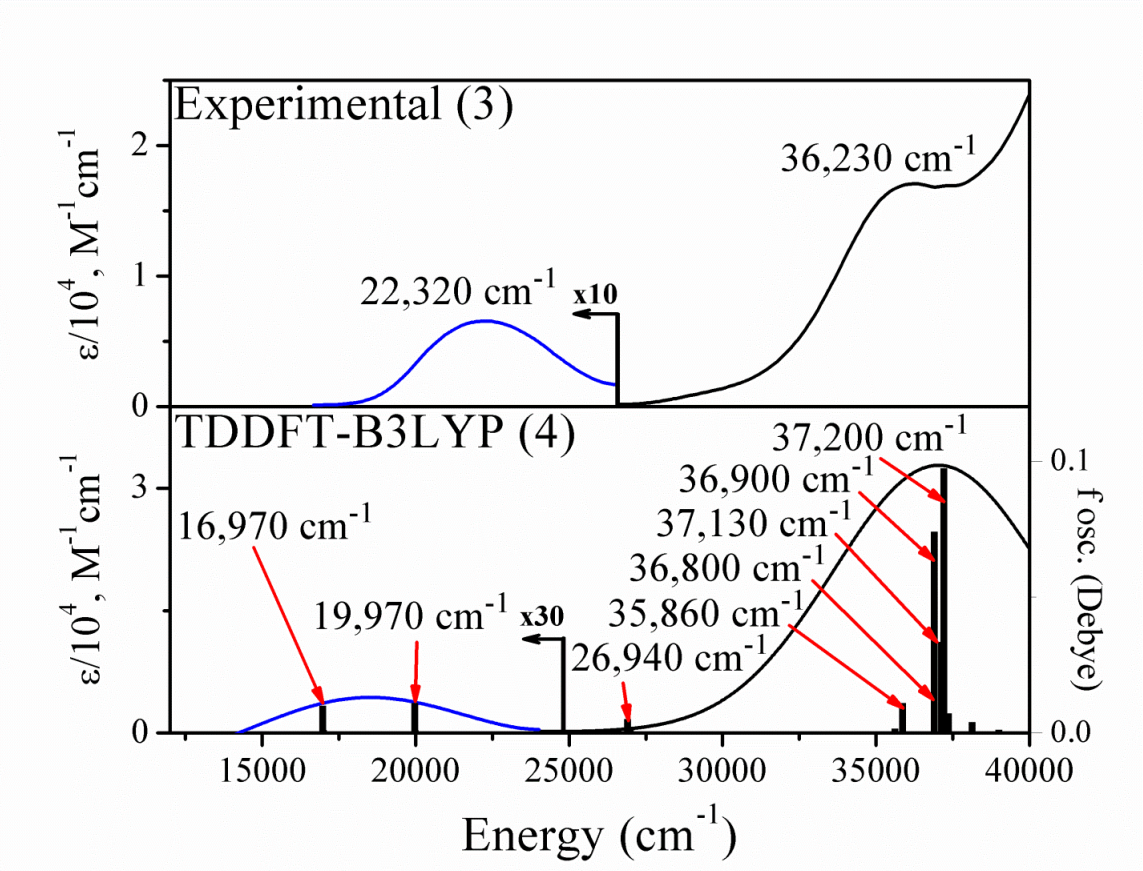

Figure 25. Experimental[70] room-temperature UV-Vis spectrum of (3) (upper) and TDDFT calculated UV-Visible spectrum of (4) utilizing the B3LYP exchange-correlation functional (lower).

Table 6. Experimentally assigned bands and contributing transitions as predicted by B3LYP-TDDFT for (4).

Exp. Band	State	Energy (cm^{-1})	Transition	Expansion coefficients	f (Debye)	Energy (cm^{-1})	
						Exp.	Calc.
1	1	16,970	109 → 116	0.3042	0.0010	22,320	18,540
			110 → 115	0.30035			
			111 → 113	0.33423			
			112 →114	0.33813			
	5	19,970	105 → 113	0.30082	0.0010		
			106 → 114	0.32436			
			109 → 116	-0.27076			
2	9	26,940	105 → 115	-0.27007	0.0005	36,230	37,040
			106 → 114	0.3199			
			109 →116	0.22678			
			110 → 115	0.2541			
			111 → 113	-0.22778			
	13	35,860	111 → 114	-0.41537	0.0110		
			112 → 113	0.50293			
	18	36,800	107 → 115	0.43266	0.0043		
			108 → 116	-0.38281			
	21	36,900	108 → 114	-0.29012	0.0739		
			111 → 115	-0.25336			
			112 → 116	0.41096			
	22	37,130	109 → 114	0.27994	0.0335		
			110 → 117	0.4023			
	25	37,200	107 → 113	0.2556	0.0973		
			108 → 114	-0.29991			
			110 → 117	0.30327			
			111 → 115	0.27011			
			112 → 116	-0.25342			

The experimental spectrum is composed of two primary bands, the first being weak and broad, centered around 22,320 cm^{-1} and spanning from 16,600 cm^{-1} to 26,600 cm^{-1}. The corresponding band 1 of the B3LYP-calculated spectrum is composed of several electronic states, all of which are primarily iron centered in nature. The second and more prominent band 2 of the experimental spectrum appears at 36,230 cm^{-1}. The corresponding B3LYP calculated spectrum predicts two major and three minor but significant electronic states which contribute to band 2. The lower energy states at 26,940 cm^{-1} and 35,860 cm^{-1} are iron and Fc-centered in nature. The first predominantly pyrrole-$\pi \rightarrow$ Fc transition appears at 36,800 cm^{-1}. The remaining transitions are primarily Fc $\rightarrow$ Fc centered, with contributions from pyrrole-$\pi \rightarrow$ Fc vertical electronic excitation to states 21 and 25. While the B3LYP-calculated vertical excitation energies underestimate band 1 by approximately 4,000 cm^{-1}, band 2 is overestimated by ~1,000 cm^{-1}.

Hildebrandt and co-workers[71,72] have demonstrated that the *N*-coordinating substituent can play a significant role in the electronic characteristics and electron-transfer properties of ferrocenyl substituted pyrroles. However, the agreement of (3) and (4), both in terms of ground state electronic structure and vertical electronic excitations, shows that the *N*-coordinating tris(isopropyl)silyl group plays a minor role in the electronic properties of (3); similarly, previous studies[60,61] have shown little difference in the first oxidation potentials between (1) and 2,3,4,5-tetraferrocenyl-1-methyl-pyrrole, as well as between (2) and 2,5-tetraferrocenyl-1-methyl-pyrrole. Therefore, in order to draw direct comparisons between the α-Fc, β-Fc, and Fc-saturated pyrroles, we compromise by modeling compounds (1), (2), and (3) with their *N*-1H analogs (4), (5), (6).

Electronic Characterization of (5) and (6) in C_2

The electronic properties of the C_2 optimized (5) and (6) were calculated using the BP86, B3LYP, and PBE1PBE exchange-correlation functionals; the resulting molecular orbital compositions and comparative energy diagrams are provided in S55 through S62. Similar to (4), the HOMO and LUMO of (5) are Fc-centered, with contributions from the pyrrole-π orbital which increase with increasing Hartree-Fock exchange; it should be noted that contributions to the HOMO and LUMO of (5) from pyrrole-π are greater than those seen in (4) (up to ~40% for PBE1PBE-(5), though the orbitals remain predominantly Fc-centered. Conversely, less contribution from pyrrole is seen in the LUMO+1 through LUMO+3 and HOMO-1 through HOMO-3 when contrasted with (4). Additionally, the pyrrole-π bonding orbitals are shifted from the HOMO-4 and HOMO-5 to HOMO-6 and HOMO-7 for the BP86 optimized (5), and to the HOMO-4 and HOMO-7 for the B3LYP and PBE1PBE optimized (5). The LUMO+1 through LUMO+3 of (5) are predominantly Fc-centered, with an increasing contribution from the iron d-orbitals with increasing Hartree-Fock exchange as was seen for (4); however, lesser contributions from pyrrole-π appear in the LUMO of (5).

The composition of the frontier molecular orbitals of (6) show a mix of characteristics from (4) and (5). In the BP86-optimized geometry of (6), the HOMO is comprised primarily of Fc-3,4 and pyrrole-π, while the LUMO primarily of Fc-2,5 and pyrrole-π (similar to that of (5)); interestingly, contributions to the HOMO from both the Fc-2,5-centered and pyrrole-π orbitals increase with increasing Hartree-Fock exchange contribution to the exchange-correlation functional. The HOMO-1 through HOMO-3 of

(6) appear virtually identical to those of (4), while the LUMO through LUMO+3 are virtually identical to those of (5).

Characterization of the Mixed-Valence States (4^+), (5^+) and (6^+) in C_2

To investigate the mixed-valence properties of the polyferrocenyl pyrroles under consideration, the oxidized complexes were generated and optimized. The resulting molecular orbital compositions and comparative energy diagrams for the C_2 symmetric (4^+), (5^+), and (6^+) are provided in S63 through S86 for each of the three exchange-correlation functionals under consideration. Additionally, spin-densities for each of the optimized geometries are provided in S87.

The uBP86 (6^+) α-HOMO and β-LUMO are composed of a mixture of Fc-2,5 and 3,4 as well as pyrrole-π centered orbitals, with greater contributions of Fc-2,5 to the α-HOMO and conversely greater contributions of Fc-3,4 to the β-LUMO. For this structure, a greater spin density is found on the Fc-3,4 iron centers. In contrast, the uPBE1PBE and uB3LYP results for (6^+) show the α-HOMO to be almost completely Fc-3,4 centered, and the β-LUMO predominantly Fc-2,5 centered with significant contributions from pyrrole-π*. For these exchange-correlation functionals, greater spin-densities are found on the Fc-2,5 iron centers, indicating a more favorable first ionization of Fc at the α-pyrrolic positions relative to those in the β- position.

To further investigate these initial findings, the energetic favorability of selectively oxidizing the α-Fc versus β-Fc was determined by separating the (6^+) structure into three fragments. For our discussion, we will refer to the pyrrole substituted Fc cyclopentadienyl rings as “Cp”, and those which are unsubstituted as “CpH”. The fragments generated consist of the CpH’s and irons of Fc-2,5, the CpH’s and irons of Fc-

3,4, and the pyrrole backbone with all Cp rings. Two single-point calculations were performed, one with the positive charge localized on Fc-2,5, and the other on 3,4. Additionally, geometry optimizations for each were performed, followed by a reassignment of charges and single-point calculation. Since these calculations are relatively costly, the B3LYP exchange-correlation functional was chosen for use in all fragmented molecular calculations since it provided the best agreement with experiment for the UV-Vis and electronic structure of (3) as discussed previously. The resulting molecular-orbital composition and energy diagrams are provided in for each of these are provided in S88 through S97. Energies and spin-densities are provided in table 7. The fragmented geometries were optimized in a step-wise fashion to hone in on their respective local minima. This becomes quite challenging; the natural tendency of an energy minimization calculation is to find the global energy minimum for a molecule, making the search for a geometry corresponding to a desired local minimum determined by charge localization a tedious affair.

The C_2 calculations of (6^+) result in three unique geometries and five different sets of energies and spin-densities, as shown in table 7 below. Charge localization between Fc-2,5 results in little change to the frontier orbital compositions previously discussed for the uB3LYP calculated (6^+). Not surprisingly, localization of charge on Fc-3,4 proves relatively unfavorable, and a degree of delocalization to Fc-2,5 occurs, as can be seen from the spin-densities provided in table 7.

Table 7. Spin densities and relative energies of (6^+) and (1^+). Geometry labels correspond to either structures optimized with a delocalized charge, or denote which of the Fc-substituents charge was localized upon during optimization. All calculations were performed using the uB3LYP exchange-correlation functional. Bold face lines indicate the method which results in the lowest energy for each structure.

	Charge localization			Spin Density			
Symmetry	Geometry	Single-point	ΔE (kcal/mol)	Fe-2	Fe-5	Fe-3	Fe-4
C_2-(6^+)	delocalized	**delocalized**	**7.30**	**0.33**	**0.33**	**0.10**	**0.10**
		Fc-2,5	7.37	0.30	0.30	0.12	0.12
		Fc-3,4	9.70	0.13	0.13	0.20	0.20
	Fc-2,5	Fc-2,5	**3.86**	**0.33**	**0.33**	**0.10**	**0.10**
	Fc-3,4	Fc-3,4	7.78	0.04	0.04	0.52	0.52
C_1-(6^+)	Fc-2	**Fc-2**	**43.14**	**1.02**	**0.00**	**0.00**	**0.00**
		Fc-5	249.21	0.00	1.21	0.00	0.00
		Fc-3	245.74	0.00	0.00	1.18	0.00
		Fc-4	234.35	0.00	0.00	0.00	1.25
	Fc-5	Fc-2	245.95	1.23	0.00	0.00	0.00
		Fc-5	**6.50**	**0.01**	**1.15**	**0.01**	**0.02**
		Fc-3	237.88	0.00	0.00	1.20	0.00
		Fc-4	237.53	0.00	0.00	0.00	1.19
	Fc-3	Fc-2	250.26	1.19	0.00	0.00	0.00
		Fc-5	243.50	0.00	1.21	0.00	0.00
		Fc-3	**0.00**	**0.00**	**0.00**	**1.27**	**0.00**
		Fc-4	239.64	0.00	0.00	0.00	1.17
	Fc-4	Fc-2	244.46	1.21	0.00	0.00	0.00
		Fc-5	240.58	0.00	1.22	0.00	0.00
		Fc-3	237.22	0.00	0.00	1.19	0.00
		Fc-4	**1.20**	**0.00**	**0.00**	**0.00**	**1.26**
C_1-(1^+)	Crystal	delocalized	0.00	0.08	0.71	0.13	0.03
		on 2	-24.58	1.18	0.00	0.00	0.00
		on 5	-17.91	0.00	1.17	0.00	0.00
		on 3	-28.19	0.00	0.00	1.16	0.00
		on 4	-20.73	0.00	0.00	0.00	1.15

Upon optimization of these structures, the Fc-2,5 localized geometry proves the most energetically favorable of the C_2 uB3LYP-calculated (6^+), as can be seen in figure 26.

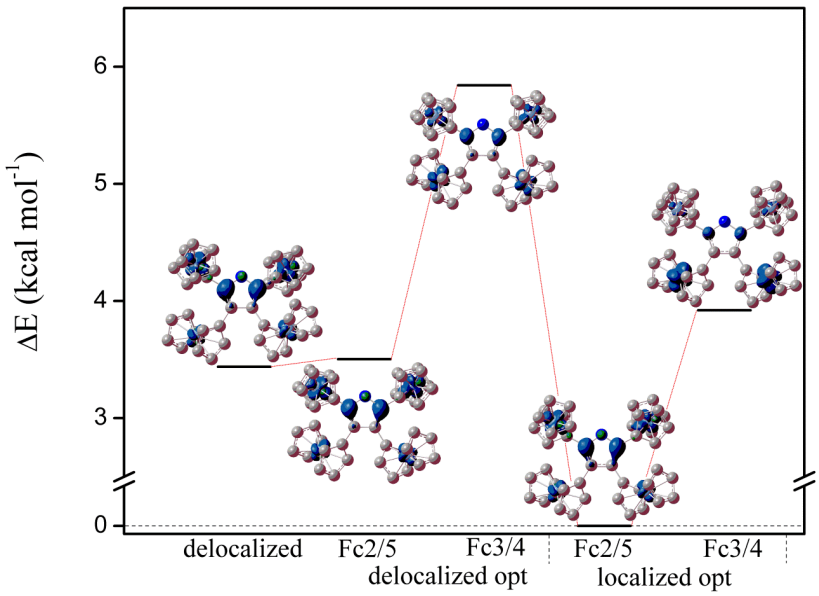

Figure 26. Comparison of spin-densities and relative absolute energies of the uB3LYP-(6^+) C_2 optimized geometries.

Optimization of the charge-localized Fc-3,4-structure results in an alternation of the frontier orbital composition, where the β-LUMO is composed predominantly of Fc-3,4 centered orbitals, and the α-HOMO primarily of Fc-2,5 and pyrrole-π centered orbitals. These results show that the (6) →(6^+) process will more likely occur via oxidation between Fc-2,5 due to the greater energetic stability of these cationic structures, as seen for not only the Fc-2,5 localized calculation, but also in the delocalized structure when treated as a C_2 system . However, as mentioned previously, while (6^+) may be effectively C_2 in solution due to the average rotation of its ferrocenyl substituents, the C_1 species must be considered since these compounds are well known to be Class II systems with discreet M and M^+ centers. Additionally, dynamic NMR studies have shown

significant rotational barriers in (1),[60] making consideration of the C_1 system imperative for a comprehensive study.

Characterization of the Mixed-Valence State of (6^+) in C_1

To properly investigate the C_1 case of (6^+), the C_2-optimized uB3LYP-(6^+) geometry was separated into five respective fragments, four of which consist of a CpH and its corresponding iron, and the fifth comprised of the pyrrole back bone and all Cp rings. Since in solution there is no effective distinction between Fc-2 and 5, or between Fc-3 and 4, the original C_2 (6^+) geometry was altered by rotating the 2 and 3 ferrocene substituents away from planarity with pyrrole by 20˚. The fragmented geometries were then optimized without symmetry restrictions, each with the removal of an electron being localized to one of the four CpH-Fe fragments, in turn generating four C_1 geometries for (6^+). The results of these calculations present four unique geometries for the C_1-(6^+), one for localization of charge on each ferrocene; the spin-densities and energies of each are provided in table 7, and depicted in figure 7. Molecular-orbital composition and energy diagrams are provided in S98 through S107. Torsion angles for the ferrocenyl substituents in all optimized geometries of (6^+) as well as the crystal structure of (1^+), as measured between the pyrrole ring, Cp-ipso, and Cp-α carbons, are provided in table 8.

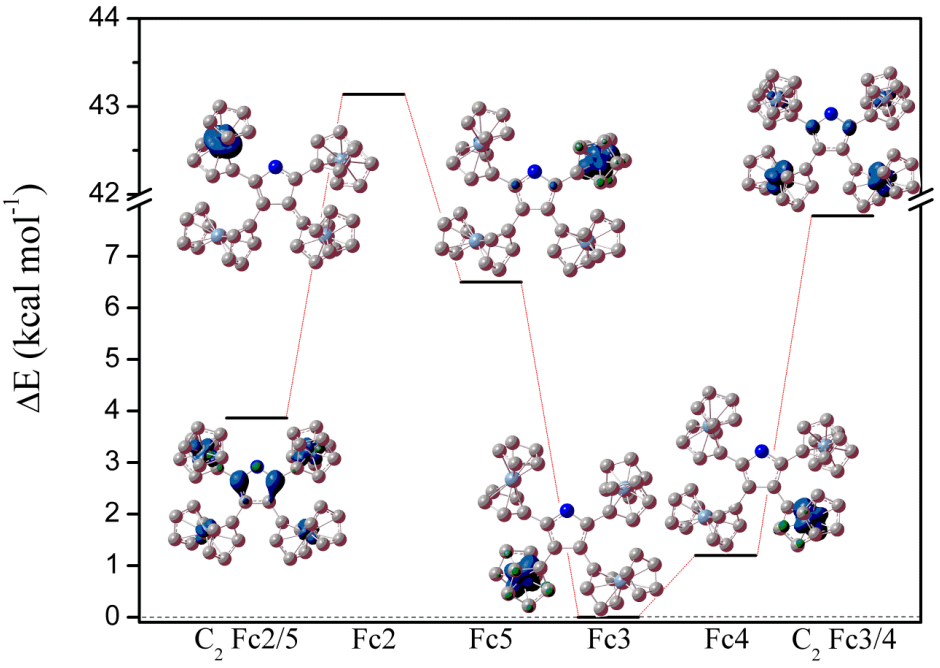

Figure 27. Comparison of spin-densities and relative absolute energies of the B3LYP-(6^+) C_1 optimized geometries and lowest energy C_2 geometries.

Table 8. Torsion angles of considered B3LYP-(6^+) and (1^+) geometries.

		Ferrocene torsion angle (°)			
Symmetry	Geometry	2	5	3	4
C_2	delocalized	-0.78	-0.78	-35.90	-35.90
	Fc-2,5	9.41	9.41	-39.44	-39.44
	Fc-3,4	9.58	9.58	-39.32	-39.32
C_1	Fc-2	42.96	-21.80	-48.56	-23.14
	Fc-5	41.78	-3.15	-48.75	-33.46
	Fc-3	61.42	23.65	-19.71	-44.88
	Fc-4	37.66	-17.07	-45.88	-26.57
C_1	(1^+)-crystal	52.90	-0.43	-30.20	-109.88

Localization of charge on Fc-2 results in an Fc-4 centered α-HOMO and Fc-2 centered β-LUMO; complementing localization on Fc-5 results in an Fc-3 centered α-HOMO and Fc-5 centered β-LUMO. Localization of charge on Fc-3 results in an Fc-4 centered α-HOMO and Fc-3 centered β-LUMO, while localization on Fc-4 results in an Fc-3 centered α-HOMO and Fc-4 centered β-LUMO. It can be seen in figure 27 and in table 7 that localization on Fc-3 proves to be most energetically favorable, followed by Fc-4, then 5, and finally 2. Interestingly, both the Fc-2 and Fc-5 localized structures are less stable under C_1 conditions than C_2.

The greatest structural variation of the C_1-optimized geometries occurs in the pyrrole-ferrocene torsion angles, which determine the degree of planarity the Fc-Cp rings may share with the pyrrole core. This planarity determines the degree of interaction of the pyrrole and Cp π-systems, which is required for intermetallic electron transfer interactions.[61] Each of the C_1-optimized geometries contains a different set of torsion angles for its ferrocenyl substituents; it can be seen in table 8 that in each geometry the ferrocenyl substituent on which the charge was localized is typically rotated such that the Fc-Cp is closer to in-plane with the central pyrrole ring, though this does not appear to be the only factor as there are several exceptions, most noticeably in the Fc-2 localized case. To ensure that the relative stabilities of the localized charges were not artifacts of geometry, ground state electronic calculations were performed for each of the C_1 optimized geometries by localization of the unpaired α-electron on each of the three other possible ferrocenyl substituents. The resulting spin-densities and relative energies are shown in table 7. If the relative stability of the cation rested primarily upon the degree of planarity the Cp (of the ferrocene on which the charge was localized) shared with the

central pyrrole ring, than it could be assumed that placement of charge on the ferrocene with the smallest torsion angle would result in the lowest energy state; for example, localization of charge on Fc-5 in the Fc-2 geometry would appear more favorable than localization on Fc-2 since the Fc-5 torsion angle is smaller. It can be clearly seen from table 7 that the local minimum for placement of the unpaired electron corresponds with its optimized geometry, even in the relatively unstable case of Fc-2, thus confirming that such results do not depend solely on geometry. Therefore, the relative stabilities of the C_1 structures appear to have a complex and significant dependence on both steric and electrostatic factors. Based upon the data presented in figure 27 for the C_1 studies of (6^+) we may conclude that localization of charge, which corresponds with to the first oxidation process, is most favorable on the β-substituted ferrocenes, contradicting conclusions that were drawn from the C_2 results as presented in figure 26.

Characterization of the Mixed-Valence State of (1^+) in C_1

To investigate the influence of substitution at the nitrogen position of pyrrole, electronic ground-state calculations were performed on (1^+) to determine the relative stability of charge localization on each of the ferrocenyl substituents. The corresponding molecular-orbital compositions and comparative energy diagrams are provided in S108 through S119. The resulting spin-densities and absolute energies relative to the delocalized ground state energy are provided in table 7. A comparative diagram illustrating these results is provided in figure 28.

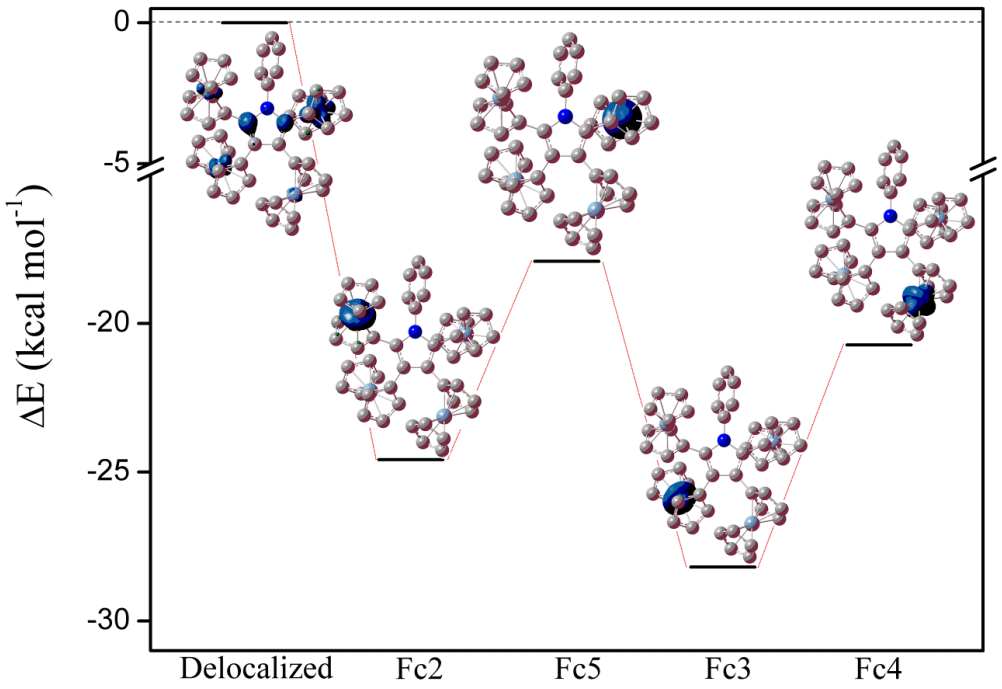

Figure 28. Relative energies and spin-densities resulting from charge localization in (1^+). Zero is set to the energy of the delocalized calculation.

Simply removing an electron, with no localization considerations, results in a majority of spin-density lying around the iron of Fc-5, with small contributions to iron of Fc-3; however, localization of charge on each of the individual ferrocene substituents shows this to be a relatively unfavorable state. Similar to (6^+), the most favorable result emerges as localization around Fc-3. Interestingly, and unlike the (6^+)-Fc-3 case, Fc-5 appears almost perfectly in plane with the central pyrrole ring while Fc-3 remains rotated out-of-plane by 30˚. Based upon the crystal structure, the first oxidation event occurs at the β-substituted ferrocenes. The question of which metal centers couple in this mixed-valence state, however, appears more complicated since there are three iron(II) and one iron(III) center present, which may give rise to several IVCT's. Energetically, the Fc-2

case is the second most stable in figure 28; therefore, the lowest energy IVCT may occur through β-α coupling, rather than β-β or α-α coupling as would be expected in (6^+).

Conclusion

The ground state electronic properties of (3), (4), (5), and (6) have been calculated and characterized for the first time using a DFT approach. Additionally, the mixed-valence states of (1^+), (4^+), (5^+), and (6^+) have been calculated, bringing insight to the metal-metal coupling behavior of these compounds. Thorough investigation of the mixed-valence state of (6^+) presents a complex interdependence of steric and electronic factors; treatment of the molecule in C_2 symmetry has resulted in a more favorable first oxidation of the α-position ferrocenes, where the C_1 symmetry results show greater stability in oxidation of the β-position ferrocenes. The first oxidation wave in (1) and subsequent metal-metal coupling through the mixed-valence state remains unassigned. The switch in favorability of first oxidation from α to β position based upon symmetry considerations indicates compounds based upon (6) may be tunable through *N*-substitution to favor either α or β oxidation.

REFERENCES

(1) (a) Hille, R.; *Chem. Rev.*, **1996**, *96*, 2757-2816. (b) Pilato, R.S.; Stiefel, E.I. *Bioinorganic Catalysis: Molybdenum and Tungsten Enzymes, 2nd Ed*. Reedijk J., Bouwman, E., Eds., Dekker, New York, **1999**, pp.81-152. (c) Sigel, A.; Sigel, H.; Eds. *Metal Ions in Biological Systems: Molybdenum and Tungsten; Their Roles in Biological Systems, Vol. 39*. Dekker, New York, **2002**. (d) Stiefel, E.I. *Progr. Inorg. Chem.*, **2004**, *52*, 1-72. (e) Pollock, V.V.; Conover, R.C.; Johnson, M.K.; Barber, M.J. *Arch. Biochem. Biophys.*, **2002**, *403*, 237-248. (f) Dias, J.; Than, M.; Humm, A.; Huber, R.; Bourenkov, G.P.; Bartunik, H.D.; Burskov, S.; Calvete, J.; Caldeira, J.; Carneiro, C.; Moura, J.J.G.; Moura, I.; Romão, M.J. *Structure (London)*, **1999**, *7*, 65-79. (g) Krafft T.; Macy J.M. *European Journal of Biochemistry*, **1998**, *255*, 647-653. (h) Afkar E.; Lisak, J.; Saltikov, C.; Basu, P.; Oremland, R.S.; Stolz, J.F. *FEMS Microbiology Letters*, **2003**, *226*, 107-112. (i) Saltikov, C.W.; Newman, D.K. *Proceedings of the National Academy of Sciences*, **2003**, *100*, 10983-10988. (j) Silver, S.; Phung, L.T. *Applied and Environmental Microbiology*, **2005**, *71*, 599-608. (k) Santini, J.M.; Sly, L.I.; Schnagl, R.D.; Macy, J.M. *Applied and Environmental Microbiology*, **2000**, *66*, 92-97. (l) Senn D.B.; Hemond, H.F. *Science*, **2002**, 296, 2373-2376. (m) Oremland, R.S.; Stolz, J.F. *Science*, **2003**, *300*, 9390944.

(2) (a) Bray, R.C.; Adams, B.; Smith, A.T.; Richards, R.L.; Lowe, D.J.; Bailey, S. *Biochemistry*, **2001**, *40*, 9810-9820. (b) Stewart, L.J.; Bailey, S.; Bennett, B.; Charnock, J.M.; Garner, C.D.; McAlpine, A.S. *J. Mol. Biol.*, **2000**, *299*, 593-600

(3) Kisker, C.; Schindelin, H.; Pacheco, A.; Wehbi, W.; Garret, R.; Rajagopalan, K.; Enemark, J.; Rees, D. *Cell*, **1997**, *87*, 251.

(4) Li, H.; Temple, C.; Rajagopalan, K.; Schindelin, H. *J. Am. Chem. Soc.*, **2000**, *122*, 7673.

(5) (a) McAlpine, A.; McEwan, A.; Bailey, S. *J. Mol. Biol.*, **1998**, *275*, 613. (b) Okamoto, K.; Kawaguchi, Y.; Eger, B.T.;Pai, E.F.; Nishino, T. *J. Am. Chem. Soc.*, **2010**, *132*, 17080-17083

(6) (a) Jones, R. M.; Inscore, F. E.; Hille, R.; Kirk, M. L. *Inorg. Chem.* **1999**, *38*, 4963-4970. (b) Helton, M. E.; Pacheco, A.; McMaster, J.; Enemark, J. H.; Kirk, M. L. *J. Inorg. Biochem.* **1999**, *80*, 227-233. (c) Benson, N.; Farrar, J. A.; McEwan, A. J.; Thomson, M. J. *FEBS Lett.* **1992**, *307*, 169-172. (d) Finnegan, M. G.; Hilton, J.; Rajagopalan, K. V.; Johnson, M. K. *Inorg. Chem.* **1993**, *32*, 2616-2617. (e) Jalilehvand, F.; Lim, B.S.; Holm, R.H.; Hedman, B.; Hodgson, K.O. *Inorg. Chem.*, **2003**, *42*, 5531-5536.

(7) (a) Cotton, F. A.; Feng, X. *Inorg. Chem.* **1996**, *35*, 4921-4925. (b) Nakai, H.; Morita, H.; Tomasello, P.; Nakatsuji, H. *J. Phys. Chem. A* **1998**, *102*, 2033-2043. (c) Rajapakshe, A.; Snyder, R.A.; Astashkin, A.V.; Bernardson, P.; Evans, D.J.; Young, C.G.; Evans, Dennis H.; Enemark, John H. *Inorganica Chimica Acta* **2009,** *362*, 4603-4608. (d) Astashkin, A.V.; Neese, F.; Raitsimring, A.M.; Cooney, J. Jon A.; Bultman, E.; Enemark, J.H. *J. Am. Chem. Soc.* **2005**, *127*, 16713-16722. (e) Enemark, J.H.; Cosper, M.M. *Metal Ions in Biological Systems* **2002**, *39*, 621-654. (f) Cooney, J.; Jon A.; Carducci, M.D.; McElhaney, A.E.; Selby, H.D.; Enemark, J.H. *Inorg. Chem*. **2002,** *41*, 7086-7093. Carducci, M.D.; Brown, C.; Solomon, E.I.; Enemark, J.H. *J. Am. Chem. Soc.* **1994**, *116*, 11856-11868. (g) McNaughton, R.L.; Mondal, S.; Nemykin, V.N.; Basu, P.; Kirk, M.L. *Inorg. Chem.* **2005**, *44*, 8216-8222. (h) Millar, A.J.; Doonan, C.J.; Smith, P.D.;

Nemykin, V.N.; Basu, P.; Young, C.G. *Chemistry—A European Journal*. **2005**, *11*, 3255-3267. (i) Fischer, B.; Enemark, J.H.; Basu, P. *J. Inorg. Biochem*. **1998**, *72*, 13-21. (j) Basu P.; Nemykin V.N.; Sengar R.S. *Inorg. Chem.* **2003**, *42*, 7489-7501.

(8) Nemykin, V. N.; Basu, P. *Inorg. Chem.* **2003**, *42*, 4046-4056.

(9) Hernandez-Marin, E.; Seth, M.; Ziegler, T. *Inorg. Chem.* **2010**, *49*, 6066-6076

(10) (a) Mtei, R.P.; Lyashenko, G.; Stein, B.; Rubie, N.; Hille, R.; Kirk, M.L. *J. Am. Chem. Soc*., **2011**, *133*, 9762-9774. (b)(6) Westphal, A.; Broda, H.; Kurz, P.; Neese, F.; Tuczek, F. *Inorg. Chem*., **2012**, 51, 5748

(11) Carducci, M.D.; Brown, C; Solomon, E.I.; Enemark, J.H. *J. Am. Chem. Soc.* **1994**, *116*, 11856-11868.

(12) Sabel, D.M.; Gewirth, A.A. *Inorg. Chem.* **1994**, *33*, 148-156.

(13) Deeth, R. J. *J. Chem. Soc., Dalton Trans.* **1991**, 1895-1900

(14) Mason, R.W. *A Practical Guide to Magnetic Circular Dichroism Spectroscopy*. John Wiley & Sons; New York, Chichester, Brisbane, Toronto, Singapore, 2007.

(15) (a) Seth, M.; Ziegler, T. *J. Chem. Phys.* **2006**, *124*, 144105. (b) Krykunov, M.; Seth, M.; Ziegler, T.; Autschbach, J. *J. Chem. Phys.* **2007**, *127*, 244102. (c) Seth, M.; Ziegler, T.; Autschbach, J. *J. Chem. Phys.* **2005**, *122*, 094112. (d) Seth, M.; Ziegler, T.; Banerjee, A.; Autschbach, J.; van Gisbergen, S.J.A.; Baerends, E.J. *J. Chem. Phys.* **2004**, *120*, 10942.

(16) Neese, F.; Solomon, E.I. *Inorg. Chem.* **1999**, *38*, 1847-1865.

(17) Ganyushin, D.; Neese, F. *J. Chem. Phys*. **2008**, *128*, 114117.

(18) Becke, A.D. *J. Chem. Phys.* **1993**, *98*, 5648-5652.

(19) Perdew, J.P. *Phys. Rev. B.* **1986**, *33*, 8822-8824.

(20) Lee, C.; Yang, W.; Parr, R.G. *Phys. Rev. B.* **1988**, *37*, 785-789.

(21) Becke, A.D. *Phys. Rev. A*, **1988**, *38*, 3098-3100.

(22) (a) Perdew, J.P; Burke, K.; Ernzerhof, M. *Phys. Rev. Lett.* **1996**, *77*, 3865-68. (b) Perdew, J.P; Burke, K.; Ernzerhof, M. *Phys. Rev. Lett.* **1997**, *78*, 1396.

(23) Perdew, J.P.; Burke, K.; Wang, Y. *Phys. Rev. B.* **1996**, *54*, 16533-39.

(24) Miehlich, B.; Savin, A.; Stoll, H.; Preuss, H. *Chem Phys.* **1982**, *65*, 239-45

(25) Frisch, Æleen; Frisch, M.J.; Clementa, F.R.; Trucks, G.W. *Gaussian 09: User's Reference*. Gaussian Inc. Wallingford, CT. **2009**. p. 88.

(26) (a) Head-Gordon, M.; Pople, J.A.; Frisch, M.J. *Chem. Phys. Lett.* **1988**, *153*, 503-06 (b) Head-Gordon, M.; Head-Gordon, T. *Chem. Phys. Lett.* **1994**, *220*, 122-28.

(27) (a) Frisch, M.J.; Head-Gordon, M.; Pople, J.A. *Chem. Phys. Lett*. **1990**, *166*, 275-80 (b) Frisch, M.J.; Head-Gordon, M.; Pople, J.A. *Chem. Phys. Lett.* **1990**, *166*, 281-89.

(28) Saebø, S.; Almhöf, J. *Chem. Phys. Lett.* **1989**, *154*, 83-89.

(29) Møller, C.; Plesset, M.S. *Phys. Rev.* **1934**, *46*, 618-622

(30) (a) Foresman, J.B.; Head-Gordon, M.; Pople, J.A.; Frisch, M. J. *J. Phys. Chem.* **1992**, *96*, 135-49. (b) Foresman, J.B.; Frisch, Æ. *Exploring Chemistry with Electronic Structure Methods*, 2nd ed. Gaussian, Inc., Pittsburgh, PA, 1996.

(31) Basis sets were obtained from the Extensible Computational Chemistry Environment Basis Set Database, Version 4/22/01, developed and distributed by the Molecular Science Computing Facility, Environmental and Molecular Sciences Laboratory, Pacific Northwest Laboratory, P.O. Box 999, WA 99352, and funded by the U.S. Department of Energy. The Pacific Northwest Laboratory is a multiprogram laboratory operated by

Battelle Memorial Institute for the U.S. Department of Energy under Contract DE-AC06-76RLO 1830.

(32) Weigend, F; Ahlrichs, R. *Phys. Chem. Chem. Phys.* **2005**, *7*, 3297-3305.

(33) Pantazis, D.A.; Chen, X.Y.; Landis, C.R.; Neese, F. *J. Chem. Theory Comput*. **2008**, *4*, 908.

(34) Kendall, R.A.; Dunning Jr., T.H.; Harrison, R.J. *J. Chem. Phys.* **1992**, *96*, 6796-806.

(35) Frisch, M.J. ; Trucks, G.W.; Schlegel, H.B.; Scuseria, G.E.; Robb, M.A.; Cheeseman, J.R.; Scalmani, G.; Barone, V.; Mennucci, B.; Petersson, G.A.; Nakatsuji, H.; Caricato, M.; Li, X.; Hratchian, H.P.; Izmaylov, A.F.; Bloino, J.; Zheng, G.; Sonnenberg, J.L.; Hada, M.; Ehara, M.; Toyota, K.; Fukuda, R.; Hasegawa, J.; Ishida, M.; Nakajima, T.; Honda, Y.; Kitao, O.; Nakai, H.; Vreven, T.; Montgomery, Jr., J.A.; Peralta, J.E.; Ogliaro, F.; Bearpark, M.; Heyd, J.J.; Brothers, E.; Kudin, K.N.; Staroverov, V.N.; Kobayashi, R.; Normand, J.; Raghavachari, K.; Rendell, A.; Burant, J.C.; Iyengar, S.S.; Tomasi, J.; Cossi, M.; Rega, N.; Millam, J.M.; Klene, M.; Knox, J.E.; Cross, J.B.; Bakken, V.; Adamo, C.; Jaramillo, J.; Gomperts, R.; Stratmann, R.E.; Yazyev, O.; Austin, A.J.; Cammi, R.; Pomelli, C.; Ochterski, J.W.; Martin, R.L.; Morokuma, K.; Zakrzewski, V.G.; Voth, G.A.; Salvador, P.; Dannenberg, J.J.; Dapprich, S.; Daniels, A.D.; Farkas, O.; Foresman, J.B.; Ortiz, J.V.; Cioslowski, J.; Fox, D.J. *Gaussian 09*; Gaussian, Inc., Wallingford CT, 2009.

(36) Neese, Frank; Becker, Ute; Ganyushin, Dmitry; Hansen, Andreas; Liakos, Dimitrios; Izsak, Robert; Kollmar, Christian; Kossmann, Simone; Petrenko, Taras; Reimann, Christoph; Roemelt, Michael; Riplinger; Cristoph; Sandhoefer, Barbara; Schapiro, Igor; Sivalingam, Kantharuban; Wezisla, Boris; Wennmohs, Frank. *Program Version 2.9.0*;

ORCA, Max Planck Institute for Bioinorganic Chemistry. D-45470 Muelheim/Ruhr, Germany.

(37) libint2, Copyright © 1996-2012 Edward F. Valeev and Justin T. Fermann.

(38) (37) 33) Veryazov, V.; Malmqvist, P.A.; Roos, B.O. *International Journal of Quantum Chemistry*. **2011**, *111*, 3329-3338.

(39) (a) Garner, D.; Hill, L. H.; Mabbs, F. E.; McFadden, D. L.; McPhail, A. T. *J. Chem. Soc., Dalton Trans.* **1977**, 838-858. (CSD code: PASCMO) (b) Limberg, C.; Boese, R.; Schiemenz, B. *J. Chem. Soc., Dalton Trans.* **1997,** 1633-1637. (CSD code: NABQIQ) (c) Knopp, B.; Lorcher, K.-P.; Strahle, J. Z. *Naturforsch*. **1977**, *32B*, 1361-1364. (CSD code: PASCMO1) (d) Chang, Y. –D.; Zubieta, *J. Inorg. Chim. Acta*. **1996**, *245*, 177-198. (CSD code: TIXLIV) (e) Klinzing, P.; El-Kholi, A.; Muler, U.; Dehnicke, K.; Findeisen, K. Z. *Anorg. Allg. Chem.* **1989**, *569*, 83-90. (CSD code: JASRIV) (f) Blake, A. J.; Pearsons, S.; Downs, A. J.; Limberg, C. *Acta Crystallogr*. **1995**, *51C*, 571-573. (CSD code: LIMRUV).

(40) Guillemoles, J.-F.; Barone, V.; Joubert, L.; Adamo, C. *J. Phys. Chem. A.* **2002**, *106*, 11354-11360.

(41) Figgis, B.N. Introduction to Ligand Fields; John Wiley & Sons: New York, 1966; p. 60, 351.

(42) (a) Hansion, G.R.; Wilson, G.L.; Bailey, T.D.; Pilbrow, J.R.; Wedd, A.G. *J. Am. Chem. Soc.* **1987**, *109*, 2609-2616. (b) Rillema, D.P.; Brubaker, C.H. Jr. *Inorg. Chem.* **1970**, *9*, 397-400. (c) Balagopalakrishna, C.; Kimbrough, J.T.; Westmoreland, T.D. *Inorg. Chem.* **1996**, *35*, 7758-7768. (d) Sunil, K.K. Ph.D. Thesis, Michigan State University, 1980 (e) Sunil, K.K.; Rogers, M.T. *Inorg. Chem.* **1983**, *28*, 2571

(43) Weber, J.; Garner, C.D. *Inorg. Chem.* **1980**, *19*, 2206-2209. Sunil, K.K.; Harrison, J.F.; Rogers, M.T. *J. Chem. Phys.* **1982**, *76*, 3087-3097.

(44) Kon, H.; Sharpless, N.E. *J. Phys. Chem.* **1966**, *70*, 105-111.

(45) Gerstman, B.S.; Brill, A.S. *J. Chem. Phys.* **1985**, *82*, 1212-1230.

(46) Lever, A.B.P. *Inorganic Electronic Spectroscopy, 2nd ed.*; Elsevier Science Publishing: New York, **1986**, p 241.

(47) Pierloot, K; Cundari, T. R., Ed. *Computational Organometallic Chemistry*. Marcel Dekker Inc, **2001**, p. 123

(48) Rokob, T.A.; Srnec, M.; Rulíšek, L. *Dalton Transactions*, **2011**, *41*, 5747

(49) Manni, G.L.; Aquilante, F.; Gagliardi, L. *J. Chem. Phys.* **2011**, *134*, 034114

(50) Bessac, F.; Hoyau, S.; Maynau, D. *J. Chem. Phys.* **2005**, *123*, 104105

(51) (a) Seth, M.; Ziegler, T.; Autschbach J. *J. Chem. Phys.*, **2008**, *129*, 104105. (b) Seth, M.; Ziegler, T.; Autschbach J. *J. Chem. Phys.*, **2008**, *128*, 234102. (c) Seth, M.; Krykunov, M.; Ziegler, T.; Autschbach J. *J. Chem. Phys.*, **2008**, *128*, 144105.

(52) van Lenthe, E.; Baerends, E.J.; Snijders, J.G. *J. Chem. Phys.* **1993**, *99*, 4597-4610.

(53) Nemykin, V.N.; Hadt, R.G.; Belosludov, R.V.; Mizuseki, H.; Kawazoe, Y. *J. Phys. Chem. A* **2007**, *111*, 12901-12913.

(54) Collison, D. *J. Chem. Soc., Dalton Trans.* **1990**, 1-6.

(55) Winkler, J.R.; Gray, H. B. *Comments Inorg. Chem.* **1981**, *1*, 257-263.

(56) (a) Gao, J.; Liu, W.; Song, B.; C. Liu, C. *J. Chem. Phys.* **2004**, *121*, 6658. (b) Toffolli, D.; Stener, M.; Decleva, P. *Phys. Rev. A* **2002** *66*, 012501. (c) Toffolli, D.; Stener, M.; Decleva, P. *J. Phys. B*, **2002**, *35*, 1275. (d). Toffolli, D.; Stener, M.; Decleva, P. *J. Phys. B* **2003**, *36*, 3097.

(57) (a) Wang, F.; Ziegler, T.; van Lenthe, E.; van Gisbergen, S.; Baerends, E.J. *J. Chem.Phys.* **2005**, *122*, 204103. (b) Wang, F.; Ziegler, T. *J. Chem. Phys,* **2004**, *121*, 12191. (c) Wang F.; Ziegler, T. *J. Chem. Phys.* **2005**, *122*, 074109. (d) Wang, F.; Ziegler, T. *J. Chem. Phys.*, **2005**, *123*, 154102.

(58) Wang, F.; Ziegler, T. *Molecular Physics*, **2004**, *102*, 2585.

(59) Dreuw, A.; Head-Gordon, M. *Chem. Rev*. **2005**, *105*, 4009-4037.

60) Hildebrandt, A.; Schaarschmidt, D.; Lang, H. *Organometallics*, **2011**, *30*, 556-563.

61) Hildebrandt, A.; Schaarschmidt, D.; Claus, R.; Lang, H. *Inorg. Chem.*, **2011**, *50*, 10623-10632.

62) Speck, J.M.; Claus, R.; Hildebrandt, A.; Rüffer, T.; Erasmus, E.; van As, L.; Swarts, J.C.; Lang, H. *Organometallics*, **2012**, *31*, 6373-6380.

63) a) Hildebrandt, A.; Rüffer, T.; Erasmus, E.; Swarts, J.C.; Lang, H. *Organometallics*, **2010**, *29*, 4900-4905. b) Yu, Y.; Bond, A. D.; Leonard, P. W.; Lorenz, U. J.; Timofeeva, T. V.; Volhardt, K. P. C.; Whitener, G. D.; Yakovenko, A. A. *Chem. Commun*., **2006**, 2572. c) Iyoda, M.; Kondo, T.; Okabe, T.; Matsuyama, H.; Sasaki, S.; Kuwatani, Y. *Chem. Lett*., **1997**, 35. d) Ogawa, S.; Muraoka, H.; Kikuta, K.; Saito, F.; Sato, R. *J. Organomet. Chem*., **2007**, 692, 60. e) Kowalski, K.; Winter, R. F. *J. Organomet. Chem*., **2009**, 694, 1041. f) Bobula, T.; Hudlicky, J.; Novák, P.; Gyepes, R.; Císarová, I.; Štěpnička, P.; Kotora, M.Eur. *J. Inorg. Chem*., **2008**, 3911–3920.

64) (a) Jones, S. C.; Barlow, S.; O'Hare, D. *Chem. Eur. J.* **2005**, *11*, 4473-4481. (b) Barlow, S.; O'Hare, D. Chem. Rev. **1997**, *97*, 637-669. (c) Bruce, I. M. Coord. Chem. Rev. **1997**, *166*, 91. (d) Ratner, M.; Jortner, J. *Molecular Electronics*. Blackwell Science: Malden, MA, **1997**. (e) Tour, M. J. Acc. Chem. Res. **2000**, *33*, 791-804. (f) Collier, P. C.;

Wong,W. E.; Belohradsky, M.; Raymo, M. F.; Stoddart, F. J.; Kuekes, J. P.; Williams, S. R.; Heath, R. J. *Science,* **1999**, *285*, 391-394. (g) Carroll, R. L.; Gorman, Ch. B. Angew. Chem., Int. Ed. **2002**, *41*, 4378-4400. (h) Robertson, N.; McGowan, C. *A. Chem. Soc. Rev.*, **2003**, *32*, 96-103. (i) Diallo, A. K.; Daran, J.-C.; Varret, F.; Ruiz, J.; Astruc, D. *Angew. Chem.*, Int. Ed. **2009**, *48*, 3141. (j) Thomas, J. K. R.; Lin, J. T. *J. Organomet. Chem*. **2001**, *637*, 139. (k) Ogawa, S.; Muraoka, H.; Sato, R. *Tetrahedron Lett*. **2006**, *47*, 2479. (l) Paul, F.; Goeb, S.; Justaud, F.; Argouarch, G.; Toupet, L.; Ziessel, R. F.; Lapinte, C. *Inorg. Chem*. **2007**, *46*, 9036. (m) Bildstein, B.; Malaun, M.; Kopacka, H.; Fontani, M.; Zanello, P. *Inorg. Chim. Acta*, **2000**, *16*, 300−302.(n) Patoux, C.; Coudret, C.; Launay, J.-P.; Joachim,C.; Gourdon, A. *Inorg. Chem*. **1997**, *36*, 5037. (o) Mathur, P.; Chatterjee, S.; Das, A.; Lahiri, G. K.; Maji, S.; Mobin, S. M. *J. Organomet. Chem*. **2007**, *692*, 1601. (p) Packheiser, R.; Lohan, M.; Brauer, B.; Justaud, F.; Lapinte, C.; Lang, H.¨ *J. Org. Chem*., **2008**, *693*, 2898. (q) Packheiser, R.; Ecorchard, P.; Walfort, B.; Lang, H. *J. Organomet. Chem*., **2008**, *693*, 933. (r) Richardson, D. E.; Taube, H. *Coord. Chem. Rev*. **1984**, *60*, 107. (s) Kaim, W.; Sarkar, B. *Coord. Chem. Rev*. **2007**, *251*, 584.

65) Creutz, C. *Prog. Inorg. Chem.*, **1983**, *30*, 1.

66) Allen, G.C.; Hush, N.S. *Prog. Inorg. Chem.* **1967**, *8*, 357.

67) Robin, M.; Day, P. *Advances in Radiochemistry*. **1967,** *10*, 248.

68) D'Alessandro, D.; Keene, R. *Chem. Soc. Rev.,* **2006**, *35*, 424.

69) Hush, N. S. *Prog. Inorg. Chem.* **1967**, *8*, 391

70) Goestch, Wil. Master's Thesis. *University of Minnesota Duluth*, **2012**

71) Tenderholt, A.L. *QMForge*, Version 2.1. Stanford University, Stanford, CA, USA.

72) Hildebrandt, A.; Lang, H. *Dalton Trans*., **2011**, *40*, 11831–11837.

SUPPLEMENT TABLE of CONTENTS

Geometric coordinates cont.

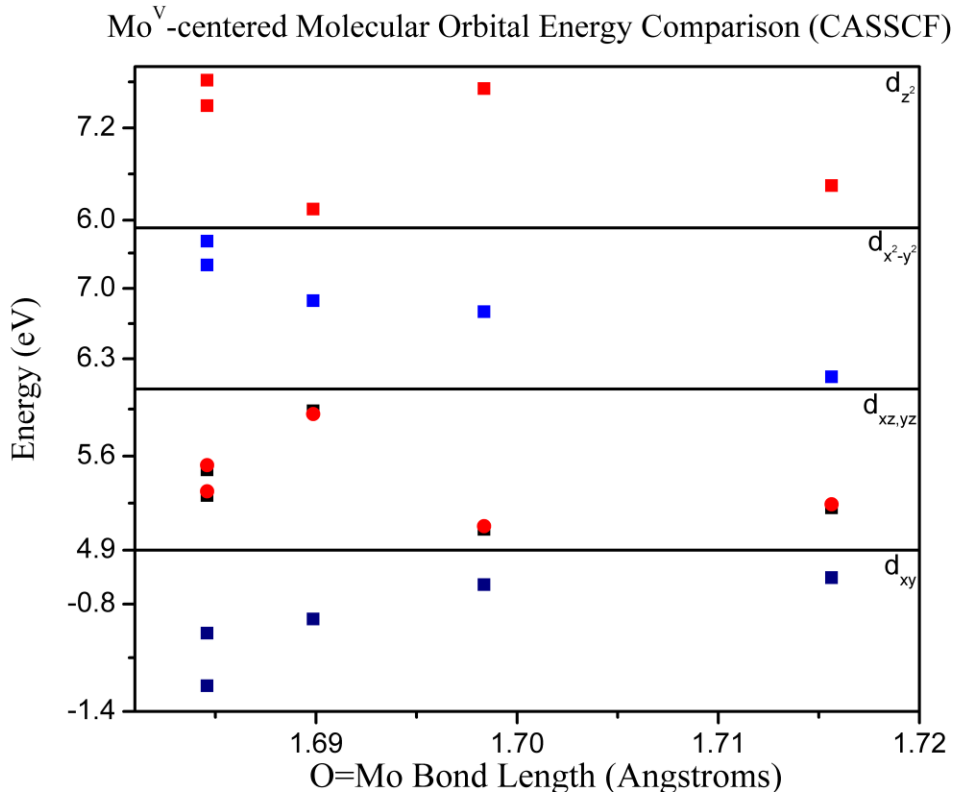

Figure S1. Energies of Mo-4d orbitals as a function of Mo=O bond length

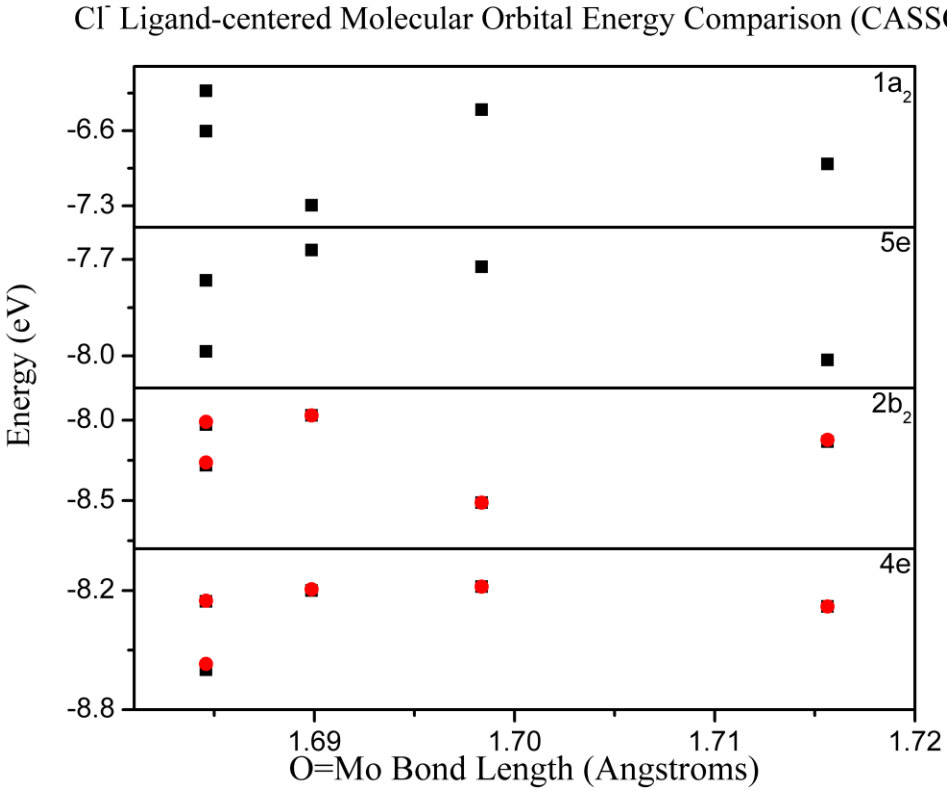

Figure S2. Energies of Ligand centered orbitals as a function of Mo=O bond length

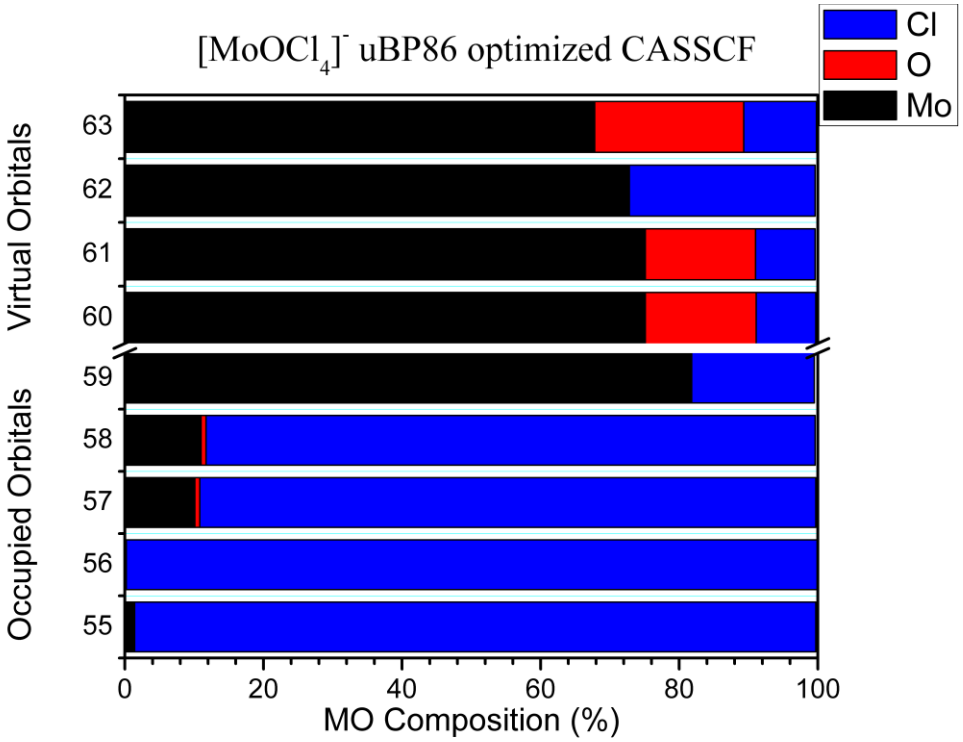

Figure S3. (9,10) CASSCF orbital compositions for the uBP86 optimized geometry

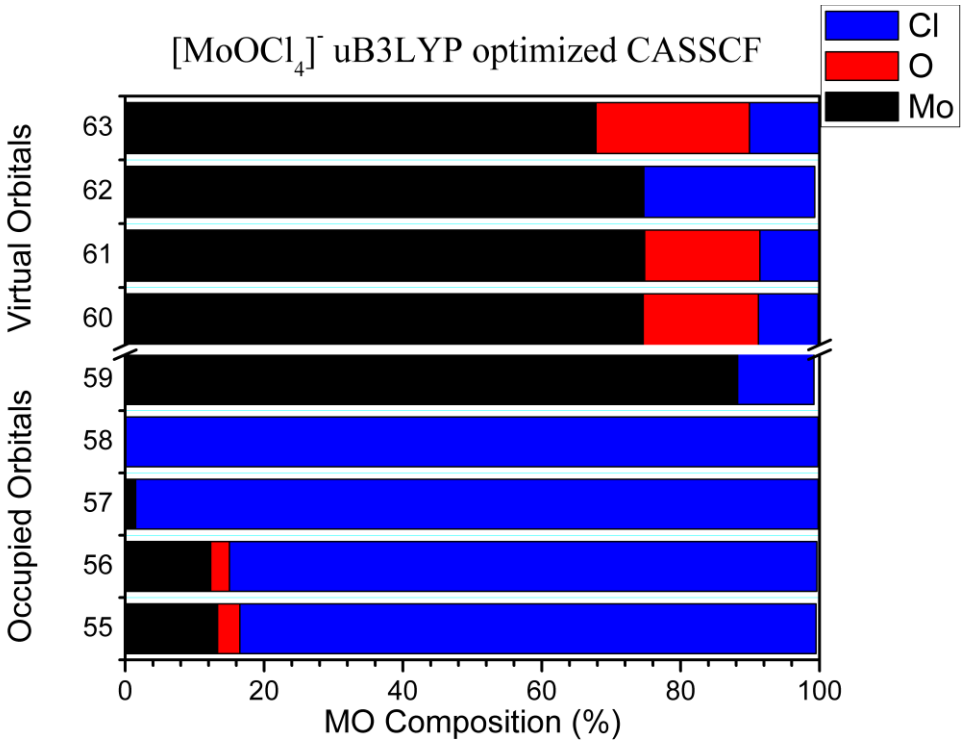

Figure S4. (9,9) CASSCF orbital compositions for the uB3LYP optimized geometry

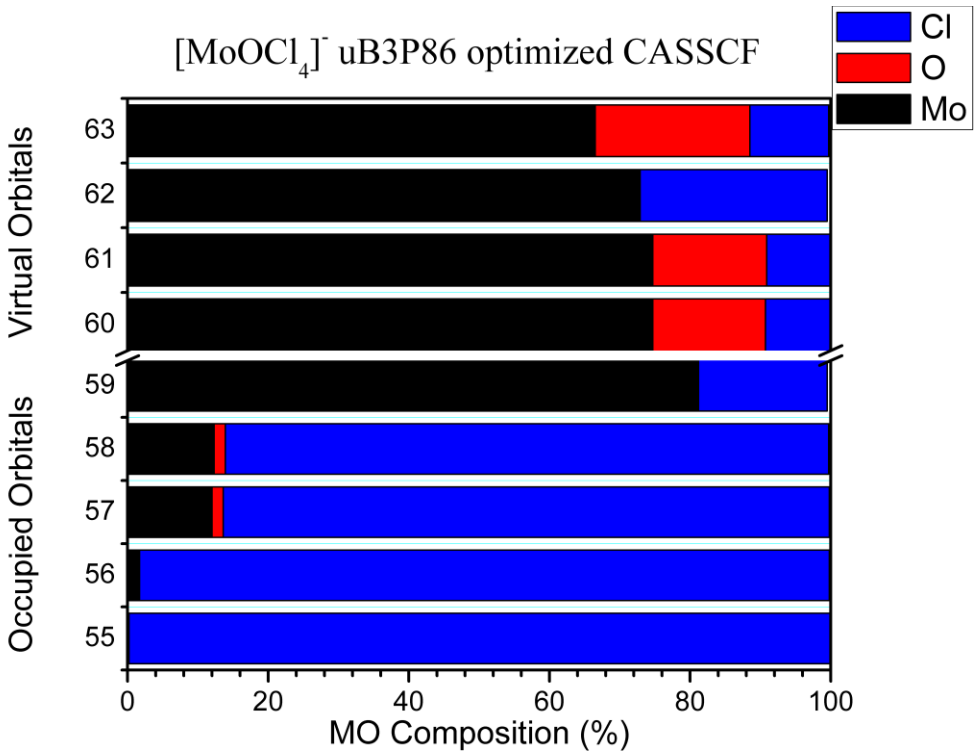

Figure S5. (9,9) CASSCF orbital compositions for the uB3P86 optimized geometry.

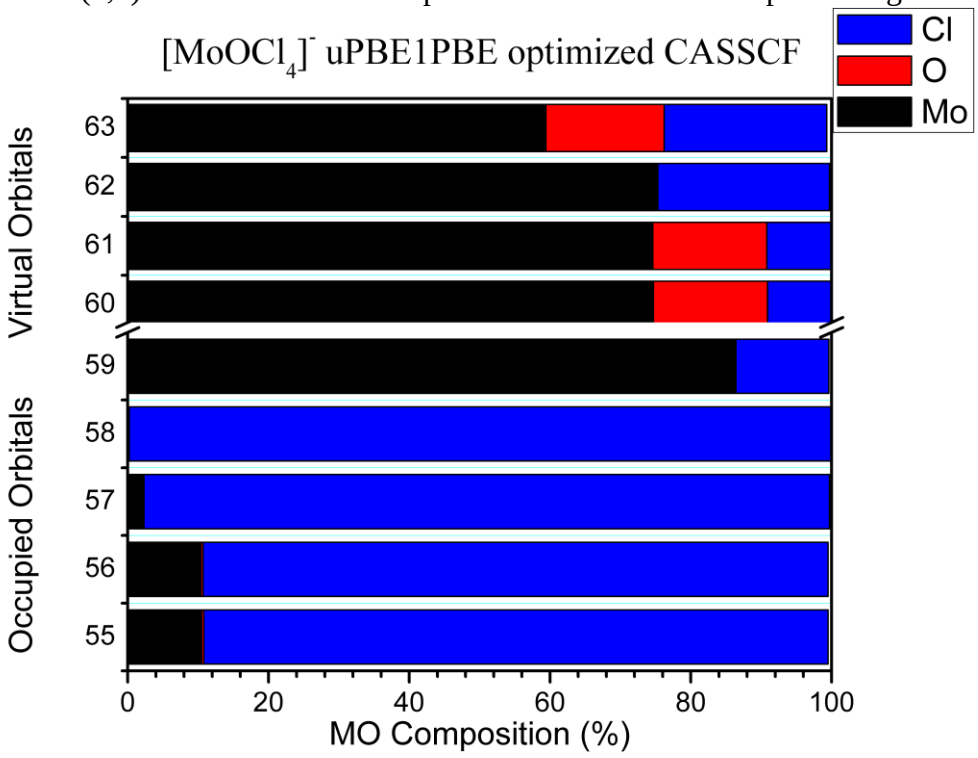

Figure S6. (9,9) CASSCF orbital compositions for the uPBE1PBE optimized geometry.

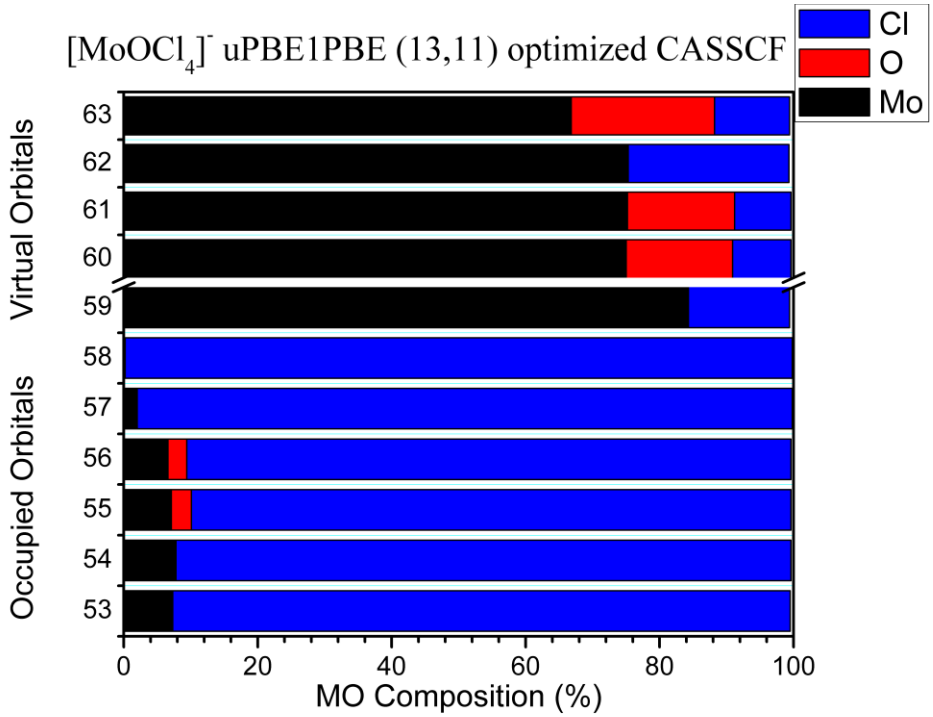

Figure S7. (13,11) CASSCF orbital compositions for the uPBE1PBE optimized geometry

Figure S8. Representatve example of CASSCF (9,9) calculated orbital surfaces (B3P86)

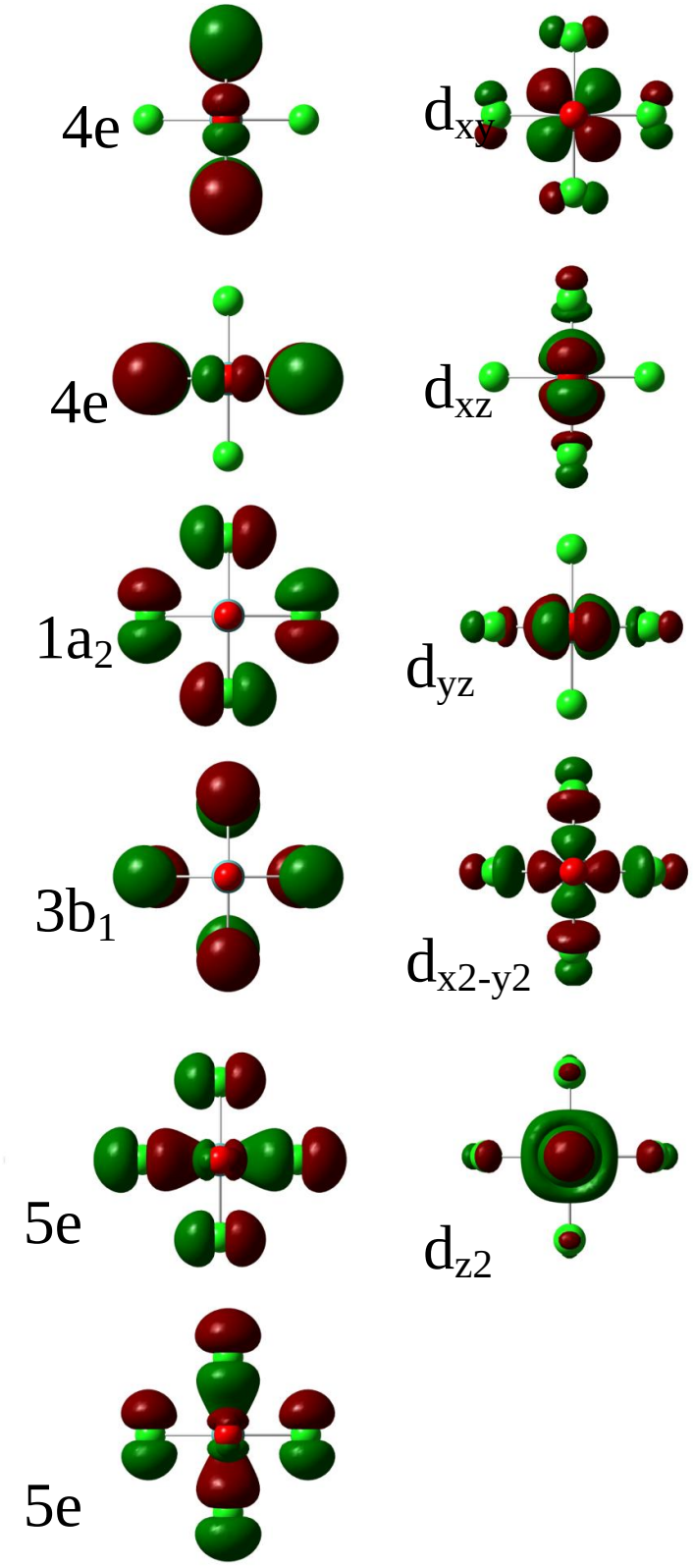

Table S9. CASSCF-MRCI calculated transition oscillator strengths

	Oscillator Strengths (deBye)									
	uBP86		uB3LYP		uB3P86		uPBE1PBE			
	(9,10)		(9,9)		(9,9)		(9,9)		(13,11)	
Band	(#st=16)		(#st=24)		(#st=24)		(#st=16)		(#st=16)	
1	1.2E-06	2.8E-05	3.6E-04	2.5E-05	7.0E-08	4.6E-05	4.3E-05	2.6E-07	9.7E-06	4.8E-05
	3.9E-07	9.7E-06	3.5E-06	2.7E-05	1.4E-08	2.1E-05	2.3E-05	1.0E-07	1.2E-05	1.9E-05
2	1.3E-06	1.3E-07	1.1E-07	7.6E-07	8.3E-07	1.0E-07	1.0E-06	7.0E-09	6.7E-07	2.3E-06
3	9.7E-06	4.4E-07	9.7E-07	1.1E-06	3.7E-07	2.4E-07	3.8E-07	1.3E-06	6.7E-08	6.5E-07
4	7.5E-05	4.5E-05	1.2E-04	7.1E-05	6.8E-06	7.7E-05	1.5E-04	8.6E-05	1.4E-04	1.4E-04
5	1.6E-02	5.0E-03	1.4E-02	2.7E-03	9.3E-06	2.1E-02	2.0E-02	7.7E-04	2.5E-03	1.5E-02
	2.0E-02	1.6E-04	2.0E-03	1.3E-02	8.4E-05	2.1E-02	1.9E-02	1.6E-03	1.1E-03	1.6E-02
6	N.A.	N.A.	N.A.	N.A.	N.A.	N.A.	N.A.	N.A.	9.8E-04	2.1E-03
	N.A.	N.A.	N.A.	N.A.	N.A.	N.A.	N.A.	N.A.	2.2E-03	1.1E-03
7	6.9E-08	5.0E-08	6.8E-08	1.1E-08	1.1E-07	1.0E-09	6.0E-08	7.6E-07	1.0E-06	9.1E-08
8	4.9E-05	3.0E-05	5.1E-05	1.3E-03	3.4E-05	8.4E-07	6.3E-05	6.6E-08	1.5E-05	1.6E-05
	9.9E-06	1.1E-06	1.3E-05	1.1E-04	5.8E-06	6.1E-07	6.9E-08	6.9E-07	1.1E-04	4.6E-05
9	5.1E-03	1.6E-02	3.2E-03	1.9E-02	2.6E-05	2.2E-02	7.5E-04	2.7E-02	2.8E-03	2.5E-02
	4.5E-03	1.7E-02	3.1E-03	1.9E-02	4.6E-04	2.0E-02	9.7E-03	1.4E-02	1.5E-02	1.2E-02

Table S10. Electronic transition Selection Rules for C_{4v} compounds

	Polarization		
State Transition	xy	z	MCD sign
C_{4v}			
$^2A_1$ <- $^2B_1$	F(E)	F(B_1)	(-)
$^2A_2$ <- $^2B_1$	F(E)	F(B_2)	(-)
$^2B_1$ <- $^2B_1$	F(E)	F	(+)
$^2B_2$ <- $^2B_1$	F(E)	A(A_1)	(+)
$^2E_2$ <- $^2B_1$	A (A_1,B_1,B_2)	F(E)	(+/-)
$C_{4v'}$			
Γ_6 <- Γ_7	A	F(Γ_3,Γ_4,Γ_5)	(-)
Γ_7 <- Γ_7	A	A	(+)
$C_{4'}$			
Γ_5 <- Γ_7	A	F	(-)
Γ_6 <- Γ_8	A	F	(-)
Γ_7 <- Γ_7	A	A	(+)
Γ_8 <- Γ_8	A	A	(+)
Γ_8 <- Γ_7	F	F	N/A
Γ_7 <- Γ_8	F	F	N/A

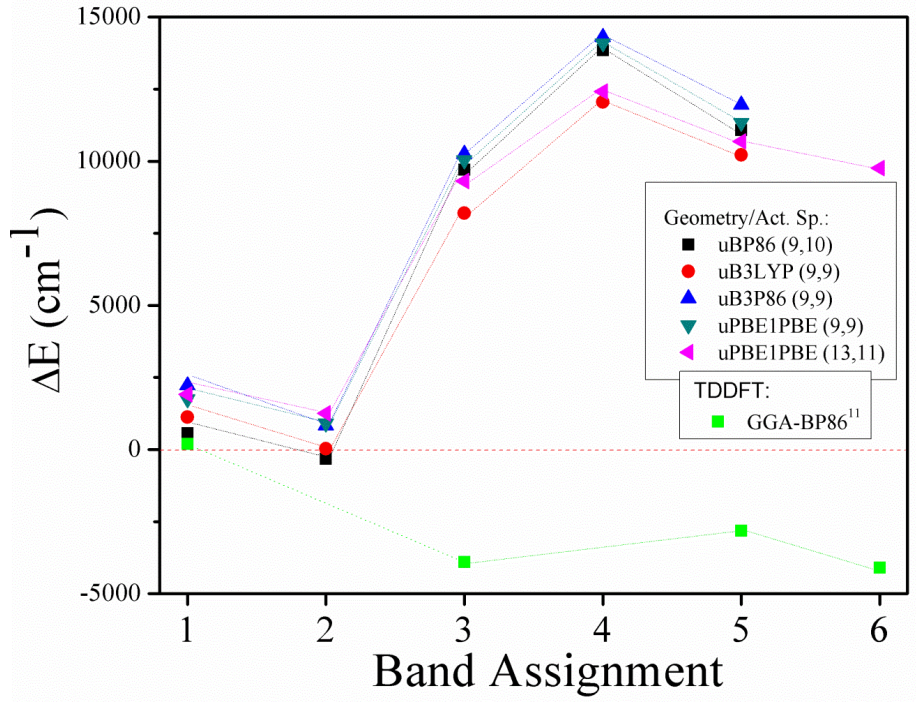

Figure S11. Energetic deviations of MRCI calculated bands from experimental work

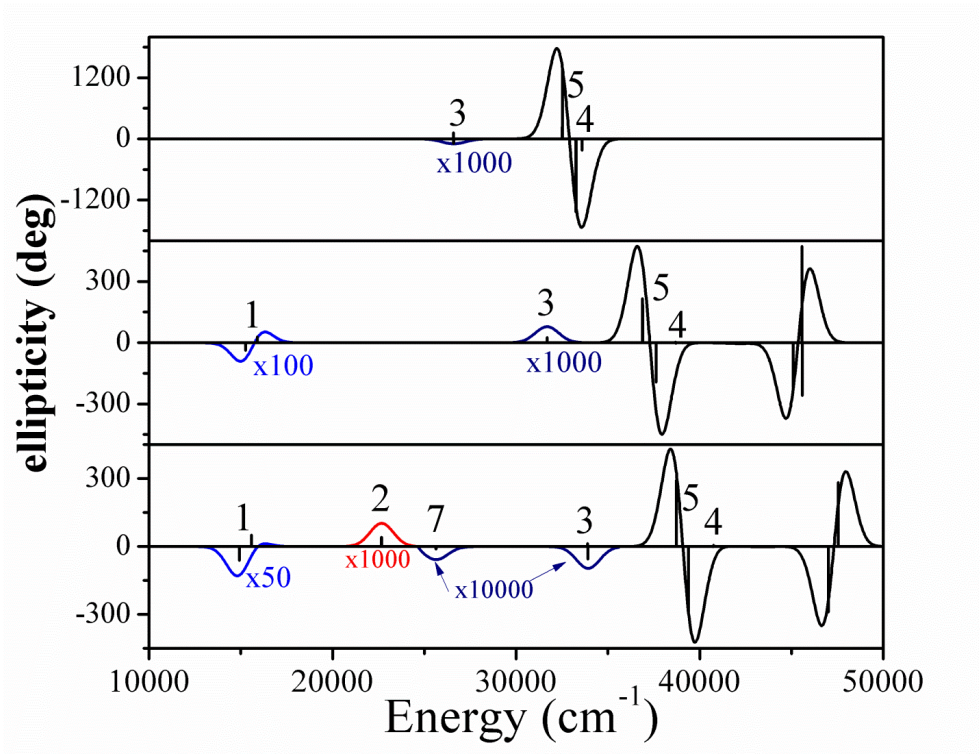

Figure S12. Influence of the inclusion of virtual d-orbitals in the active space on LMCT transitions for the uBP86 geometry; Top to Bottom: (9,5), (9,7), (9,9).

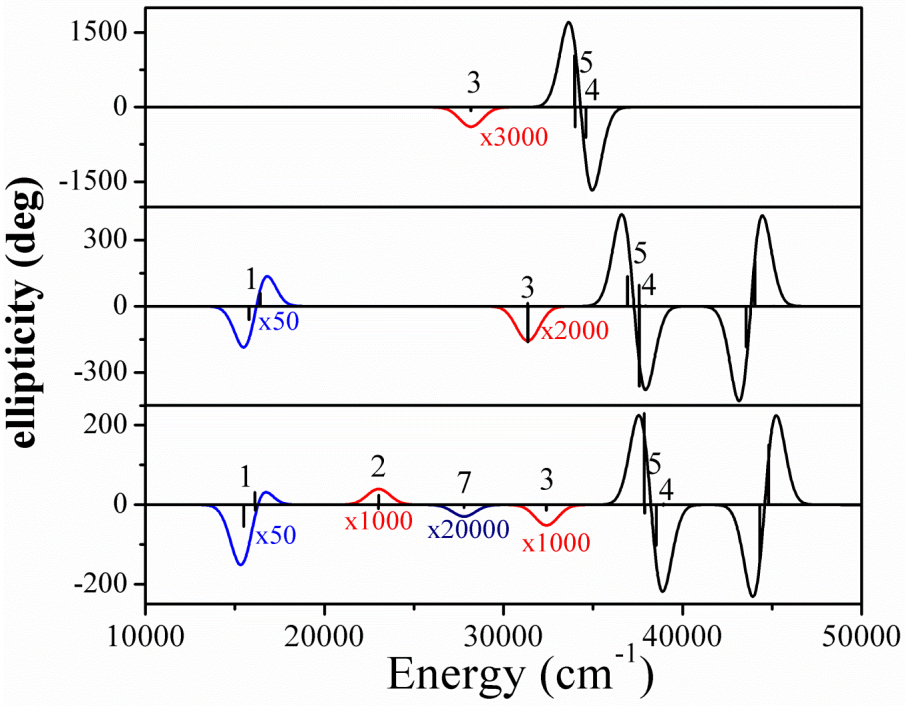

Figure S13. Influence of the inclusion of virtual d-orbitals in the active space on LMCT transitions for the uB3LYP geometry; Top to Bottom: (9,5), (9,7), (9,9).

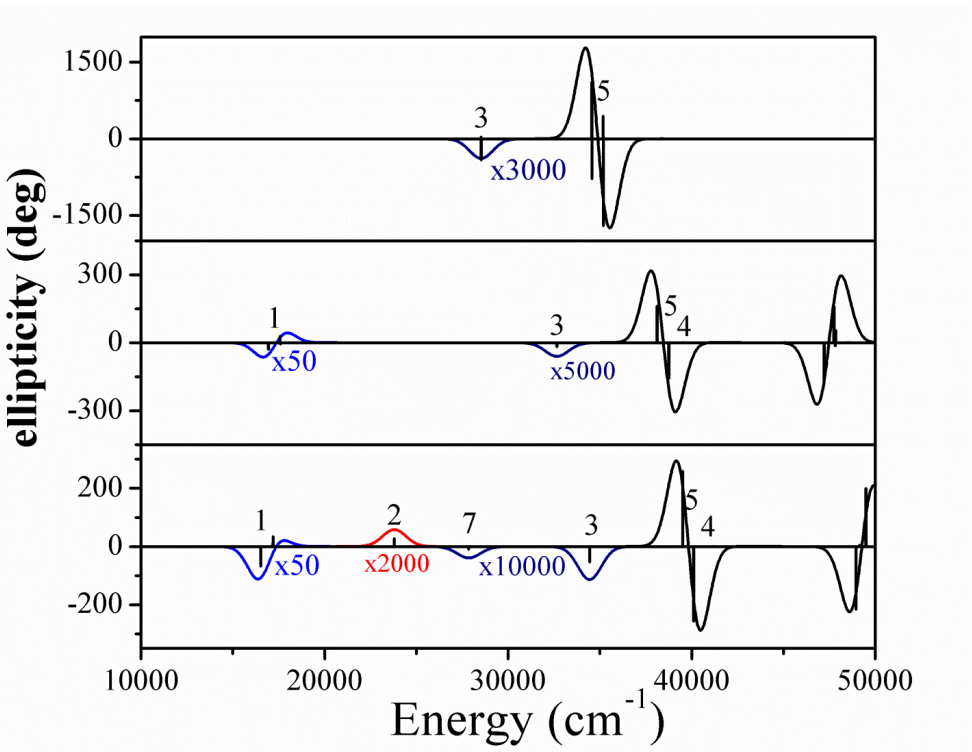

Figure S14. Influence of the inclusion of virtual d-orbitals in the active space on LMCT transitions for the uB3P86 geometry; Top to Bottom: (9,5), (9,7), (9,9).

Table S15. Table of energies (in cm^{-1}) for each active space investigated for each geometry with the $d_{xz,yz}$-centered orbitals included in the active space (d_{x2-y2} and d_{z2} rotated into the external space).

		Active Space & Included Ligand centered orbitals												
Geo.	Band	(1,3)	(3,4) $2a_2$	(3,4) $8b_1$	(5,5) $2a_2$, $8b_1$	(5,5) 14e	(5,5) 13e	(7,6) $2a_2$, 14e	(7,6) $2a_2$, 13e	(7,6) $8b_1$, 14e	(7,6) $8b_1$, 13e	(9,7) $2a_2$, $8b_1$, 14e	(9,7) $2a_2$, $8b_1$, 13e	(13,9)
uBP86	1	15,050	14,869	15,200	15,001	15,310	---	15,185	---	15,409	---	15,266	---	---
		15,715	15,506	15,835	15,637	15,952	---	15,829	---	16,050	---	15,909	---	---
	3	---	32,330	---	32,375	---	---	31,704	---	---	---	31,694	---	---
	4	---	---	38,833	38,824	---	---	---	---	38,667	---	38,728	---	---
	5	---	---	---	---	37,541	---	37,043	---	37,449	---	36,908	---	---
		---	---	---	---	38,223	---	37,782	---	38,129	---	37,636	---	---
	6	---	---	---	---	---	---	---	---	---	---	---	---	---
		---	---	---	---	---	---	---	---	---	---	---	---	---
	8	---	---	---	39,049	---	---	38,641	---	---	---	38,684	---	---
		---	---	---	39,488	---	---	39,064	---	---	---	39,105	---	---
		---	---	---	46,475	---	---	46,035	---	---	---	46,063	---	---
		---	---	---	46,595	---	---	46,138	---	---	---	46,179	---	---
	9	---	---	---	44,893	---	---	---	---	44,977	---	45,106	---	---
		---	---	---	45,429	---	---	---	---	45,239	---	45,601	---	---
uB3LYP	1	15,664	15,466	15,763	15,604	15,882	---	15,796	---	15,911	---	15,799	---	---
		16,273	16,076	16,372	16,213	16,499	---	16,044	---	16,524	---	16,412	---	---

	3	---	32,206	---	32,280	---	---	31,652	---	---	---	31,354	---	---
	4	---	---	38,707	38,671	---	---	---	---	37,952	---	37,950	---	---
	5	---	---	---	---	37,605	---	37,073	---	37,420	---	36,934	---	---
		---	---	---	---	38,276	---	38,349	---	38,069	---	37,591	---	---
	6	---	---	---	---	---	---	---	---	---	---	---	---	---
		---	---	---	---	---	---	---	---	---	---	---	---	---
	8	---	38,050	---	38,177	---	---	37,715	---	---	---	37,661	---	---
		---	38,485	---	38,607	---	---	38,192	---	---	---	38,064	---	---
		---	45,587	---	45,634	---	---	45,123	---	---	---	45,064	---	---
		---	45,655	---	45,698	---	---	45,299	---	---	---	45,130	---	---
	9	---	---	44,052	43,920	---	---	43,790	---	43,599	---	43,559	---	---
		---	---	44,479	44,398	---	---	44,222	---	44,089	---	44,045	---	---
uB3P86	1	16,771	16,566	16,855	16,692	17,061	---	16,879	---	17,045	---	16,946	---	---
		17,413	17,209	17,498	17,335	17,709	---	17,528	---	17,693	---	17,595	---	---
	3	---	33,121	---	33,197	---	---	32,703	---	---	---	32,656	---	---
	4	---	---	39,798	39,788	---	---	---	---	39,512	---	39,537	---	---
	5	---	---	---	---	38,707	---	38,290	---	38,537	---	38,127	---	---
		---	---	---	---	39,365	---	38,943	---	39,187	---	38,771	---	---
	6	---	41,136	---	41,264	---	---	41,134	---	---	---	41,142	---	---
		---	41,576	---	41,698	---	---	41,563	---	---	---	41,562	---	---
	8	---	---	---	48,634	---	---	48,501	---	---	---	48,492	---	---
		---	---	---	49,724	---	---	48,578	---	---	---	48,573	---	---
		---	---	---	---	---	---	---	---	---	---	---	---	---
		---	---	---	---	---	---	---	---	---	---	---	---	---
	9	---	---	47,119	47,097	---	---	---	---	47,243	---	47,230	---	---
		---	---	47,646	47,628	---	---	---	---	47,785	---	47,763	---	---
uPBE1PBE	1	16,764	16,316	16,641	16,464	16,499	16,874	16,353	16,694	16,576	16,913	16,443	16,757	16,809
		16,898	16,948	17,273	17,097	17,138	17,517	16,991	17,337	17,212	17,558	17,081	17,402	17,456
	3	---	32,590	---	32,635	---	---	32,073	32,772	---	---	32,064	32,729	32,352
	4	---	---	39,225	39,203	---	---	---	---	38,164	38,034	38,231	38,077	38,271
	5	---	---	---	---	38,760	---	38,280	---	---	---	38,284	---	37,973
		---	---	---	---	40,705	---	40,648	---	---	---	40,102	---	38,596
	6	---	---	---	---	---	38,804	---	38,332	---	38,618	---	38,177	40,375
		---	---	---	---	---	40,192	---	40,036	---	39,479	---	39,381	40,517
	8	---	39,745	---	39,862	---	---	39,407	40,261	38,738	---	39,439	40,262	39,997
		---	40,180	---	40,297	---	---	39,812	40,688	40,074	---	39,833	40,677	40,375
		---	47,125	---	47,230	---	---	46,752	47,621	---	---	46,785	47,599	47,345
		---	47,246	---	47,367	---	---	46,840	47,782	---	---	46,875	47,782	47,441
	9	---	---	45,856	45,776	---	---	---	---	45,028	44,828	---	44,914	45,293
		---	---	46,374	46,279	---	---	---	---	45,592	45,256	---	45,386	45,848

Table S16. Table of energies (in cm^{-1}) for each active space investigated for each geometry with no unoccupied *d*-centered orbitals included in the active space.

		Active Space & Included Ligand-centered orbitals											
Geo.	Band	(3,2) $2a_2$	(3,2) $8b_1$	(5,3) $2a_2$, $8b_1$	(5,3) 14e	(5,3) 13e	(7,4) $2a_2$, 14e	(7,4) $2a_2$, 13e	(7,4) $8b_1$, 14e	(7,4) $8b_1$, 13e	(9,5) 2a, $8b_1$, 14e	(9,5) 2a, $8b_1$, 13e	(13, 7)
uBP86	3	27,506	---	27,244	---	---	26,985	---	---	---	26,591	---	---
	4	---	33,611	33,661	---	---	---	---	33,536	---	33,601	---	---
	5	---	---	---	33,253	---	32,551	---	33,137	---	32,531	---	---
		---	---	---	33,989	---	33,294	---	33,846	---	33,265	---	---
uB3LYP	3	28,836	---	28,509	---	---	28,206	---	---	---	28,184	---	---
	4	---	34,764	34,759	---	---	---	---	34,698	---	34,683	---	---
	5	---	---	---	34,723	---	34,001	---	34,567	---	33,995	---	---
		---	---	---	35,345	---	34,608	---	35,232	---	34,608	---	---
uB3P86	3	28,984	---	28,728	---	---	28,532	---	---	---	28,530	---	---
	4	---	35,216	35,235	---	---	---	---	35,286	---	35,231	---	---
	5	---	---	---	35,472	---	34,593	---	35,100	---	34,571	---	---
		---	---	---	35,579	---	35,208	---	35,739	---	35,189	---	---
uPBE1PBE	3	29,367	---	29,050	---	---	28337	29,366	---	---	28,242	29,234	28,947
	4	---	35,440	35,420	---	---	---	---	34,264	34,296	34,311	34,383	34,675
	5	---	---	---	35,219	---	34,576	---	35,089	---	34,536	---	34,915
		---	---	---	36,696	---	38,021	---	36,425	---	37,090	---	35,461
	6	---	---	---	---	35,872	---	34,997	---	35,748	---	34,945	37,570
		---	---	---	---	36,798	---	35,820	---	36,529	---	35,713	37,630

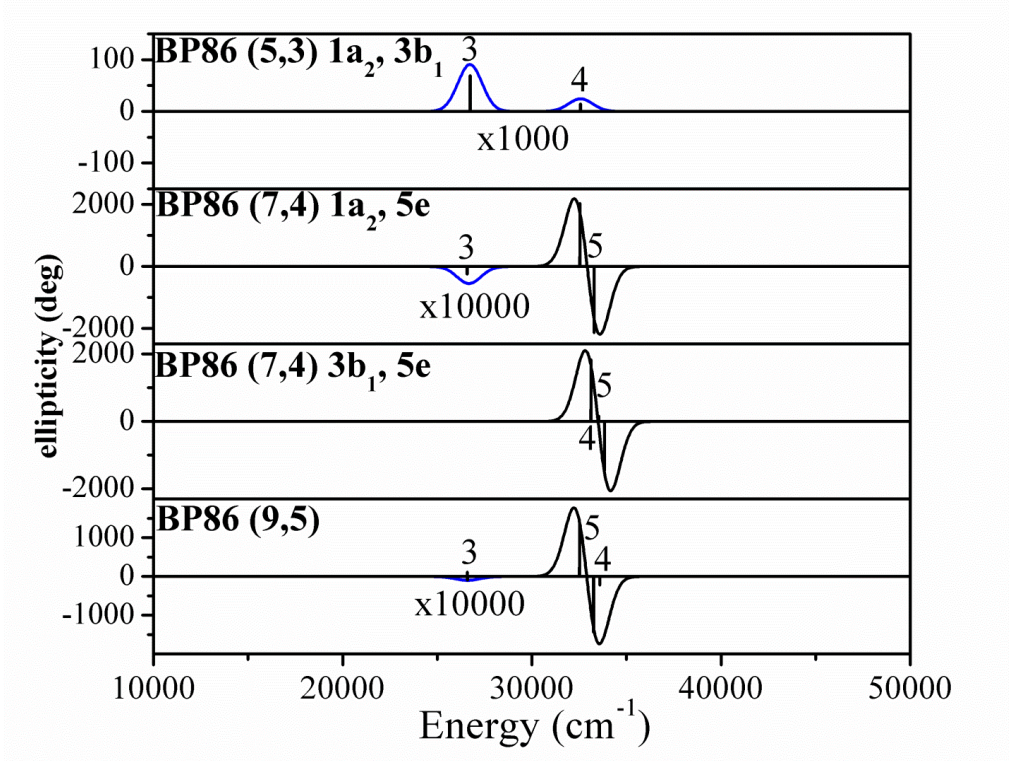

Figure S17. Influence of active space on LMCT transitions for the uBP86 geometry.

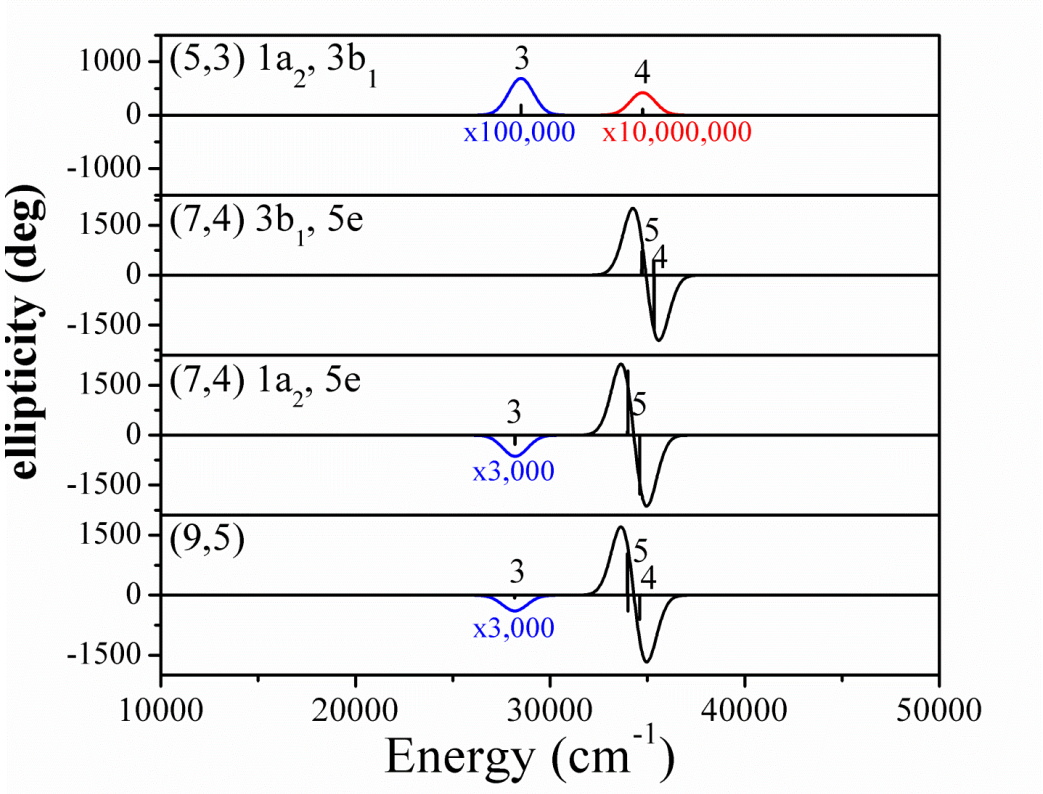

Figure S18. Influence of active space on LMCT transitions for the uB3LYP geometry

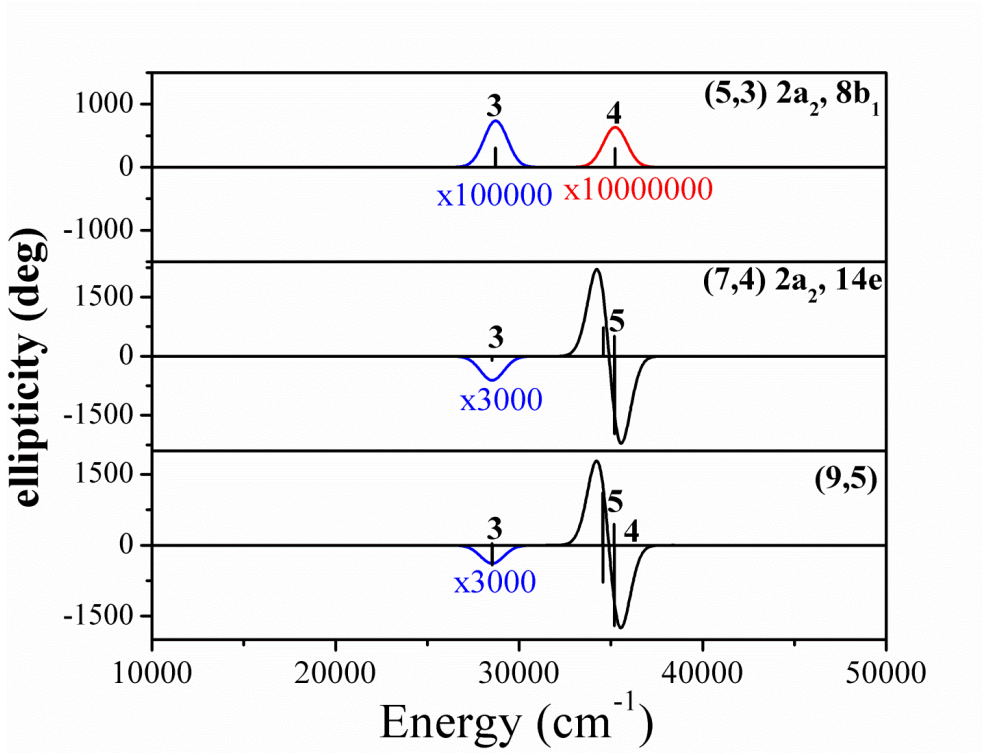

Figure S19. Influence of active space on LMCT transitions for the uB3P86 geometry.

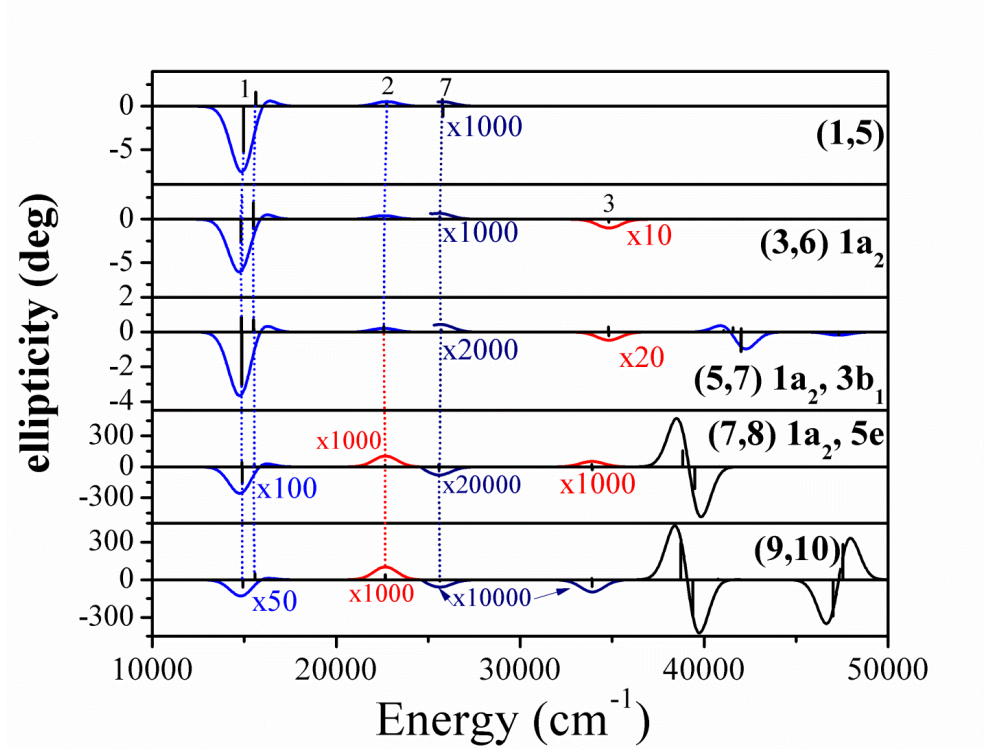

Figure S20. Influence of active space on the d-d electronic states for the uBP86 geometry

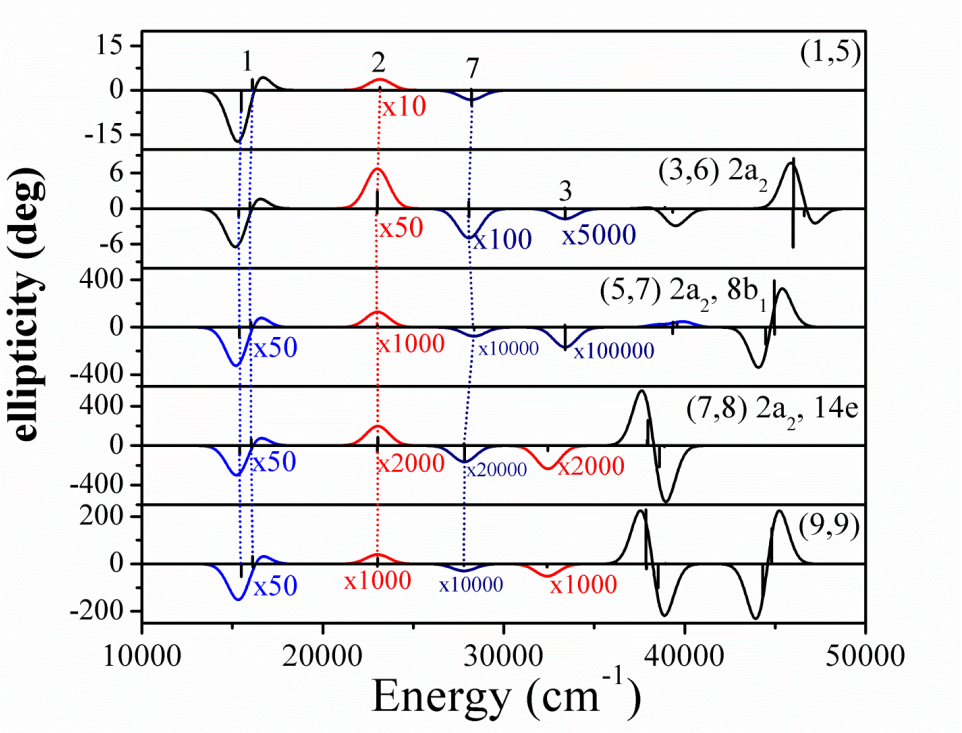

Figure S21. Influence of active space on the d-d electronic states for the uB3LYP geometry

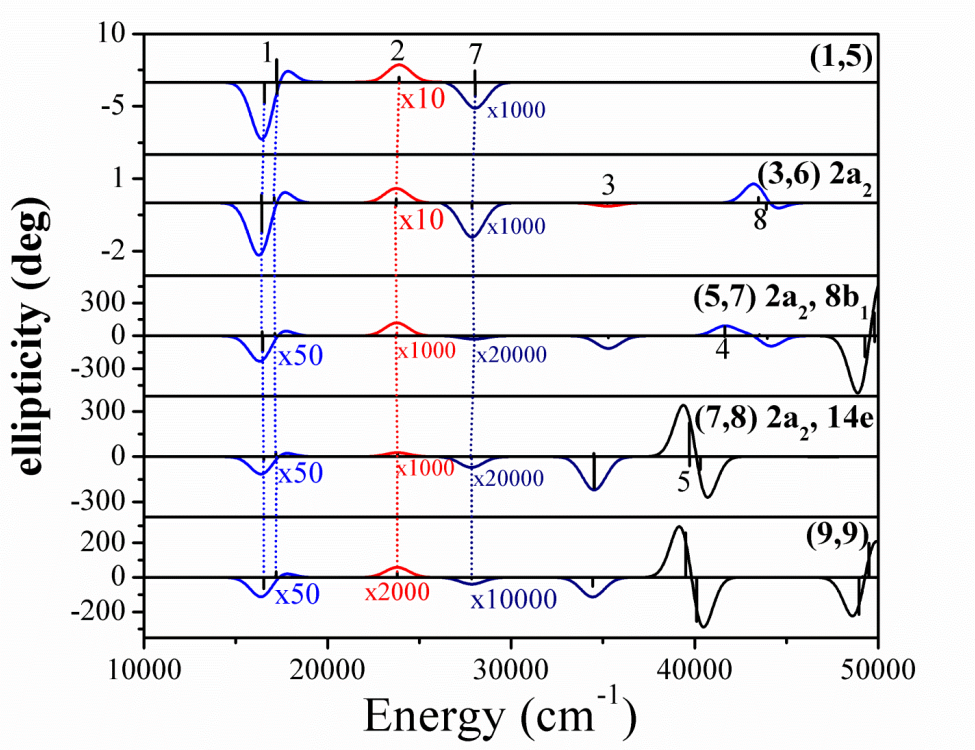

Figure S22. Influence of active space on the d-d electronic states for the uB3P86 geometry

Table S23. Table of energies (in cm^{-1}) for each active space investigated for each geometry with all *d*-centered orbitals included in the active space.

		Active Space & Included Ligand-centered orbitals												
Geometry	Band	(1,5)	(3,6) $2a_2$	(3,6) $8b_1$	(5,7) $2a_2$, $8b_1$	(5,7) 14e	(5,7) 13e	(7,8) $2a_2$, 14e	(7,8) $2a_2$, 13e	(7,8) $8b_1$ 14e	(7,8) $8b_1$, 13e	(9,9) $2a_2$, $8b_1$, 14e	(9,9) $2a_2$, $8b_1$, 13e	(13,11)
uBP86	1	14,970	14,841	15,018	14,864	15,028	---	14,884	---	15,067	---	14,933	---	---
		15636	15,508	15,684	15,532	15,698	---	15,555	---	15,737	---	15,603	---	---
	2	22,746	22,596	22,700	22,580	22,821	---	22,676	---	22,807	---	22,673	---	---
	3	---	34,830	---	34,820	---	---	33,915	---	---	---	33,910	---	---
	4	---	---	41,027	41,083	---	---	---	---	40,758	---	40,751	---	---
	5	---	---	---	---	39,310	---	38,853	---	39,198	---	38,747	---	---
		---	---	---	---	39,935	---	39,510	---	39,821	---	39,049	---	---
	6	---	---	---	---	---	---	---	---	---	---	---	---	---
	7	25,786	25,461	25,840	25,717	25,721	---	25,598	---	25,777	---	25,637	---	---
	8	---	---	---	41,594	---	---	40,846	---	---	---	40,891	---	---
		---	---	---	42,028	---	---	41,278	---	---	---	41,323	---	---
	9	---	---	---	47,318	---	---	---	---	47,052	---	47,035	---	---
		---	---	---	---	---	---	---	---	47,607	---	47,566	---	---
uB3LYP	1	15,800	15,366	15,531	15,398	15,594	---	15,423	---	15,576	---	15,508	---	---
		15,812	15,994	16,160	16,027	16,223	---	16,052	---	16,205	---	16,137	---	---
	2	23,105	23,014	23,137	23,020	23,211	---	23,053	---	23,187	---	23,026	---	---
	3	---	33,387	---	33,389	---	---	32,447	---	---	---	32,402	---	---
	4	---	---	39,584	39,594	---	---	---	---	38,944	---	38,950	---	---
	5	---	---	---	---	38,323	---	37,967	---	38,091	---	37,894	---	---
		---	---	---	---	38,976	---	38,615	---	38,720	---	38,550	---	---
	6	---	---	---	---	---	---	---	---	---	---	---	---	---
	7	28,150	28,078	28,264	28,143	27,970	---	27,821	---	28,004	---	27,796	---	---
	8	---	38,932	---	38,925	---	---	38,446	---	---	---	38,498	---	---
		---	39,340	---	39,347	---	---	38,884	---	---	---	38,919	---	---
		---	46,001	---	45,965	---	---	45,745	---	---	---	---	---	---
		---	46,025	---	---	---	---	45,817	---	---	---	---	---	---
	9	---	---	44,552	44,475	---	---	---	---	44,251	---	44,330	---	---
		---	---	45,058	44,978	---	---	---	---	44,754	---	44,819	---	---
uB3P86	1	16,581	16,430	16,609	16,470	16696	---	16,540	---	16,660	---	16,535	---	---
		17,248	17,098	17,277	17,139	17366	---	17,211	---	17,331	---	17,206	---	---
	2	23,901	23,739	23,863	23,769	23977	---	23,811	---	23,949	---	23,796	---	---
	3	---	35,260	---	35,295	---	---	34,522	---	---	---	34,437	---	---
	4	---	---	41,633	41,655	---	---	---	---	41,210	---	41,205	---	---
	5	---	---	---	---	40095	---	39,721	---	39,906	---	39,567	---	---
		---	---	---	---	40712	---	40,319	---	40,510	---	40,255	---	---
	6	---	---	---	---	---	---	---	---	---	---	---	---	---

	7	28,038	27,869	28,085	27,972	27970	---	27,830	---	28,005	---	27,856	---	---
	8	---	43,483	---	43,547	---	---	42,921	---	---	---	42,984	---	---
		---	43,924	---	43,970	---	---	43,345	---	---	---	43,409	---	---
		---	50,863	---	50,793	---	---	50,118	---	---	---	50,191	---	---
		---	51,157	---	---	---	---	50,430	---	---	---	50,462	---	---
	9	---	---	48,942	49,281	---	---	---	---	48,822	---	49,002	---	---
		---	---	49,796	49,799	---	---	---	---	49,394	---	49,560	---	---
uPBE1PBE	1	16,350	16,205	16,380	16,279	16,388	16,492	16,311	16,379	16,428	16,504	16,336	16,375	16,436
		17,005	16,858	17,034	16,932	17,050	17,133	16,971	17,021	17,090	17,156	16,997	17,016	17,089
	2	24,088	23,932	24,069	23,952	24,160	24,114	24,039	23,975	24,143	24,092	24,053	23,951	24,048
	3	---	33,947	---	33,919	---	---	33,799	33,734	---	---	33,752	33,661	33,506
	4	---	---	40,307	40,355	---	---	---	---	40,041	39,675	40,087	39,726	39,514
	5	---	---	---	---	40,189	---	39,801	39,186	40,135	---	39,717	---	38,657
		---	---	---	---	41,729	---	41,751	40,502	41,362	---	41,066	---	39,215
	6	---	---	---	---	---	39,354	---	---	---	39,262	---	39,010	41,020
		---	---	---	---	---	40,467	---	---	---	40,181	---	40,213	41,091
	7	29,384	29,228	29,433	29,306	29,396	29,313	29,289	29,190	29,434	29,341	29,343	29,220	29,232
	8	---	41,108	---	41,556	---	---	41,027	41,092	---	---	---	41,068	40,915
		---	41,519	---	41,551	---	---	41,420	41,509	---	---	---	41,475	41,327
		---	48,280	---	48,427	---	---	48,261	48,390	---	---	---	48,372	---
		---	48,358	---	48,462	---	---	48,367	48,415	---	---	---	48,385	---
	9	---	---	46,814	46,901	---	---	---	---	46,603	46,146	---	46,122	46,084
		---	---	47,273	47,250	---	---	---	---	47,161	46,560	---	46,473	46,613

Table S24. Table of energies (cm^{-1}) for the DFT-CASSCF-MRCI partitioned active spaces. The energies of bands 1, 2, and 7 were calculated via a (1,5) active space, while bands 3, 4, 5, and 6 were calculated via (13,7) active space.

	DFT Geometry & Initial guess			
Band	uBP86	uB3LYP	uB3P86	uPBE1PBE
1	14,107	14,683	15,516	15,160
2	23,290	23,215	24,289	24,247
3	25,474	25,524	26,288	26,312
4	31,647	31,627	32,837	32,814
5	30,940	31,128	32,343	32,211
6	33,729	34,117	35,486	35,176
7	27,001	27,887	28,737	28,582

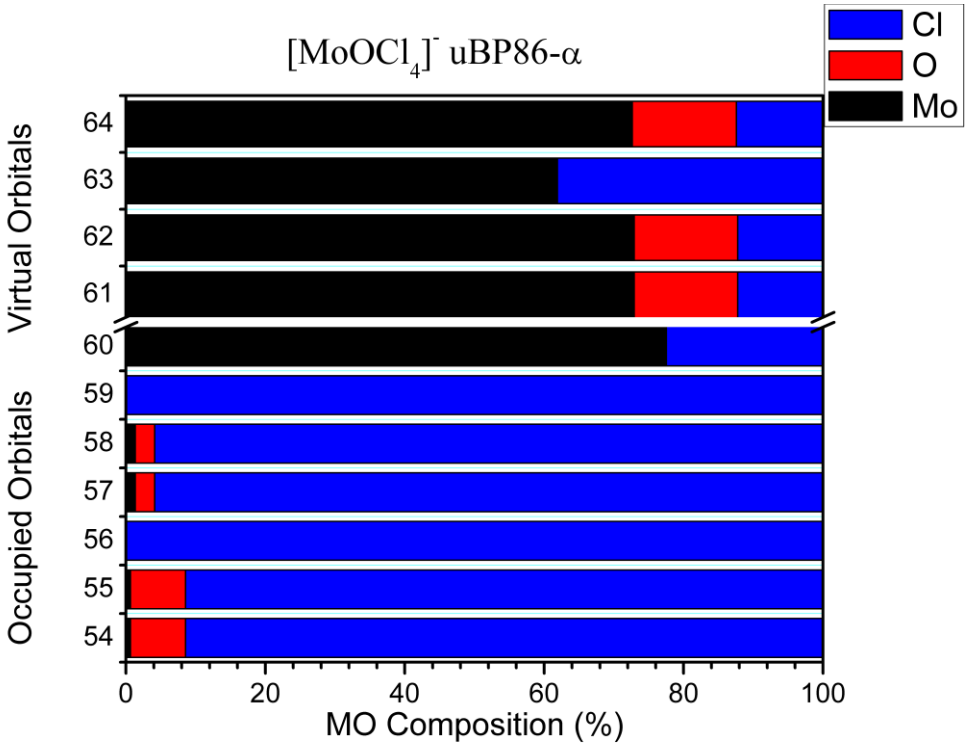

Figure S25. DFT calculated uBP86 α-orbital compositions

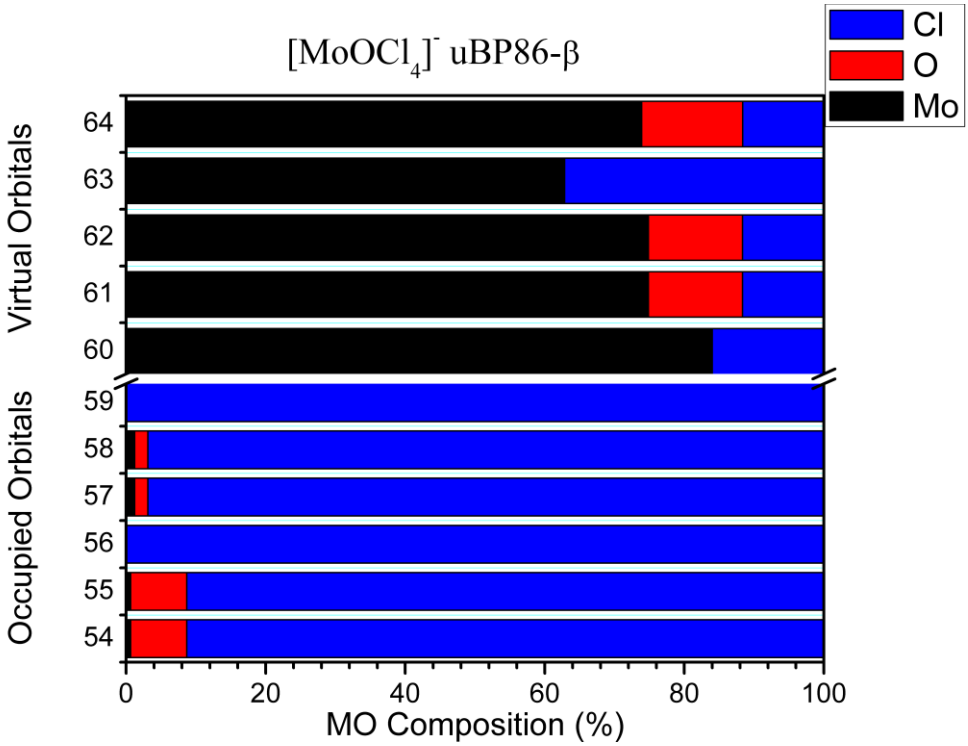

Figure S26. DFT calculated uBP86 β-orbital compositions

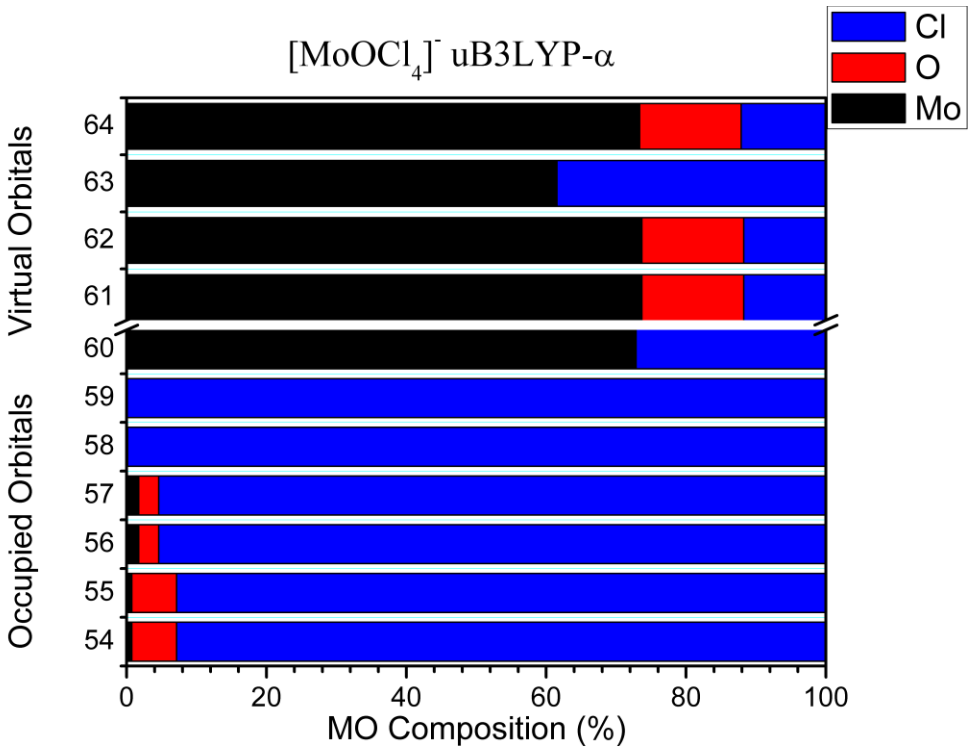

Figure S27. DFT calculated uB3LYP α-orbital compositions

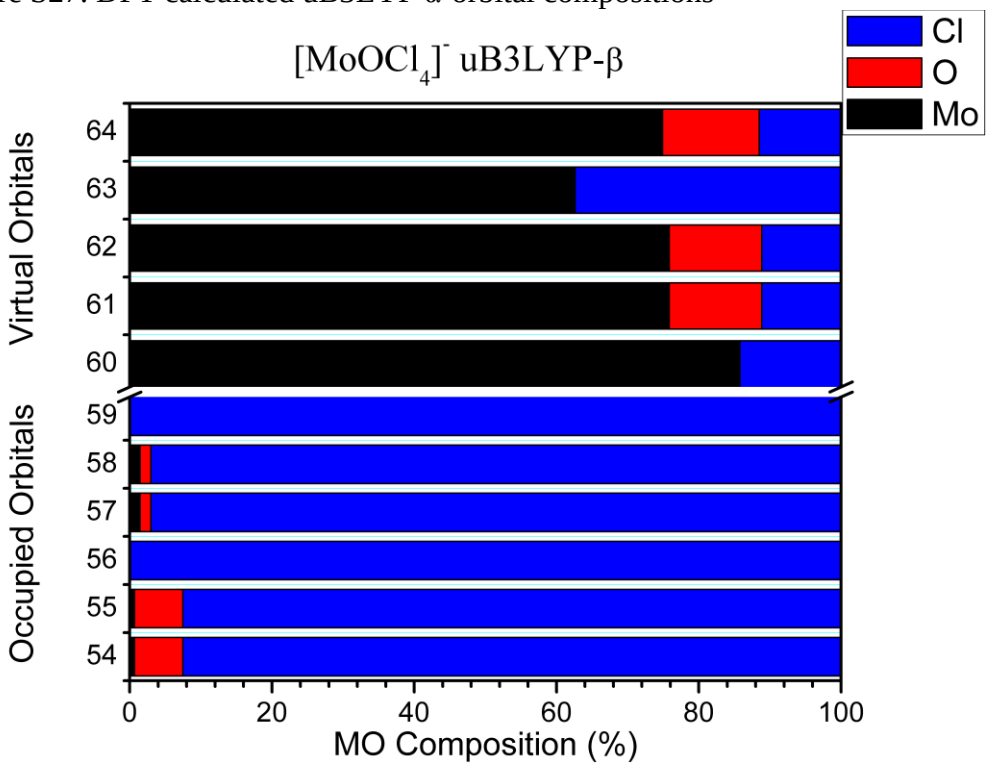

Figure S28. DFT calculated uB3LYP β-orbital compositions.

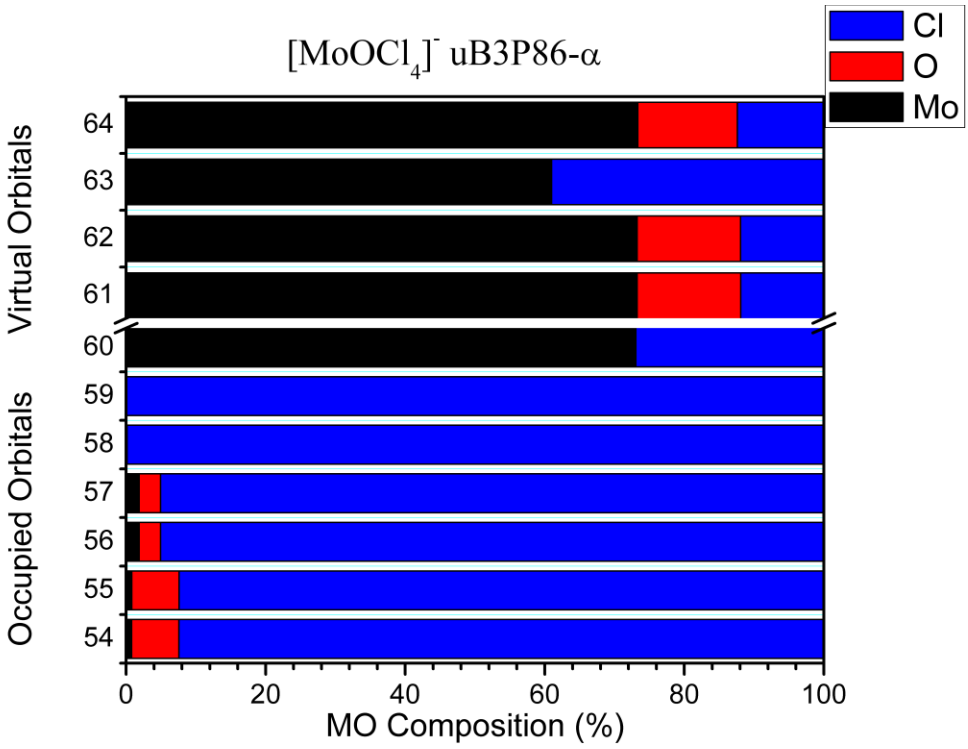

Figure S29. DFT calculated uB3P86 α-orbital compositions

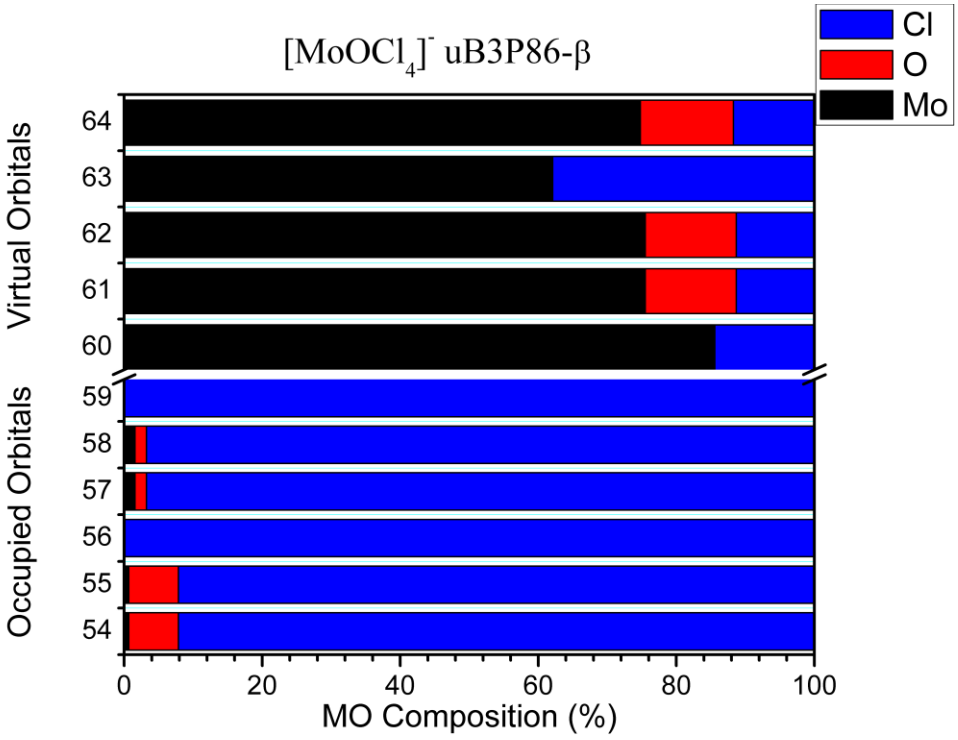

Figure S30. DFT calculated uB3P86 β-orbital compositions

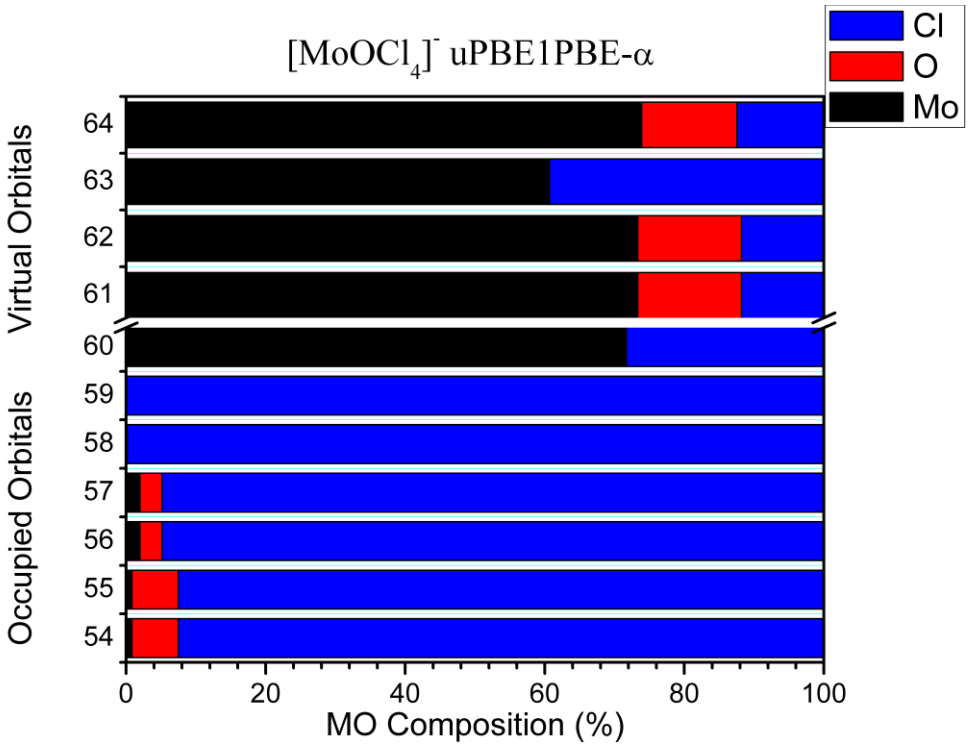

Figure S31. DFT calculated uPBE1PBE α-orbital compositions

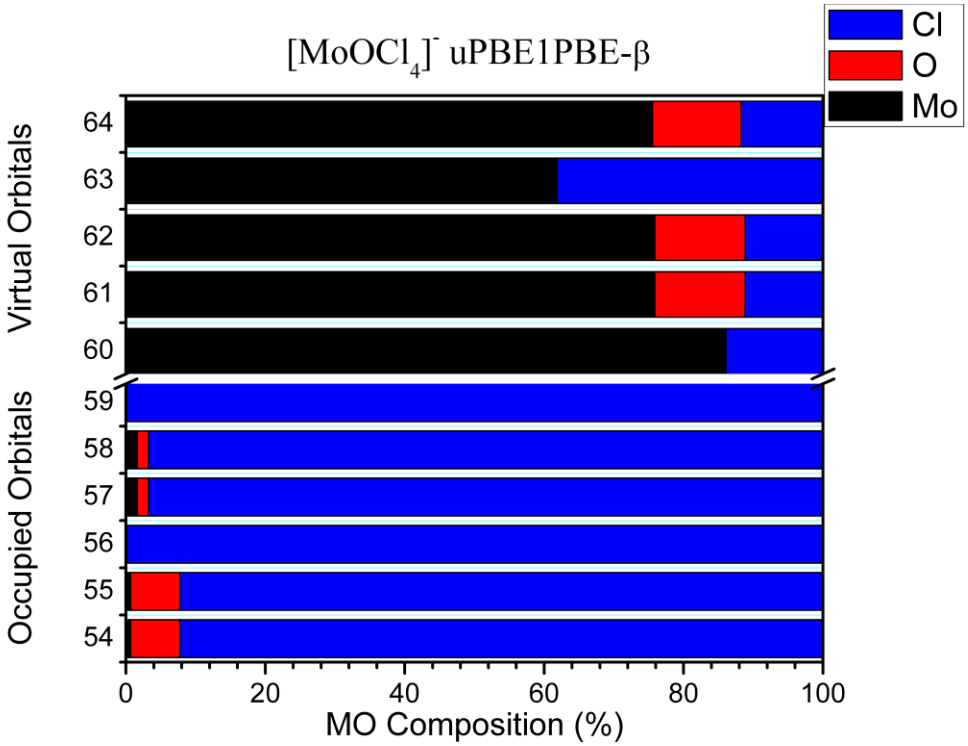

Figure S32. DFT calculated uPBE1PBE β-orbital compositions.

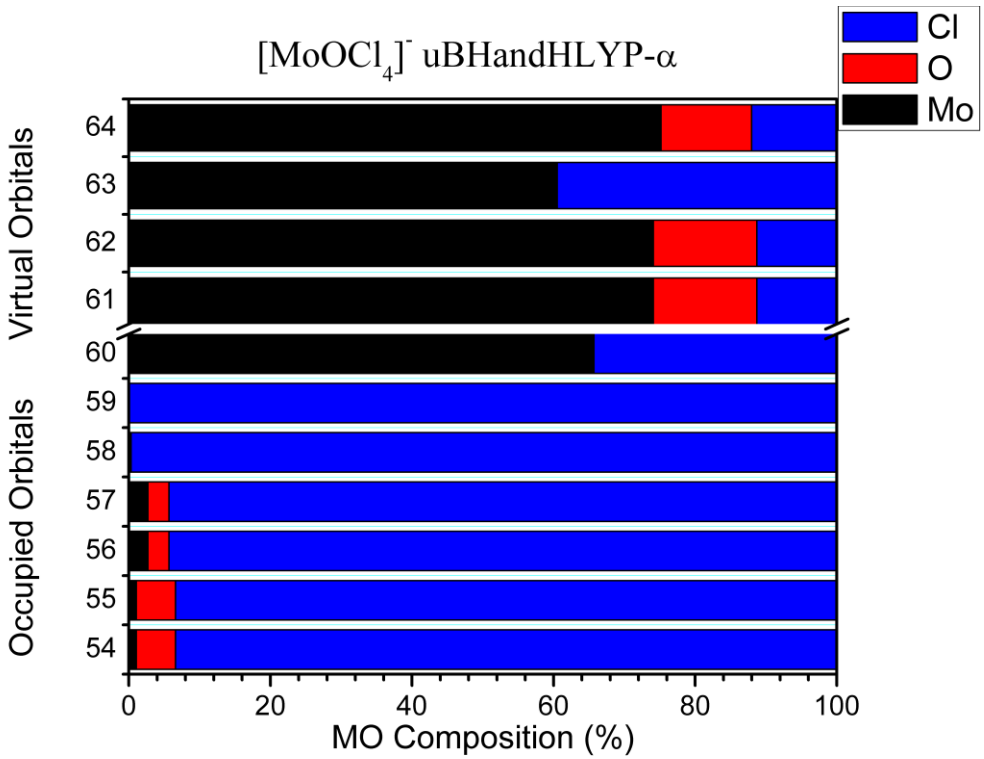

Figure S33. DFT calculated uBHandHLYP α-orbital compositions.

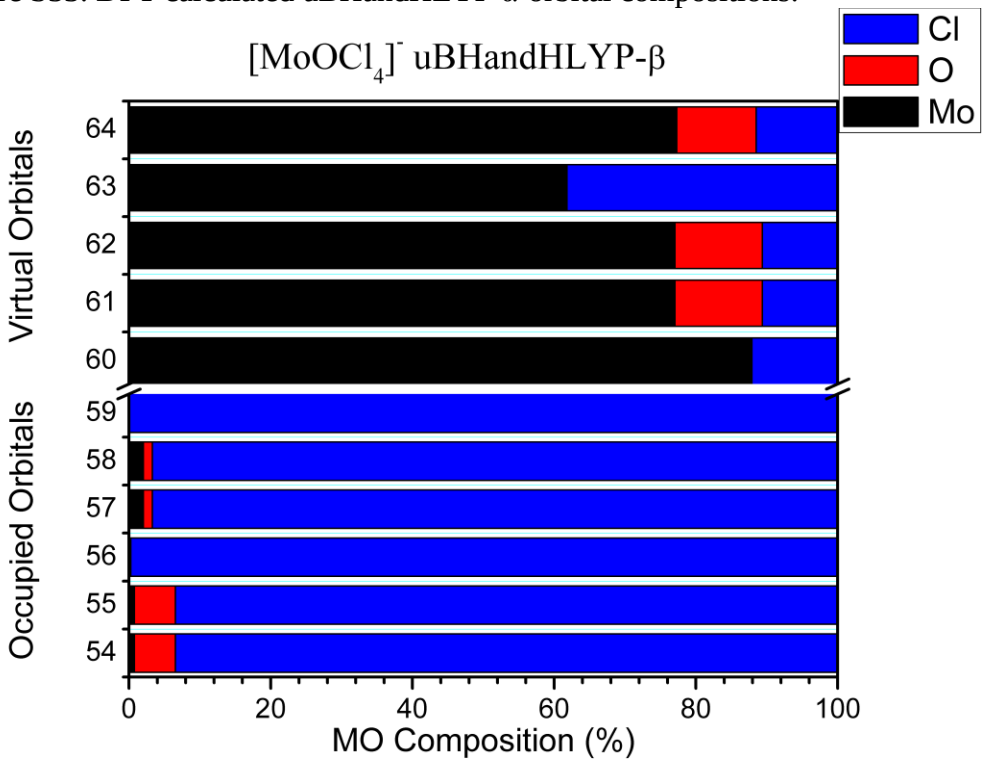

Figure S34. DFT calculated uBHandHLYP β-orbital compositions

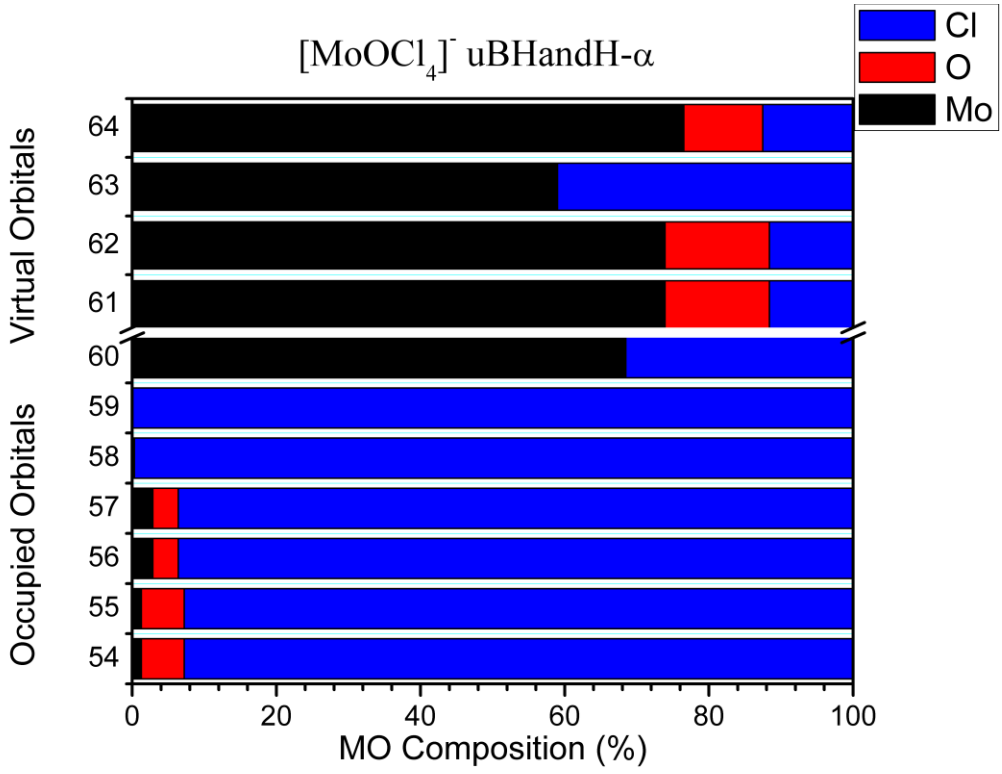

Figure S35. DFT calculated uBHandH α-orbital compositions

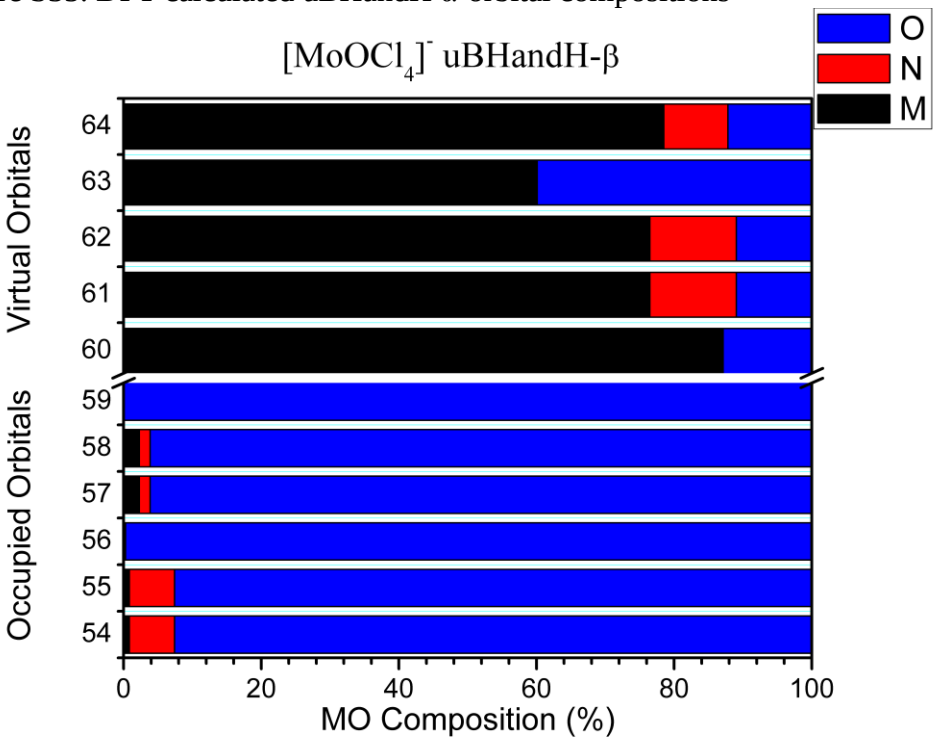

Figure S36. DFT calculated uBHandH β-orbital compositions

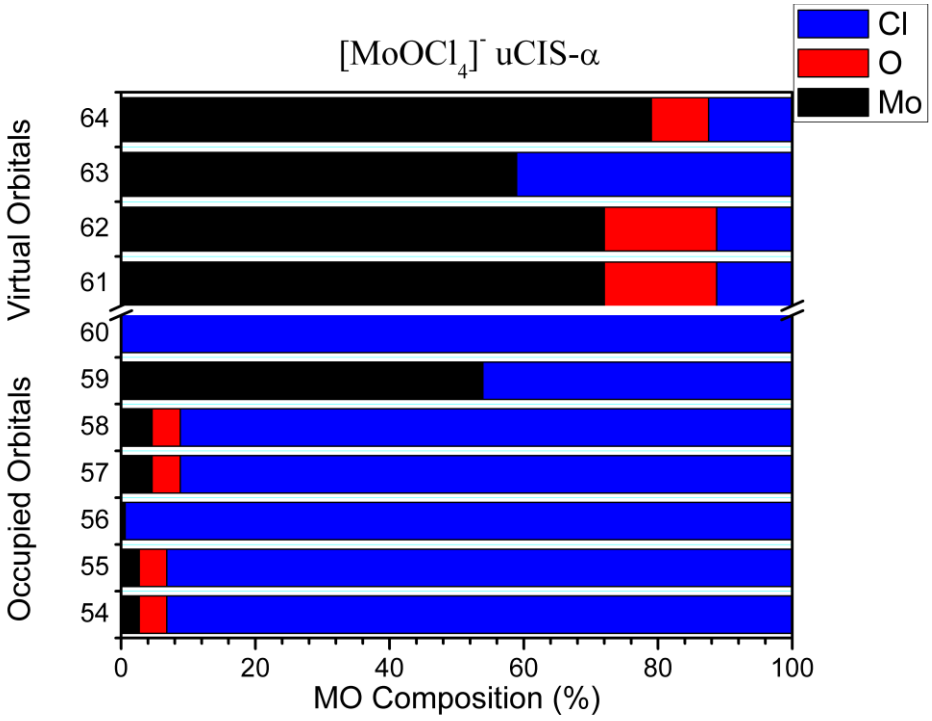

Figure S37. uMP2-CIS calculated α-orbital compositions

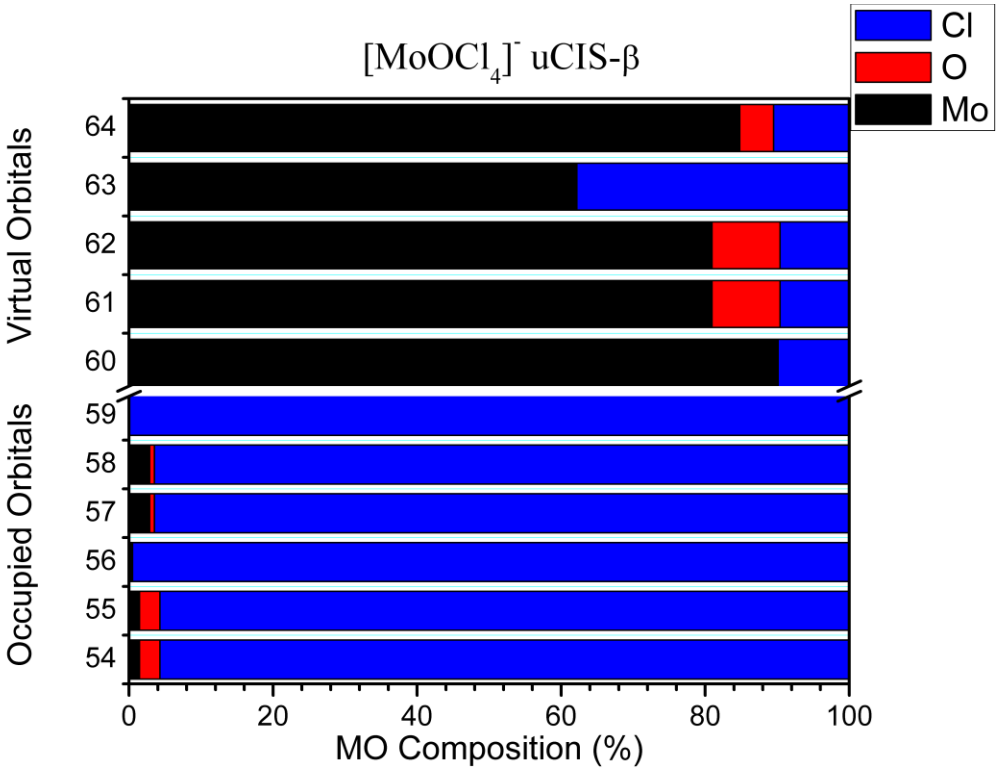

Figure S38. uMP2-CIS calculated β-orbital compositions

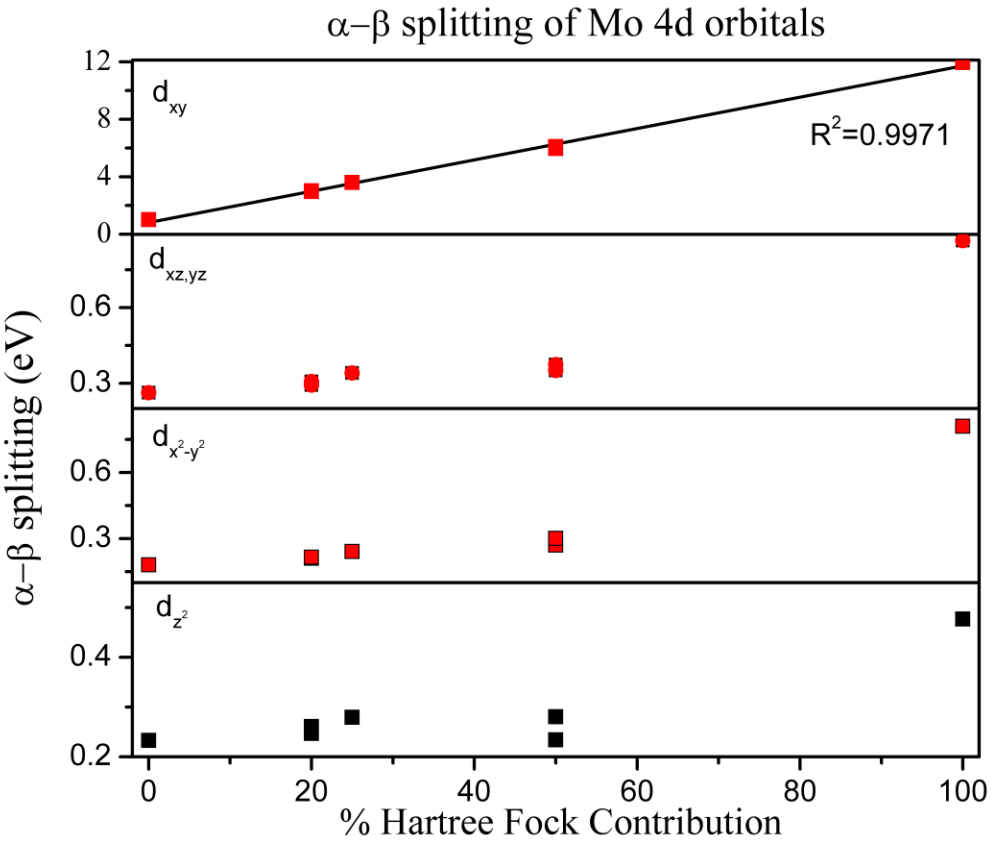

Figure S39. Spin-polarization energy as a function of Hartree-Fock contribution to the exchange functional

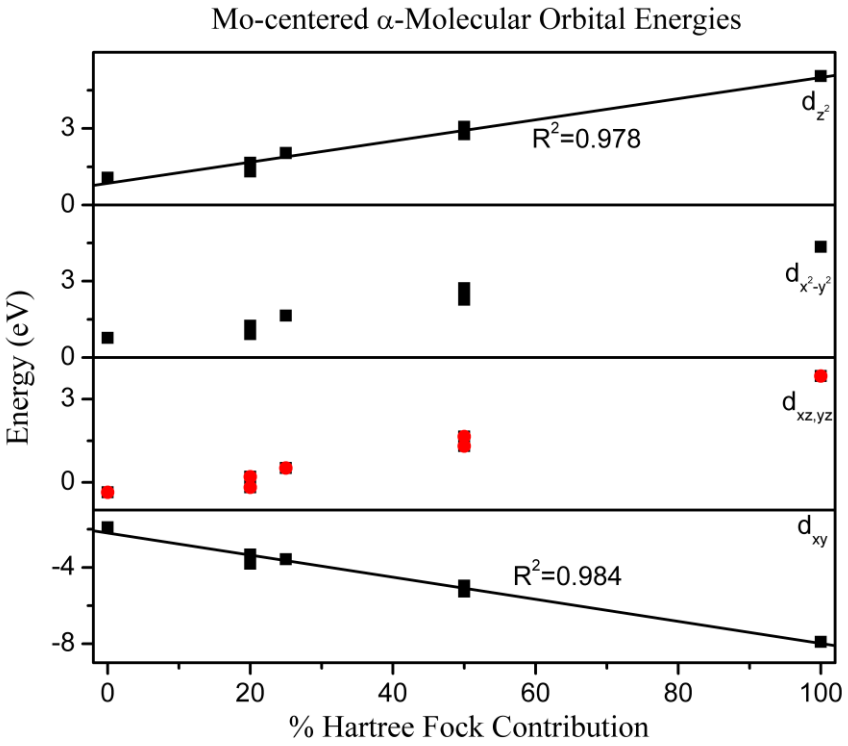

Figure S40. Energies of α-d centered orbitals as a function of Hartree-Fock contribution to the exchange functional

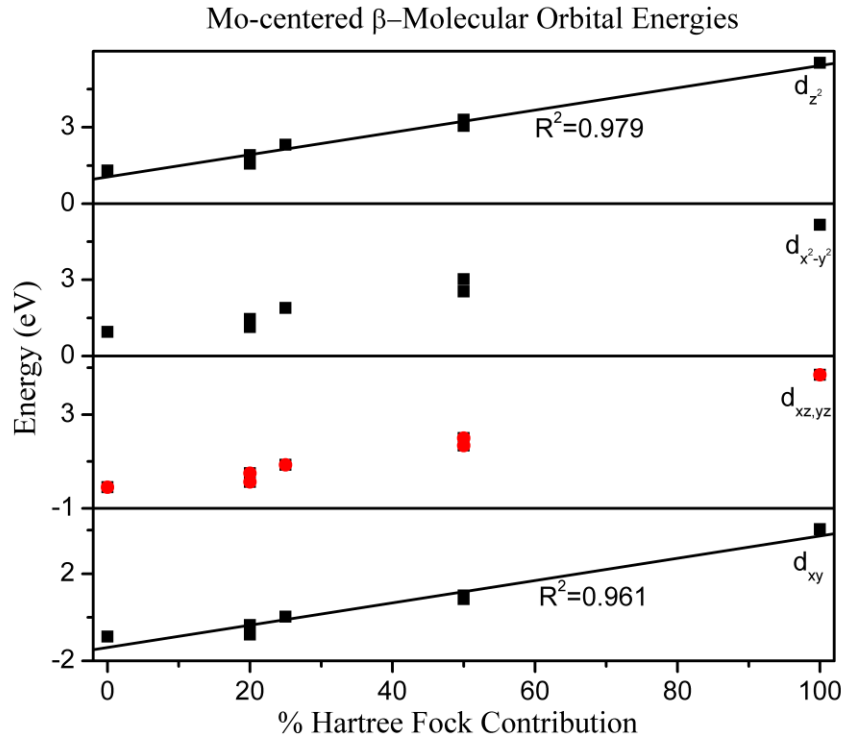

Figure S41. Energies of β-d centered orbitals as a function of Hartree-Fock contribution to the exchange functional

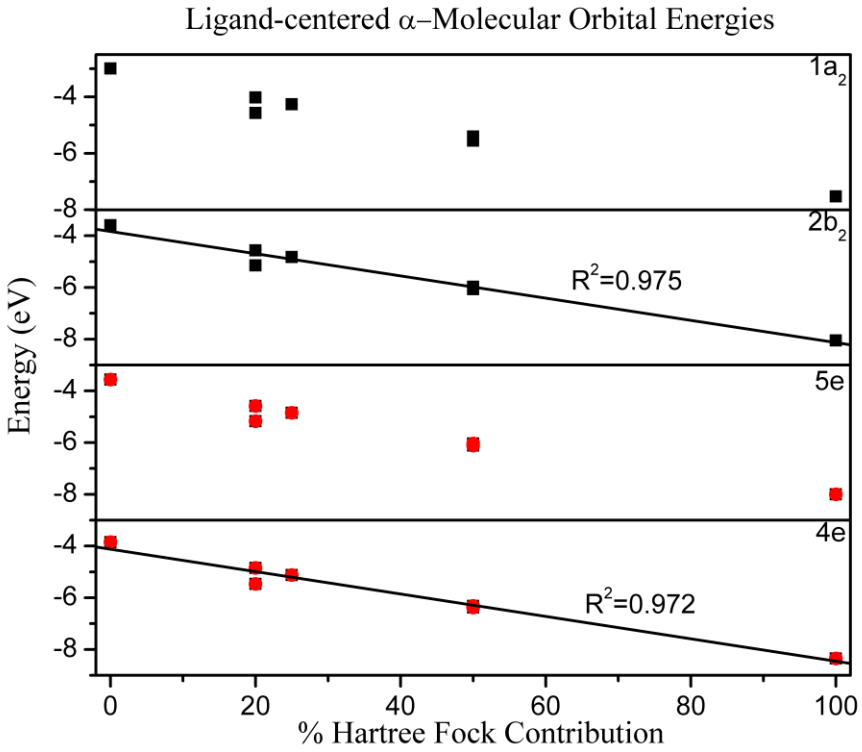

Figure S42. Energies of α-ligand centered orbitals as a function of Hartree-Fock contribution to the exchange functional

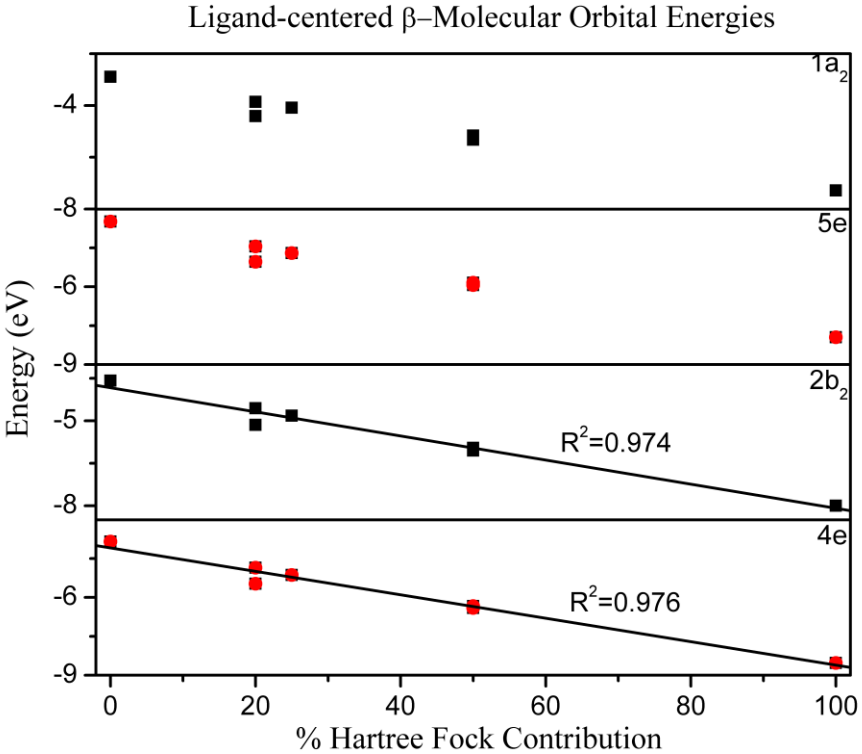

Figure S43. Energies of β-ligand orbitals as a function of Hartree-Fock contribution to the exchange functional

Table S44. TDDFT calculated oscillator strengths for the assigned bands

band	Elec. state	Orbital Trans.	method						
			BP86	B3LYP	B3P86	PBE1PBE	BHandH	BHandHLYP	CIS
1	$^2E_2$	$6e<-2b_2$	0.0000	0.0001	0.0000	0.0001	0.0001	0.0001	0.0003
2	$^2B_1$	$4b_1<-2b_2$	0.0000	0.0000	0.0000	0.0000	0.0000	0.0000	0.0000
3	$^2A_2$	$2b_2<-1a_2$	0.0000	0.0000	0.0000	0.0000	0.0000	0.0000	0.0000
4	$^2B_1$	$2b_2<-3b_1$	0.0000	0.0000	0.0000	0.0000	0.0000	0.0000	0.0000
5	$^2E_2$	$2b_2<-5e$	0.0172	0.0191	0.0198	0.0193	0.0254	0.0212	0.0050
6	$^2E_2$	$2b_2<-4e$	0.0016	0.0009	0.0010	0.0008	0.0004	0.0004	0.0007
7	$^2A_1$	$6a_1<-2b_2$	0.0000	0.0000	0.0000	0.0000	0.0000	0.0000	0.0000
8	$^2E_2$	$6e <- \alpha\text{-}1a_2$	0.0005	0.0014	0.0021	0.0027	0.0005	0.0005	0.0190
		$6e <- \beta\text{-}1a_2$	0.0007	0.0004	0.0003	0.0002	0.0001	0.0004	0.0150
9	$^2E_2$	$6e<- \alpha\text{-}3b_1$	0.0063	0.0061	0.0069	0.0076	0.0060	0.0058	0.0072
		$6e<- \beta\text{-}3b_1$	0.0192	0.0189	0.0210	0.0207	0.0170	0.0154	N.A.

S45. **Theory:** Development of MCD began in the 1930's, but its potential as a powerful tool for the investigation of electronic structure was not called to attention until the 1960's.[1] The development of MCD theory was greatly refined by Stephens and coworkers with the added dimension of the differential absorption, which is described as the difference between the absorption of left circularly polarized (lcp) and right circularly polarized (rcp) light which are induced by a magnetic field oriented parallel to direction of the light propagation.[1,2] The MCD signal obeys the Beer-Lambert law, and thus the differential absorption is described as

$$\Delta A = A_{\mathrm{lcp}} - A_{\mathrm{rcp}} = \Delta\varepsilon_M cl\mathbf{B} \qquad (1)$$

where ΔA is the difference between the absorption of left circularly polarized (A_{lcp}) and the absorption of right circularly polarized (A_{rcp}) light, which is proportional to the molar concentration c, path length l (in cm) and magnetic field **B** (in Tesla). The differential molar absorptivity per Tesla , $\Delta\varepsilon_M$, is the analog of the molar absorptivity ε.[1] The basic equation of MCD spectroscopy describing the excitation from ground state A to excited states J, utilizing the Born-Oppenheimer/Franck-Condon approximations (BO-FC), may be written as

$$\Delta A/E = \gamma\Sigma[(N_A\text{-}N_J)/N](|\langle\Psi_A|m_{\mathrm{lcp}}|\Psi_J\rangle|^2 - |\langle\Psi_A|m_{\mathrm{rcp}}|\Psi_J\rangle|^2)\rho_{AJ}(E) \qquad (2)$$

where $\Delta\varepsilon$ is the differential molar extinction coefficient, E is the energy of incident radiation, $m_{\pm}$ is the electric dipole matrix operator, and $\rho_{AJ}(E)$ is the line shape. Here, γ is a constant where $\gamma = 326.6cl(\alpha^2/n) \approx 326.6cl$, since under normal conditions the effective field correction α^2/n can be ignored.[1,3] Assuming states A and J are well separated, the excited-state population will be near zero, making $N_J = 0$, allowing the simplification

$$N_A - N_J \approx N_A(B,T) = \exp(-E_A/kT)/\Sigma_i\exp(-E_i/kT) \qquad (3)$$

Applying the Rigid-Shift approximation (RS), which assumes a band shift due to the Zeeman effect, equation 2 may be rearranged and rewritten as

$$\Delta A/E = \gamma\mu_B B[A_1(-\delta f(E)/\delta E) + (B_0 + C_0/(kT))f(E)] \qquad (4)$$

where μ_B is the Bohr magneton, $f(E)$ is the lineshape function[1], and A_1, B_0, C_0 are the parameter which define the MCD A, B, and C terms.[1,4] These MCD terms have been described by Stephens as

$$A_1 = (1/|A|)\Sigma_{AJ}[\langle\Psi_J|L_Z + g_eS_Z|\Psi_J\rangle - \langle\Psi_A|L_Z + g_eS_Z|\Psi_A\rangle]\mathrm{x}[|\langle\Psi_A|m_{-1}|\Psi_J\rangle|^2 - |\langle\Psi_A|m_{+1}|\Psi_J\rangle|^2], \qquad (5)$$

$$B_0 = (2/|A|)\mathrm{R_e}\Sigma_A\Sigma_{k\neq J}\{\langle\Psi_J|L_Z + g_eS_Z|\Psi_k\rangle/(E_k - E_J)\}[\langle\Psi_A|m_{-1}|\Psi_J\rangle \mathrm{x} \langle\Psi_k|m_{+1}|\Psi_A\rangle \langle\Psi_A|m_{+1}|\Psi_J\rangle \mathrm{x} \langle\Psi_k|m_{+1}|\Psi_A\rangle] + (2/|A|)\mathrm{R_e}\Sigma_A\Sigma_{k\neq J}\{\langle\Psi_k|L_Z + g_eS_Z|\Psi_A\rangle/(E_k - E_J)\} [\langle\Psi_A|m_{-1}|\Psi_J\rangle \mathrm{x} \langle\Psi_J|m_{+1}|\Psi_k\rangle - \langle\Psi_A|m_{+1}|\Psi_J\rangle \mathrm{x} \langle\Psi_J|m_{+1}|\Psi_k\rangle] \qquad (6)$$

$$C_0 = -(1/|A|)\Sigma_{AJ}[\langle\Psi_A|L_Z + g_eS_Z|\Psi_A\rangle]\mathrm{x}[|\langle\Psi_A|m_{-1}|\Psi_J\rangle|^2 - |\langle\Psi_A|m_{+1}|\Psi_J\rangle|^2], \qquad (7)$$

where $|A|$ is the degeneracy of ground state A, and $m_{+1} = -(1/\sqrt{2})(m_x - im_y) = (1/\sqrt{2})m_{rcp}$ and $m_{-1} = (1/\sqrt{2})(m_x - im_y) = (1/\sqrt{2})m_{lcp}$.[4,5]

It can be noted in equation 4 that the C-term is inversely proportional to temperature, T, and so will dominate at the MCD signal at low temperatures. The importance of spin-orbit coupling (SOC) in determining realistic signs and relative signal intensities in paramagnetic systems has been noted previously.[5] A method of calculating C-terms in the presence of SOC was presented by Neese and Solomon which related M projection components of ground and excited electronic states through vector coupling of the nonrelativistic Born-Oppenheimer (BO) wavefunctions.[5] More recently, a method of calculating MCD terms which holds validity into the non-linear regime has been formulated through the inclusion of SOC and spin-spin coupled (SSC) N-electronic states into a multi-reference type BO Hamiltonian through quasi-degenerate perturbation theory (QDPT).[6] This method has been implemented into the program ORCA 2.9.0, and is detailed elsewhere.[6,7]

(1) Mason, R.W. "A Practical Guide to Magnetic Circular Dichroism Spectroscopy". John Wiley & Sons; New York, Chichester, Brisbane, Toronto, Singapore, 2007.

(2) (a) Stephens, P.J. *J. Chem. Phys.* **1970**, *52* (7), 3489. (b) Stephens, P. J. *Adv. Chem. Phys.* **1976**, *35*, 197 (c) Stephens P.J. *Annu. Rev. Phys. Chem.* **1974**, *25*, 201. (d) Buckingham, A. D.; Stephens, P.J. *Annu. Rev. Phys. Chem.* **1966**, *17*, 399.

(3) Hernandez-Marin, Elizabeth; Seth, Michael; Ziegler, Tom. "Density Function Theory Study of the Magnetic Circular Dichroism Spectra of Molybdenyl Complexes". *Inorg. Chem.* **2010**, *49*, 6066-6076

(4) Piepho, S.D.; Schatz, P.N. "Group theory in Spectroscopy with Applications to Magnetic Circular Dichroism". John Wiley & Sons; New York. 1983

(5) Neese, F.; Solomon, E.I. *Inorg. Chem.* **1999**, *38*, 1847

(6) Ganyushin, D.; Neese, F. *J. Chem. Phys.* **2008**, *128*, 114117

(7) Neese, Frank; Becker, Ute; Ganyushin, Dmitry; Hansen, Andreas; Liakos, Dimitrios; Izsak, Robert; Kollmar, Christian; Kossmann, Simone; Petrenko, Taras; Reimann, Christoph; Roemelt, Michael; Riplinger; Cristoph; Sandhoefer, Barbara; Schapiro, Igor; Sivalingam, Kantharuban; Wezisla, Boris; Wennmohs, Frank. *Program Version 2.9.0*; ORCA, Max Planck Institute for Bioinorganic Chemistry. D-45470 Muelheim/Ruhr, Germany.

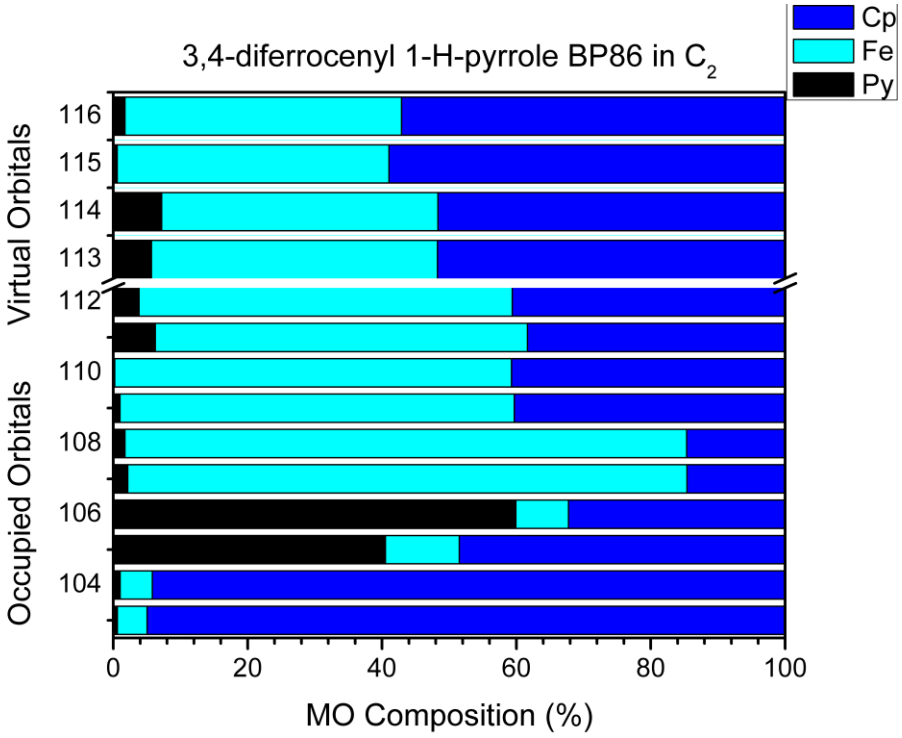

Figure S46. Molecular orbital compositions of BP86-(4) for the HOMO-10 through LUMO+3.

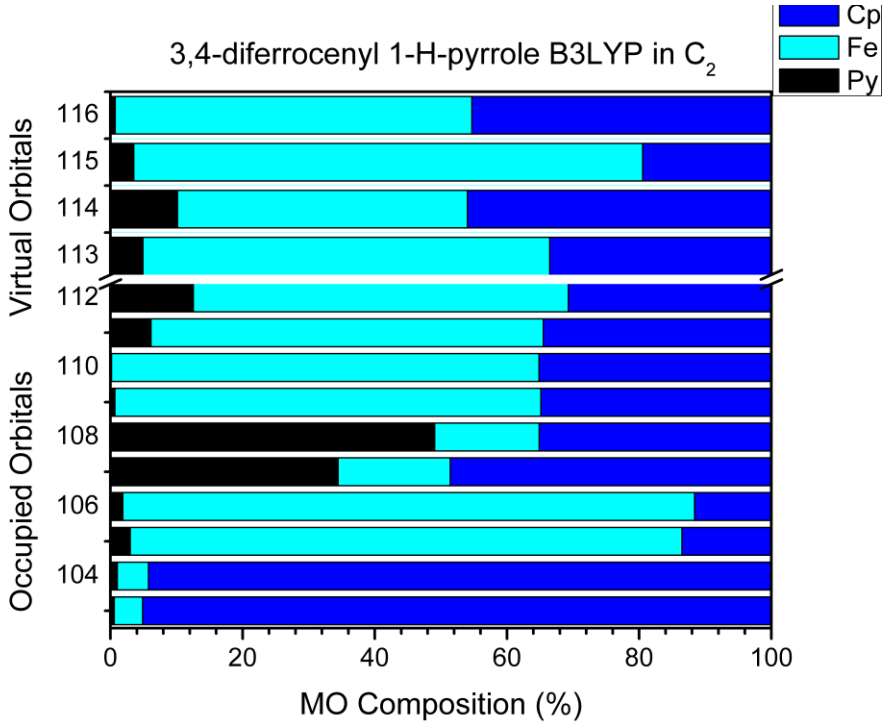

Figure S47. Molecular orbital compositions of B3LYP-(4) for the HOMO-10 through LUMO+3

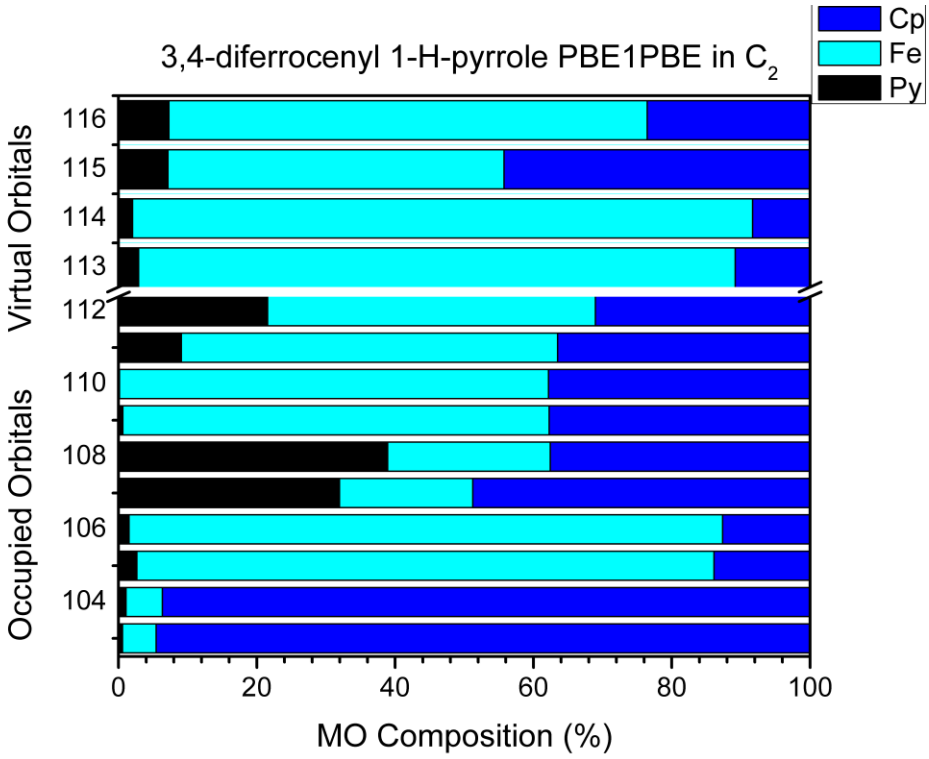

Figure S48. Molecular orbital compositions of PBE1PBE-(4) for the HOMO-10 through LUMO+3

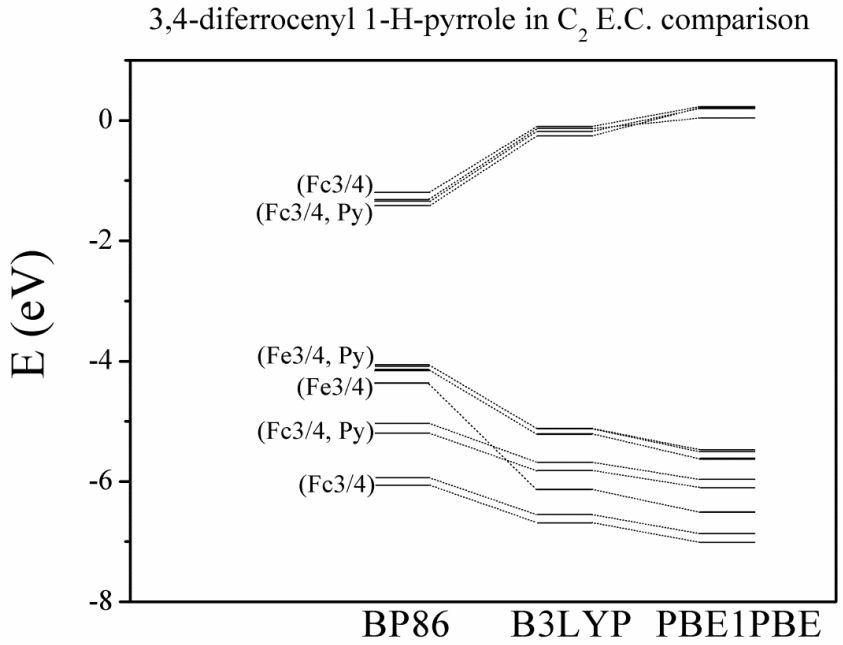

Figure S49. Comparative energetic diagram for (4) of the three exchange corrleation functionals under consideration. HOMO-10 through LUMO+3

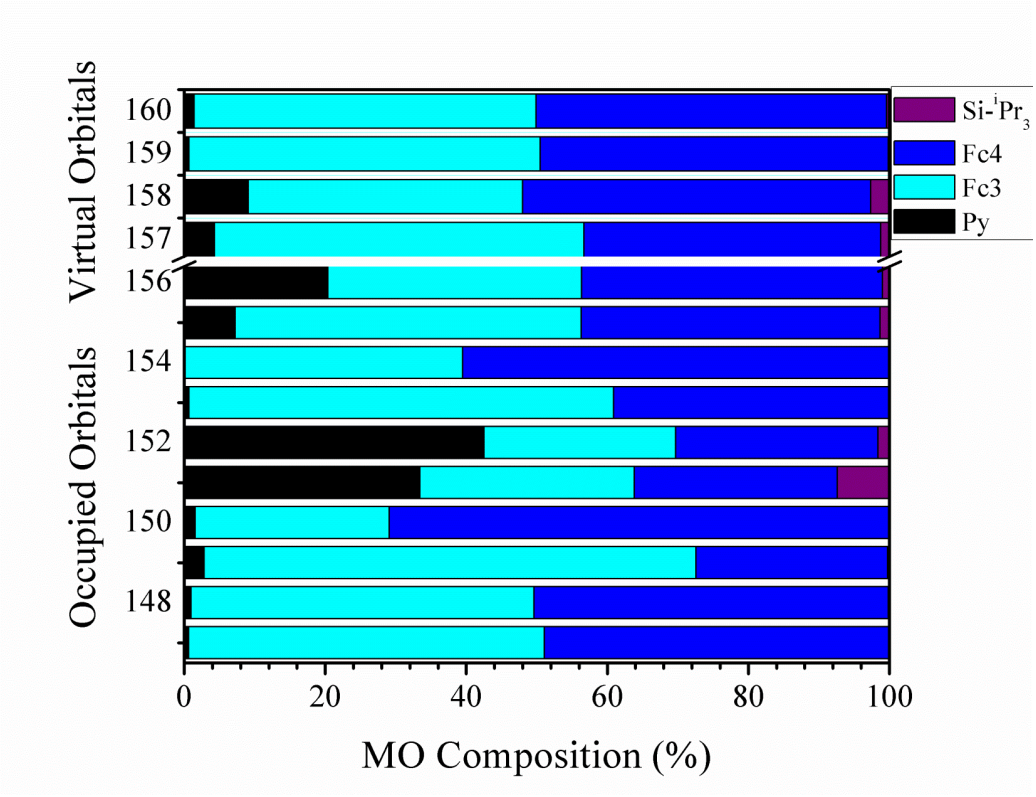

Figure S50. Molecular orbital compositions of B3LYP-(3) crystal structure.

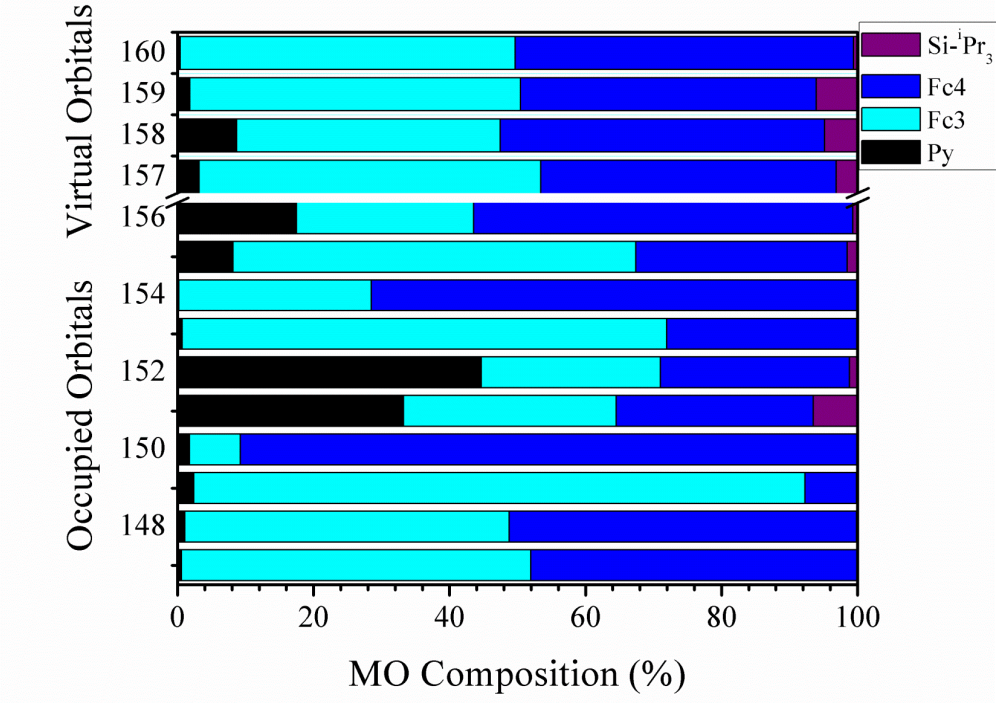

Figure S51. Molecular orbital compositions of B3LYP-(3) crystal structure.

Table S52. BP86- TDDFT predicted energies for the (4) electronic spectrum.

Exp. Band	State	Energy (cm^{-1})	Transition	Expansion coefficients	f (Debye)	Energy (cm^{-1})	
						Exp.	Calc.
1	1	21,700	111 → 113	-0.2673	0.0077	22,320	22,810
			112 →114	0.62512			
	8	22,680	109 → 114	0.42925	0.0009		
			110 →115	0.42136			
	10	23,120	109 → 114	0.36167	0.0008		
			111 → 116	0.53456			
	12	23,300	109 → 116	0.45326	0.0064		
			110 → 115	-0.44052			
	14	23,940	107 → 113	0.62252	0.0010		
			109 → 116	0.29243			
2	19	25330	108 →116	0.62796	0.0007	36,230	28,690
	23	28,840	107 → 114	-0.24485	0.0014		
			109 → 115	0.30044			
			110 → 116	0.32334			
			111 → 113	0.23581			
			112 → 114	0.23034			
	24	28,870	108 → 114	-0.2423	0.0099		
			109 → 116	0.29209			
			110 → 115	0.30207			
			112 → 113	0.23572			
	25	29,740	106 → 113	0.64162	0.0011		
	26	30,200	106 → 114	0.62701	0.0011		

Table S53. PBE1PBE- TDDFT predicted energies for the (4) electronic spectrum.

Exp. Band	State	Energy (cm^{-1})	Transition	Expansion coefficients	f (Debye)	Energy (cm^{-1}) Exp.	Energy (cm^{-1}) Calc.
1	1	18790	109 → 118	-0.2963	0.0008	22,320	19,680
			110 → 117	-0.30941			
			111 → 115	0.32748			
			112 →116	0.25346			
	5	21090	105 → 115	0.30372	0.0006		
			106 → 116	0.25541			
			109 → 118	0.26374			
			110 → 117	0.24555			
2	9	28030	105 → 115	-0.23897	0.0004	36,230	40,870
			105 → 117	-0.21866			
			106 →116	-0.2495			
			109 → 118	0.24753			
			110 → 117	0.26228			
			111 → 115				
	14	38830	111 → 114	0.57602	0.0020		
			112 → 113	0.25811			
			112 → 116	0.23019			
	17	40250	111 → 114	0.28299	0.0026		
			112 → 115	0.41985			
	18	40400	107 → 117	0.43169	0.0217		
			108 → 118	-0.34279			
	19	40540	107 → 115	0.33124	0.1004		
			108 → 116	-0.32105			
			112 → 116	-0.28138			
	21	41020	107 → 116	0.2556	0.0058		
			108 → 115	-0.29991			

22	41040	111 → 113	-0.20919	0.0836
		111 → 115	0.39388	
		112 → 114	0.39723	
		112 → 116	-0.18259	
24	41700	111 → 113	-0.27182	0.0039
		111 → 115	-0.22402	
		112 → 114	0.32902	
		112 → 116	0.46039	
25	42020	109 → 114	0.30678	0.0024
		110 → 115	0.30378	
		110 → 120	-0.2846	
27	42480	111 → 120	0.24139	0.0151
		112 → 118	0.39216	
28	42490	109 → 115	-0.22503	0.0029
		109 → 120	-0.20012	
		110 → 114	-0.22821	
		110 → 116	0.28441	
		110 → 119	0.20361	
		111 → 118	-0.26852	
		112 → 117	0.25589	
29	42670	109 → 114	0.21196	0.0028
		109 → 116	-0.25988	
		109 →119	-0.27177	
		112 → 118	-0.2336	

Table S54. B3LYP-TDDFT predicted energies for the B3LYP-optimized (3) electronic spectrum.

Exp. Band	State	Energy (cm^{-1})	Transition	Expansion coefficients	f (Debye)	Energy (cm^{-1}) Exp.	Energy (cm^{-1}) Calc.
1	1	16930	153 → 160	0.29456	0.0010	22,320	18340
			154 → 159	-0.30604			
			155 → 157	0.33888			
			156 →158	-0.32757			
	5	19930	149 → 157	-0.28542	0.0010		
			150 → 158	0.3274			
			153 → 160	0.26096			
			154 → 159	-0.23434			
			156 → 158	0.20506			
2	13	35230	155 → 158	0.39447	0.0020	36,230	36740
			156 → 157	0.51469			
	14	35530	155 →157	0.38889	0.0020		
			156 → 158	0.53452			
	17	36330	155 → 161	0.50799	0.0319		
			156 → 162	0.30856			
	19	36670	151 → 157	0.36088	0.1199		
			152 → 158	0.319			
			155 → 157	0.20669			
			155 → 161	0.29663			
	20	36680	153 → 157	0.36497	0.0052		
			154 → 157	-0.27713			
			154 → 158	0.37754			
	22	36930	151 → 158	0.28594	0.0211		
			152 → 157	0.38101			
			152 → 159	0.23805			
			155 → 158	0.23349			

23	36960	155 → 159	0.43701	0.0396
		156 → 160	0.38956	
24	37130	153 → 162	0.27234	0.0032
		154 → 161	0.52559	
26	37170	155 → 160	0.47916	0.0055
		156 → 159	0.29357	
30	38790	155 → 162	0.59117	0.0042
		156 → 161	-0.28834	

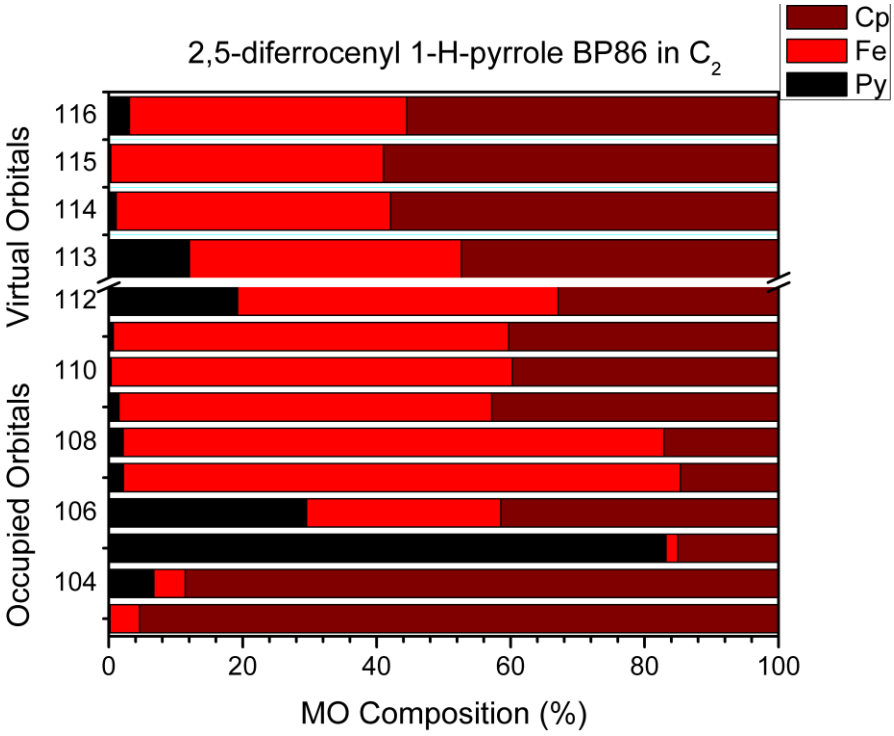

Figure S55. Molecular orbital compositions of BP86-(5) for the HOMO-10 through LUMO+3.

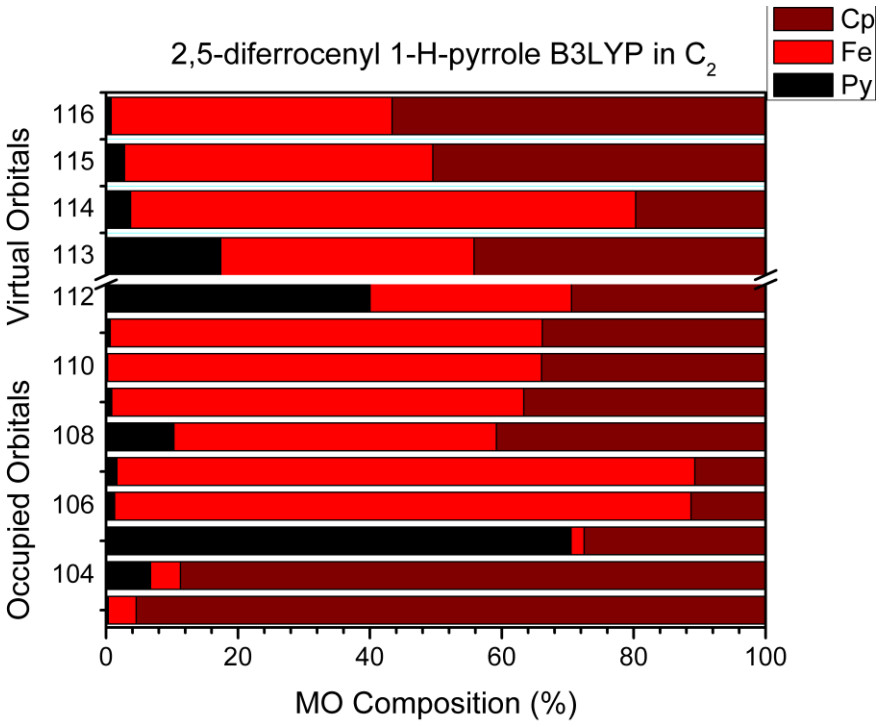

Figure S56. Molecular orbital compositions of B3LYP-(5) for the HOMO-10 through LUMO+3

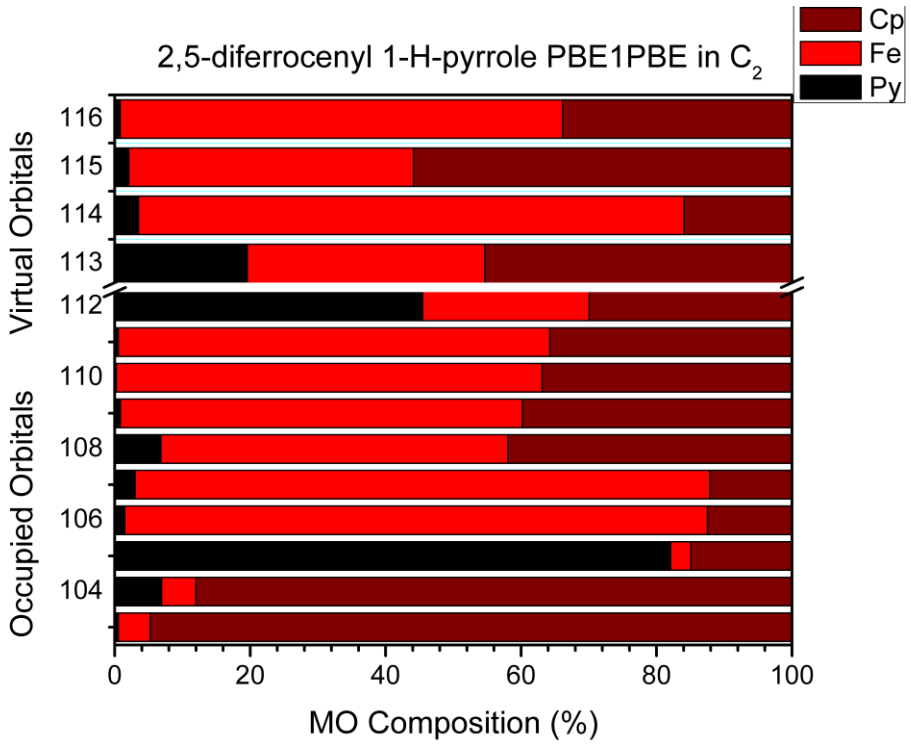

Figure S57. Molecular orbital compositions of PBE1PBE-(5) for the HOMO-10 through LUMO+3

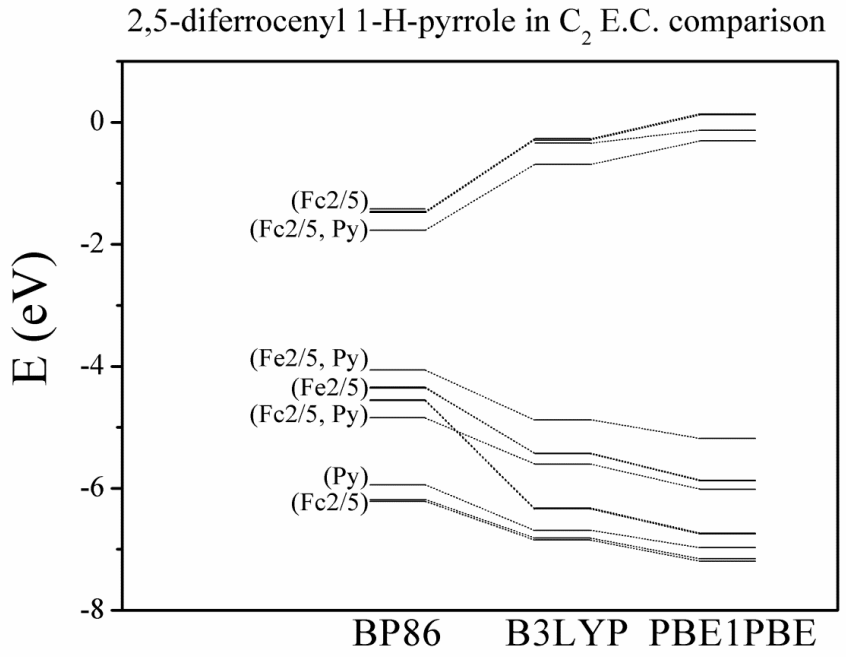

Figure S58. Comparative energetic diagram for (5) of the three exchange corrleation functionals under consideration. HOMO-10 through LUMO+3

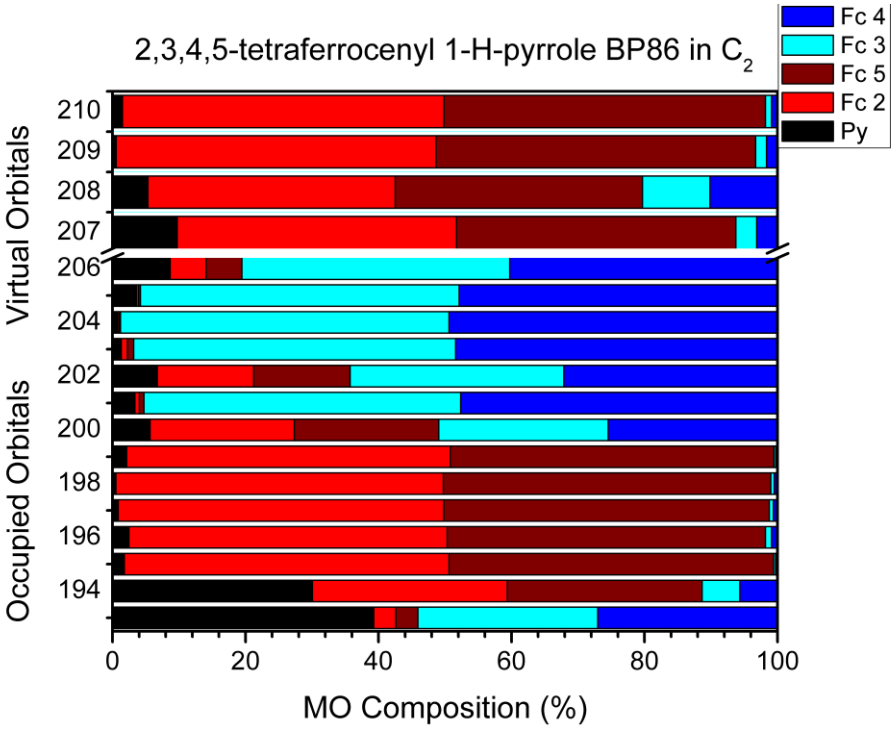

Figure S59. Molecular orbital compositions of BP86-(6) for the HOMO-14 through LUMO+3.

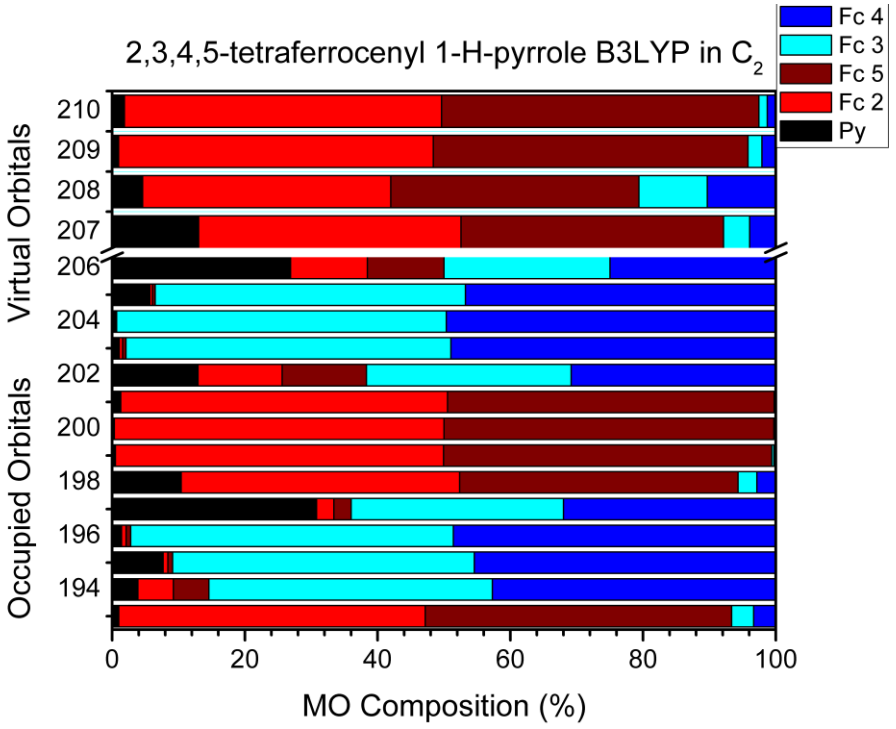

Figure S60. Molecular orbital compositions of B3LYP-(6) for the HOMO-14 through LUMO+3.

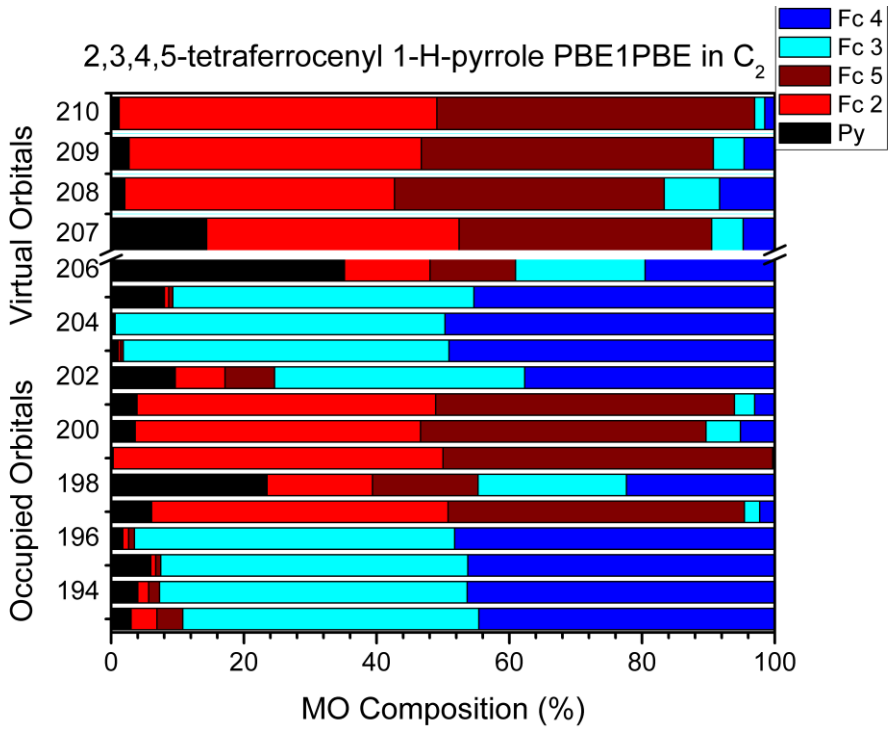

Figure S61. Molecular orbital compositions of PBE1PBE-(6) for the HOMO-14 through LUMO+3.

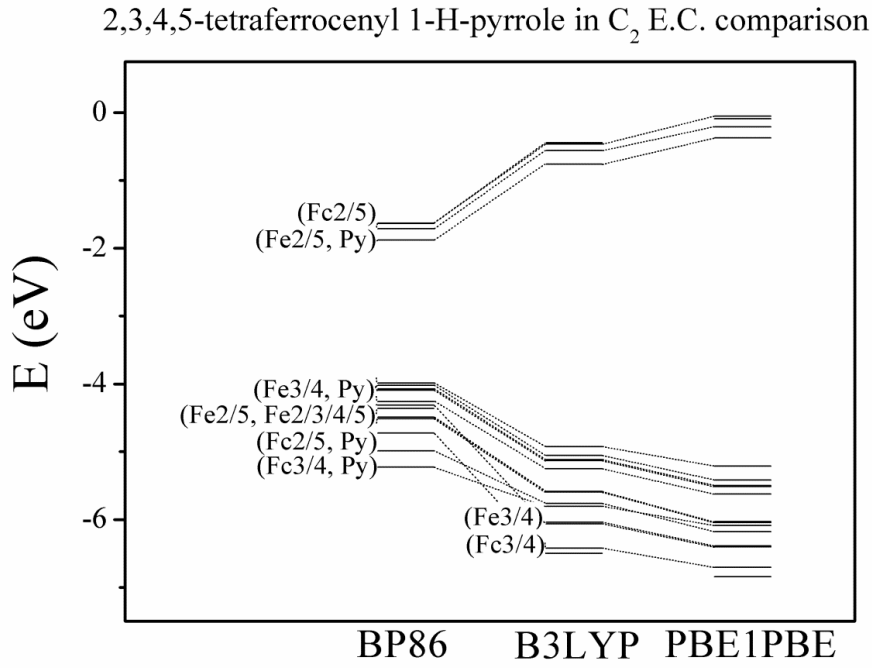

Figure S62. Comparative energetic diagram for (6) of the three exchange corrleation functionals under consideration. HOMO-14 through LUMO+3.

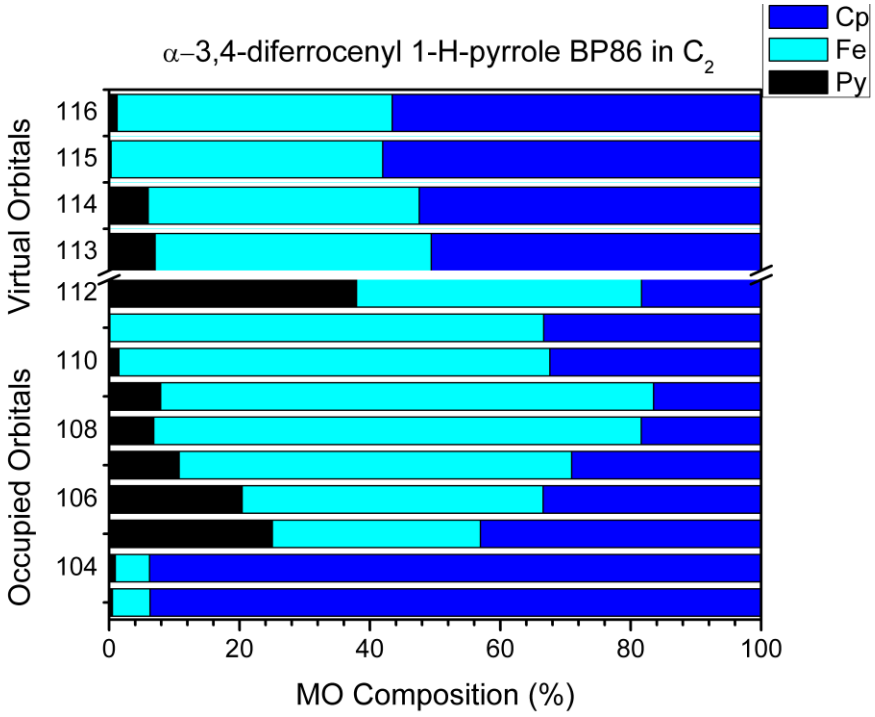

Figure S63. Molecular orbital compositions of BP86-(4^+) for the α-HOMO-10 through α-LUMO+3.

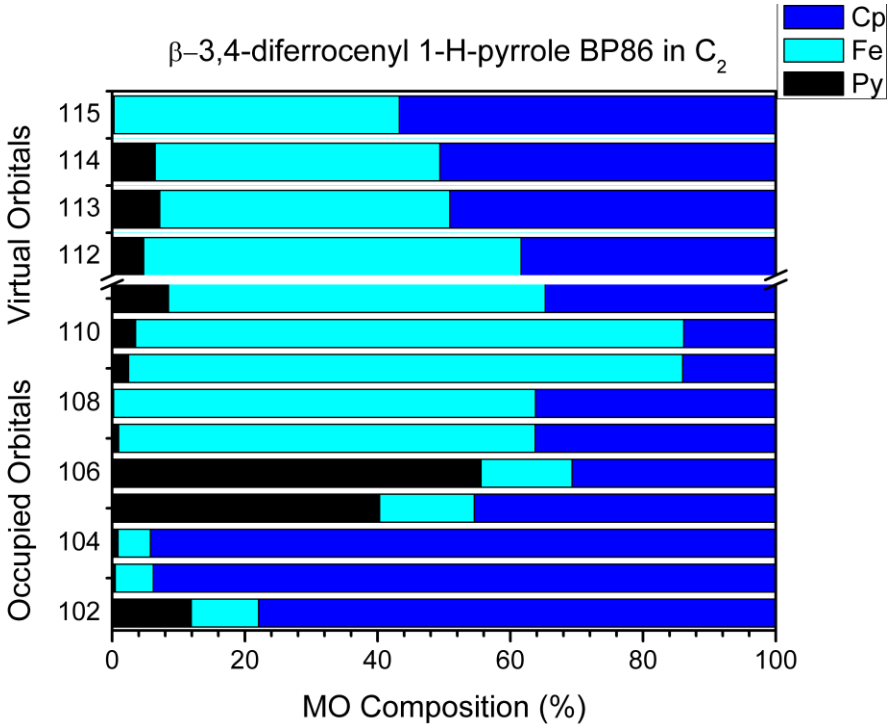

Figure S64. Molecular orbital compositions of BP86-(4^+) for the β-HOMO-10 through β-LUMO+3

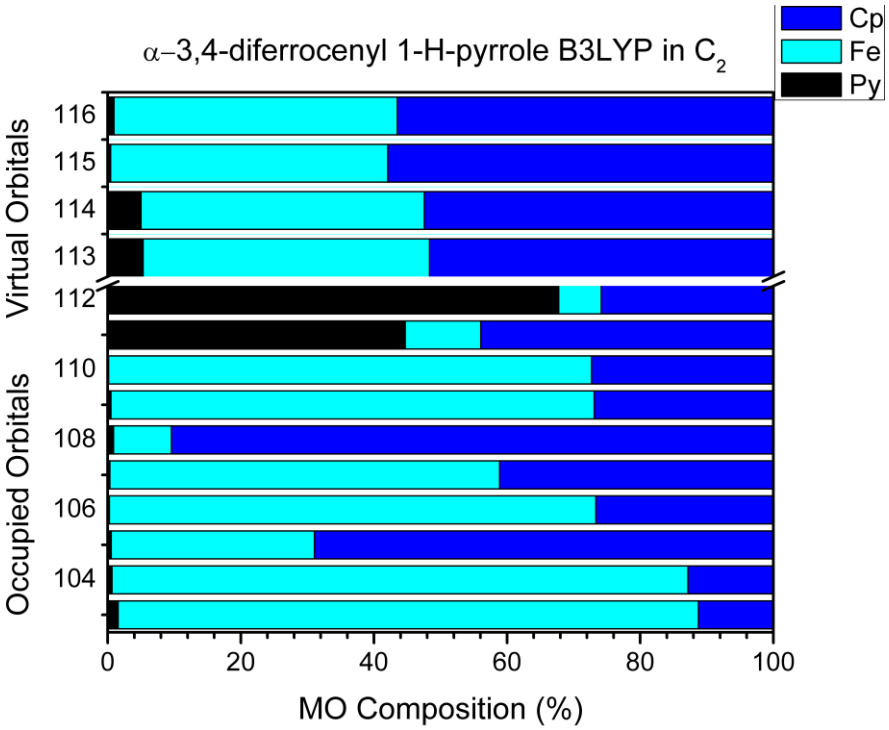

Figure S65. Molecular orbital compositions of B3LYP-(4^+) for the α-HOMO-10 through α-LUMO+3.

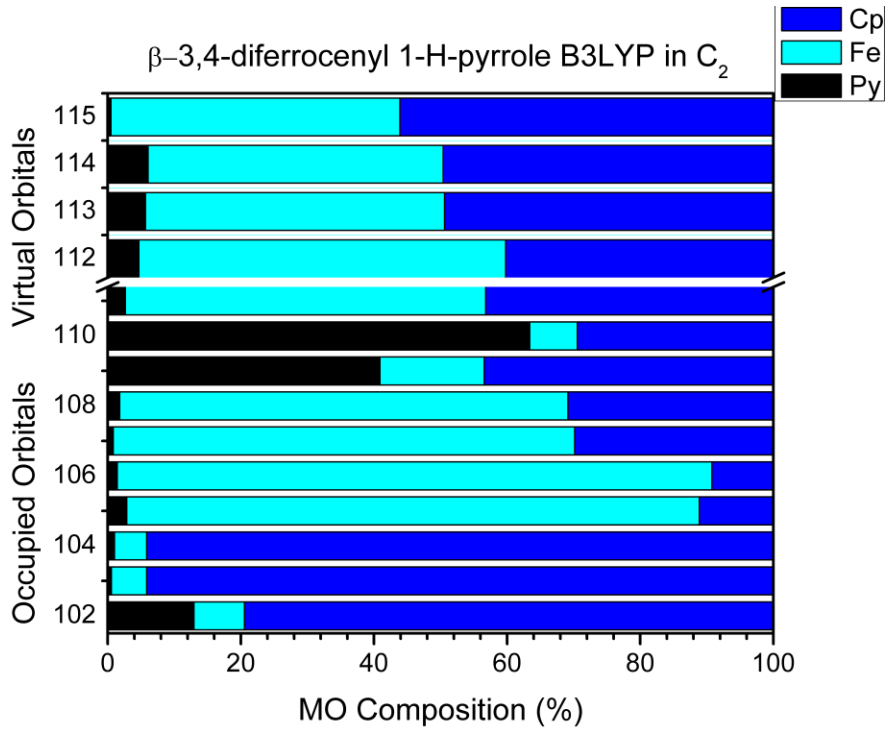

Figure S66. Molecular orbital compositions of B3LYP-(4^+) for the β-HOMO-10 through β-LUMO+3.

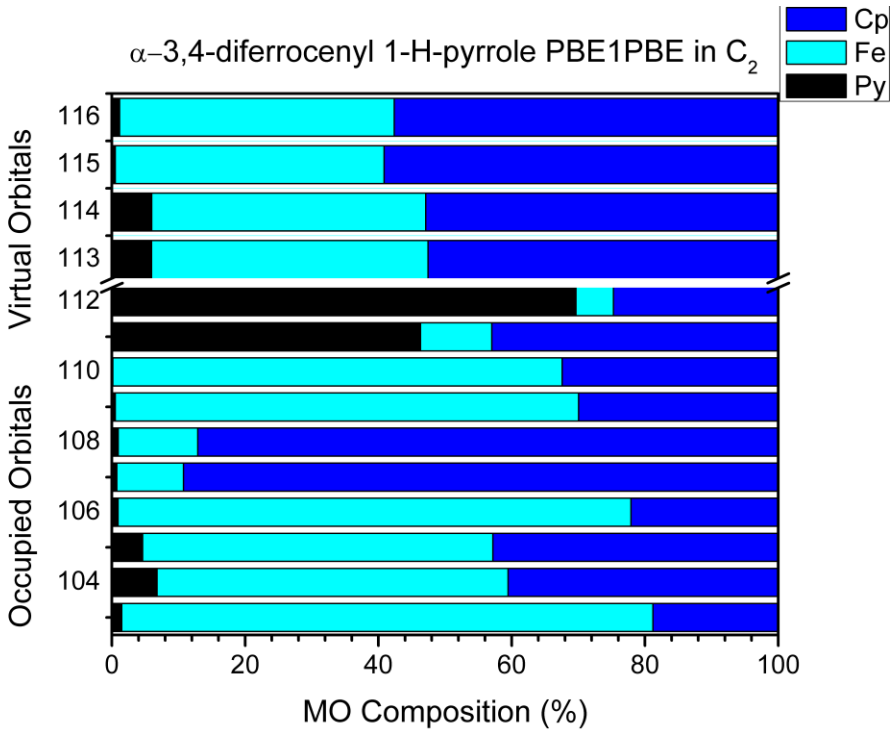

Figure S67. Molecular orbital compositions of PBE1PBE-(4^{+}) for the α-HOMO-10 through α-LUMO+3

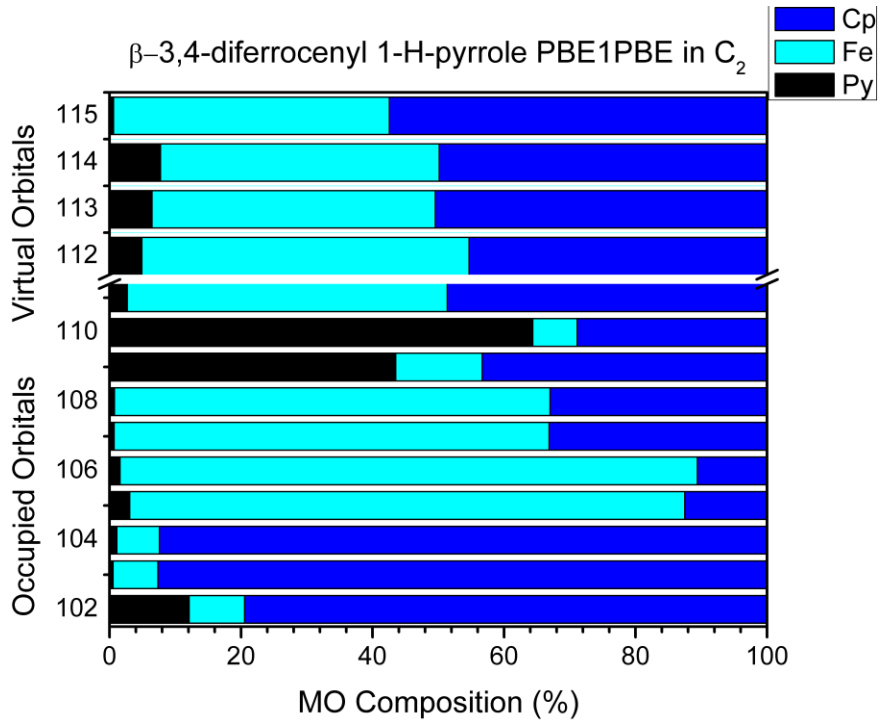

Figure S68. Molecular orbital compositions of PBE1PBE-(4^{+}) for the β-HOMO-10 through β-LUMO+3

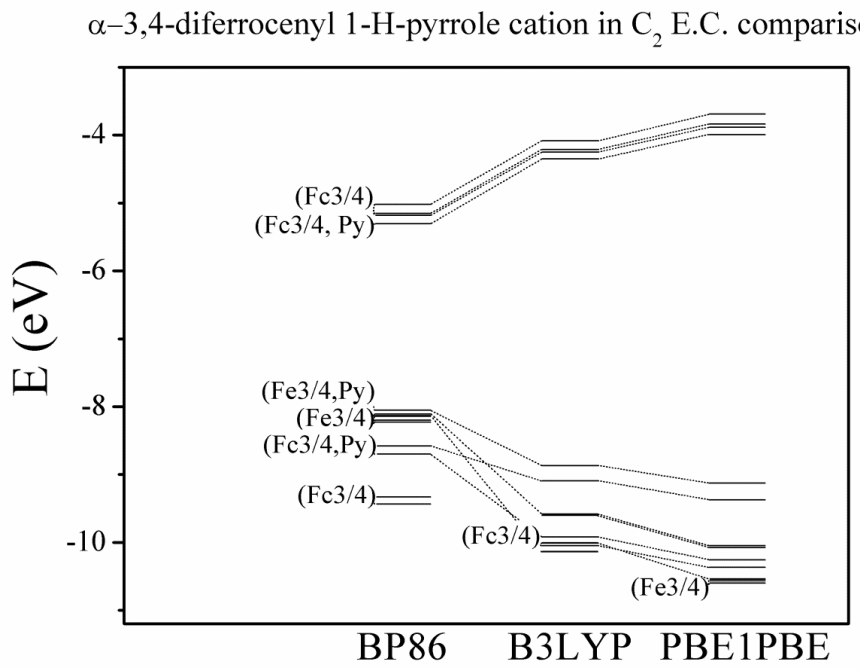

Figure S69. Comparative energetic diagram for (1^{+}) of the three exchange corrleation functionals under consideration. α-HOMO-10 through α-LUMO+3

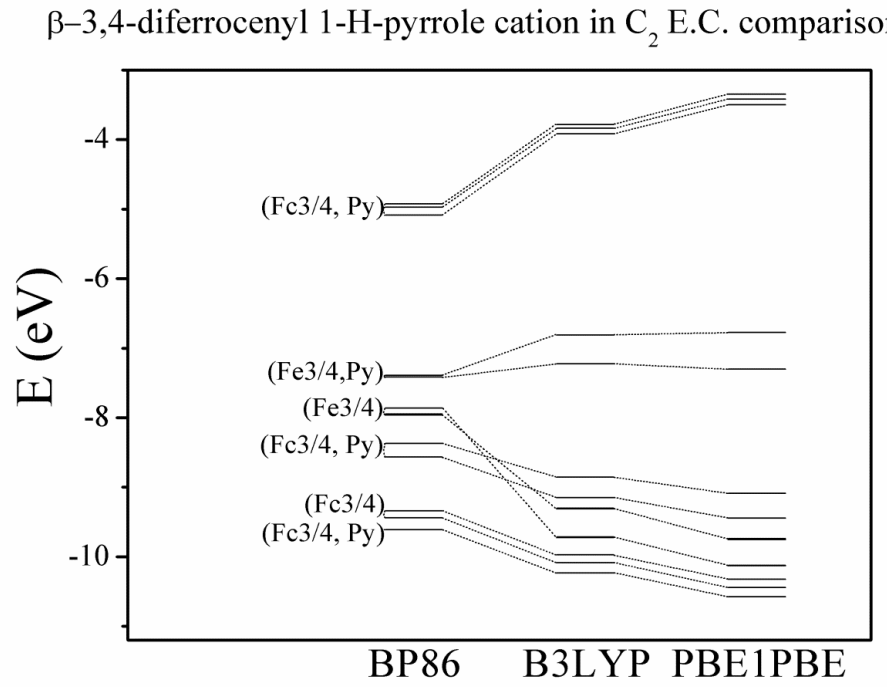

Figure S70. Comparative energetic diagram for (4^{+}) of the three exchange corrleation functionals under consideration. β-HOMO-10 through β-LUMO+3

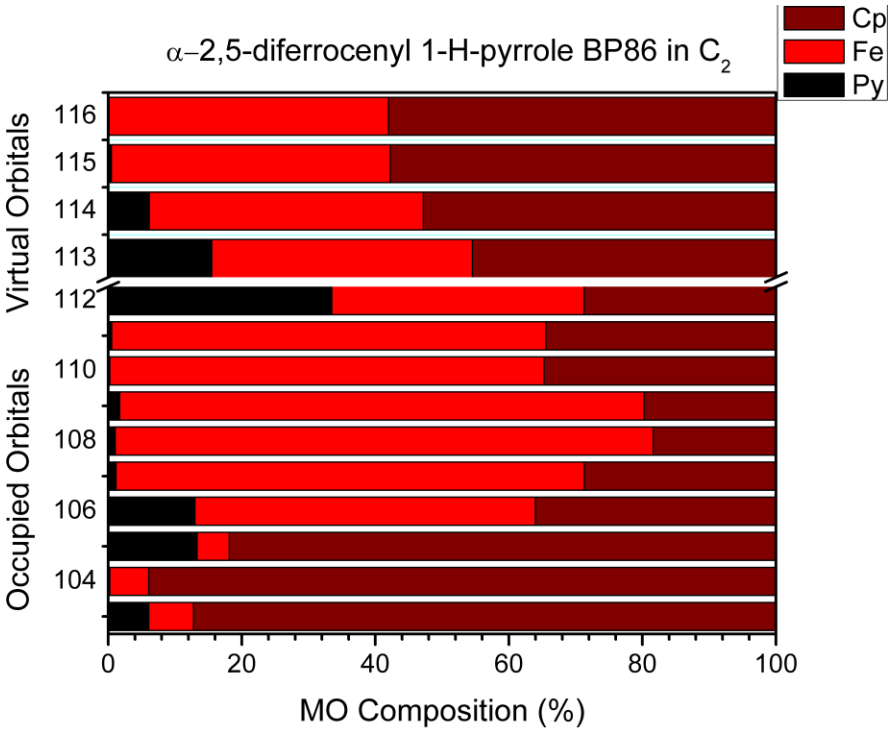

Figure S71. Molecular orbital compositions of BP86-(5^{+}) for the α-HOMO-10 through α-LUMO+3

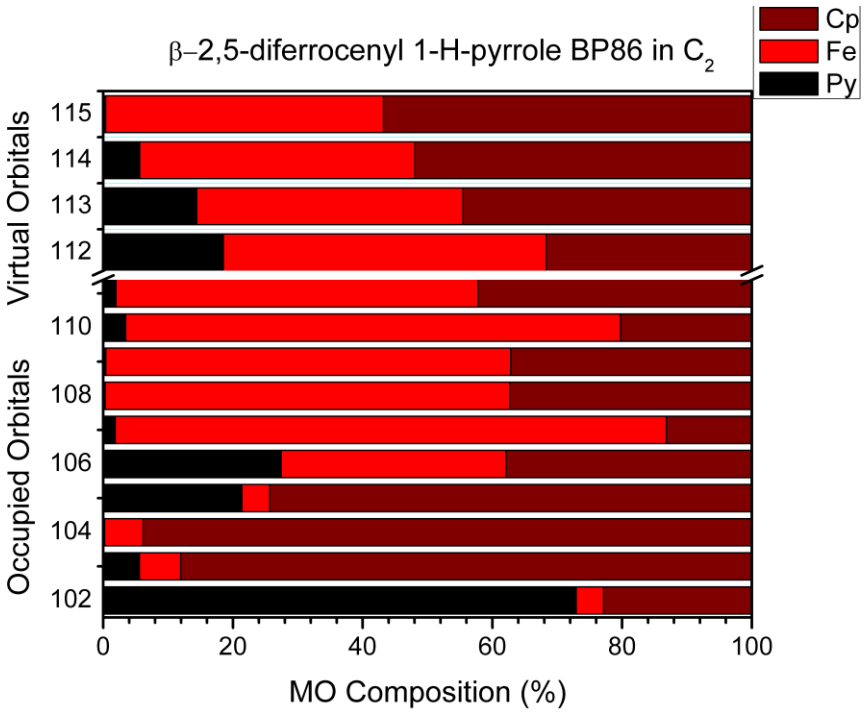

Figure S72. Molecular orbital compositions of BP86-(5^{+}) for the β-HOMO-10 through β-LUMO+3.

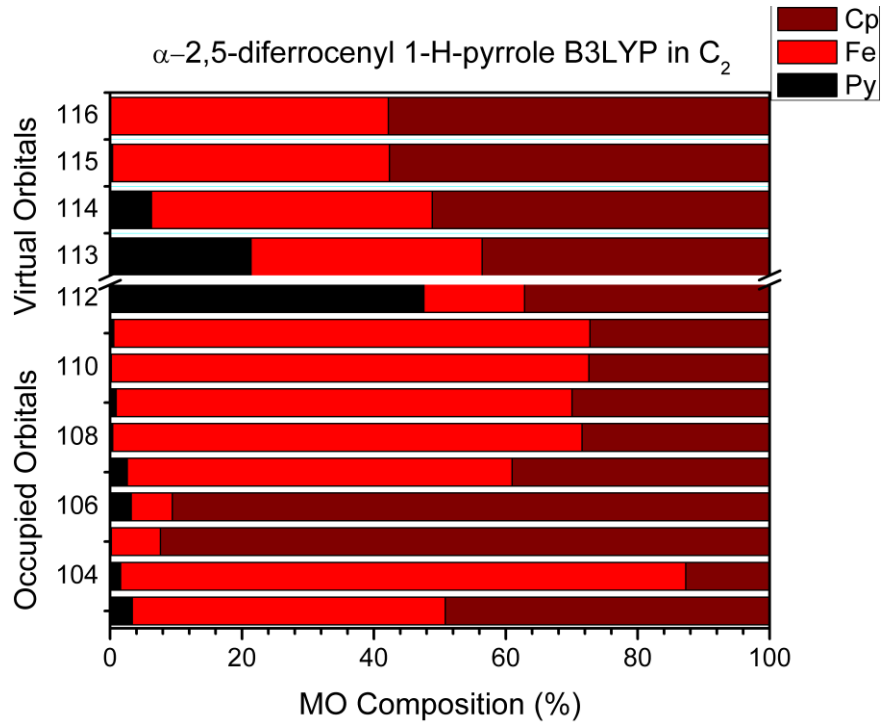

Figure S73. Molecular orbital compositions of B3LYP-(5^{+}) for the α-HOMO-10 through α-LUMO+3

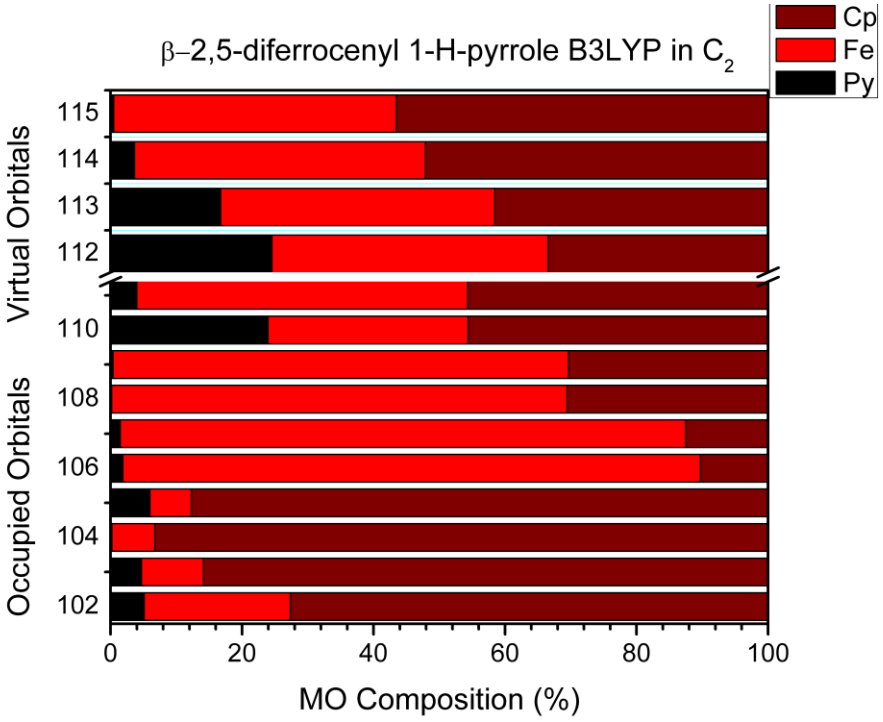

Figure S74. Molecular orbital compositions of B3LYP-(5^{+}) for the β-HOMO-10 through β-LUMO+3.

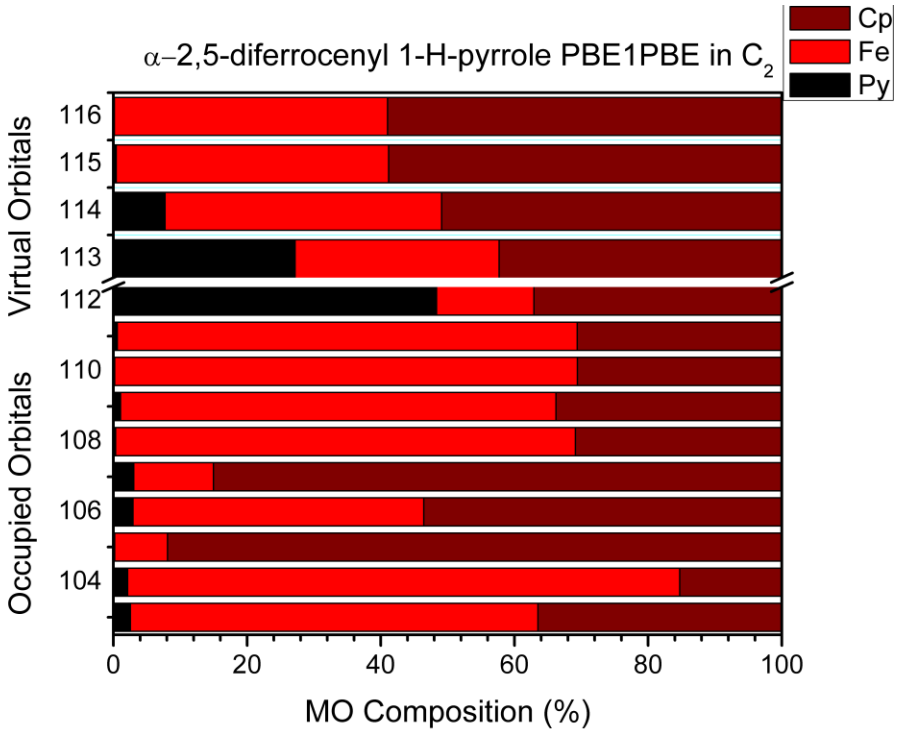

Figure S75. Molecular orbital compositions of PBE1PBE-(5^{+}) for the α-HOMO-10 through α-LUMO+3

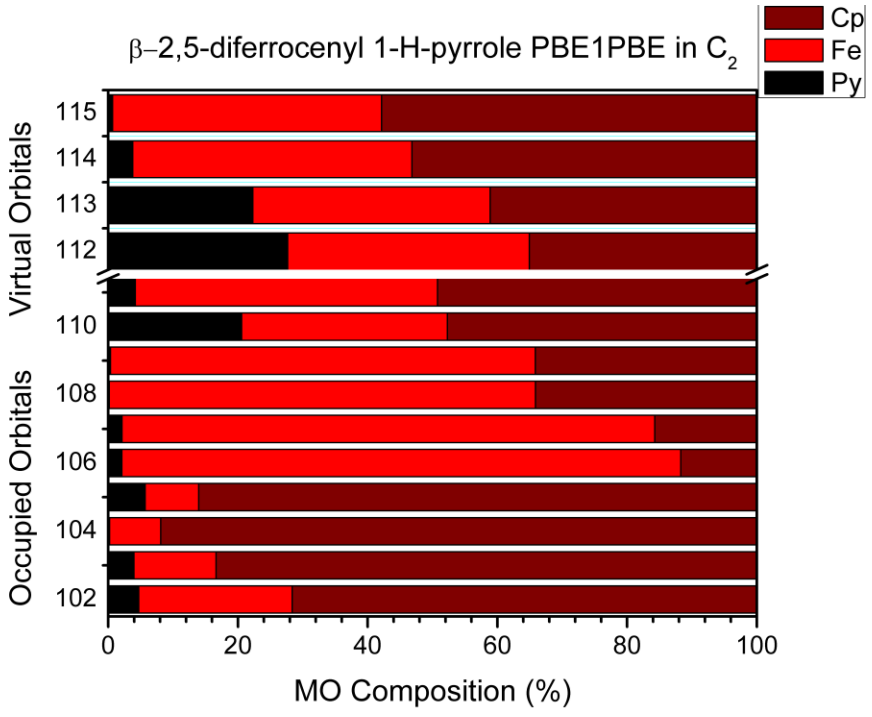

Figure S76. Molecular orbital compositions of PBE1PBE-(5^{+}) for the β-HOMO-10 through β-LUMO+3.

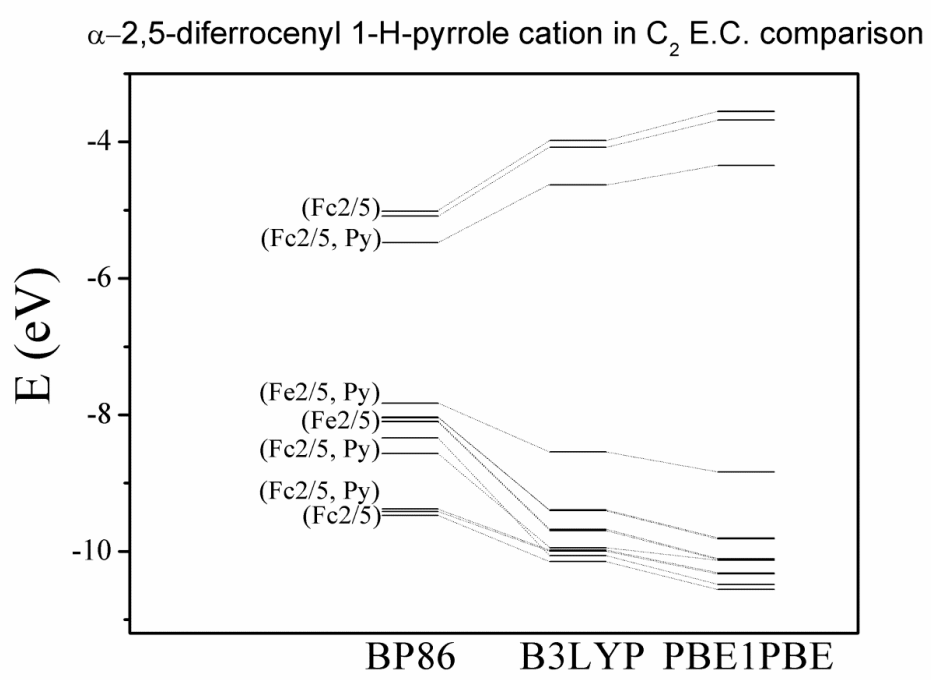

Figure S77. Comparative energetic diagram for (5^{+}) of the three exchange corrleation functionals under consideration. α-HOMO-10 through α-LUMO+3

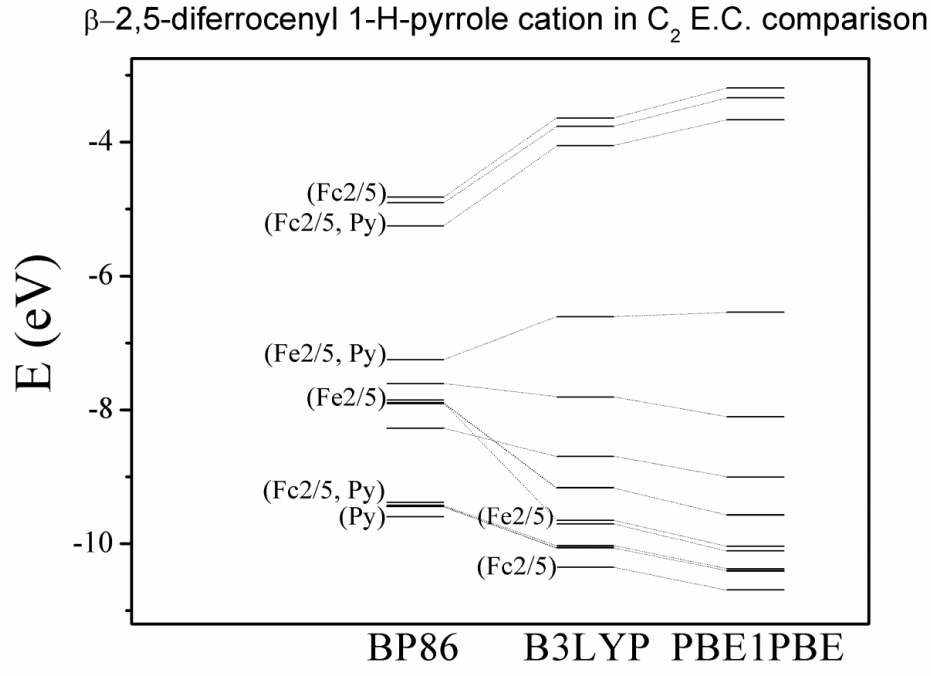

Figure S78. Comparative energetic diagram for (5^{+}) of the three exchange corrleation functionals under consideration. β-HOMO-10 through β-LUMO+3.

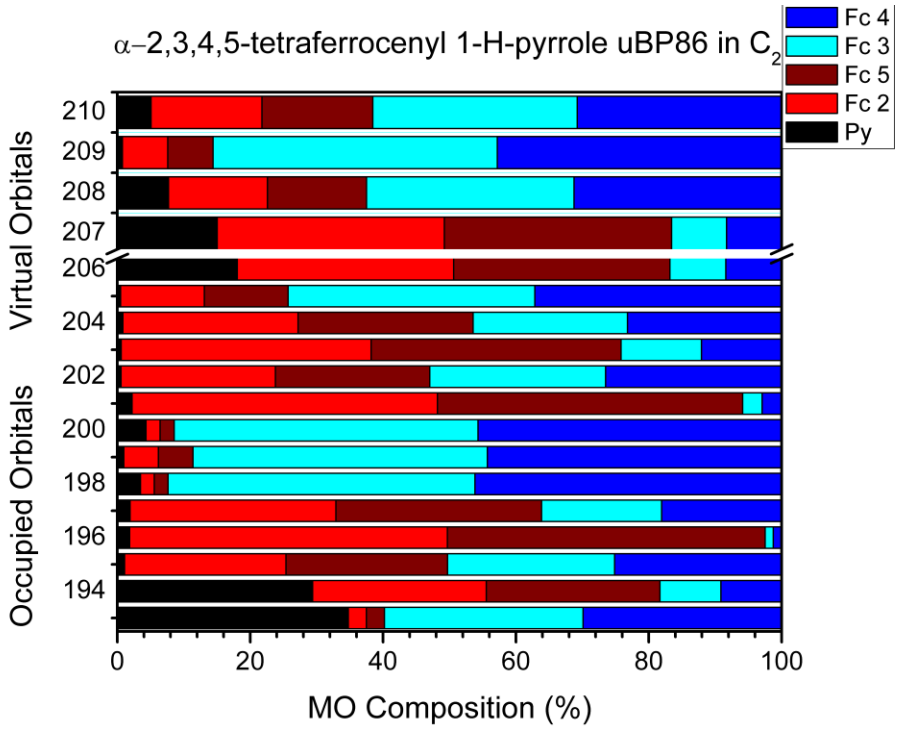

Figure S79. Molecular orbital compositions of BP86-(6^+) for the α-HOMO-14 through α-LUMO+3.

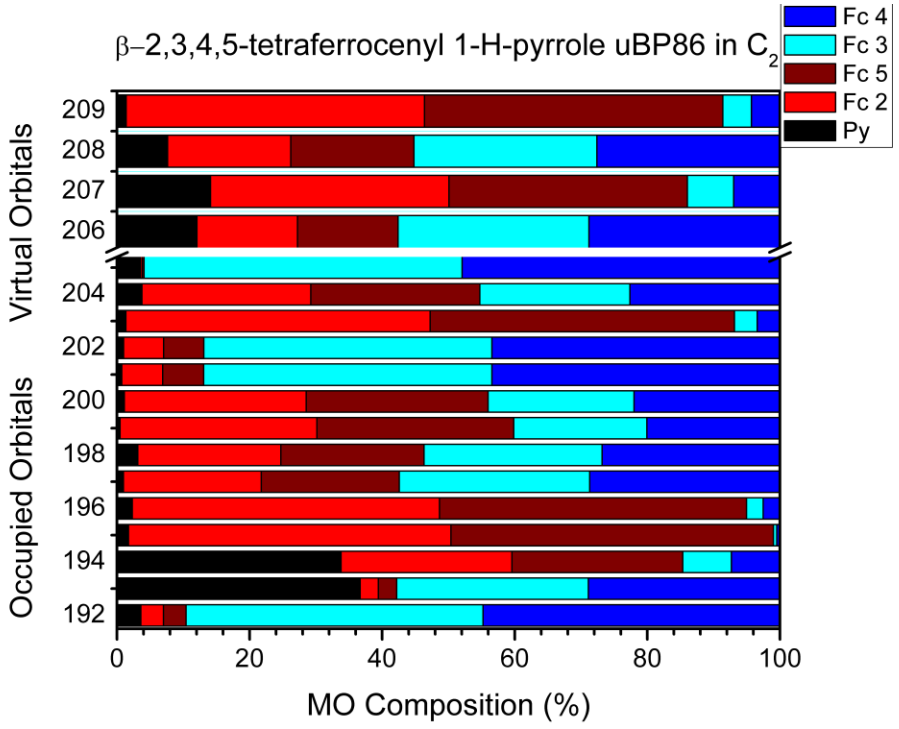

Figure S80. Molecular orbital compositions of BP86-(6^+) for the β-HOMO-14 through β-LUMO+3.

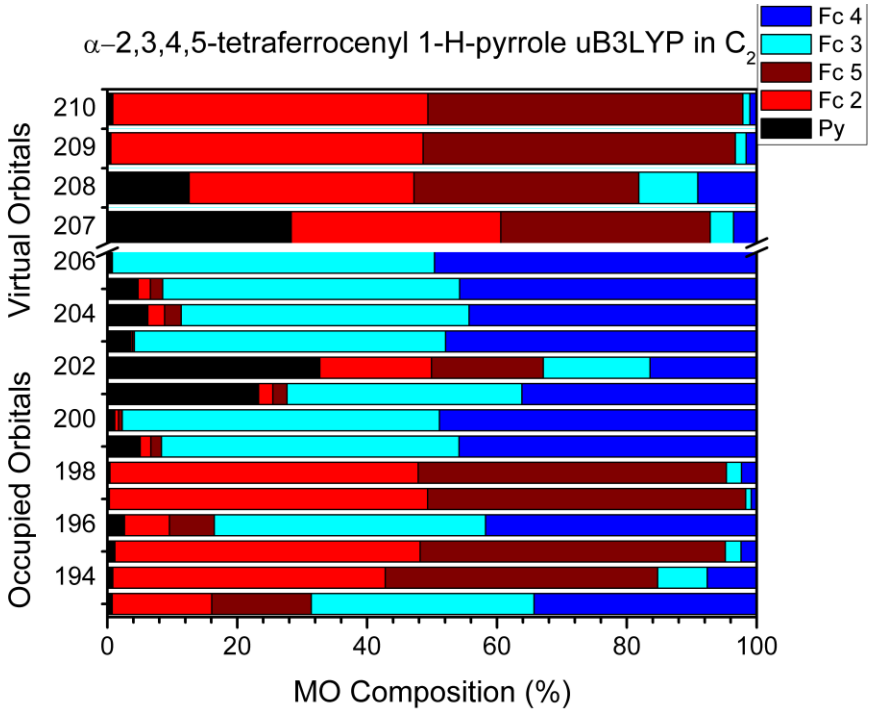

Figure S81. Molecular orbital compositions of B3LYP-(6^{+}) for the α-HOMO-14 through α-LUMO+3.

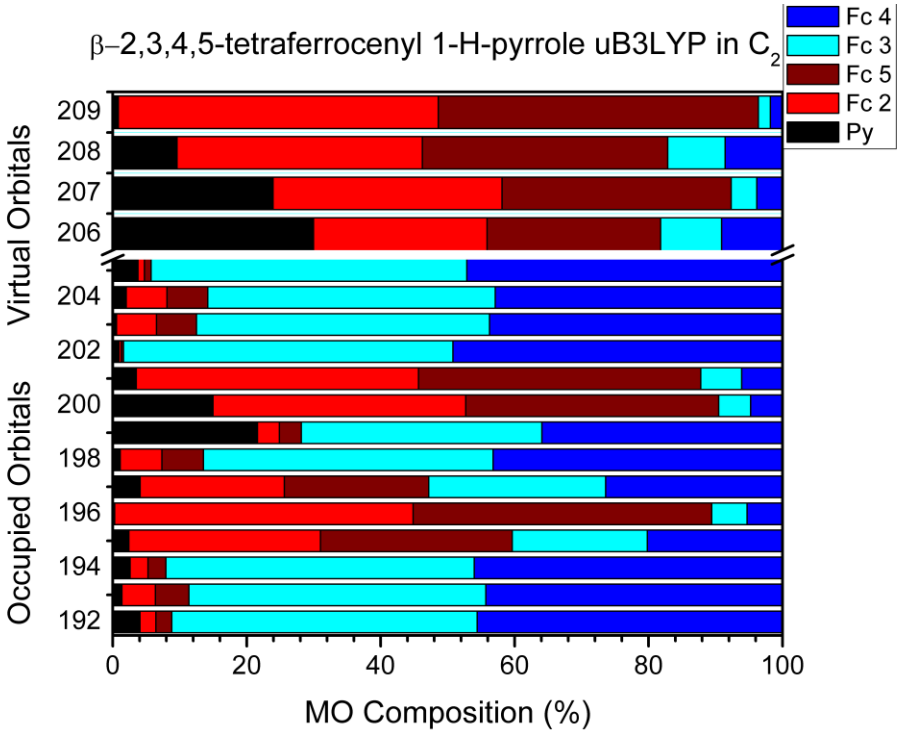

Figure S82. Molecular orbital compositions of B3LYP-(6^{+}) for the β-HOMO-14 through β-LUMO+3.

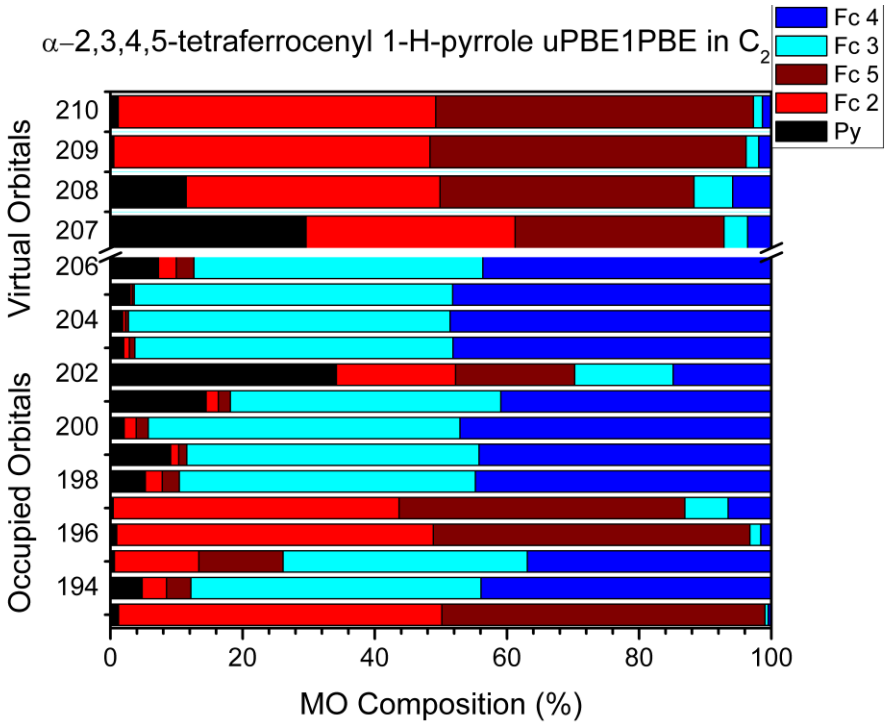

Figure S83. Molecular orbital compositions of PBE1PBE-(6^{+}) for the α-HOMO-14 through α-LUMO+3.

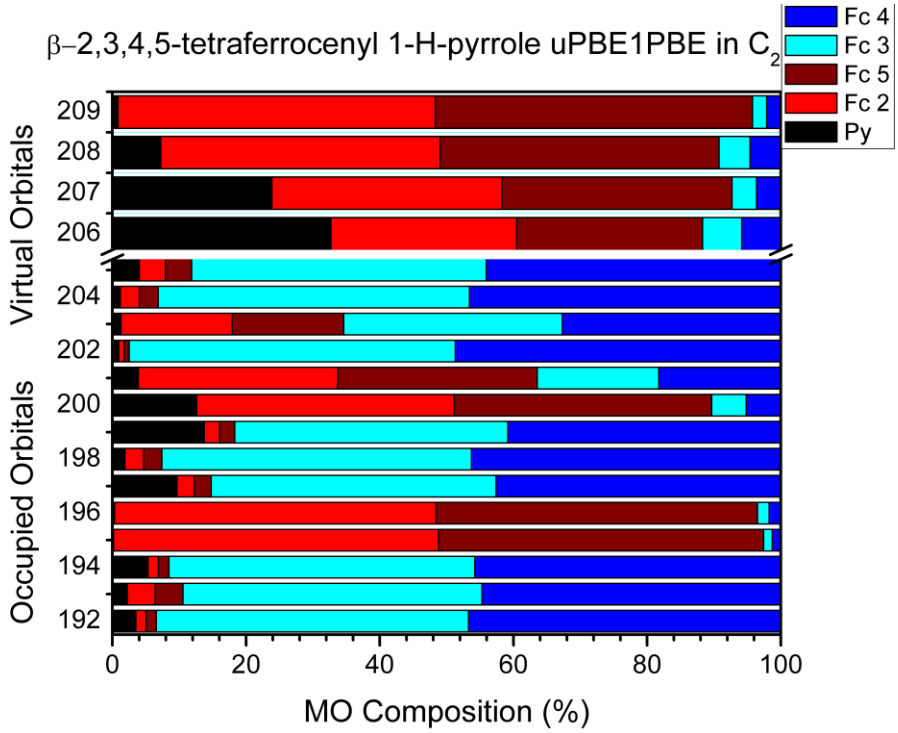

Figure S84. Molecular orbital compositions of PBE1PBE-(6^{+}) for the β-HOMO-14 through β-LUMO+3.

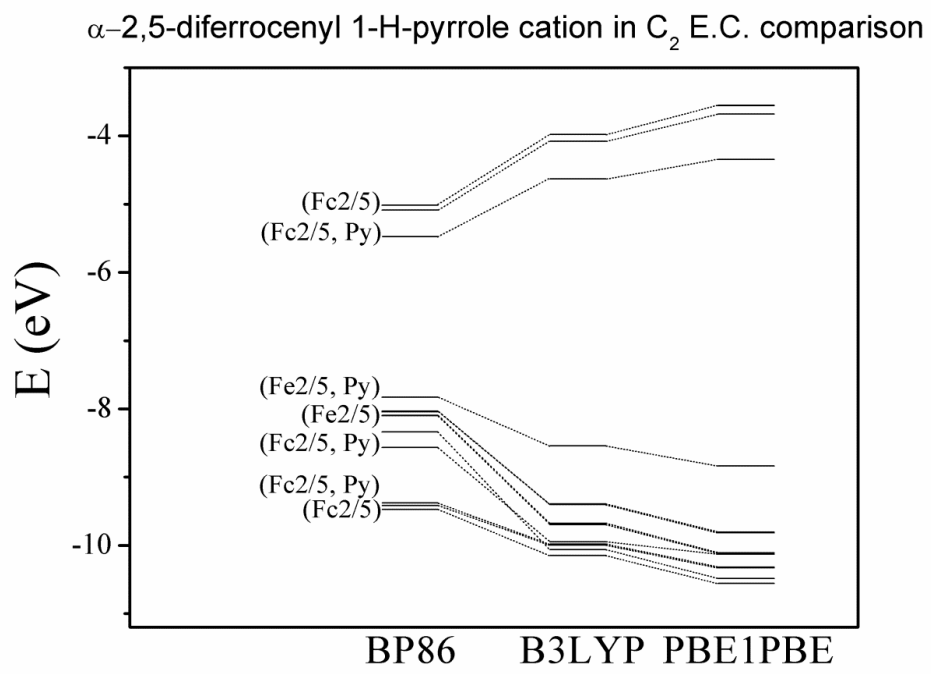

Figure S85. Comparative energetic diagram for (6^{+}) of the three exchange corrleation functionals under consideration. α-HOMO-14 through α-LUMO+3.

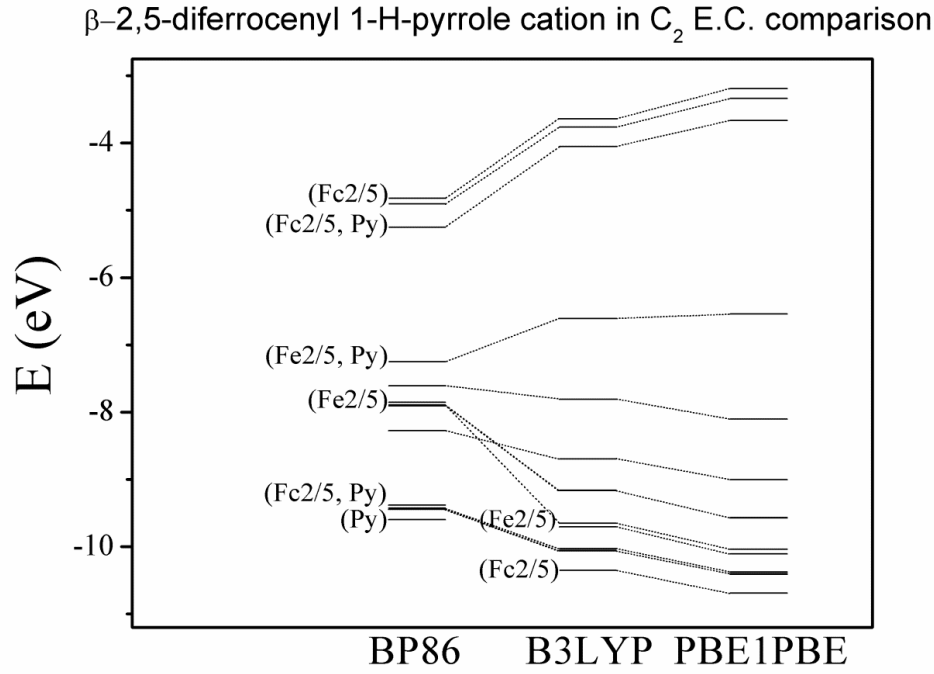

Figure S86. Comparative energetic diagram for (6^{+}) of the three exchange corrleation functionals under consideration. β-HOMO-14 through β-LUMO+3.

Table S87. Spin-densities of the C_2 optimized cationic geometries.

Compound	E.C.	Spin Densities			
		Fe2	Fe-5	Fe-3	Fe-4
(4^+)	BP86	---	---	0.56	0.56
	B3LYP	---	---	0.64	0.64
	PBE1PBE	---	---	0.66	0.66
(5^+)	BP86	0.45	0.45	---	----
	B3LYP	0.49	0.49	---	---
	PBE1PBE	0.47	0.47	---	---
(6^+)	BP86	0.17	0.17	0.34	0.34
	B3LYP	0.33	0.33	0.10	0.10
	PBE1PBE	0.95	0.95	0.00	0.00

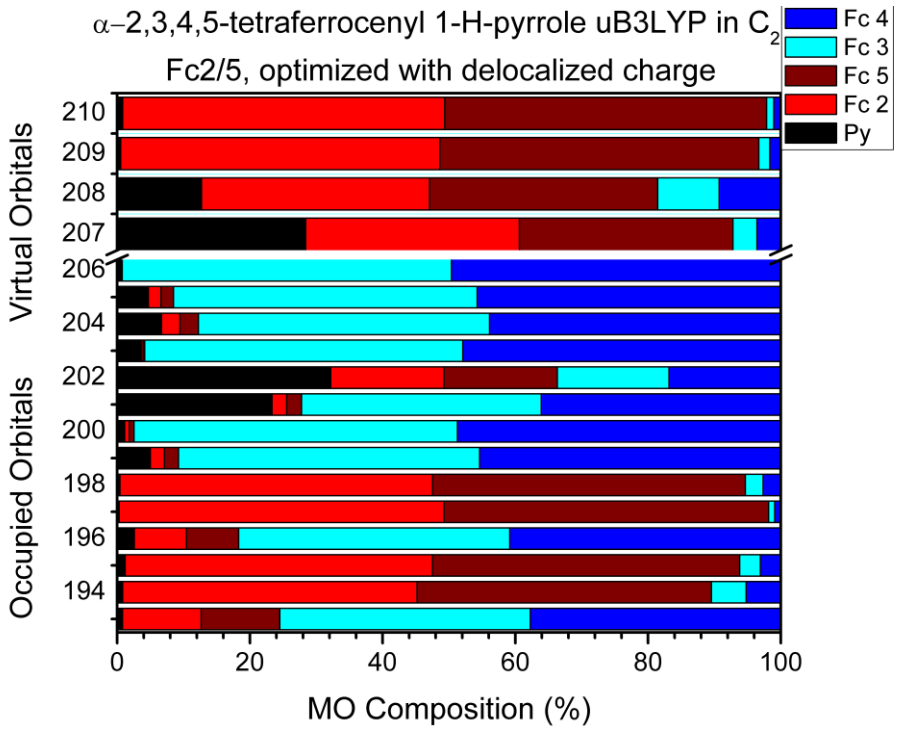

Figure S88. Molecular orbital compositions of B3LYP-(6^+) for the delocalized geometry with reassigned charge on ferrocenes-2,5 for the α-HOMO-14 through α-LUMO+3.

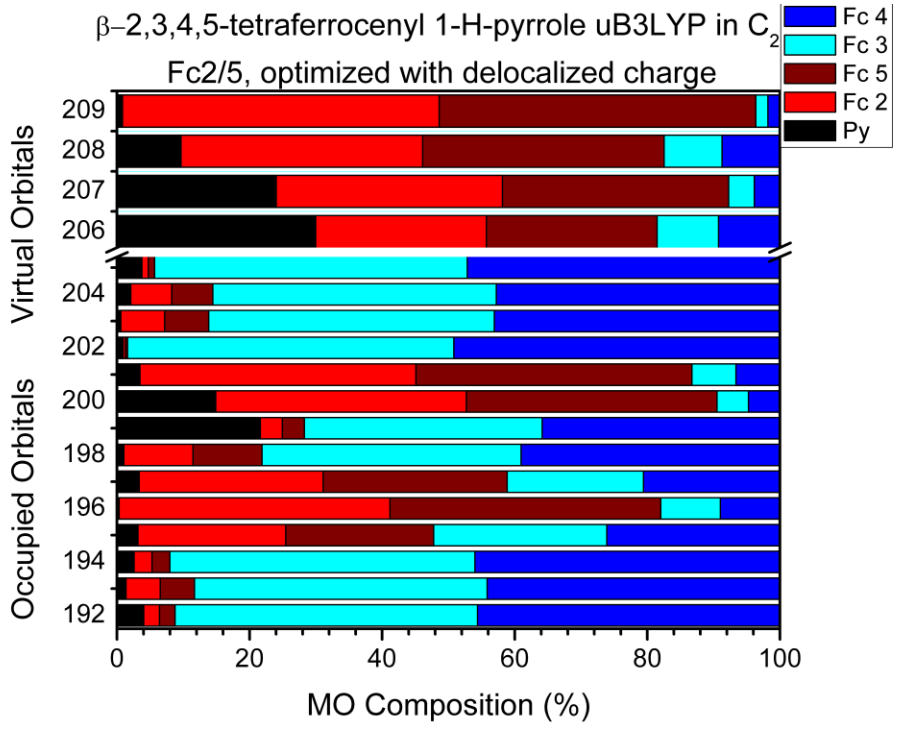

Figure S89. Molecular orbital compositions of B3LYP-(6^+) for the delocalized geometry with reassigned charge on ferrocenes-2,5 for the β-HOMO-14 through β-LUMO+3.

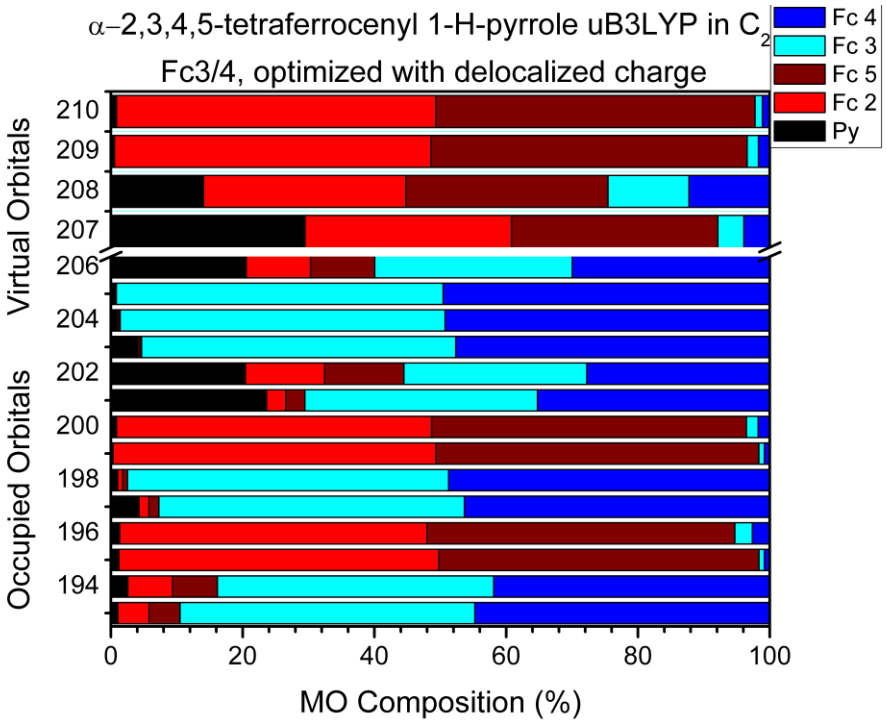

Figure S90. Molecular orbital compositions of B3LYP-(6^{+}) for the delocalized geometry with reassigned charges on ferrocenes-3,4 for the α-HOMO-14 through α-LUMO+3.

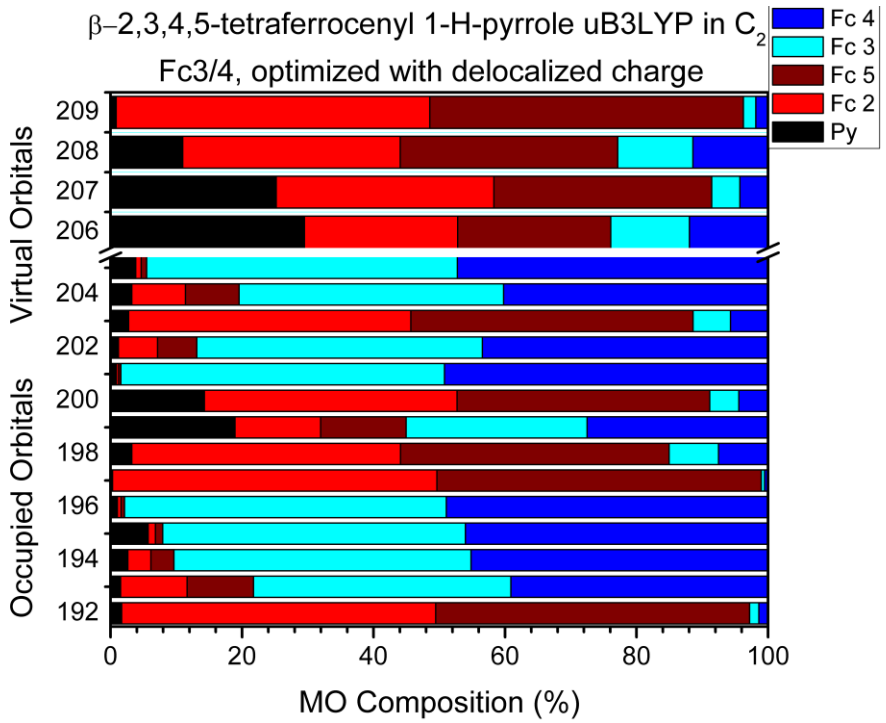

Figure S91. Molecular orbital compositions of B3LYP-(6^{+}) for the delocalized geometry with reassigned charge on ferrocenes-3,4 for the β-HOMO-14 through β-LUMO+3.

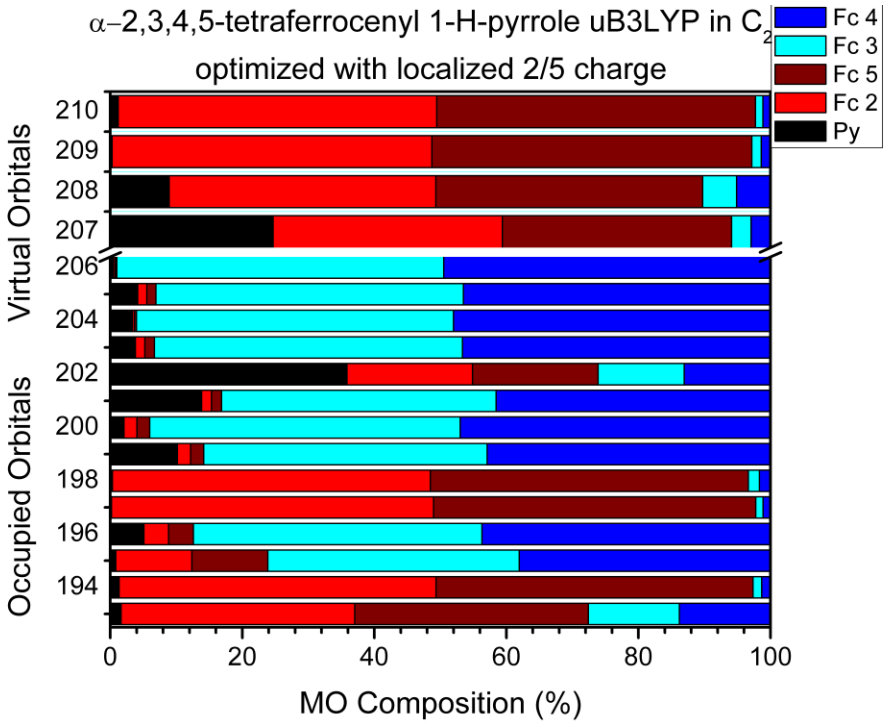

Figure S92. Molecular orbital compositions of B3LYP-(6^{+}) with the 2,5-ferrocene charge localized geometry for the α-HOMO-14 through α-LUMO+3.

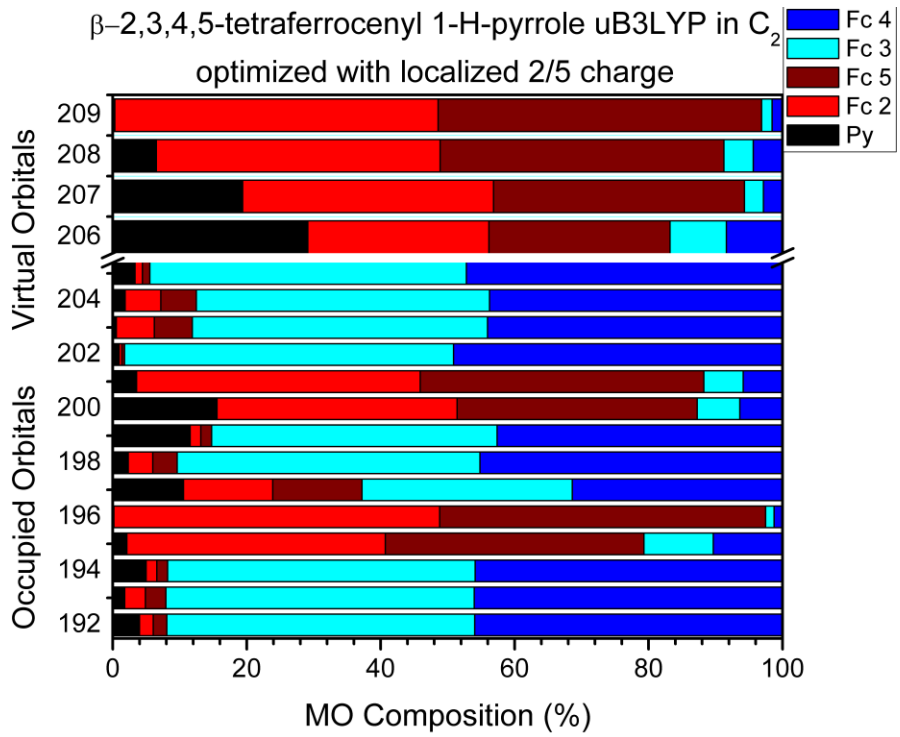

Figure S93. Molecular orbital compositions of B3LYP-(6^{+}) with the 2,5-ferrocene charge localized geometry for the β-HOMO-14 through β-LUMO+3.

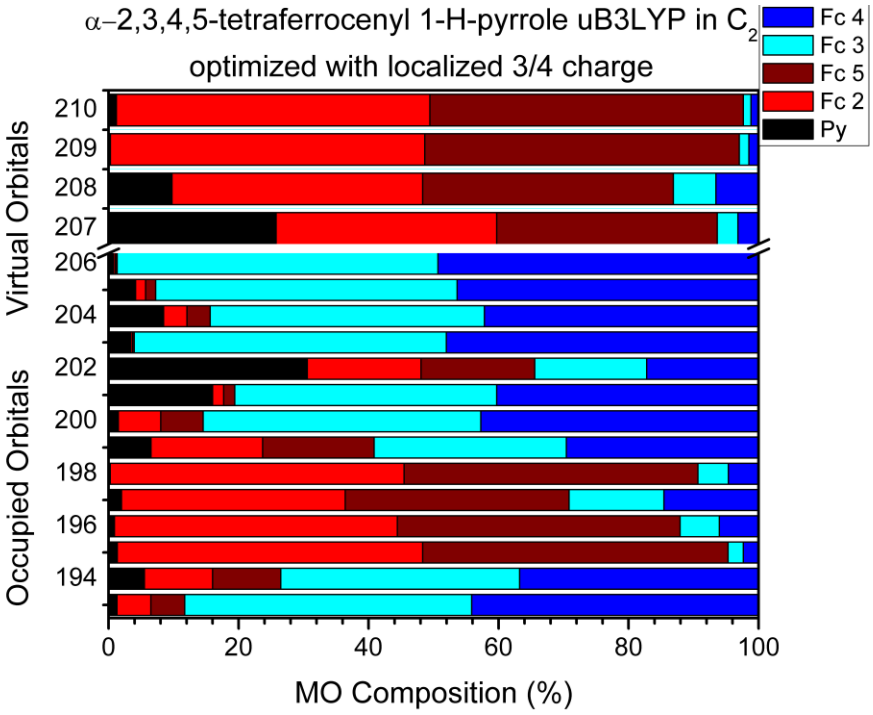

Figure S94. Molecular orbital compositions of B3LYP-(6^{+}) with the 3,4-ferrocene charge localized geometry for the α-HOMO-14 through α-LUMO+3.

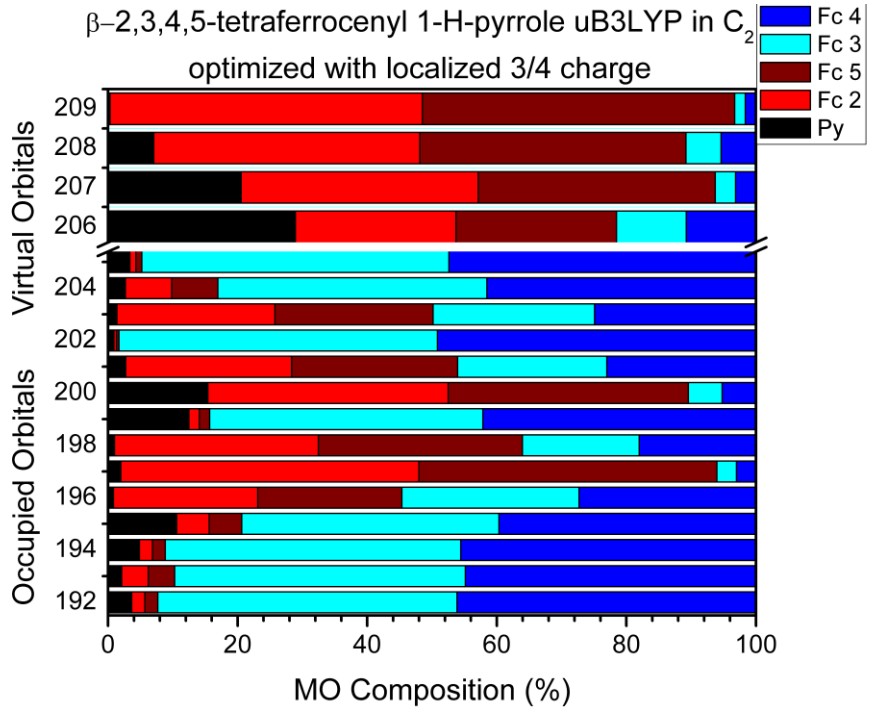

Figure S95. Molecular orbital compositions of B3LYP-(6^{+}) with the 3,4-ferrocene charge localized geometry for the β-HOMO-14 through β-LUMO+3.

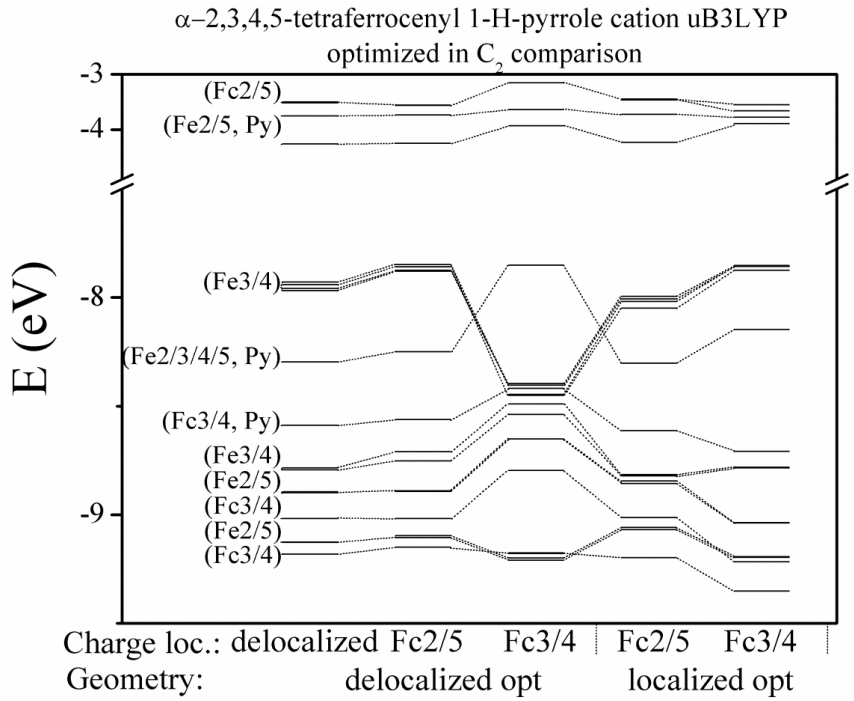

Figure S96. Comparative energetic diagram for the C_2 optimized geometries of (6^+) for the α-HOMO-14 through α-LUMO+3.

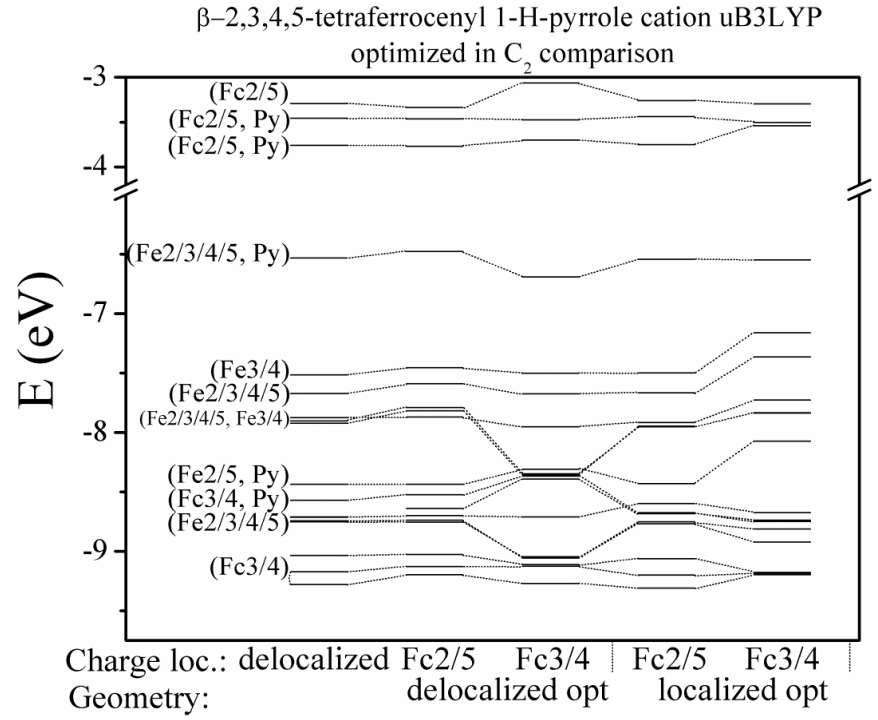

Figure S97. Comparative energetic diagram for the C_2 optimized geometries of (6^+) for the β-HOMO-14 through β-LUMO+3.

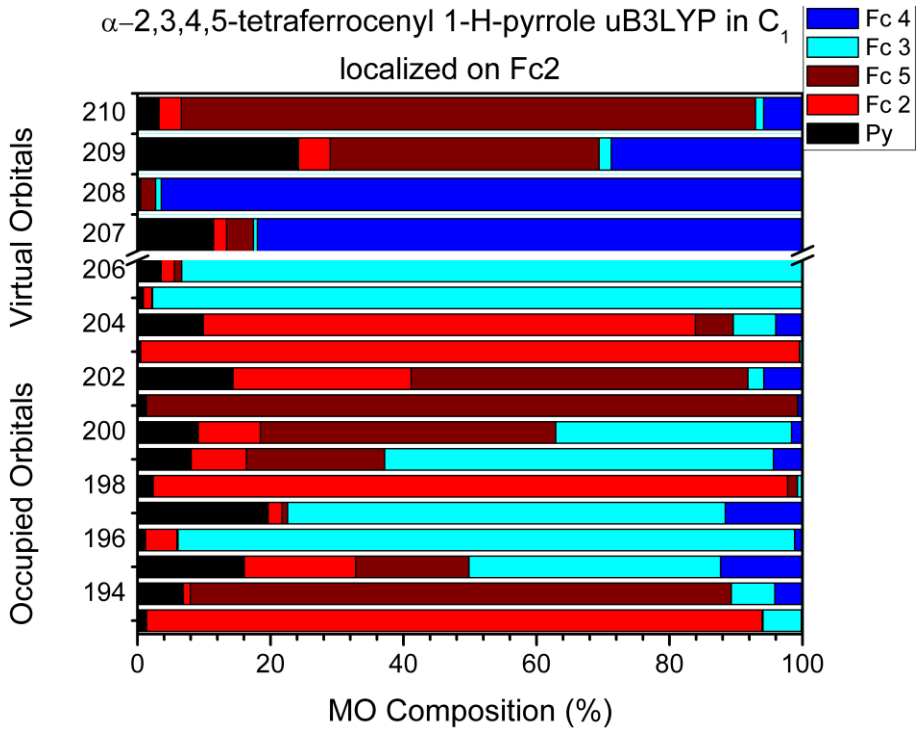

Figure S98. Molecular orbital compositions of B3LYP-(6^{+}) with the 2-ferrocene charge localized C_1-geometry for the α-HOMO-14 through α-LUMO+3.

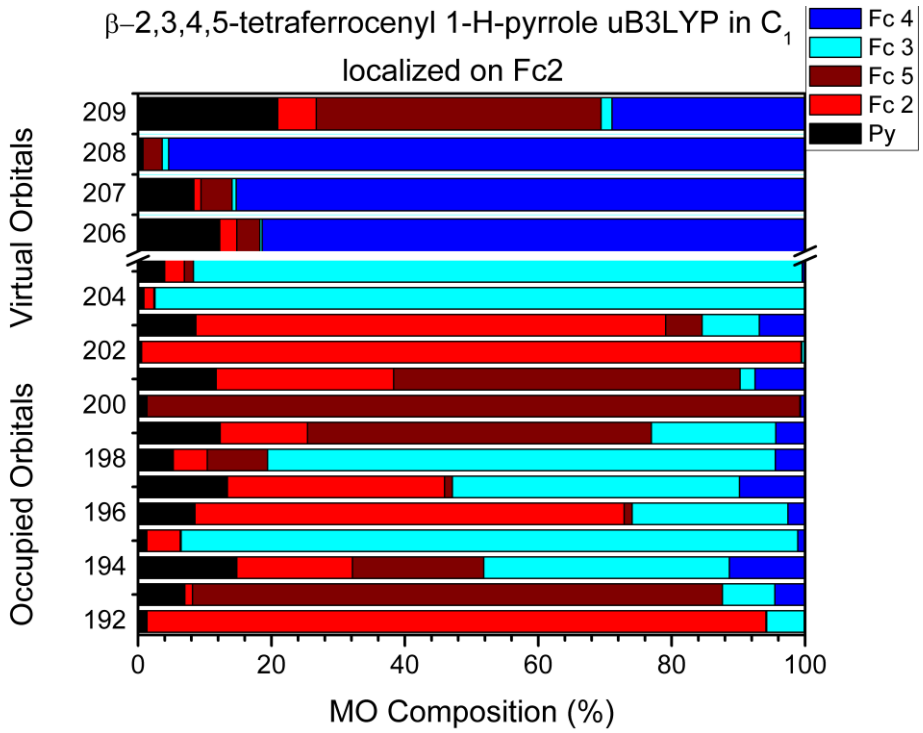

Figure S99. Molecular orbital compositions of B3LYP-(6^{+}) with the 2-ferrocene charge localized C_1-geometry for the β-HOMO-14 through β-LUMO+3.

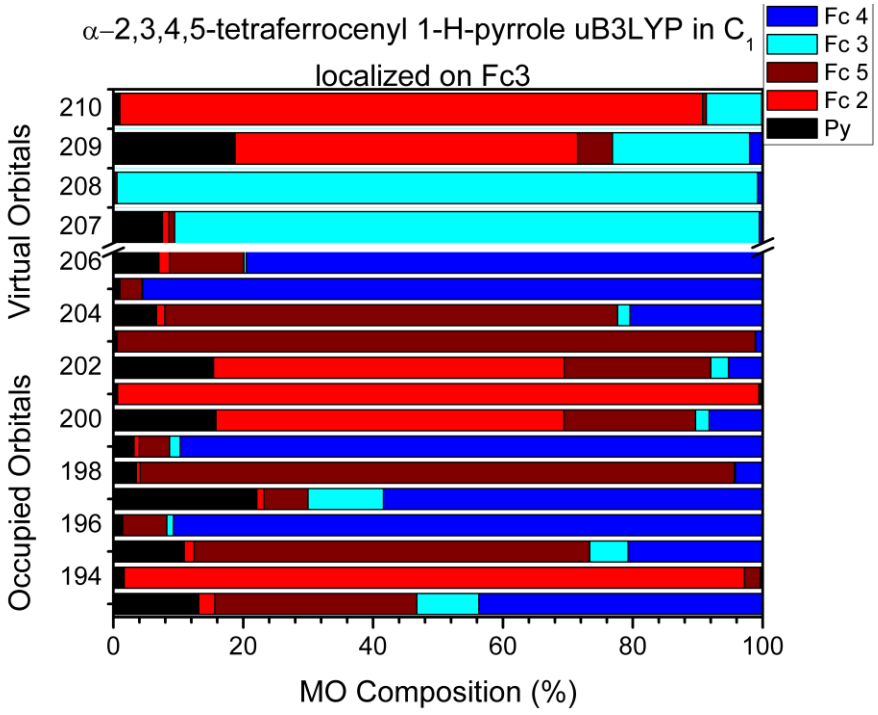

Figure S100. Molecular orbital compositions of B3LYP-(6^{+}) with the 3-ferrocene charge localized C_1-geometry for the α-HOMO-14 through α-LUMO+3.

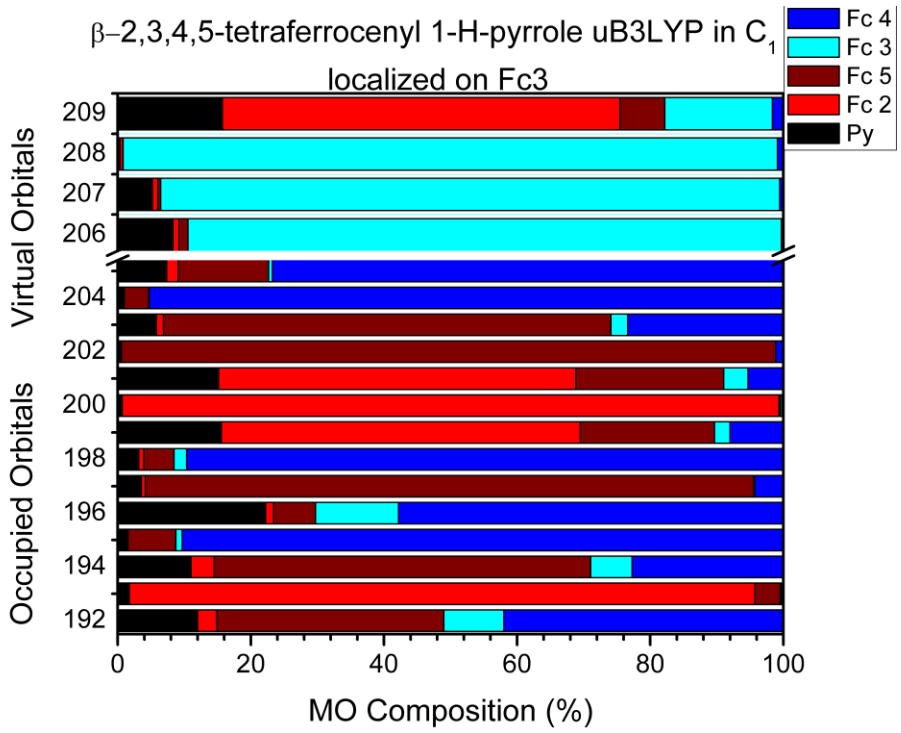

Figure S101. Molecular orbital compositions of B3LYP-(6^{+}) with the 3-ferrocene charge localized C_1-geometry for the β-HOMO-14 through β-LUMO+3.

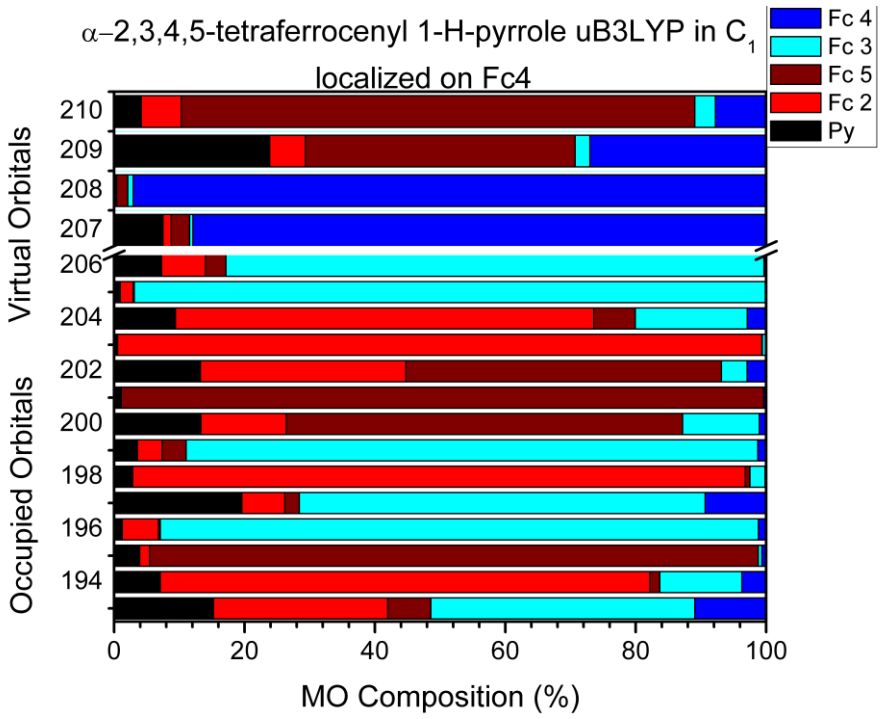

Figure S102. Molecular orbital compositions of B3LYP-(6^{+}) with the 4-ferrocene charge localized C_1-geometry for the α-HOMO-14 through α-LUMO+3.

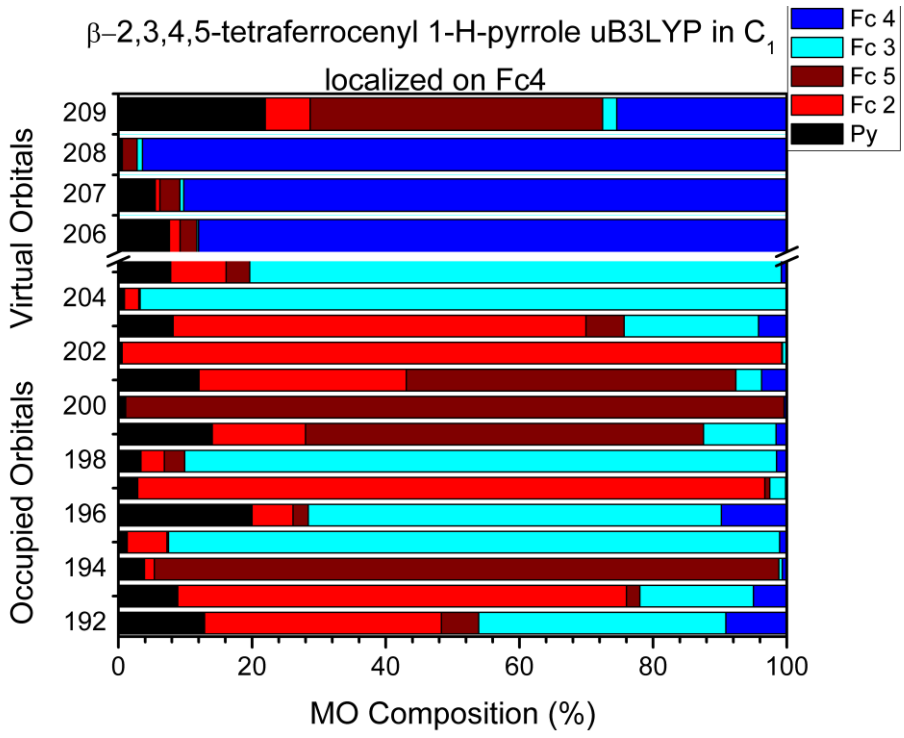

Figure S103. Molecular orbital compositions of B3LYP-(6^{+}) with the 4-ferrocene charge localized C_1-geometry for the β-HOMO-14 through β-LUMO+3.

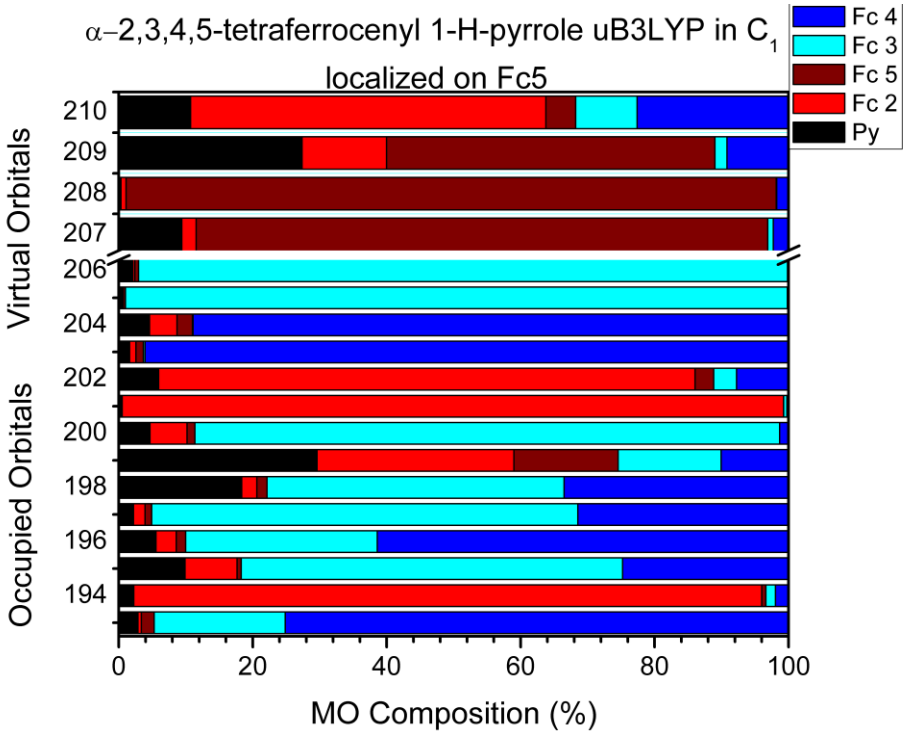

Figure S104. Molecular orbital compositions of B3LYP-(6^{+}) with the 5-ferrocene charge localized C_1-geometry for the α-HOMO-14 through α-LUMO+3.

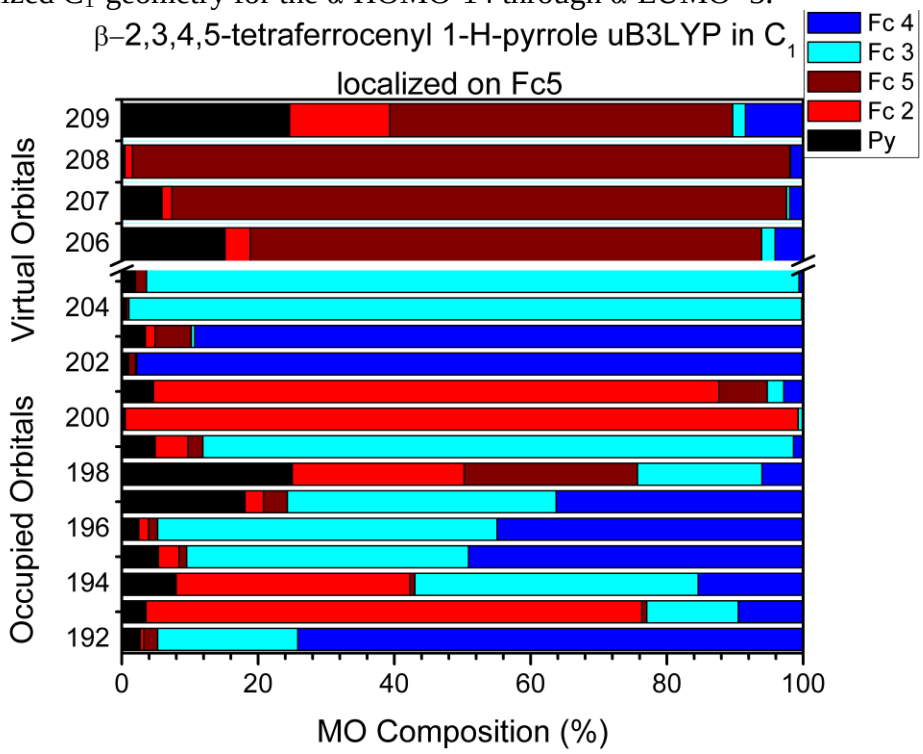

S105. Molecular orbital compositions of B3LYP-(6^{+}) with the 5-ferrocene charge localized C_1-geometry for the β-HOMO-14 through β-LUMO+3.

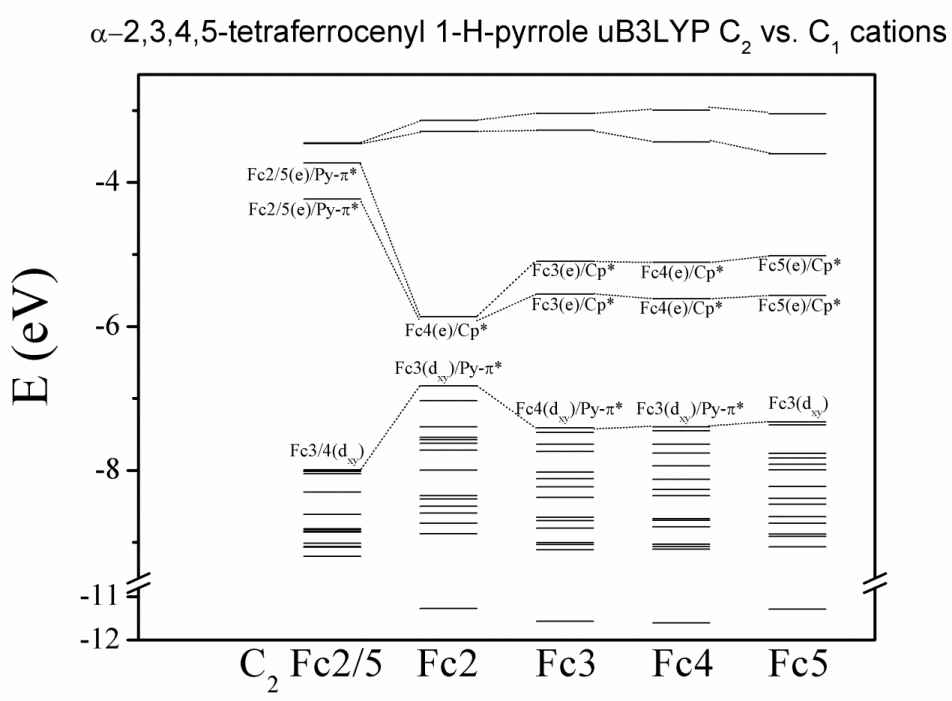

Figure S106. Comparative energetic diagram for the C_1 and lowest energy C_2 optimized geometries of (6^+) for the α-HOMO-14 through α-LUMO+3.

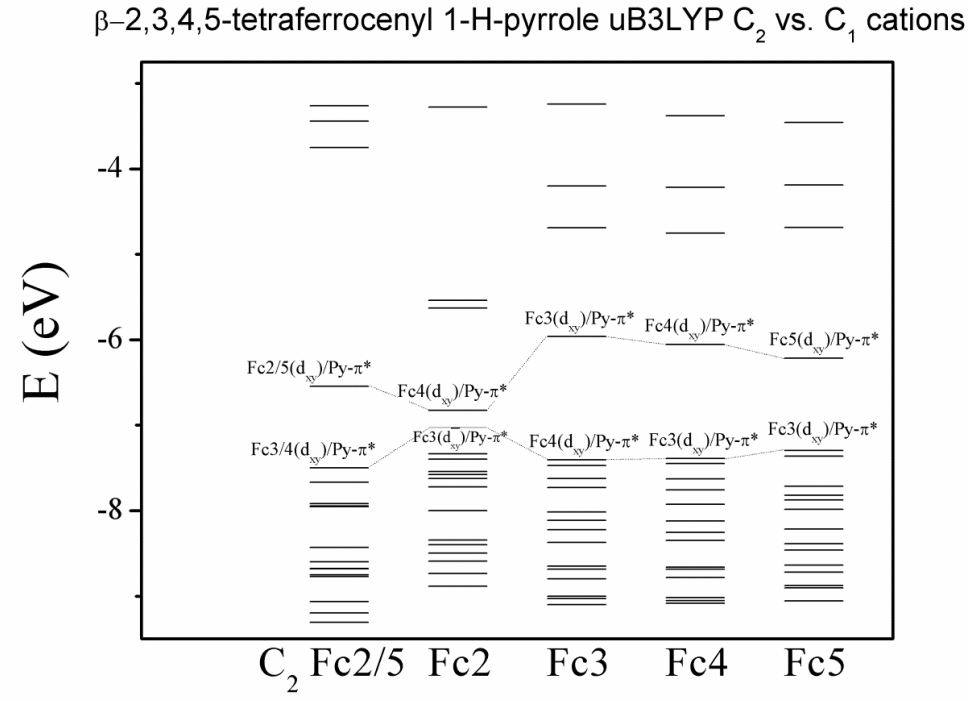

Figure S107. Comparative energetic diagram for the C_1 and lowest energy C_2 optimized geometries of (6^+) for the β-HOMO-14 through β-LUMO+3.

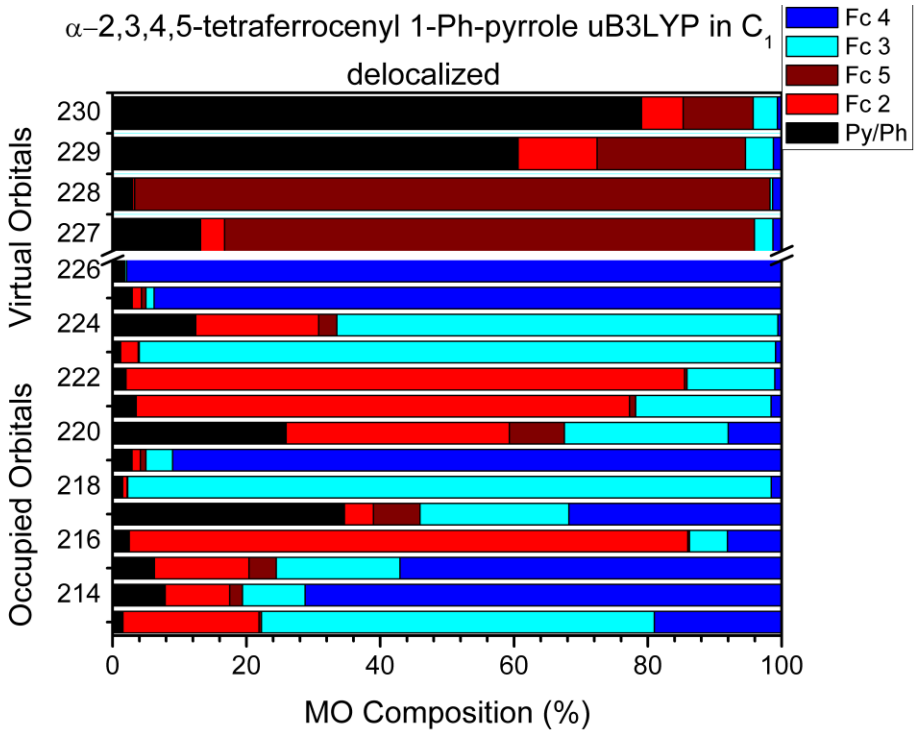

Figure S108. Molecular orbital compositions of B3LYP-(1^+) with the charge delocalized C_1-geometry for the α-HOMO-14 through α-LUMO+3.

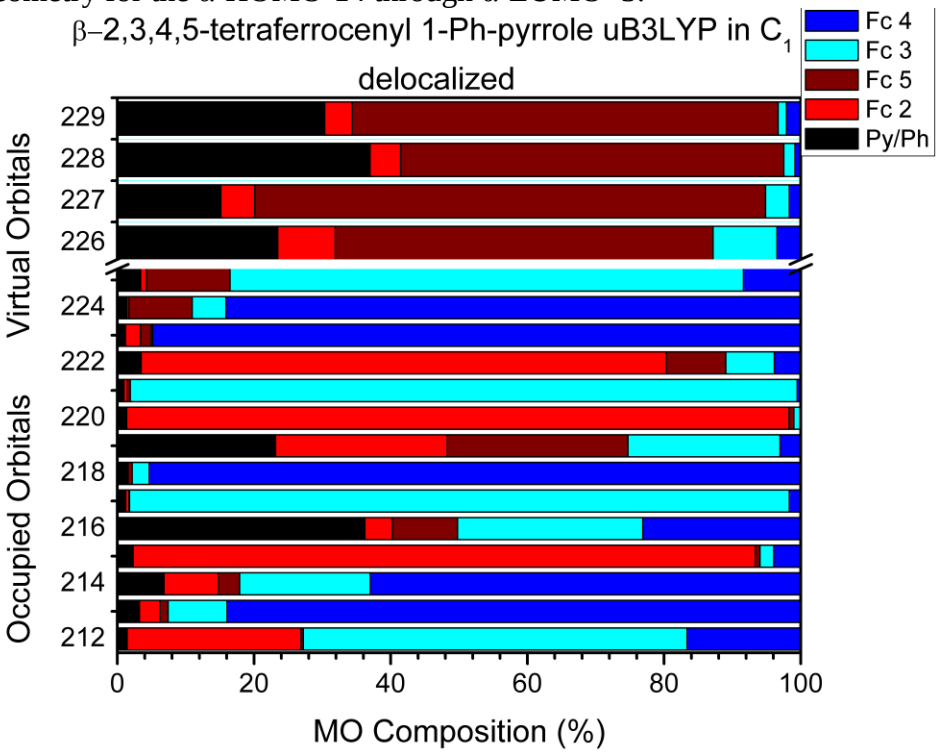

Figure S109. Molecular orbital compositions of B3LYP-(1^+) with the charge delocalized C_1-geometry for the β-HOMO-14 through β-LUMO+3.

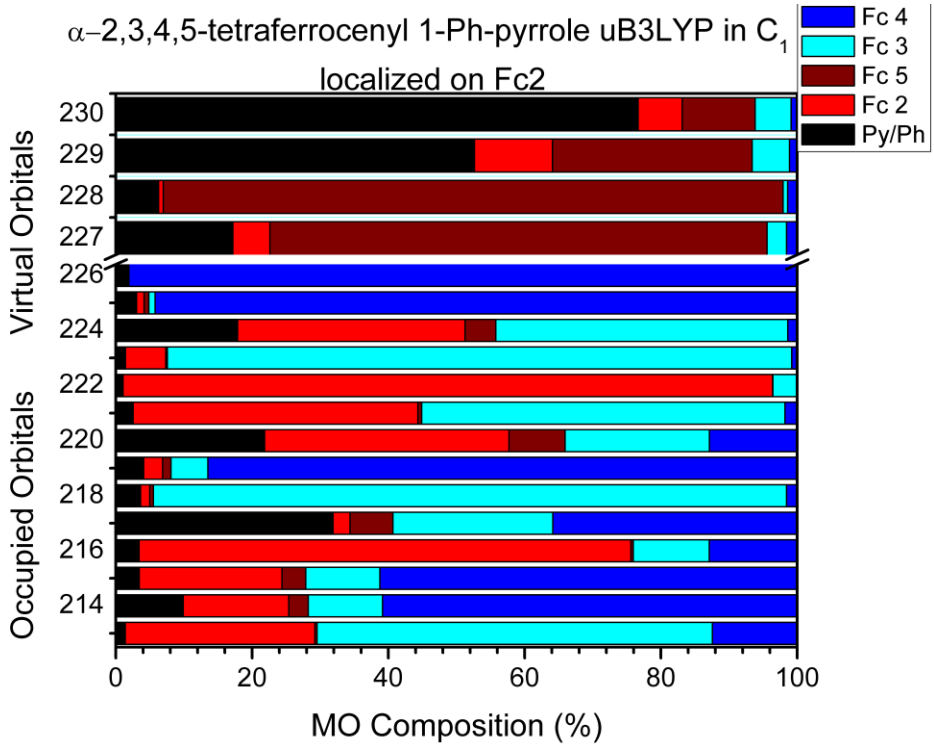

Figure S110. Molecular orbital compositions of B3LYP-(1^{+}) with the 2-ferrocene charge localized C_1-geometry for the α-HOMO-14 through α-LUMO+3.

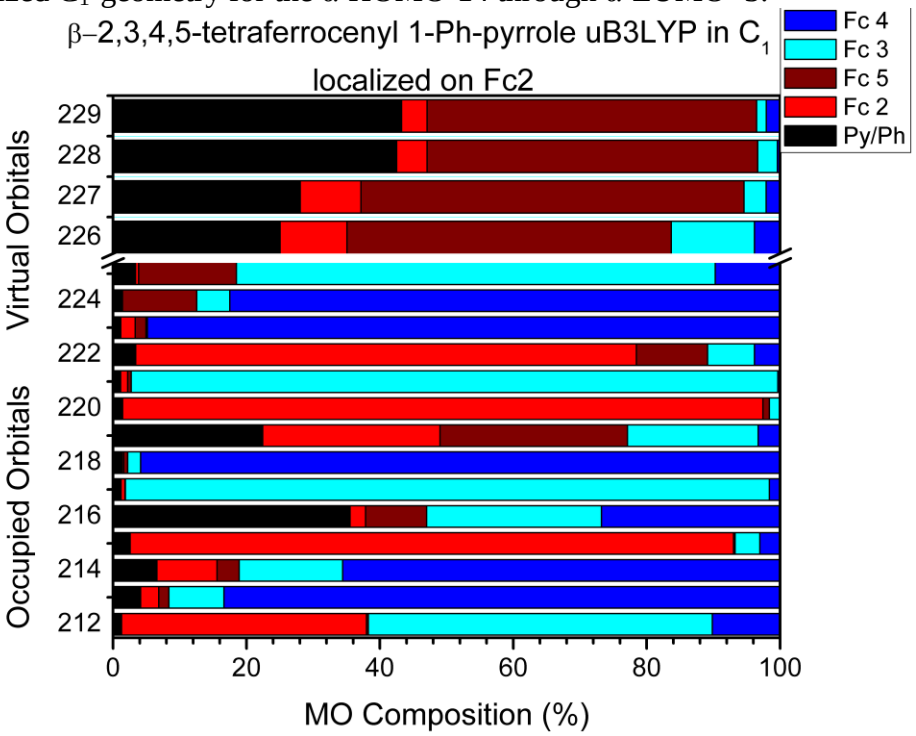

Figure S111. Molecular orbital compositions of B3LYP-(1^{+}) with the 2-ferrocene charge localized C_1-geometry for the β-HOMO-14 through β-LUMO+3.

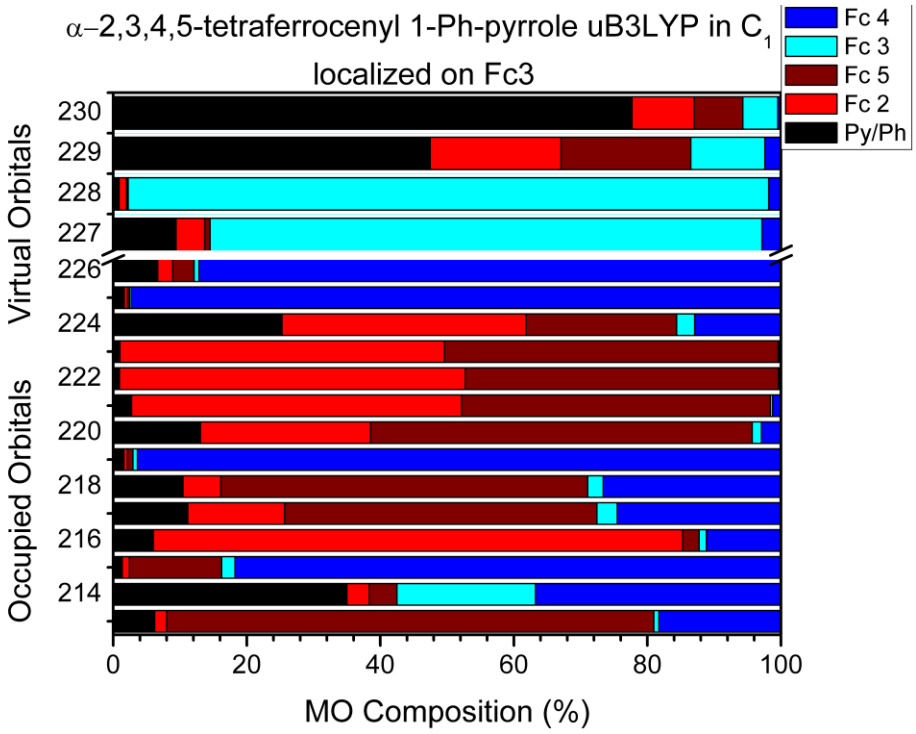

Figure S112. Molecular orbital compositions of B3LYP-(1^+) with the 3-ferrocene charge localized C_1-geometry for the α-HOMO-14 through α-LUMO+3.

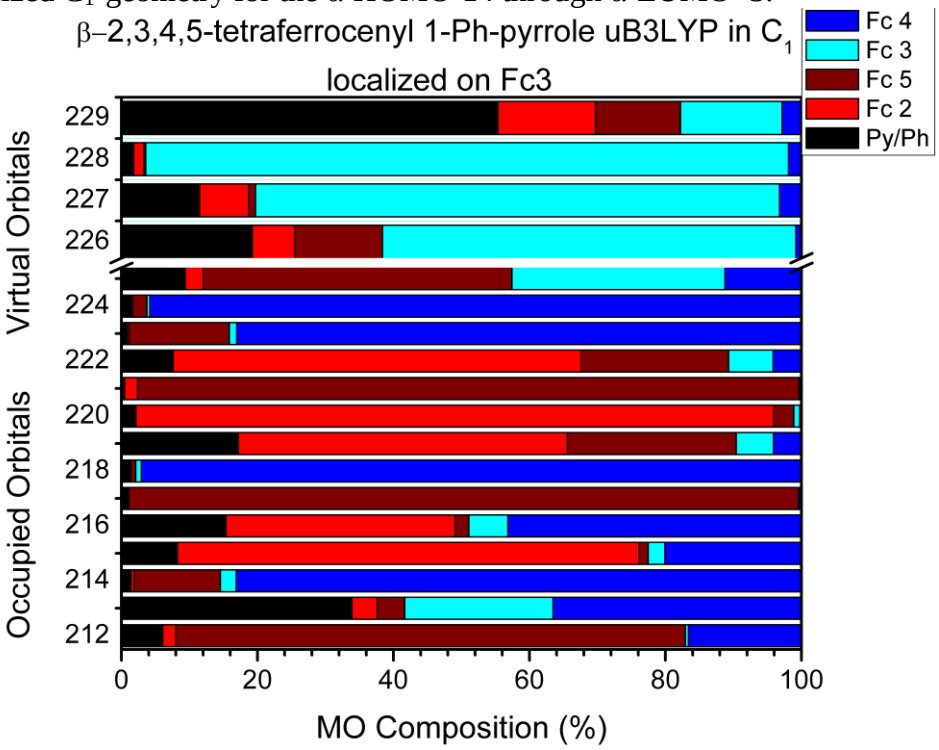

Figure S113. Molecular orbital compositions of B3LYP-(1^+) with the 3-ferrocene charge localized C_1-geometry for the β-HOMO-14 through β-LUMO+3.

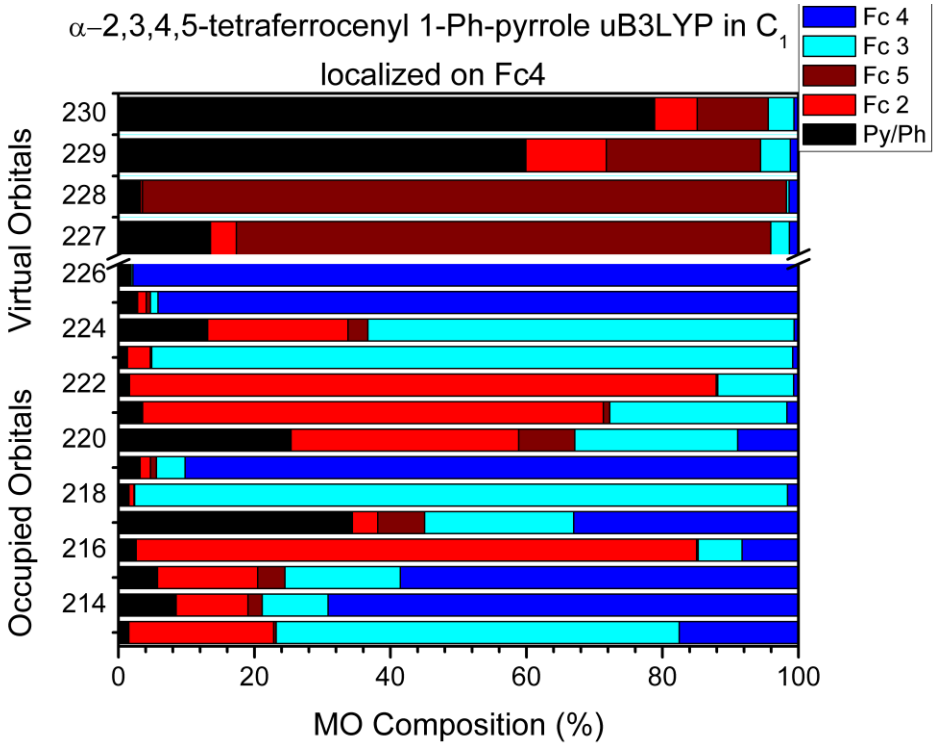

Figure S114. Molecular orbital compositions of B3LYP-(1^{+}) with the 4-ferrocene charge localized C_1-geometry for the α-HOMO-14 through α-LUMO+3.

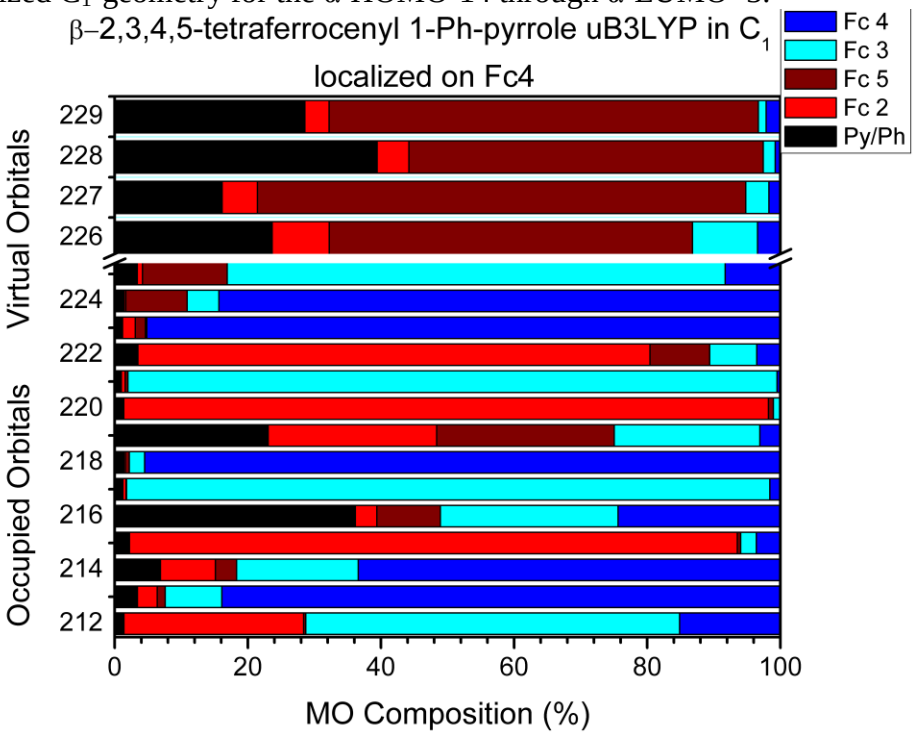

Figure S115. Molecular orbital compositions of B3LYP-(1^{+}) with the 4-ferrocene charge localized C_1-geometry for the β-HOMO-14 through β-LUMO+3.

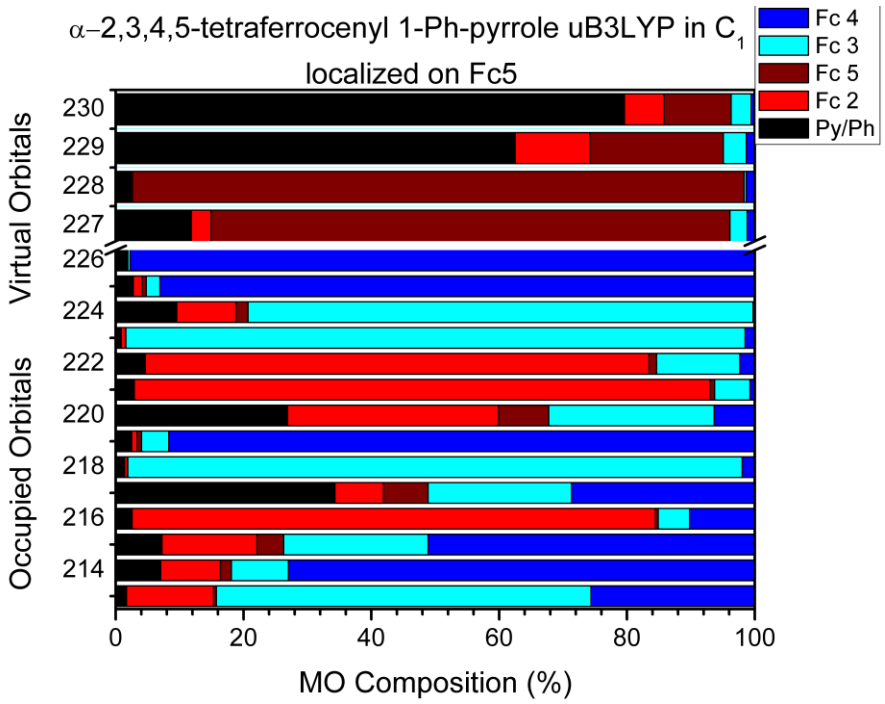

Figure S116. Molecular orbital compositions of B3LYP-(1^+) with the 5-ferrocene charge localized C_1-geometry for the α-HOMO-14 through α-LUMO+3.

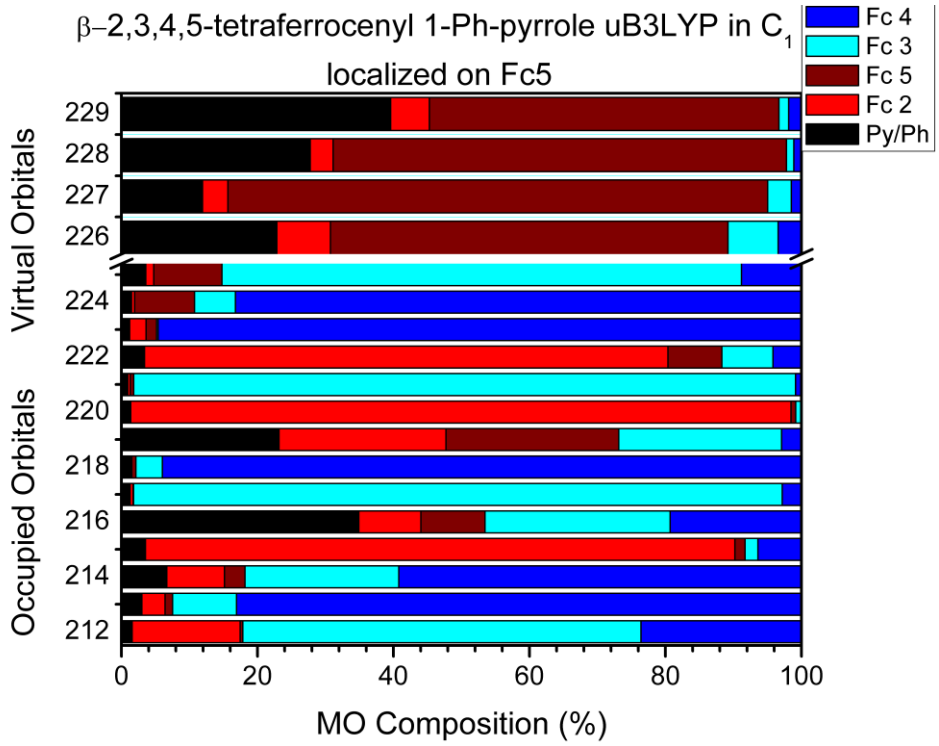

Figure S117. Molecular orbital compositions of B3LYP-(1^+) with the 5-ferrocene charge localized C_1-geometry for the β-HOMO-14 through β-LUMO+3.

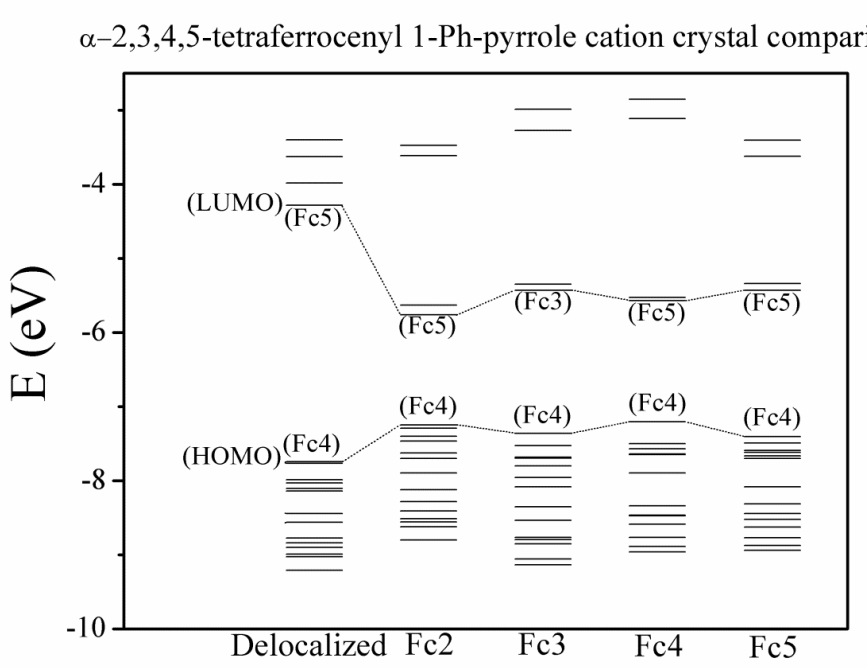

Figure S118. Comparative energetic diagram for the C_1 and lowest energy C_2 optimized geometries of (1^+) for the α-HOMO-14 through α-LUMO+3.

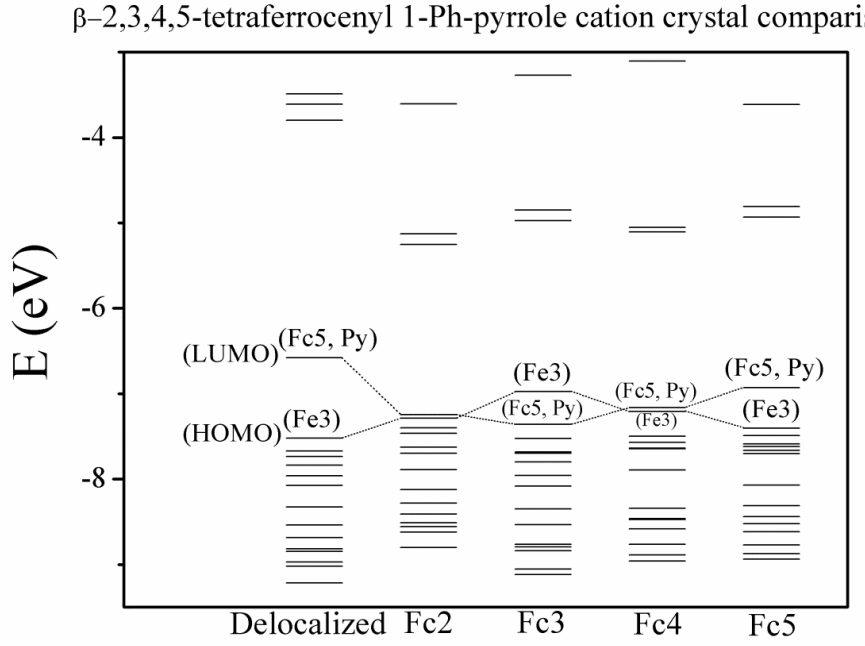

Figure S119. Comparative energetic diagram for the C_1 and lowest energy C_2 optimized geometries of (1^+) for the β-HOMO-14 through β-LUMO+3.

Table S120. Table of $[MoOCl_4]^-$ uBP86 cartesian coordinates

Atom	x	y	z
Mo	0	0	0.24779
Cl	0	2.31257	-0.38404
Cl	-2.31257	0	-0.38404
Cl	2.31257	0	-0.38404
Cl	0	-2.31257	-0.38404
O	0	0	1.96342

Table S121. Table of $[MoOCl_4]^-$ uB3LYP cartesian coordinates

Atom	x	y	z
Mo	0	0	0.24928
Cl	0	2.31473	-0.3831
Cl	-2.31473	0	-0.3831
Cl	2.31473	0	-0.3831
Cl	0	-2.31473	-0.3831
O	0	0	1.94764

Table S122. Table of $[MoOCl_4]^-$ uB3P86 cartesian coordinates

Atom	x	y	z
Mo	0	0	0.25653292
Cl	0	2.28005646	-0.3865095
Cl	-2.28005646	-0	-0.3865095
Cl	2.28005646	0	-0.3865095
Cl	0	-2.28005646	-0.3865095
O	0	0	1.93853292

Table S123. Table of $[MoOCl_4]^-$ uPBE1PBE cartesian coordinates

Atom	x	y	z
Mo	0	0	0.2446
Cl	0	2.28942	-0.37804
Cl	-2.28942	0	-0.37804
Cl	2.28942	0	-0.37804
Cl	0	-2.28942	-0.37804
O	0	0	1.92919

Table S124. Table of $[MoOCl_4]^-$ uBHandHLYP cartesian coordinates

Atom	x	y	z
Mo	0	0	0.246717
Cl	0	2.297591	-0.377784
Cl	-2.297591	0	-0.377784
Cl	2.297591	0	-0.377784
Cl	0	-2.297591	-0.377784
O	0	0	1.9159

Table S125. Table of $[MoOCl_4]^-$ uBHandH cartesian coordinates

Atom	x	y	z
Mo	0	0	0.245014
Cl	0	2.261018	-0.374777
Cl	-2.261018	0	-0.374777
Cl	2.261018	0	-0.374777
Cl	0	-2.261018	-0.374777
O	0	0	1.903232

Table S126. Table of $[MoOCl_4]^-$ uMP2 cartesian coordinates

Atom	x	y	z
Mo	0	0	0.280818
Cl	0	2.277199	-0.399155
Cl	-2.277199	0	-0.399155
Cl	2.277199	0	-0.399155
Cl	0	-2.277199	-0.399155
O	0	0	1.918525

Table S127. Table of C_2-BP86 optimized (4) cartesian coordinates

Atom	x	y	z
C	0.010116	-1.126849	2.522657
C	0.001188	-0.724617	1.18828
C	-0.001188	0.724617	1.18828
C	-0.010116	1.126849	2.522657
C	0	-1.632798	0.031337
Fe	-1.272989	-3.224675	-0.391707
C	0	1.632798	0.031337
Fe	1.272989	3.224675	-0.391707

C	-1.932255	-4.516003	1.066902
H	-1.326397	-4.928285	1.877345
C	-2.106117	-5.10096	-0.235747
H	-1.654482	-6.031539	-0.587411
C	-2.958626	-4.232613	-1.001367
H	-3.265876	-4.386671	-2.038444
C	-3.312248	-3.111683	-0.17247
H	-3.933288	-2.2633	-0.469103
C	0.508413	-3.433674	-1.380483
H	0.921856	-4.372152	-1.757814
C	-0.364892	-2.542973	-2.095902
H	-0.740043	-2.687559	-3.111858
C	0.364892	2.542973	-2.095902
H	0.740043	2.687559	-3.111858
C	-0.508413	3.433674	-1.380483
H	-0.921856	4.372152	-1.757814
C	2.106117	5.10096	-0.235747
H	1.654482	6.031539	-0.587411
C	2.958626	4.232613	-1.001367
H	3.265876	4.386671	-2.038444
C	3.312248	3.111683	-0.17247
H	3.933288	2.2633	-0.469103
C	1.932255	4.516003	1.066902
H	1.326397	4.928285	1.877345
C	2.677792	3.286764	1.105011
H	2.723278	2.584878	1.941331
C	-0.727718	2.879446	-0.073661
H	-1.35287	3.311498	0.711729
C	0.687257	1.445041	-1.226554
H	1.34754	0.609228	-1.465457
C	-0.687257	-1.445041	-1.226554
H	-1.34754	-0.609228	-1.465457
C	-2.677792	-3.286764	1.105011
H	-2.723278	-2.584878	1.941331
C	0.727718	-2.879446	-0.073661
H	1.35287	-3.311498	0.711729
N	0	0	3.312823
H	0.017714	2.126038	2.956239
H	-0.017714	-2.126038	2.956239
H	0	0	4.329829

Table S128. Table of C_2-B3LYP optimized (4) cartesian coordinates

Atom	x	y	z
C	-0.002648	1.119948	2.461846
C	0.002365	0.72135	1.138353
C	-0.002365	-0.72135	1.138353
C	0.002648	-1.119948	2.461846
C	0	1.624289	-0.022183
Fe	1.239974	3.285421	-0.383798
C	0	-1.624289	-0.022183
Fe	-1.239974	-3.285421	-0.383798
C	1.836955	4.561866	1.146958
H	1.206306	4.885234	1.966818
C	1.969641	5.217257	-0.113096
H	1.456747	6.121617	-0.41802
C	2.876699	4.458657	-0.90968
H	3.172155	4.684308	-1.927389
C	3.304846	3.3353	-0.14232
H	3.980528	2.556498	-0.474741
C	-0.53695	3.380355	-1.446078
H	-0.97427	4.291354	-1.837147
C	0.393583	2.536482	-2.1207
H	0.795106	2.695116	-3.114481
C	-0.393583	-2.536482	-2.1207
H	-0.795106	-2.695116	-3.114481
C	0.53695	-3.380355	-1.446078
H	0.97427	-4.291354	-1.837147
C	-1.969641	-5.217257	-0.113096
H	-1.456747	-6.121617	-0.41802
C	-2.876699	-4.458657	-0.90968
H	-3.172155	-4.684308	-1.927389
C	-3.304846	-3.3353	-0.14232
H	-3.980528	-2.556498	-0.474741
C	-1.836955	-4.561866	1.146958
H	-1.206306	-4.885234	1.966818
C	-2.661491	-3.398333	1.127991
H	-2.753767	-2.667233	1.922225
C	0.776134	-2.822689	-0.156818
H	1.440179	-3.224588	0.599525
C	-0.730227	-1.464347	-1.24405
H	-1.427535	-0.663949	-1.456112
C	0.730227	1.464347	-1.24405

H	1.427535	0.663949	-1.456112
C	2.661491	3.398333	1.127991
H	2.753767	2.667233	1.922225
C	-0.776134	2.822689	-0.156818
H	-1.440179	3.224588	0.599525
N	0	0	3.250474
H	-0.024671	-2.111999	2.890675
H	0.024671	2.111999	2.890675
H	0	0	4.258781

Table S129. Table of C_2-PBE1PBE optimized (4) cartesian coordinates

Atom	x	y	z
C	0.00204	1.115224	2.464225
C	0.004392	0.71731	1.143963
C	-0.004392	-0.71731	1.143963
C	-0.00204	-1.115224	2.464225
C	0	1.613914	-0.014384
Fe	1.236157	3.227613	-0.384293
C	0	-1.613914	-0.014384
Fe	-1.236157	-3.227613	-0.384293
C	1.840606	4.447539	1.145044
H	1.218281	4.762851	1.97474
C	1.968618	5.120759	-0.102613
H	1.459758	6.033571	-0.38935
C	2.853519	4.364227	-0.920201
H	3.134847	4.598638	-1.940197
C	3.272203	3.224204	-0.178358
H	3.92557	2.436509	-0.534536
C	-0.513795	3.378709	-1.425025
H	-0.93073	4.303047	-1.807626
C	0.395712	2.522536	-2.106598
H	0.800771	2.682113	-3.099051
C	-0.395712	-2.522536	-2.106598
H	-0.800771	-2.682113	-3.099051
C	0.513795	-3.378709	-1.425025
H	0.93073	-4.303047	-1.807626
C	-1.968618	-5.120759	-0.102613
H	-1.459758	-6.033571	-0.38935
C	-2.853519	-4.364227	-0.920201
H	-3.134847	-4.598638	-1.940197
C	-3.272203	-3.224204	-0.178358

H	-3.92557	-2.436509	-0.534536
C	-1.840606	-4.447539	1.145044
H	-1.218281	-4.762851	1.97474
C	-2.645497	-3.275044	1.097336
H	-2.729223	-2.525212	1.875638
C	0.756232	-2.821418	-0.139702
H	1.402811	-3.235345	0.625712
C	-0.717464	-1.443213	-1.238189
H	-1.404885	-0.63394	-1.452514
C	0.717464	1.443213	-1.238189
H	1.404885	0.63394	-1.452514
C	2.645497	3.275044	1.097336
H	2.729223	2.525212	1.875638
C	-0.756232	2.821418	-0.139702
H	-1.402811	3.235345	0.625712
N	0	0	3.247694
H	-0.030915	-2.108353	2.891832
H	0.030915	2.108353	2.891832
H	0	0	4.254135

Table S130. Table of C_2-BP86 optimized (5) cartesian coordinates

Atom	x	y	z
C	-0.49032022	1.03241951	1.02346281
C	-0.30550584	0.63949166	2.35416081
C	0.30550584	-0.63949166	2.35416081
C	0.49032022	-1.03241951	1.02346281
C	-1.06739606	2.23801539	0.45395981
C	-1.47361823	3.41448983	1.19060081
H	-1.35615826	3.55958778	2.26675381
C	-2.05146421	4.35561698	0.27293881
H	-2.44771417	5.34038546	0.53101881
C	-1.98823723	3.78762102	-1.04496519
H	-2.33210012	4.25887442	-1.96855719
C	-1.37342429	2.49358877	-0.93905319
H	-1.19132815	1.81588977	-1.77788619
C	1.91093217	3.67350123	0.04548981
H	2.35819607	2.78931018	0.50578781
C	0.89424851	5.74902478	-0.22847819
H	0.44953831	6.7239557	-0.01577419
C	0.9965426	5.13175398	-1.52220219
H	0.64268805	5.55420942	-2.46548619

C	1.62341328	3.84812806	-1.35218419
H	1.8331932	3.12775696	-2.14639219
C	1.45694217	4.84655363	0.74021681
H	1.51300873	5.01527123	1.81802381
C	1.06739606	-2.23801539	0.45395981
C	1.47361823	-3.41448983	1.19060081
H	1.35615826	-3.55958778	2.26675381
C	2.05146421	-4.35561698	0.27293881
H	2.44771417	-5.34038546	0.53101881
C	1.98823723	-3.78762102	-1.04496519
H	2.33210012	-4.25887442	-1.96855719
C	1.37342429	-2.49358877	-0.93905319
H	1.19132815	-1.81588977	-1.77788619
C	-1.91093217	-3.67350123	0.04548981
H	-2.35819607	-2.78931018	0.50578781
C	-1.45694217	-4.84655363	0.74021681
H	-1.51300873	-5.01527123	1.81802381
C	-0.89424851	-5.74902478	-0.22847819
H	-0.44953831	-6.7239557	-0.01577419
C	-0.9965426	-5.13175398	-1.52220219
H	-0.64268805	-5.55420942	-2.46548619
C	-1.62341328	-3.84812806	-1.35218419
H	-1.8331932	-3.12775696	-2.14639219
Fe	-0.10897279	3.95176478	-0.24573419
Fe	0.10897279	-3.95176478	-0.24573419
N	0	0	0.23916381
H	-0.5895117	1.22500946	3.22978181
H	0.5895117	-1.22500946	3.22978181
H	0	0	-0.77787019

Table S131. Table of C_2-B3LYP optimized (5) cartesian coordinates

Atom	x	y	z
C	-0.49149155	1.02380564	1.17316098
C	-0.30752969	0.63768836	2.49137398
C	0.30752969	-0.63768836	2.49137398
C	0.49149155	-1.02380564	1.17316098
C	-1.08408363	2.22502669	0.60774998
C	-1.37122154	3.43437436	1.32062798
H	-1.1346235	3.6204232	2.36105698
C	-2.00215444	4.34953282	0.43004598
H	-2.32997169	5.35199748	0.67723098

C	-2.09439766	3.72747656	-0.84802302
H	-2.50960013	4.16794967	-1.74649902
C	-1.52478629	2.42516481	-0.74361902
H	-1.45513537	1.70714799	-1.55319502
C	1.93981615	3.49395129	-0.28335902
H	2.39381344	2.57878895	0.07766898
C	1.0264629	5.61240254	-0.34385102
H	0.67356257	6.59108895	-0.04153802
C	0.91659861	5.04887995	-1.64894802
H	0.46666924	5.52377966	-2.51256602
C	1.48065746	3.73969179	-1.61107502
H	1.53943014	3.04923351	-2.44429502
C	1.65840827	4.65123943	0.49949098
H	1.86847861	4.77020093	1.55556298
C	1.08408363	-2.22502669	0.60774998
C	1.37122154	-3.43437436	1.32062798
H	1.1346235	-3.6204232	2.36105698
C	2.00215444	-4.34953282	0.43004598
H	2.32997169	-5.35199748	0.67723098
C	2.09439766	-3.72747656	-0.84802302
H	2.50960013	-4.16794967	-1.74649902
C	1.52478629	-2.42516481	-0.74361902
H	1.45513537	-1.70714799	-1.55319502
C	-1.93981615	-3.49395129	-0.28335902
H	-2.39381344	-2.57878895	0.07766898
C	-1.65840827	-4.65123943	0.49949098
H	-1.86847861	-4.77020093	1.55556298
C	-1.0264629	-5.61240254	-0.34385102
H	-0.67356257	-6.59108895	-0.04153802
C	-0.91659861	-5.04887995	-1.64894802
H	-0.46666924	-5.52377966	-2.51256602
C	-1.48065746	-3.73969179	-1.61107502
H	-1.53943014	-3.04923351	-2.44429502
Fe	-0.10786131	3.86889976	-0.27119602
Fe	0.10786131	-3.86889976	-0.27119602
N	-0	0	0.39008798
H	-0.59771111	1.21475065	3.36014798
H	0.59771111	-1.21475065	3.36014798
H	-0	0	-0.61847002

Table S132. Table of C_2-PBE1PBE optimized (5) cartesian coordinates

Atom	x	y	z
C	-0.46247932	1.02938784	1.36289897
C	-0.28986574	0.64452091	2.67787797
C	0.28986574	-0.64452091	2.67787797
C	0.46247932	-1.02938784	1.36289897
C	-1.03242618	2.23923401	0.79849697
C	-1.10717437	3.50798928	1.45061697
H	-0.70143922	3.73401196	2.42962397
C	-1.76439554	4.42367177	0.58481097
H	-1.95213255	5.47054264	0.79177297
C	-2.08958755	3.73665065	-0.61650403
H	-2.57605848	4.16285657	-1.48595503
C	-1.63797478	2.39424932	-0.48897803
H	-1.74736487	1.62008399	-1.24064603
C	1.8789739	3.10719889	-0.52067203
H	2.28322195	2.1787358	-0.13350003
C	1.16353644	5.29179927	-0.65445603
H	0.93780933	6.31955943	-0.39545803
C	0.8327124	4.64631821	-1.87842903
H	0.31190233	5.09572382	-2.71575303
C	1.27489834	3.29632754	-1.79549403
H	1.15233	2.54116909	-2.56350703
C	1.80957253	4.34055077	0.18399997
H	2.16003722	4.51436783	1.19443997
C	1.03242618	-2.23923401	0.79849697
C	1.10717437	-3.50798928	1.45061697
H	0.70143922	-3.73401196	2.42962397
C	1.76439554	-4.42367177	0.58481097
H	1.95213255	-5.47054264	0.79177297
C	2.08958755	-3.73665065	-0.61650403
H	2.57605848	-4.16285657	-1.48595503
C	1.63797478	-2.39424932	-0.48897803
H	1.74736487	-1.62008399	-1.24064603
C	-1.8789739	-3.10719889	-0.52067203
H	-2.28322195	-2.1787358	-0.13350003
C	-1.80957253	-4.34055077	0.18399997
H	-2.16003722	-4.51436783	1.19443997
C	-1.16353644	-5.29179927	-0.65445603
H	-0.93780933	-6.31955943	-0.39545803
C	-0.8327124	-4.64631821	-1.87842903

H	-0.31190233	-5.09572382	-2.71575303
C	-1.27489834	-3.29632754	-1.79549403
H	-1.15233	-2.54116909	-2.56350703
Fe	-0.07056575	3.69579839	-0.30313003
Fe	0.07056575	-3.69579839	-0.30313003
N	-0	0	0.58389597
H	-0.57265351	1.23002218	3.54357897
H	0.57265351	-1.23002218	3.54357897
H	-0	0	-0.42372803

Table S133. Table of C_2-BP86 optimized (6) cartesian coordinates

Atom	x	y	z
C	0.290127	1.109497	0.486782
C	0.196281	0.700837	-0.857015
C	-0.196281	-0.700837	-0.857015
C	-0.290127	-1.109497	0.486782
C	0.713817	2.332483	1.168472
C	0.46382	3.708012	0.807998
H	-0.12163	4.042854	-0.047075
C	1.101597	4.562407	1.770916
H	1.082071	5.654749	1.768869
C	1.733719	3.729939	2.756143
H	2.292993	4.073237	3.629658
C	1.487033	2.362357	2.398038
H	1.85915	1.487502	2.937539
C	-2.139808	2.503593	2.929615
H	-2.536398	1.679669	2.331635
C	-1.577794	4.646874	3.637413
H	-1.4738	5.733661	3.677448
C	-1.024708	3.711643	4.577722
H	-0.430876	3.962152	5.459749
C	-1.371956	2.386448	4.139955
H	-1.102854	1.457182	4.648483
C	-2.265281	3.900541	2.618319
H	-2.777648	4.319992	1.749618
C	-0.713817	-2.332483	1.168472
C	-0.46382	-3.708012	0.807998
H	0.12163	-4.042854	-0.047075
C	-1.101597	-4.562407	1.770916
H	-1.082071	-5.654749	1.768869
C	-1.733719	-3.729939	2.756143

H	-2.292993	-4.073237	3.629658
C	-1.487033	-2.362357	2.398038
H	-1.85915	-1.487502	2.937539
C	2.139808	-2.503593	2.929615
H	2.536398	-1.679669	2.331635
C	2.265281	-3.900541	2.618319
H	2.777648	-4.319992	1.749618
C	1.577794	-4.646874	3.637413
H	1.4738	-5.733661	3.677448
C	1.024708	-3.711643	4.577722
H	0.430876	-3.962152	5.459749
C	1.371956	-2.386448	4.139955
H	1.102854	-1.457182	4.648483
Fe	-0.282483	3.362888	2.687501
Fe	0.282483	-3.362888	2.687501
C	0.50252	1.446399	-2.093902
Fe	2.058944	2.707507	-2.696562
C	-0.50252	-1.446399	-2.093902
Fe	-2.058944	-2.707507	-2.696562
C	2.861057	4.277278	-1.625263
H	2.298449	5.026947	-1.065799
C	3.243414	4.362646	-3.007765
H	3.016969	5.186305	-3.689133
C	3.953204	3.158709	-3.345822
H	4.35556	2.905403	-4.32956
C	4.009592	2.330716	-2.170781
H	4.465808	1.34016	-2.105848
C	0.413998	2.943834	-3.899479
H	0.191236	3.826111	-4.504914
C	1.186579	1.804391	-4.310975
H	1.666423	1.667616	-5.28307
C	-1.186579	-1.804391	-4.310975
H	-1.666423	-1.667616	-5.28307
C	-0.413998	-2.943834	-3.899479
H	-0.191236	-3.826111	-4.504914
C	-3.243414	-4.362646	-3.007765
H	-3.016969	-5.186305	-3.689133
C	-3.953204	-3.158709	-3.345822
H	-4.35556	-2.905403	-4.32956
C	-4.009592	-2.330716	-2.170781
H	-4.465808	-1.34016	-2.105848
C	-2.861057	-4.277278	-1.625263

H	-2.298449	-5.026947	-1.065799
C	-3.335005	-3.022773	-1.107756
H	-3.179305	-2.65257	-0.092644
C	0	-2.728077	-2.541026
H	0.630401	-3.403073	-1.959297
C	-1.251922	-0.895537	-3.203601
H	-1.771797	0.064369	-3.191286
C	1.251922	0.895537	-3.203601
H	1.771797	-0.064369	-3.191286
C	3.335005	3.022773	-1.107756
H	3.179305	2.65257	-0.092644
C	0	2.728077	-2.541026
H	-0.630401	3.403073	-1.959297
N	0	0	1.255934
H	0	0	2.275018

Table S134. Table of C_2-B3LYP optimized (6) cartesian coordinates

Atom	x	y	z
C	0.393708	1.069086	0.444159
C	0.264323	0.676172	-0.886822
C	-0.264323	-0.676172	-0.886822
C	-0.393708	-1.069086	0.444159
C	0.915848	2.255538	1.124527
C	0.736226	3.634724	0.788568
H	0.144948	4.009698	-0.033753
C	1.44677	4.432891	1.731277
H	1.48811	5.51545	1.742625
C	2.059726	3.559895	2.675569
H	2.659099	3.857027	3.527752
C	1.728526	2.224087	2.311677
H	2.059587	1.329452	2.826127
C	-1.919472	2.567859	3.018964
H	-2.379656	1.786277	2.426087
C	-1.217073	4.643367	3.740085
H	-1.05069	5.712488	3.796143
C	-0.692507	3.666981	4.636205
H	-0.061701	3.863645	5.494768
C	-1.126579	2.383661	4.19044
H	-0.893664	1.437492	4.665344
C	-1.974726	3.964421	2.740889
H	-2.485372	4.426029	1.904446

C	-0.915848	-2.255538	1.124527
C	-0.736226	-3.634724	0.788568
H	-0.144948	-4.009698	-0.033753
C	-1.44677	-4.432891	1.731277
H	-1.48811	-5.51545	1.742625
C	-2.059726	-3.559895	2.675569
H	-2.659099	-3.857027	3.527752
C	-1.728526	-2.224087	2.311677
H	-2.059587	-1.329452	2.826127
C	1.919472	-2.567859	3.018964
H	2.379656	-1.786277	2.426087
C	1.974726	-3.964421	2.740889
H	2.485372	-4.426029	1.904446
C	1.217073	-4.643367	3.740085
H	1.05069	-5.712488	3.796143
C	0.692507	-3.666981	4.636205
H	0.061701	-3.863645	5.494768
C	1.126579	-2.383661	4.19044
H	0.893664	-1.437492	4.665344
Fe	0	3.313372	2.702638
Fe	0	-3.313372	2.702638
C	0.638186	1.391255	-2.1234
Fe	2.318325	2.548749	-2.705014
C	-0.638186	-1.391255	-2.1234
Fe	-2.318325	-2.548749	-2.705014
C	3.256737	4.087651	-1.653896
H	2.744212	4.877668	-1.119943
C	3.65015	4.115562	-3.023579
H	3.484391	4.929829	-3.719047
C	4.273139	2.868974	-3.327421
H	4.660266	2.569388	-4.294061
C	4.264565	2.072431	-2.144244
H	4.645751	1.06224	-2.054364
C	0.668315	2.870586	-3.919152
H	0.516114	3.757621	-4.522872
C	1.355294	1.687199	-4.317469
H	1.825991	1.513166	-5.277803
C	-1.355294	-1.687199	-4.317469
H	-1.825991	-1.513166	-5.277803
C	-0.668315	-2.870586	-3.919152
H	-0.516114	-3.757621	-4.522872
C	-3.65015	-4.115562	-3.023579

H	-3.484391	-4.929829	-3.719047
C	-4.273139	-2.868974	-3.327421
H	-4.660266	-2.569388	-4.294061
C	-4.264565	-2.072431	-2.144244
H	-4.645751	-1.06224	-2.054364
C	-3.256737	-4.087651	-1.653896
H	-2.744212	-4.877668	-1.119943
C	-3.636731	-2.825758	-1.110625
H	-3.455504	-2.492719	-0.096997
C	-0.233394	-2.69092	-2.574202
H	0.341775	-3.407094	-2.002237
C	-1.34924	-0.789158	-3.214382
H	-1.794567	0.197362	-3.19541
C	1.34924	0.789158	-3.214382
H	1.794567	-0.197362	-3.19541
C	3.636731	2.825758	-1.110625
H	3.455504	2.492719	-0.096997
C	0.233394	2.69092	-2.574202
H	-0.341775	3.407094	-2.002237
N	0	0	1.211799
H	0	0	2.221307

Table S135. Table of C_2-PBE1PBE optimized (6) cartesian coordinates

Atom	x	y	z
C	0.328446	1.082694	0.396234
C	0.218623	0.687586	-0.930367
C	-0.218623	-0.687586	-0.930367
C	-0.328446	-1.082694	0.396234
C	0.81614	2.282854	1.069074
C	0.499542	3.649475	0.810785
H	-0.203051	4.003719	0.068911
C	1.228675	4.464128	1.720322
H	1.180697	5.545008	1.783371
C	1.992923	3.610745	2.562466
H	2.637659	3.924516	3.374937
C	1.736075	2.270201	2.169899
H	2.17549	1.382516	2.611762
C	-1.820292	2.329125	3.134523
H	-2.299171	1.586441	2.506483
C	-1.13391	4.354339	3.986119
H	-0.998382	5.420418	4.125374

C	-0.487679	3.327024	4.727221
H	0.223617	3.471439	5.531756
C	-0.912353	2.074777	4.201115
H	-0.594338	1.100601	4.555757
C	-1.956893	3.738031	3.00269
H	-2.559877	4.251167	2.262962
C	-0.81614	-2.282854	1.069074
C	-0.499542	-3.649475	0.810785
H	0.203051	-4.003719	0.068911
C	-1.228675	-4.464128	1.720322
H	-1.180697	-5.545008	1.783371
C	-1.992923	-3.610745	2.562466
H	-2.637659	-3.924516	3.374937
C	-1.736075	-2.270201	2.169899
H	-2.17549	-1.382516	2.611762
C	1.820292	-2.329125	3.134523
H	2.299171	-1.586441	2.506483
C	1.956893	-3.738031	3.00269
H	2.559877	-4.251167	2.262962
C	1.13391	-4.354339	3.986119
H	0.998382	-5.420418	4.125374
C	0.487679	-3.327024	4.727221
H	-0.223617	-3.471439	5.531756
C	0.912353	-2.074777	4.201115
H	0.594338	-1.100601	4.555757
Fe	0	3.189877	2.74113
Fe	0	-3.189877	2.74113
C	0.51715	1.436743	-2.158796
Fe	2.066818	2.697883	-2.740718
C	-0.51715	-1.436743	-2.158796
Fe	-2.066818	-2.697883	-2.740718
C	2.8749	4.241198	-1.653878
H	2.308386	4.9643	-1.080393
C	3.237907	4.354786	-3.024271
H	2.992206	5.179125	-3.683723
C	3.945237	3.175385	-3.389711
H	4.328303	2.942688	-4.376481
C	4.019574	2.334461	-2.243756
H	4.471788	1.350377	-2.205257
C	0.415029	2.947532	-3.916184
H	0.201096	3.83823	-4.495809
C	1.171937	1.82413	-4.349827

H	1.645415	1.707328	-5.317696
C	-1.171937	-1.82413	-4.349827
H	-1.645415	-1.707328	-5.317696
C	-0.415029	-2.947532	-3.916184
H	-0.201096	-3.83823	-4.495809
C	-3.237907	-4.354786	-3.024271
H	-2.992206	-5.179125	-3.683723
C	-3.945237	-3.175385	-3.389711
H	-4.328303	-2.942688	-4.376481
C	-4.019574	-2.334461	-2.243756
H	-4.471788	-1.350377	-2.205257
C	-2.8749	-4.241198	-1.653878
H	-2.308386	-4.9643	-1.080393
C	-3.358066	-2.993297	-1.171379
H	-3.213985	-2.60412	-0.171323
C	-0.0157	-2.711112	-2.572175
H	0.588309	-3.377197	-1.969129
C	-1.243351	-0.904872	-3.270564
H	-1.757695	0.048504	-3.277391
C	1.243351	0.904872	-3.270564
H	1.757695	-0.048504	-3.277391
C	3.358066	2.993297	-1.171379
H	3.213985	2.60412	-0.171323
C	0.0157	2.711112	-2.572175
H	-0.588309	3.377197	-1.969129
N	0	0	1.160836
H	0	0	2.170002

Table S136. Table of C_2-BP86 optimized (4^+) cartesian coordinates

Atom	x	y	z
C	-0.740054	0.84989	2.51203
C	-0.4708	0.554512	1.175246
C	0.4708	-0.554512	1.175246
C	0.740054	-0.84989	2.51203
C	-1.021952	1.279517	0.029537
Fe	-0.890126	3.377928	-0.377081
C	1.021952	-1.279517	0.029537
Fe	0.890126	-3.377928	-0.377081
C	-1.173533	4.960748	0.960731
H	-1.969179	5.028212	1.706068
C	-1.255899	5.411266	-0.401559

H	-2.120843	5.885526	-0.870273
C	0	5.121429	-1.038142
H	0.259714	5.335459	-2.076985
C	0.853156	4.493527	-0.067213
H	1.870358	4.135762	-0.239982
C	-2.483167	2.507855	-1.327508
H	-3.368669	3.040824	-1.680267
C	-1.275154	2.279205	-2.071057
H	-1.069758	2.619174	-3.088432
C	1.275154	-2.279205	-2.071057
H	1.069758	-2.619174	-3.088432
C	2.483167	-2.507855	-1.327508
H	3.368669	-3.040824	-1.680267
C	1.255899	-5.411266	-0.401559
H	2.120843	-5.885526	-0.870273
C	0	-5.121429	-1.038142
H	-0.259714	-5.335459	-2.076985
C	-0.853156	-4.493527	-0.067213
H	-1.870358	-4.135762	-0.239982
C	1.173533	-4.960748	0.960731
H	1.969179	-5.028212	1.706068
C	-0.128787	-4.401736	1.163081
H	-0.492354	-3.936344	2.082337
C	2.319101	-1.91419	-0.029531
H	3.064772	-1.902662	0.768541
C	0.371629	-1.546301	-1.229978
H	-0.647229	-1.253134	-1.490554
C	-0.371629	1.546301	-1.229978
H	0.647229	1.253134	-1.490554
C	0.128787	4.401736	1.163081
H	0.492354	3.936344	2.082337
C	-2.319101	1.91419	-0.029531
H	-3.064772	1.902662	0.768541
N	0	0	3.294299
H	0	0	4.313461
H	1.365558	-1.624996	2.953051
H	-1.365558	1.624996	2.953051

Table S137. Table of C_2-B3LYP optimized (4^+) cartesian coordinates

Atom	x	y	z
C	-0.021478	1.118376	2.45755
C	-0.010328	0.720819	1.13271
C	0.010328	-0.720819	1.13271
C	0.021478	-1.118376	2.45755
C	0	1.617176	-0.027862
Fe	1.279589	3.306979	-0.375346
C	0	-1.617176	-0.027862
Fe	-1.279589	-3.306979	-0.375346
C	1.848053	4.710648	1.08429
H	1.191936	5.1056	1.850594
C	2.026459	5.251733	-0.222947
H	1.532187	6.128862	-0.622457
C	2.963196	4.428497	-0.913825
H	3.303194	4.566917	-1.932965
C	3.362645	3.381955	-0.0329
H	4.052811	2.580695	-0.267391
C	-0.48675	3.375544	-1.464862
H	-0.916152	4.283766	-1.870029
C	0.453771	2.525639	-2.115793
H	0.875487	2.676057	-3.102182
C	-0.453771	-2.525639	-2.115793
H	-0.875487	-2.676057	-3.102182
C	0.48675	-3.375544	-1.464862
H	0.916152	-4.283766	-1.870029
C	-2.026459	-5.251733	-0.222947
H	-1.532187	-6.128862	-0.622457
C	-2.963196	-4.428497	-0.913825
H	-3.303194	-4.566917	-1.932965
C	-3.362645	-3.381955	-0.0329
H	-4.052811	-2.580695	-0.267391
C	-1.848053	-4.710648	1.08429
H	-1.191936	-5.1056	1.850594
C	-2.675535	-3.558034	1.199078
H	-2.743824	-2.903268	2.05944
C	0.757547	-2.823577	-0.179079
H	1.436698	-3.233344	0.55912
C	-0.765295	-1.456325	-1.227277
H	-1.473088	-0.658965	-1.416718
C	0.765295	1.456325	-1.227277

H	1.473088	0.658965	-1.416718
C	2.675535	3.558034	1.199078
H	2.743824	2.903268	2.05944
C	-0.757547	2.823577	-0.179079
H	-1.436698	3.233344	0.55912
N	0	0	3.242919
H	0	0	4.25294
H	0.00974	-2.108981	2.890396
H	-0.00974	2.108981	2.890396

Table S138. Table of C_2-PBE1PBE optimized (4^+) cartesian coordinates

Atom	x	y	z
C	-0.009631	1.114004	2.485992
C	-0.00376	0.71708	1.164533
C	0.00376	-0.71708	1.164533
C	0.009631	-1.114004	2.485992
C	0	1.604238	0.003722
Fe	1.254633	3.257983	-0.376664
C	0	-1.604238	0.003722
Fe	-1.254633	-3.257983	-0.376664
C	1.810787	4.714689	0.990894
H	1.144892	5.179437	1.708199
C	2.040694	5.159465	-0.340656
H	1.584939	6.021873	-0.812632
C	2.956723	4.258647	-0.951231
H	3.320587	4.313168	-1.970547
C	3.292025	3.259025	0.003775
H	3.949636	2.413811	-0.162146
C	-0.493302	3.350396	-1.43509
H	-0.917468	4.262219	-1.838499
C	0.435505	2.494656	-2.088551
H	0.854298	2.643136	-3.076911
C	-0.435505	-2.494656	-2.088551
H	-0.854298	-2.643136	-3.076911
C	0.493302	-3.350396	-1.43509
H	0.917468	-4.262219	-1.838499
C	-2.040694	-5.159465	-0.340656
H	-1.584939	-6.021873	-0.812632
C	-2.956723	-4.258647	-0.951231
H	-3.320587	-4.313168	-1.970547
C	-3.292025	-3.259025	0.003775

H	-3.949636	-2.413811	-0.162146
C	-1.810787	-4.714689	0.990894
H	-1.144892	-5.179437	1.708199
C	-2.585628	-3.543235	1.20128
H	-2.601293	-2.94101	2.102367
C	0.753504	-2.808712	-0.146059
H	1.417812	-3.227914	0.600629
C	-0.751849	-1.431627	-1.198543
H	-1.460277	-0.633119	-1.385212
C	0.751849	1.431627	-1.198543
H	1.460277	0.633119	-1.385212
C	2.585628	3.543235	1.20128
H	2.601293	2.94101	2.102367
C	-0.753504	2.808712	-0.146059
H	-1.417812	3.227914	0.600629
N	0	0	3.266406
H	0	0	4.274613
H	-0.00726	-2.105568	2.917897
H	0.00726	2.105568	2.917897

Table S139. Table of C_2-BP86 optimized (5^+) cartesian coordinates

Atom	x	y	z
C	0.018379	1.139133	0.665814
C	0.008448	0.699155	2.010875
C	-0.008448	-0.699155	2.010875
C	-0.018379	-1.139133	0.665814
C	0.029849	2.473112	0.122866
C	-0.034691	3.696884	0.89748
H	-0.138724	3.760208	1.982336
C	0	4.806185	-0.008949
H	-0.051919	5.859839	0.272599
C	0.141719	4.29281	-1.340483
H	0.219926	4.884042	-2.255079
C	0.188635	2.861493	-1.264019
H	0.30575	2.193131	-2.120688
C	3.516592	2.755584	0.412398
H	3.577102	1.747195	0.828914
C	3.236477	5.051415	0.229958
H	3.084024	6.10248	0.483825
C	3.387854	4.515012	-1.093957
H	3.37017	5.085725	-2.024833

C	3.554919	3.092144	-0.979033
H	3.688112	2.392753	-1.807106
C	3.308186	3.958734	1.161733
H	3.222323	4.033879	2.247659
C	-0.029849	-2.473112	0.122866
C	0.034691	-3.696884	0.89748
H	0.138724	-3.760208	1.982336
C	0	-4.806185	-0.008949
H	0.051919	-5.859839	0.272599
C	-0.141719	-4.29281	-1.340483
H	-0.219926	-4.884042	-2.255079
C	-0.188635	-2.861493	-1.264019
H	-0.30575	-2.193131	-2.120688
C	-3.516592	-2.755584	0.412398
H	-3.577102	-1.747195	0.828914
C	-3.308186	-3.958734	1.161733
H	-3.222323	-4.033879	2.247659
C	-3.236477	-5.051415	0.229958
H	-3.084024	-6.10248	0.483825
C	-3.387854	-4.515012	-1.093957
H	-3.37017	-5.085725	-2.024833
C	-3.554919	-3.092144	-0.979033
H	-3.688112	-2.392753	-1.807106
Fe	1.728912	3.699362	-0.168974
Fe	-1.728912	-3.699362	-0.168974
N	0	0	-0.119894
H	0	0	-1.138062
H	-0.017814	-1.349314	2.886263
H	0.017814	1.349314	2.886263

Table S140. Table of C_2-B3LYP optimized (5^+) cartesian coordinates

Atom	x	y	z
C	0.014919	1.13344	0.677741
C	0.006001	0.694157	2.017161
C	-0.006001	-0.694157	2.017161
C	-0.014919	-1.13344	0.677741
C	0.026471	2.459741	0.142931
C	-0.017182	3.679299	0.912415
H	-0.099055	3.743535	1.990127
C	0	4.777457	0.013227
H	-0.039032	5.823063	0.292759

C	0.117425	4.26907	-1.310378
H	0.182773	4.857832	-2.21704
C	0.165459	2.850251	-1.238108
H	0.261818	2.187612	-2.090265
C	3.561581	2.707625	0.364871
H	3.61703	1.700429	0.761212
C	3.329014	4.994741	0.223383
H	3.196596	6.035416	0.493329
C	3.453858	4.483227	-1.098728
H	3.434161	5.065678	-2.011859
C	3.593571	3.065975	-1.011151
H	3.703539	2.384872	-1.846253
C	3.391121	3.894642	1.130242
H	3.320145	3.953811	2.209425
C	-0.026471	-2.459741	0.142931
C	0.017182	-3.679299	0.912415
H	0.099055	-3.743535	1.990127
C	0	-4.777457	0.013227
H	0.039032	-5.823063	0.292759
C	-0.117425	-4.26907	-1.310378
H	-0.182773	-4.857832	-2.21704
C	-0.165459	-2.850251	-1.238108
H	-0.261818	-2.187612	-2.090265
C	-3.561581	-2.707625	0.364871
H	-3.61703	-1.700429	0.761212
C	-3.391121	-3.894642	1.130242
H	-3.320145	-3.953811	2.209425
C	-3.329014	-4.994741	0.223383
H	-3.196596	-6.035416	0.493329
C	-3.453858	-4.483227	-1.098728
H	-3.434161	-5.065678	-2.011859
C	-3.593571	-3.065975	-1.011151
H	-3.703539	-2.384872	-1.846253
Fe	1.757337	3.670415	-0.172634
Fe	-1.757337	-3.670415	-0.172634
N	0	0	-0.103898
H	0	0	-1.113342
H	0.012874	1.339424	2.885733
H	-0.012874	-1.339424	2.885733

Table S141. Table of C_2-PBE1PBE optimized (5^+) cartesian coordinates

Atom	x	y	z
C	-0.006663	2.448996	0.11641
C	-0.046314	3.661623	0.890886
H	-0.136326	3.72157	1.968609
C	0	4.76019	-0.001335
H	-0.019943	5.805332	0.282984
C	0.129529	4.257446	-1.322751
H	0.225287	4.850198	-2.224373
C	0.155472	2.84099	-1.258307
H	0.262285	2.181536	-2.112183
C	3.441383	2.625296	0.389101
H	3.463881	1.615071	0.782263
C	3.254598	4.911735	0.253487
H	3.129778	5.953266	0.524936
C	3.388852	4.40397	-1.065635
H	3.385725	4.989804	-1.977169
C	3.500409	2.98707	-0.982071
H	3.604451	2.306682	-1.818818
C	3.282297	3.809947	1.154979
H	3.190619	3.866254	2.233013
Fe	1.703499	3.62214	-0.167248
C	0.006663	-2.448996	0.11641
C	0.046314	-3.661623	0.890886
H	0.136326	-3.72157	1.968609
C	0	-4.76019	-0.001335
H	0.019943	-5.805332	0.282984
C	-0.129529	-4.257446	-1.322751
H	-0.225287	-4.850198	-2.224373
C	-0.155472	-2.84099	-1.258307
H	-0.262285	-2.181536	-2.112183
C	-3.441383	-2.625296	0.389101
H	-3.463881	-1.615071	0.782263
C	-3.282297	-3.809947	1.154979
H	-3.190619	-3.866254	2.233013
C	-3.254598	-4.911735	0.253487
H	-3.129778	-5.953266	0.524936
C	-3.388852	-4.40397	-1.065635
H	-3.385725	-4.989804	-1.977169
C	-3.500409	-2.98707	-0.982071
H	-3.604451	-2.306682	-1.818818

Fe	-1.703499	-3.62214	-0.167248
N	0	0	-0.128876
H	0	0	-1.13692
H	0.00855	-1.339208	2.853513
H	-0.00855	1.339208	2.853513
C	-0.00316	1.126876	0.647752
C	-0.005112	0.691315	1.986684
C	0.005112	-0.691315	1.986684
C	0.00316	-1.126876	0.647752

Table S142. Table of C_2-BP86 optimized (6^+) cartesian coordinates

Atom	x	y	z
C	-0.715756	0.896144	0.480477
C	-0.444316	0.572394	-0.870231
C	0.444316	-0.572394	-0.870231
C	0.715756	-0.896144	0.480477
C	-1.427863	1.977621	1.150385
C	-2.668056	2.618947	0.77925
H	-3.291761	2.362156	-0.075436
C	-2.967601	3.635909	1.74672
H	-3.846823	4.283897	1.74148
C	-1.935855	3.623704	2.743727
H	-1.878642	4.27087	3.621536
C	-0.998809	2.594523	2.397104
H	-0.081846	2.362048	2.944522
C	-3.285909	-0.208383	3.010618
H	-2.813049	-1.052454	2.502477
C	-4.735999	1.538223	3.493723
H	-5.561011	2.250829	3.429655
C	-3.721197	1.512872	4.509709
H	-3.641496	2.198841	5.355546
C	-2.821572	0.43248	4.209429
H	-1.948623	0.147792	4.801391
C	-4.464774	0.476131	2.565861
H	-5.047361	0.23758	1.673546
C	1.427863	-1.977621	1.150385
C	2.668056	-2.618947	0.77925
H	3.291761	-2.362156	-0.075436
C	2.967601	-3.635909	1.74672
H	3.846823	-4.283897	1.74148
C	1.935855	-3.623704	2.743727

H	1.878642	-4.27087	3.621536
C	0.998809	-2.594523	2.397104
H	0.081846	-2.362048	2.944522
C	3.285909	0.208383	3.010618
H	2.813049	1.052454	2.502477
C	4.464774	-0.476131	2.565861
H	5.047361	-0.23758	1.673546
C	4.735999	-1.538223	3.493723
H	5.561011	-2.250829	3.429655
C	3.721197	-1.512872	4.509709
H	3.641496	-2.198841	5.355546
C	2.821572	-0.43248	4.209429
H	1.948623	-0.147792	4.801391
Fe	-2.868319	1.79503	2.65439
Fe	2.868319	-1.79503	2.65439
C	-0.833675	1.2759	-2.102419
Fe	-0.82316	3.320026	-2.661273
C	0.833675	-1.2759	-2.102419
Fe	0.82316	-3.320026	-2.661273
C	-1.54178	4.949031	-1.58397
H	-2.474482	4.976544	-1.018091
C	-1.38306	5.281329	-2.97208
H	-2.174088	5.610084	-3.64952
C	0	5.092573	-3.315257
H	0.44423	5.248951	-4.300689
C	0.691702	4.643904	-2.138415
H	1.753507	4.396779	-2.074121
C	-2.034128	2.205821	-3.888076
H	-2.856016	2.600633	-4.489693
C	-0.661959	2.088659	-4.295184
H	-0.246839	2.392016	-5.258743
C	0.661959	-2.088659	-4.295184
H	0.246839	-2.392016	-5.258743
C	2.034128	-2.205821	-3.888076
H	2.856016	-2.600633	-4.489693
C	1.38306	-5.281329	-2.97208
H	2.174088	-5.610084	-3.64952
C	0	-5.092573	-3.315257
H	-0.44423	-5.248951	-4.300689
C	-0.691702	-4.643904	-2.138415
H	-1.753507	-4.396779	-2.074121
C	1.54178	-4.949031	-1.58397

H	2.474482	-4.976544	-1.018091
C	0.260725	-4.559959	-1.071678
H	0.058567	-4.219206	-0.054069
C	2.138086	-1.720185	-2.540526
H	3.065206	-1.646725	-1.970784
C	-0.07518	-1.538284	-3.196671
H	-1.1492	-1.343779	-3.178557
C	0.07518	1.538284	-3.196671
H	1.1492	1.343779	-3.178557
C	-0.260725	4.559959	-1.071678
H	-0.058567	4.219206	-0.054069
C	-2.138086	1.720185	-2.540526
H	-3.065206	1.646725	-1.970784
N	0	0	1.248417
H	0	0	2.26811

Table S143. Table of C_2-B3LYP optimized (6^+) cartesian coordinates

Atom	x	y	z
C	0.028241	1.141215	0.830393
C	0.060206	0.713684	-0.532408
C	-0.060206	-0.713684	-0.532408
C	-0.028241	-1.141215	0.830393
C	0.036139	2.387232	1.554111
C	0.018439	3.740891	1.05744
H	0.013275	4.028163	0.020596
C	0.03568	4.634414	2.159161
H	0.02894	5.715709	2.097267
C	0.026662	3.867899	3.357282
H	0.013103	4.26062	4.366363
C	0	2.495332	3.002014
H	-0.01983	1.677301	3.712406
C	-3.366222	2.415223	1.569682
H	-3.348029	1.501658	0.986809
C	-3.347598	4.64738	2.145886
H	-3.330339	5.728606	2.082388
C	-3.349496	3.883623	3.348037
H	-3.333209	4.282218	4.355041
C	-3.359719	2.501176	2.991746
H	-3.353212	1.666648	3.682308
C	-3.354311	3.739721	1.044491
H	-3.346076	4.012693	-0.003668

C	-0.036139	-2.387232	1.554111
C	-0.018439	-3.740891	1.05744
H	-0.013275	-4.028163	0.020596
C	-0.03568	-4.634414	2.159161
H	-0.02894	-5.715709	2.097267
C	-0.026662	-3.867899	3.357282
H	-0.013103	-4.26062	4.366363
C	0	-2.495332	3.002014
H	0.01983	-1.677301	3.712406
C	3.366222	-2.415223	1.569682
H	3.348029	-1.501658	0.986809
C	3.354311	-3.739721	1.044491
H	3.346076	-4.012693	-0.003668
C	3.347598	-4.64738	2.145886
H	3.330339	-5.728606	2.082388
C	3.349496	-3.883623	3.348037
H	3.333209	-4.282218	4.355041
C	3.359719	-2.501176	2.991746
H	3.353212	-1.666648	3.682308
Fe	-1.662262	3.428613	2.219107
Fe	1.662262	-3.428613	2.219107
C	0.263432	1.491543	-1.765648
Fe	1.773789	2.880912	-2.306551
C	-0.263432	-1.491543	-1.765648
Fe	-1.773789	-2.880912	-2.306551
C	2.466935	4.435138	-1.099172
H	1.863448	5.10473	-0.500517
C	2.861138	4.654609	-2.450087
H	2.595924	5.506487	-3.063981
C	3.662818	3.551115	-2.860208
H	4.110422	3.418144	-3.837408
C	3.765075	2.647662	-1.76129
H	4.306413	1.709702	-1.763699
C	0.085918	3.030411	-3.507103
H	-0.202631	3.896248	-4.090188
C	0.921823	1.966895	-3.949665
H	1.390577	1.883657	-4.922281
C	-0.921823	-1.966895	-3.949665
H	-1.390577	-1.883657	-4.922281
C	-0.085918	-3.030411	-3.507103
H	0.202631	-3.896248	-4.090188
C	-2.861138	-4.654609	-2.450087

H	-2.595924	-5.506487	-3.063981
C	-3.662818	-3.551115	-2.860208
H	-4.110422	-3.418144	-3.837408
C	-3.765075	-2.647662	-1.76129
H	-4.306413	-1.709702	-1.763699
C	-2.466935	-4.435138	-1.099172
H	-1.863448	-5.10473	-0.500517
C	-3.022588	-3.192441	-0.673529
H	-2.901314	-2.737502	0.301636
C	0.306198	-2.752337	-2.167814
H	0.980779	-3.360723	-1.584538
C	-1.056684	-1.040831	-2.879376
H	-1.642337	-0.131932	-2.91218
C	1.056684	1.040831	-2.879376
H	1.642337	0.131932	-2.91218
C	3.022588	3.192441	-0.673529
H	2.901314	2.737502	0.301636
C	-0.306198	2.752337	-2.167814
H	-0.980779	3.360723	-1.584538
N	0	0	1.589919
H	0	0	2.597589

Table S144. Table of C_2-PBE1PBE optimized (6^+) cartesian coordinates

Atom	x	y	z
C	-0.214718	-1.149099	0.799991
C	-0.153255	-0.691147	-0.583496
C	0.153255	0.691147	-0.583496
C	0.214718	1.149099	0.799991
C	-0.425089	-2.37973	1.447323
C	-0.410569	-3.775237	0.968106
H	-0.357997	-4.05599	-0.077377
C	-1.01969	-4.652615	1.971967
H	-1.534559	-5.590633	1.776993
C	-0.964126	-3.927723	3.218189
H	-1.435686	-4.195538	4.160839
C	-0.321754	-2.647715	2.902931
H	-0.197759	-1.882013	3.665408
C	2.802272	-4.119533	2.310371
H	3.372023	-3.329678	1.814015
C	1.566918	-6.05647	2.675417
H	1.135449	-7.047693	2.534486

C	1.625951	-5.320684	3.918958
H	1.253949	-5.661277	4.885253
C	2.395644	-4.128829	3.683419
H	2.628878	-3.360856	4.423954
C	2.300766	-5.309026	1.691265
H	2.440657	-5.592499	0.64548
C	0.425089	2.37973	1.447323
C	0.410569	3.775237	0.968106
H	0.357997	4.05599	-0.077377
C	1.01969	4.652615	1.971967
H	1.534559	5.590633	1.776993
C	0.964126	3.927723	3.218189
H	1.435686	4.195538	4.160839
C	0.321754	2.647715	2.902931
H	0.197759	1.882013	3.665408
C	-2.802272	4.119533	2.310371
H	-3.372023	3.329678	1.814015
C	-2.300766	5.309026	1.691265
H	-2.440657	5.592499	0.64548
C	-1.566918	6.05647	2.675417
H	-1.135449	7.047693	2.534486
C	-1.625951	5.320684	3.918958
H	-1.253949	5.661277	4.885253
C	-2.395644	4.128829	3.683419
H	-2.628878	3.360856	4.423954
Fe	0.671097	-4.275934	2.518691
Fe	-0.671097	4.275934	2.518691
C	-0.45466	-1.45036	-1.821052
Fe	-1.874845	-2.590472	-2.538126
C	0.45466	1.45036	-1.821052
Fe	1.874845	2.590472	-2.538126
C	-2.694288	-4.044155	-1.522396
H	-2.290957	-4.836258	-0.897956
C	-2.960769	-4.137935	-2.939486
H	-2.785894	-5.009184	-3.5662
C	-3.596247	-2.910529	-3.353637
H	-3.97208	-2.691492	-4.350066
C	-3.71683	-2.055545	-2.195729
H	-4.188433	-1.076214	-2.170476
C	-0.341222	-2.944373	-3.653313
H	-0.070823	-3.798836	-4.268864
C	-1.064572	-1.7806	-4.085514

H	-1.44818	-1.600022	-5.086139
C	1.064572	1.7806	-4.085514
H	1.44818	1.600022	-5.086139
C	0.341222	2.944373	-3.653313
H	0.070823	3.798836	-4.268864
C	2.960769	4.137935	-2.939486
H	2.785894	5.009184	-3.5662
C	3.596247	2.910529	-3.353637
H	3.97208	2.691492	-4.350066
C	3.71683	2.055545	-2.195729
H	4.188433	1.076214	-2.170476
C	2.694288	4.044155	-1.522396
H	2.290957	4.836258	-0.897956
C	3.153898	2.755196	-1.068773
H	3.118545	2.392983	-0.043485
C	0	2.769855	-2.259652
H	-0.644932	3.434934	-1.694905
C	1.178813	0.888086	-2.9591
H	1.622339	-0.102284	-2.983512
C	-1.178813	-0.888086	-2.9591
H	-1.622339	0.102284	-2.983512
C	-3.153898	-2.755196	-1.068773
H	-3.118545	-2.392983	-0.043485
C	0	-2.769855	-2.259652
H	0.644932	-3.434934	-1.694905
N	0	0	1.586311
H	0	0	2.622088

Table S145. Table of C_2-B3LYP Fc-2,5-localized (6^+) optimized cartesian coordinates

Atom	x	y	z
C(Fragment=1)	0.02462381	-1.14025969	-0.75000894
C(Fragment=1)	0.03614274	-0.71280611	0.60870106
C(Fragment=1)	-0.03614274	0.71280611	0.60870106
C(Fragment=1)	-0.02462381	1.14025969	-0.75000894
C(Fragment=1)	0.07556535	-2.40985806	-1.42795595
C(Fragment=1)	-0.18740851	-3.73038864	-0.91960396
H(Fragment=1)	-0.41386472	-3.97836133	0.10426203
C(Fragment=1)	-0.05373334	-4.66332073	-1.98110897
H(Fragment=1)	-0.19174805	-5.73463486	-1.90077098
C(Fragment=1)	0.24864873	-3.94764811	-3.17176996
H(Fragment=1)	0.39269071	-4.37338767	-4.15719796

C(Fragment=1)	0.29869144	-2.56637953	-2.85252595
H(Fragment=1)	0.53771307	-1.78408719	-3.56318194
C(Fragment=2)	-3.37651991	-2.24979722	-2.10023198
H(Fragment=2)	-3.46052621	-1.35284356	-1.49797298
C(Fragment=2)	-3.29834261	-4.46428418	-2.730016
H(Fragment=2)	-3.32444675	-5.54660153	-2.69457401
C(Fragment=2)	-3.0203135	-3.67189582	-3.87865699
H(Fragment=2)	-2.80086422	-4.04521749	-4.87158599
C(Fragment=2)	-3.06531732	-2.29978715	-3.48899798
H(Fragment=2)	-2.90454621	-1.44929384	-4.14028297
C(Fragment=2)	-3.51483103	-3.58458037	-1.628397
H(Fragment=2)	-3.73940671	-3.88148997	-0.611278
C(Fragment=1)	-0.07556535	2.40985806	-1.42795595
C(Fragment=1)	0.18740851	3.73038864	-0.91960396
H(Fragment=1)	0.41386472	3.97836133	0.10426203
C(Fragment=1)	0.05373334	4.66332073	-1.98110897
H(Fragment=1)	0.19174805	5.73463486	-1.90077098
C(Fragment=1)	-0.24864873	3.94764811	-3.17176996
H(Fragment=1)	-0.39269071	4.37338767	-4.15719796
C(Fragment=1)	-0.29869144	2.56637953	-2.85252595
H(Fragment=1)	-0.53771307	1.78408719	-3.56318194
C(Fragment=2)	3.37651991	2.24979722	-2.10023198
H(Fragment=2)	3.46052621	1.35284356	-1.49797298
C(Fragment=2)	3.51483103	3.58458037	-1.628397
H(Fragment=2)	3.73940671	3.88148997	-0.611278
C(Fragment=2)	3.29834261	4.46428418	-2.730016
H(Fragment=2)	3.32444675	5.54660153	-2.69457401
C(Fragment=2)	3.0203135	3.67189582	-3.87865699
H(Fragment=2)	2.80086422	4.04521749	-4.87158599
C(Fragment=2)	3.06531732	2.29978715	-3.48899798
H(Fragment=2)	2.90454621	1.44929384	-4.14028297
Fe(Fragment=2)	-1.5824462	-3.30972663	-2.40469697
Fe(Fragment=2)	1.5824462	3.30972663	-2.40469697
C(Fragment=1)	0.18899956	-1.50402023	1.84028706
Fe(Fragment=3)	1.47832345	-3.07145269	2.44121806
C(Fragment=1)	-0.18899956	1.50402023	1.84028706
Fe(Fragment=3)	-1.47832345	3.07145269	2.44121806
C(Fragment=3)	2.01458054	-4.85544801	1.48473305
H(Fragment=3)	1.3443854	-5.5307106	0.96825604
C(Fragment=3)	2.35365366	-4.91607852	2.86690905
H(Fragment=3)	1.96918839	-5.62798637	3.58721604
C(Fragment=3)	3.27068523	-3.86150319	3.14099007

H(Fragment=3)	3.7013602	-3.62865597	4.10737808
C(Fragment=3)	3.49811437	-3.14719745	1.92874508
H(Fragment=3)	4.13911571	-2.28188336	1.81177009
C(Fragment=1)	-0.21194016	-2.90479694	3.65137404
H(Fragment=1)	-0.61378197	-3.70293069	4.26398603
C(Fragment=1)	0.77839207	-1.95991483	4.04282906
H(Fragment=1)	1.27431085	-1.91700524	5.00467707
C(Fragment=1)	-0.77839207	1.95991483	4.04282906
H(Fragment=1)	-1.27431085	1.91700524	5.00467707
C(Fragment=1)	0.21194016	2.90479694	3.65137404
H(Fragment=1)	0.61378197	3.70293069	4.26398603
C(Fragment=3)	-2.35365366	4.91607852	2.86690905
H(Fragment=3)	-1.96918839	5.62798637	3.58721604
C(Fragment=3)	-3.27068523	3.86150319	3.14099007
H(Fragment=3)	-3.7013602	3.62865597	4.10737808
C(Fragment=3)	-3.49811437	3.14719745	1.92874508
H(Fragment=3)	-4.13911571	2.28188336	1.81177009
C(Fragment=3)	-2.01458054	4.85544801	1.48473305
H(Fragment=3)	-1.3443854	5.5307106	0.96825604
C(Fragment=3)	-2.72138527	3.76298057	0.90629907
H(Fragment=3)	-2.67046504	3.44863621	-0.12861293
C(Fragment=1)	0.56920987	2.63625739	2.3015441
H(Fragment=1)	1.33758094	3.15813406	1.74562611
C(Fragment=1)	-1.03555645	1.11153556	2.93387207
H(Fragment=1)	-1.74233316	0.29219608	2.91279106
C(Fragment=1)	1.03555645	-1.11153556	2.93387207
H(Fragment=1)	1.74233316	-0.29219608	2.91279106
C(Fragment=3)	2.72138527	-3.76298057	0.90629907
H(Fragment=3)	2.67046504	-3.44863621	-0.12861293
C(Fragment=1)	-0.56920987	-2.63625739	2.3015441
H(Fragment=1)	-1.33758094	-3.15813406	1.74562611
N(Fragment=1)	0	0	-1.51208693
H(Fragment=1)	0	0	-2.51961793

Table S146. Table of C_2-B3LYP Fc-3,4-localized (6^+) optimized cartesian coordinates

Atom	x	y	z
C(Fragment=1)	0	1.140771	0.741113
C(Fragment=1)	0.021225	0.713425	-0.617574
C(Fragment=1)	-0.021225	-0.713425	-0.617574
C(Fragment=1)	0	-1.140771	0.741113
C(Fragment=1)	0.021954	2.410934	1.419836
C(Fragment=1)	-0.273361	3.725407	0.913341
H(Fragment=1)	-0.506107	3.969468	-0.11002
C(Fragment=1)	-0.161082	4.660001	1.975869
H(Fragment=1)	-0.325238	5.72776	1.897177
C(Fragment=1)	0.16023	3.950418	3.165202
H(Fragment=1)	0.295093	4.378348	4.150979
C(Fragment=1)	0.243569	2.571264	2.844154
H(Fragment=1)	0.502849	1.794087	3.553301
C(Fragment=2)	-3.428174	2.174614	2.087582
H(Fragment=2)	-3.495909	1.283863	1.474185
C(Fragment=2)	-3.395792	4.381876	2.745859
H(Fragment=2)	-3.44557	5.463749	2.72466
C(Fragment=2)	-3.095934	3.580973	3.883012
H(Fragment=2)	-2.880213	3.946167	4.879778
C(Fragment=2)	-3.112262	2.213457	3.475704
H(Fragment=2)	-2.930052	1.358315	4.115097
C(Fragment=2)	-3.597448	3.511965	1.633752
H(Fragment=2)	-3.83314	3.8171	0.62158
C(Fragment=1)	-0.021954	-2.410934	1.419836
C(Fragment=1)	0.273361	-3.725407	0.913341
H(Fragment=1)	0.506107	-3.969468	-0.11002
C(Fragment=1)	0.161082	-4.660001	1.975869
H(Fragment=1)	0.325238	-5.72776	1.897177
C(Fragment=1)	-0.16023	-3.950418	3.165202
H(Fragment=1)	-0.295093	-4.378348	4.150979
C(Fragment=1)	-0.243569	-2.571264	2.844154
H(Fragment=1)	-0.502849	-1.794087	3.553301
C(Fragment=2)	3.428174	-2.174614	2.087582
H(Fragment=2)	3.495909	-1.283863	1.474185
C(Fragment=2)	3.597448	-3.511965	1.633752
H(Fragment=2)	3.83314	-3.8171	0.62158
C(Fragment=2)	3.395792	-4.381876	2.745859
H(Fragment=2)	3.44557	-5.463749	2.72466
C(Fragment=2)	3.095934	-3.580973	3.883012

H(Fragment=2)	2.880213	-3.946167	4.879778
C(Fragment=2)	3.112262	-2.213457	3.475704
H(Fragment=2)	2.930052	-1.358315	4.115097
Fe(Fragment=2)	-1.656002	3.26921	2.399861
Fe(Fragment=2)	1.656002	-3.26921	2.399861
C(Fragment=1)	0.161947	1.50747	-1.848705
Fe(Fragment=3)	1.430152	3.094879	-2.438024
C(Fragment=1)	-0.161947	-1.50747	-1.848705
Fe(Fragment=3)	-1.430152	-3.094879	-2.438024
C(Fragment=3)	1.937372	4.875615	-1.458881
H(Fragment=3)	1.25649	5.534121	-0.934894
C(Fragment=3)	2.277783	4.958559	-2.839507
H(Fragment=3)	1.884003	5.673629	-3.551597
C(Fragment=3)	3.21138	3.921741	-3.124948
H(Fragment=3)	3.647805	3.708067	-4.093211
C(Fragment=3)	3.447653	3.195926	-1.921219
H(Fragment=3)	4.101407	2.338936	-1.813895
C(Fragment=1)	-0.252149	2.907926	-3.657093
H(Fragment=1)	-0.663037	3.702199	-4.268699
C(Fragment=1)	0.753745	1.979202	-4.047361
H(Fragment=1)	1.254263	1.946735	-5.007278
C(Fragment=1)	-0.753745	-1.979202	-4.047361
H(Fragment=1)	-1.254263	-1.946735	-5.007278
C(Fragment=1)	0.252149	-2.907926	-3.657093
H(Fragment=1)	0.663037	-3.702199	-4.268699
C(Fragment=3)	-2.277783	-4.958559	-2.839507
H(Fragment=3)	-1.884003	-5.673629	-3.551597
C(Fragment=3)	-3.21138	-3.921741	-3.124948
H(Fragment=3)	-3.647805	-3.708067	-4.093211
C(Fragment=3)	-3.447653	-3.195926	-1.921219
H(Fragment=3)	-4.101407	-2.338936	-1.813895
C(Fragment=3)	-1.937372	-4.875615	-1.458881
H(Fragment=3)	-1.25649	-5.534121	-0.934894
C(Fragment=3)	-2.660351	-3.786279	-0.891826
H(Fragment=3)	-2.611671	-3.457983	0.138858
C(Fragment=1)	0.610902	-2.629688	-2.309259
H(Fragment=1)	1.38927	-3.138257	-1.754956
C(Fragment=1)	-1.018783	-1.131037	-2.940081
H(Fragment=1)	-1.73755	-0.322146	-2.918904
C(Fragment=1)	1.018783	1.131037	-2.940081
H(Fragment=1)	1.73755	0.322146	-2.918904
C(Fragment=3)	2.660351	3.786279	-0.891826

H(Fragment=3)	2.611671	3.457983	0.138858
C(Fragment=1)	-0.610902	2.629688	-2.309259
H(Fragment=1)	-1.38927	3.138257	-1.754956
N(Fragment=1)	0	0	1.503129
H(Fragment=1)	0	0	2.510646

S147. Table of C_1-B3LYP Fc-2-localized (6^+) optimized cartesian coordinates

Atom	x	y	z
C(Fragment=1)	-1.291487	-0.599448	0.048187
C(Fragment=1)	-0.776451	0.654288	0.062402
C(Fragment=1)	0.704398	0.560363	0.065047
C(Fragment=1)	0.986256	-0.871147	0.120991
C(Fragment=1)	-2.62668	-1.185567	0.037546
C(Fragment=1)	-3.744022	-0.793473	-0.771548
H(Fragment=1)	-3.734424	-0.014889	-1.521175
C(Fragment=1)	-4.853309	-1.617323	-0.435172
H(Fragment=1)	-5.836358	-1.574358	-0.88777
C(Fragment=1)	-4.4373	-2.536146	0.572521
H(Fragment=1)	-5.049665	-3.304376	1.02793
C(Fragment=1)	-3.067749	-2.283576	0.858904
H(Fragment=1)	-2.466632	-2.801726	1.596803
C(Fragment=2)	-1.810185	-3.410654	-2.478401
H(Fragment=2)	-0.827096	-2.96762	-2.588774
C(Fragment=2)	-4.054146	-3.854291	-2.758559
H(Fragment=2)	-5.080131	-3.798458	-3.101009
C(Fragment=2)	-3.548273	-4.755591	-1.778522
H(Fragment=2)	-4.120627	-5.506054	-1.247664
C(Fragment=2)	-2.159921	-4.482873	-1.604141
H(Fragment=2)	-1.492458	-5.010243	-0.932879
C(Fragment=2)	-2.981206	-3.021434	-3.19063
H(Fragment=2)	-3.047777	-2.226423	-3.922735
C(Fragment=1)	2.183798	-1.694681	0.146243
C(Fragment=1)	3.516723	-1.476149	-0.371254
H(Fragment=1)	3.88075	-0.561572	-0.809241
C(Fragment=1)	4.255634	-2.679657	-0.253917
H(Fragment=1)	5.289413	-2.81869	-0.547956
C(Fragment=1)	3.418028	-3.665077	0.34707
H(Fragment=1)	3.70442	-4.677949	0.599307
C(Fragment=1)	2.159384	-3.069351	0.603609
H(Fragment=1)	1.327607	-3.555182	1.09732
C(Fragment=3)	3.380877	-0.750918	3.254956

H(Fragment=3)	2.663155	0.060473	3.304508
C(Fragment=3)	4.717711	-0.66575	2.76973
H(Fragment=3)	5.21405	0.223968	2.402958
C(Fragment=3)	5.305498	-1.961678	2.870041
H(Fragment=3)	6.311113	-2.229168	2.570156
C(Fragment=3)	4.332549	-2.843628	3.418646
H(Fragment=3)	4.466949	-3.901939	3.604309
C(Fragment=3)	3.141103	-2.097067	3.655425
H(Fragment=3)	2.215049	-2.486241	4.058842
Fe(Fragment=2)	-3.289356	-2.787905	-1.14178
Fe(Fragment=3)	3.626333	-2.039369	1.632013
C(Fragment=1)	-1.468545	1.955888	0.198857
Fe(Fragment=4)	-3.20477	2.646315	1.1849
C(Fragment=1)	1.583776	1.631682	-0.003463
Fe(Fragment=5)	2.933546	2.315248	-1.692348
C(Fragment=4)	-5.098087	1.766365	1.223509
H(Fragment=4)	-5.586135	1.299271	0.37837
C(Fragment=4)	-5.188019	3.139704	1.589722
H(Fragment=4)	-5.750776	3.903756	1.066945
C(Fragment=4)	-4.385567	3.339348	2.750078
H(Fragment=4)	-4.229956	4.281404	3.262019
C(Fragment=4)	-3.800841	2.087551	3.101935
H(Fragment=4)	-3.126823	1.911616	3.931543
C(Fragment=1)	-2.576111	3.933156	-0.319437
H(Fragment=1)	-3.218187	4.653019	-0.812903
C(Fragment=1)	-1.82798	4.153162	0.874598
H(Fragment=1)	-1.804143	5.069592	1.452427
C(Fragment=1)	2.407998	3.813568	-0.381452
H(Fragment=1)	2.449526	4.865602	-0.645401
C(Fragment=1)	3.47047	3.037853	0.172125
H(Fragment=1)	4.467408	3.391716	0.415935
C(Fragment=5)	4.450975	2.767387	-3.166671
H(Fragment=5)	5.304904	3.40782	-2.981693
C(Fragment=5)	3.164552	3.186135	-3.602148
H(Fragment=5)	2.867708	4.203139	-3.834511
C(Fragment=5)	2.330603	2.025121	-3.698527
H(Fragment=5)	1.293666	2.010201	-4.013119
C(Fragment=5)	4.410677	1.358516	-2.976964
H(Fragment=5)	5.231883	0.743242	-2.626785
C(Fragment=5)	3.108481	0.901914	-3.31529
H(Fragment=5)	2.762076	-0.124366	-3.253185
C(Fragment=1)	3.001488	1.713035	0.345315

H(Fragment=1)	3.560031	0.891684	0.766757
C(Fragment=1)	1.292707	2.961654	-0.551031
H(Fragment=1)	0.342325	3.243952	-0.97869
C(Fragment=1)	-1.162469	2.93764	1.203179
H(Fragment=1)	-0.522825	2.772946	2.062014
C(Fragment=4)	-4.241958	1.116104	2.15918
H(Fragment=4)	-3.964384	0.070614	2.143847
C(Fragment=1)	-2.362857	2.585714	-0.732008
H(Fragment=1)	-2.786257	2.12003	-1.612822
N(Fragment=1)	-0.180749	-1.490635	0.097544
H(Fragment=1)	-0.314847	-2.485878	-0.023005

Table S148. Table of C_1-B3LYP Fc-3-localized (6^+) optimized cartesian coordinates

Atom	x	y	z
C(Fragment=1)	1.303686	-0.064497	0.593131
C(Fragment=1)	0.489411	1.089142	0.538464
C(Fragment=1)	-0.891059	0.645475	0.337486
C(Fragment=1)	-0.850029	-0.742678	0.206416
C(Fragment=1)	2.759593	-0.263204	0.727082
C(Fragment=1)	3.584116	0.065757	1.86375
H(Fragment=1)	3.22278	0.449538	2.816868
C(Fragment=1)	4.94613	-0.226963	1.533096
H(Fragment=1)	5.802182	-0.108329	2.194905
C(Fragment=1)	4.977519	-0.761265	0.203833
H(Fragment=1)	5.861571	-1.109057	-0.327817
C(Fragment=1)	3.63647	-0.795292	-0.29312
H(Fragment=1)	3.323363	-1.157064	-1.271745
C(Fragment=2)	2.489348	-3.368318	2.284827
H(Fragment=2)	1.428328	-3.233481	2.484375
C(Fragment=2)	4.784227	-3.401842	2.570006
H(Fragment=2)	5.775082	-3.278081	3.000502
C(Fragment=2)	4.495022	-3.922541	1.269639
H(Fragment=2)	5.228177	-4.256059	0.538769
C(Fragment=2)	3.076078	-3.903755	1.091814
H(Fragment=2)	2.543107	-4.242623	0.205285
C(Fragment=2)	3.545264	-3.063927	3.19887
H(Fragment=2)	3.427088	-2.630366	4.189183
C(Fragment=1)	-1.845583	-1.798411	0.003451
C(Fragment=1)	-3.13093	-1.714787	-0.635269
H(Fragment=1)	-3.560818	-0.827972	-1.084899
C(Fragment=1)	-3.75295	-3.000059	-0.575485

H(Fragment=1)	-4.728384	-3.254553	-0.982679
C(Fragment=1)	-2.855452	-3.900517	0.075632
H(Fragment=1)	-3.023772	-4.958662	0.260359
C(Fragment=1)	-1.678808	-3.172357	0.422259
H(Fragment=1)	-0.825201	-3.5864	0.954334
C(Fragment=3)	-0.570507	-2.567453	-3.103779
H(Fragment=3)	0.117769	-1.726547	-3.025729
C(Fragment=3)	-1.893575	-2.52183	-3.651823
H(Fragment=3)	-2.390875	-1.641566	-4.056194
C(Fragment=3)	-2.460808	-3.832746	-3.544671
H(Fragment=3)	-3.462358	-4.124303	-3.856963
C(Fragment=3)	-1.489172	-4.689163	-2.934494
H(Fragment=3)	-1.623127	-5.745198	-2.705195
C(Fragment=3)	-0.319723	-3.908048	-2.662389
H(Fragment=3)	0.598775	-4.274484	-2.205774
Fe(Fragment=2)	3.785558	-1.955436	1.430272
Fe(Fragment=3)	-1.964764	-3.109378	-1.651282
C(Fragment=1)	0.955395	2.465964	0.508817
Fe(Fragment=4)	2.153767	3.486908	-1.096766
C(Fragment=1)	-2.040016	1.582741	0.380945
Fe(Fragment=5)	-4.012104	1.597662	1.185315
C(Fragment=4)	3.718913	2.517754	-2.159035
H(Fragment=4)	4.385575	1.788022	-1.703809
C(Fragment=4)	3.908779	3.940467	-2.181934
H(Fragment=4)	4.757277	4.478629	-1.764526
C(Fragment=4)	2.793951	4.521958	-2.867142
H(Fragment=4)	2.628078	5.583881	-3.039885
C(Fragment=4)	1.917927	3.462579	-3.258718
H(Fragment=4)	0.966523	3.577391	-3.774499
C(Fragment=1)	2.24691	4.409772	0.759075
H(Fragment=1)	3.05247	5.081395	1.050342
C(Fragment=1)	1.033452	4.774134	0.093012
H(Fragment=1)	0.741932	5.774839	-0.218467
C(Fragment=1)	-3.232672	3.507406	0.968371
H(Fragment=1)	-3.597156	4.369193	1.523494
C(Fragment=1)	-3.731117	3.047351	-0.292909
H(Fragment=1)	-4.536737	3.498356	-0.869065
C(Fragment=5)	-6.078819	1.372892	1.411232
H(Fragment=5)	-6.823857	1.901457	0.819911
C(Fragment=5)	-5.494976	1.831209	2.634774
H(Fragment=5)	-5.717302	2.771761	3.135102
C(Fragment=5)	-4.544642	0.851245	3.06631

H(Fragment=5)	-3.924455	0.913262	3.958184
C(Fragment=5)	-5.489649	0.110485	1.087776
H(Fragment=5)	-5.724149	-0.49705	0.217551
C(Fragment=5)	-4.54104	-0.212534	2.109948
H(Fragment=5)	-3.918318	-1.102795	2.145356
C(Fragment=1)	-3.007382	1.865306	-0.649313
H(Fragment=1)	-3.132722	1.296353	-1.567908
C(Fragment=1)	-2.208514	2.602143	1.391606
H(Fragment=1)	-1.641176	2.667136	2.318162
C(Fragment=1)	0.267467	3.583532	-0.099163
H(Fragment=1)	-0.686364	3.530079	-0.615605
C(Fragment=4)	2.491737	2.230458	-2.831949
H(Fragment=4)	2.043397	1.246189	-2.953446
C(Fragment=1)	2.22157	2.993814	0.965768
H(Fragment=1)	3.013127	2.413079	1.427983
N(Fragment=1)	0.479091	-1.121667	0.363523
H(Fragment=1)	0.809411	-2.084305	0.345688

Table S149. Table of C_1-B3LYP Fc-4-localized (6^+) optimized cartesian coordinates

Atom	x	y	z
C(Fragment=1)	1.272839	-0.612956	-0.005353
C(Fragment=1)	0.746595	0.667523	-0.021204
C(Fragment=1)	-0.706706	0.527408	-0.020032
C(Fragment=1)	-1.002925	-0.858046	-0.065161
C(Fragment=1)	2.619475	-1.176594	-0.033052
C(Fragment=1)	3.788448	-0.74503	0.67115
H(Fragment=1)	3.839973	0.08118	1.367473
C(Fragment=1)	4.870312	-1.597966	0.313215
H(Fragment=1)	5.882369	-1.532215	0.694297
C(Fragment=1)	4.383847	-2.5741	-0.60247
H(Fragment=1)	4.961349	-3.373766	-1.050356
C(Fragment=1)	2.999737	-2.327484	-0.811853
H(Fragment=1)	2.349634	-2.885572	-1.47661
C(Fragment=2)	1.946526	-3.182295	2.677412
H(Fragment=2)	0.984499	-2.700641	2.813668
C(Fragment=2)	4.193701	-3.669239	2.838576
H(Fragment=2)	5.242065	-3.617212	3.10455
C(Fragment=2)	3.598619	-4.627351	1.969249
H(Fragment=2)	4.113635	-5.433777	1.462257
C(Fragment=2)	2.20859	-4.327987	1.869466
H(Fragment=2)	1.481845	-4.887771	1.291169

C(Fragment=2)	3.173368	-2.77471	3.275851
H(Fragment=2)	3.310366	-1.926214	3.935597
C(Fragment=1)	-2.195535	-1.706129	-0.098024
C(Fragment=1)	-3.556561	-1.435626	0.280411
H(Fragment=1)	-3.950432	-0.489421	0.61655
C(Fragment=1)	-4.311098	-2.637728	0.1762
H(Fragment=1)	-5.368802	-2.74043	0.386966
C(Fragment=1)	-3.443194	-3.667433	-0.278576
H(Fragment=1)	-3.720719	-4.693361	-0.485626
C(Fragment=1)	-2.152629	-3.103849	-0.460914
H(Fragment=1)	-1.293559	-3.640645	-0.844969
C(Fragment=3)	-2.989978	-1.005815	-3.365164
H(Fragment=3)	-2.180015	-0.286488	-3.405074
C(Fragment=3)	-4.341306	-0.735963	-3.00055
H(Fragment=3)	-4.757053	0.231976	-2.744788
C(Fragment=3)	-5.068372	-1.96036	-3.058445
H(Fragment=3)	-6.118578	-2.089691	-2.826847
C(Fragment=3)	-4.166654	-2.986222	-3.46074
H(Fragment=3)	-4.411317	-4.034009	-3.583406
C(Fragment=3)	-2.882581	-2.397848	-3.65037
H(Fragment=3)	-1.980878	-2.919487	-3.947104
Fe(Fragment=2)	3.345235	-2.703029	1.202203
Fe(Fragment=3)	-3.506108	-2.125064	-1.681207
C(Fragment=1)	1.438929	1.966088	-0.151314
Fe(Fragment=4)	3.136693	2.678611	-1.192311
C(Fragment=1)	-1.616184	1.647709	0.052764
Fe(Fragment=5)	-3.042391	2.272696	1.675726
C(Fragment=4)	5.02978	1.805358	-1.336162
H(Fragment=4)	5.565147	1.334307	-0.522082
C(Fragment=4)	5.096396	3.182167	-1.695506
H(Fragment=4)	5.684105	3.94329	-1.197284
C(Fragment=4)	4.232324	3.387499	-2.809782
H(Fragment=4)	4.046424	4.332898	-3.304869
C(Fragment=4)	3.633737	2.136537	-3.140013
H(Fragment=4)	2.916879	1.964514	-3.934084
C(Fragment=1)	2.569581	3.930327	0.371015
H(Fragment=1)	3.230322	4.637013	0.858768
C(Fragment=1)	1.775787	4.181056	-0.786388
H(Fragment=1)	1.730837	5.111723	-1.339401
C(Fragment=1)	-2.401947	3.813572	0.456988
H(Fragment=1)	-2.43597	4.852932	0.76195
C(Fragment=1)	-3.439855	3.086194	-0.192839

H(Fragment=1)	-4.409206	3.470256	-0.488644
C(Fragment=5)	-4.643009	2.676952	3.04937
H(Fragment=5)	-5.48149	3.32772	2.832986
C(Fragment=5)	-3.385642	3.076938	3.587822
H(Fragment=5)	-3.103727	4.084085	3.871136
C(Fragment=5)	-2.566268	1.911492	3.70341
H(Fragment=5)	-1.551541	1.879666	4.082366
C(Fragment=5)	-4.595241	1.274662	2.825031
H(Fragment=5)	-5.39123	0.674486	2.400927
C(Fragment=5)	-3.320012	0.801701	3.232844
H(Fragment=5)	-2.969961	-0.221252	3.158612
C(Fragment=1)	-2.975575	1.754296	-0.396061
H(Fragment=1)	-3.530913	0.964599	-0.884816
C(Fragment=1)	-1.311339	2.922409	0.656893
H(Fragment=1)	-0.386409	3.169138	1.160005
C(Fragment=1)	1.095293	2.974285	-1.119064
H(Fragment=1)	0.426884	2.831102	-1.960303
C(Fragment=4)	4.12759	1.159317	-2.229331
H(Fragment=4)	3.854464	0.112348	-2.206862
C(Fragment=1)	2.36845	2.573247	0.757662
H(Fragment=1)	2.820474	2.087787	1.613947
N(Fragment=1)	0.203703	-1.48785	-0.039719
H(Fragment=1)	0.321581	-2.483752	0.091475

Table S150. Table of C_1-B3LYP Fc-5-localized (6^+) optimized cartesian coordinates

Atom	x	y	z
C(Fragment=1)	-1.235466	-0.577226	-0.067168
C(Fragment=1)	-0.732402	0.737073	-0.015062
C(Fragment=1)	0.704431	0.65088	-0.052533
C(Fragment=1)	1.043174	-0.736695	-0.071621
C(Fragment=1)	-2.583965	-1.154024	-0.06763
C(Fragment=1)	-3.730247	-0.752262	-0.832217
H(Fragment=1)	-3.758376	0.054379	-1.558787
C(Fragment=1)	-4.820224	-1.611121	-0.485038
H(Fragment=1)	-5.814465	-1.570629	-0.926796
C(Fragment=1)	-4.364708	-2.558673	0.477615
H(Fragment=1)	-4.955139	-3.352813	0.927696
C(Fragment=1)	-2.98205	-2.295534	0.733138
H(Fragment=1)	-2.353257	-2.825534	1.448964
C(Fragment=2)	-1.7951	-3.310393	-2.681203
H(Fragment=2)	-0.817879	-2.846559	-2.808781

C(Fragment=2)	-4.051362	-3.775202	-2.91251
H(Fragment=2)	-5.090842	-3.722346	-3.227695
C(Fragment=2)	-3.507039	-4.70133	-1.967525
H(Fragment=2)	-4.056698	-5.477432	-1.443424
C(Fragment=2)	-2.114103	-4.416772	-1.825606
H(Fragment=2)	-1.412701	-4.960481	-1.178949
C(Fragment=2)	-2.993749	-2.916729	-3.358981
H(Fragment=2)	-3.093408	-2.096201	-4.062172
C(Fragment=1)	2.255342	-1.494883	-0.149193
C(Fragment=1)	3.628659	-1.04281	-0.123338
H(Fragment=1)	3.947364	-0.005345	-0.086847
C(Fragment=1)	4.500241	-2.168557	-0.261852
H(Fragment=1)	5.58658	-2.125637	-0.316591
C(Fragment=1)	3.697245	-3.348492	-0.286588
H(Fragment=1)	4.056429	-4.369125	-0.367661
C(Fragment=1)	2.330442	-2.9491	-0.156396
H(Fragment=1)	1.490612	-3.646998	-0.138681
C(Fragment=3)	2.694111	-1.811116	3.480788
H(Fragment=3)	1.845131	-1.146984	3.636619
C(Fragment=3)	4.057381	-1.410214	3.35793
H(Fragment=3)	4.432128	-0.391306	3.436924
C(Fragment=3)	4.844944	-2.58069	3.112746
H(Fragment=3)	5.923822	-2.607383	2.978063
C(Fragment=3)	3.961781	-3.705492	3.072922
H(Fragment=3)	4.24681	-4.741792	2.906072
C(Fragment=3)	2.628789	-3.225383	3.296358
H(Fragment=3)	1.723661	-3.836787	3.322855
Fe(Fragment=2)	-3.249722	-2.743307	-1.278199
Fe(Fragment=3)	3.441739	-2.355211	1.524295
C(Fragment=1)	-1.476659	2.00943	0.162011
Fe(Fragment=4)	-3.240922	2.635825	1.177273
C(Fragment=1)	1.577415	1.842399	-0.078304
Fe(Fragment=5)	3.111884	2.506131	-1.39108
C(Fragment=4)	-5.149199	1.772657	1.160025
H(Fragment=4)	-5.641329	1.358269	0.281644
C(Fragment=4)	-5.221883	3.13736	1.599543
H(Fragment=4)	-5.77035	3.93663	1.103306
C(Fragment=4)	-4.422644	3.261504	2.778867
H(Fragment=4)	-4.258714	4.18012	3.341627
C(Fragment=4)	-3.858695	1.983172	3.073357
H(Fragment=4)	-3.194231	1.749226	3.902549
C(Fragment=1)	-2.641814	3.977171	-0.297029

H(Fragment=1)	-3.305865	4.697843	-0.770604
C(Fragment=1)	-1.884878	4.18843	0.899739
H(Fragment=1)	-1.871539	5.09432	1.505569
C(Fragment=1)	2.189399	4.077431	-0.381737
H(Fragment=1)	2.196504	5.107714	-0.729486
C(Fragment=1)	3.161654	3.471706	0.471037
H(Fragment=1)	4.03414	3.956283	0.90157
C(Fragment=5)	4.902771	2.955242	-2.395815
H(Fragment=5)	5.69456	3.591113	-2.000938
C(Fragment=5)	3.778737	3.391941	-3.166047
H(Fragment=5)	3.562546	4.418209	-3.453043
C(Fragment=5)	2.971291	2.247328	-3.462187
H(Fragment=5)	2.046657	2.245947	-4.021366
C(Fragment=5)	4.792005	1.540797	-2.217485
H(Fragment=5)	5.508831	0.899993	-1.690652
C(Fragment=5)	3.604139	1.10145	-2.868624
H(Fragment=5)	3.225828	0.08087	-2.933433
C(Fragment=1)	2.796877	2.100581	0.650465
H(Fragment=1)	3.320926	1.395575	1.300588
C(Fragment=1)	1.231309	3.084784	-0.733865
H(Fragment=1)	0.372235	3.232455	-1.379768
C(Fragment=1)	-1.181123	2.979622	1.189002
H(Fragment=1)	-0.5139	2.81821	2.033035
C(Fragment=4)	-4.306342	1.061524	2.076045
H(Fragment=4)	-4.049312	0.008578	2.011356
C(Fragment=1)	-2.402658	2.640109	-0.748763
H(Fragment=1)	-2.818522	2.190803	-1.648731
N(Fragment=1)	-0.167664	-1.431283	-0.064489
H(Fragment=1)	-0.27699	-2.422955	-0.245729

Table S151. Table of (1) crystal cartesian coordinates

Atom	x	y	z
C(Fragment=1)	8.79440267	2.64844016	3.71419827
C(Fragment=1)	9.87100267	3.26094016	4.36739827
C(Fragment=1)	10.43490267	4.21764016	3.45959827
C(Fragment=1)	9.79250267	4.06914016	2.24029827
C(Fragment=1)	7.91500267	2.67524016	1.35919827
C(Fragment=1)	8.13190267	1.42234016	0.80269827
H(Fragment=1)	8.88239878	0.77641195	1.20820084
C(Fragment=1)	7.37400267	1.01234016	-0.27540173
H(Fragment=1)	7.52905759	0.04155159	-0.69780855

C(Fragment=1)	6.41650267	1.84824016	-0.81090173
H(Fragment=1)	5.90950267	1.57064016	-1.53880173
C(Fragment=1)	6.21240267	3.10444016	-0.26320173
H(Fragment=1)	5.4759834	3.75791016	-0.68220486
C(Fragment=1)	6.96510267	3.51804016	0.83159827
H(Fragment=1)	6.80608138	4.48539097	1.26036935
C(Fragment=1)	7.81890267	1.71434016	4.29599827
C(Fragment=1)	7.36720267	0.43114016	3.82519827
H(Fragment=1)	7.56989733	0.01895984	2.85880173
C(Fragment=1)	6.60930267	-0.20285984	4.84479827
H(Fragment=1)	6.21660267	-1.04505984	4.79589827
C(Fragment=1)	6.56200267	0.68524016	5.95549827
H(Fragment=1)	6.07986826	0.49673389	6.89193395
C(Fragment=1)	7.26970267	1.86404016	5.60209827
H(Fragment=1)	7.37351655	2.7313809	6.22003251
C(Fragment=2)	4.85250267	3.18194016	3.42999827
H(Fragment=2)	5.35667062	4.05779396	3.07843773
C(Fragment=2)	4.59910267	2.01174016	2.67649827
H(Fragment=2)	4.87550633	1.84389487	1.65653308
C(Fragment=2)	3.90970267	1.09814016	3.52449827
H(Fragment=2)	3.57017856	0.12169183	3.24850545
C(Fragment=2)	3.75190267	1.69674016	4.78589827
H(Fragment=2)	3.28437096	1.25406981	5.64050757
C(Fragment=2)	4.32560267	2.99464016	4.72509827
H(Fragment=2)	4.35400499	3.70711276	5.52289279
C(Fragment=1)	10.54280267	2.83974016	5.61159827
C(Fragment=1)	10.05460267	2.33644016	6.86519827
H(Fragment=1)	9.02430629	2.19880647	7.11906109
C(Fragment=1)	11.15220267	2.05134016	7.70969827
H(Fragment=1)	11.09391037	1.67226772	8.70860071
C(Fragment=1)	12.35370267	2.35864016	6.99779827
H(Fragment=1)	13.35333022	2.26049324	7.36659624
C(Fragment=1)	11.97410267	2.81654016	5.71799827
H(Fragment=1)	12.65264161	3.10352574	4.94203165
C(Fragment=4)	10.69060267	-0.21665984	4.43919827
H(Fragment=4)	10.13144776	0.12320061	3.5925929
C(Fragment=4)	10.14420267	-0.72765984	5.63179827
H(Fragment=4)	9.10274222	-0.85290677	5.84292223
C(Fragment=4)	11.20560267	-1.04395984	6.49619827
H(Fragment=4)	11.11242493	-1.44680978	7.4830771
C(Fragment=4)	12.42740267	-0.73705984	5.83279827
H(Fragment=4)	13.41280759	-0.86598595	6.22935244

C(Fragment=4)	12.10110267	-0.22745984	4.54669827
H(Fragment=4)	12.79498095	0.09093222	3.79699203
C(Fragment=1)	11.38060267	5.34654016	3.69869827
C(Fragment=1)	10.92010267	6.70464016	3.59559827
H(Fragment=1)	9.89708178	7.01249047	3.53596234
C(Fragment=1)	12.04540267	7.56974016	3.58689827
H(Fragment=1)	12.02260151	8.63609763	3.50168179
C(Fragment=1)	13.20270267	6.76044016	3.71119827
H(Fragment=1)	14.21085844	7.11727485	3.74570839
C(Fragment=1)	12.80670267	5.40964016	3.78279827
H(Fragment=1)	13.4639236	4.57134699	3.88391803
C(Fragment=5)	11.29560267	5.70764016	7.06359827
H(Fragment=5)	10.73418586	4.80309054	7.17084165
C(Fragment=5)	10.75960267	7.00014016	6.86149827
H(Fragment=5)	9.72056975	7.24536988	6.78957496
C(Fragment=5)	11.83410267	7.91244016	6.77139827
H(Fragment=5)	11.75248738	8.96699268	6.60966414
C(Fragment=5)	13.03550267	7.18704016	6.93089827
H(Fragment=5)	14.02283168	7.59942502	6.92640831
C(Fragment=5)	12.70590267	5.82194016	7.09769827
H(Fragment=5)	13.399989	5.01803732	7.22763822
C(Fragment=1)	10.23150267	4.57374016	0.92109827
C(Fragment=1)	9.75990267	4.24804016	-0.40430173
H(Fragment=1)	8.89868782	3.65546641	-0.63247999
C(Fragment=1)	10.62440267	4.84254016	-1.35130173
H(Fragment=1)	10.52525284	4.77904746	-2.41480443
C(Fragment=1)	11.63700267	5.53074016	-0.66000173
H(Fragment=1)	12.43700055	6.08168101	-1.10874173
C(Fragment=1)	11.42190267	5.37514016	0.72149827
H(Fragment=1)	12.03686124	5.78166159	1.49704085
C(Fragment=3)	11.88180267	1.80404016	0.87129827
H(Fragment=3)	11.31008085	1.50426006	1.72462473
C(Fragment=3)	11.56230267	1.54554016	-0.47960173
H(Fragment=3)	10.70459628	1.00822349	-0.82677682
C(Fragment=3)	12.56460267	2.11384016	-1.29410173
H(Fragment=3)	12.59934745	2.08910464	-2.36325137
C(Fragment=3)	13.52240267	2.72684016	-0.43280173
H(Fragment=3)	14.40849313	3.24195285	-0.74005184
C(Fragment=3)	13.09280267	2.53094016	0.89289827
H(Fragment=3)	13.59858753	2.87541196	1.77063448
N(Fragment=1)	8.77080267	3.13554016	2.40899827
Fe(Fragment=2)	5.72980267	1.56154016	4.32529827

Fe(Fragment=4)	11.27050267	0.93794016	6.00989827
Fe(Fragment=5)	11.98900267	6.50134016	5.31509827
Fe(Fragment=3)	11.65570267	3.55094016	-0.15020173